On the Development of Fold Initiator Patterns to Promote Progressive Folding of Hot Stamped Ultra-High Strength Axial Crush Structures

by

Suh Ho Lee

A thesis
presented to the University of Waterloo
in fulfillment of the
thesis requirement for the degree of
Master of Applied Science
in
Mechanical and Mechatronics Engineering

Waterloo, Ontario, Canada, 2021

Author’s Declaration

I hereby declare that I am the sole author of this thesis. This is a true copy of the thesis, including any required final revisions, as accepted by my examiners.

I understand that my thesis may be made electronically available to the public.

Abstract

The effect of fold initiator design on the performance of axial crush rails fabricated using ultra high strength steels (UHSS) is examined in a combined experimental-numerical-analytical study. Of particular interest is the effect of fold initiator pattern and spacing in promoting stable folding. A key factor in introducing UHSS into energy absorbing components is the loss of ductility with increases in strength. Thus, the effect of material fracture limit on the ability of crush structures to fold is also considered.

The UHSS steel grade considered for the majority of this research (and all of the experiments) was hot stamped Ductibor® 1000-AS, with a thickness of 1.2 or 1.6 mm and tensile strength of 1000 MPa. In addition, performance metrics, developed as part of this research, are applied to a broader range of steel grades spanning strengths in the range of 270-1500 MPa.

Ductibor® 1000-AS double hat sections were hot stamped, spot welded and tested in axial crush under quasi-static and dynamic loading conditions. A baseline fold initiator pattern was first evaluated on axial crush rails that incorporated rudimentary single initiators indented on two opposing faces. Dynamic crush tests considering this baseline pattern repeatedly showed a global buckling mode, parent metal fracture and spot weld failure. The numerical models demonstrated close agreement with the observed buckling and failure modes and the measured force-displacement response.

Following these baseline results, a numerical parametric study was undertaken to evaluate the effect of six different fold initiator patterns on the dynamic axial crush response. These patterns consider different design variables such as fold initiator location, sequence, orientation, spacing and symmetry. The progressive folding mode was predicted for three of the six patterns considered. The most stable pattern corresponded to that identified by Wierzbicki and Abramowicz (1983) within their Superfolding Element analysis. This pattern utilizes fold initiators placed on the channel section faces and flanges in an alternating fashion to promote a rolling (serpentine) collapse of the flange. The effect of fold initiator spacing on stability (for the most stable initiator pattern) was further examined for each sheet thickness. The numerical models revealed a strong dependence on initiator spacing and served to identify a specific initiator spacing for each thickness that resulted in stable folding and largely suppressed fracture within the tight folds that form during axial crush; moreover, these initiator spacing values agreed well with those predicted using the analytical model of Wierzbicki and Abramowicz (1983).

Experimental assessment of the model predictions was undertaken by performing quasi-static and dynamic axial crush experiments for a subset of the parametric cases comprising the baseline and stable folding initiator patterns and a range of initiator spacing. In general, the crush response of the 1.6 mm specimens agreed extremely well with the model predictions and served to validate the predicted effect of fold initiator pattern and spacing on folding stability and fracture suppression. The 1.2 mm specimens exhibited a global buckling instability that was not predicted by the numerical models. The cause of this instability was attributed to the fold initiator forming process which resulted in significant distortion of the cross-section and a loss of buckling resistance. Subsequent numerical models that combined detailed simulation of the indentation process and mapped the forming predictions onto the crush simulations were able to capture the observed buckling response.

As part of the continued analysis of axial crush results, three metrics were developed to predict axial crush performance and potentially serve as design tools for screening material selection and initiator design. One metric, termed the "Relative Bending Limit," was derived from the ratio of the measured plastic work in V-bend fracture characterization tests to the predicted plastic work in the Superfolding Element analysis. This metric was successfully demonstrated to be a predictor of the fracture extent observed in crush columns made of different materials. Another metric, termed the "Folding Transition Indicator," was derived from the ratio of the measured slenderness ratio of the crush specimens to the theoretical critical slenderness ratio. The metric strongly reflected the various collapse modes observed in these axial columns. By plotting the two metrics on the same graph, a 2D response map was constructed that successfully captured the overall trends in the fracture extent *vs.* deformation mode response.

This research demonstrates that the analytical design approach in configuring fold initiator patterns has significant potential in promoting progressive folding in hot stamped UHSS. By adopting a carefully designed fold initiator pattern and analytically determined fold initiator spacing, improved folding stability was achieved without significant sacrifice in absorbed energy. The results support the application of Ductibor® 1000-AS in frontal crush structures, but point to the need for considerable care in design of fold initiators for which the current performance metrics should serve as design tools. The current findings are tempered by the fact the axial crush specimens, particularly the thinner 1.2 mm samples, were subject to shape distortion due to the indentation method in producing the fold initiators. In future work, as well as in industrial hot stamping practice, these specimens should be fabricated with fold initiators integrated within the hot stamping dies in order to limit distortion and further improve the axial crush performance of hot stamped Ductibor® 1000-AS components.

Acknowledgements

First and foremost, I would like to thank Professor Michael Worswick for providing me with this great opportunity and guidance throughout my journey. His teachings broadened my horizons in the field of solid mechanics and granted me invaluable engineering skill sets that will carry on to the future.

I would also like to thank Professor Clifford Butcher, Dr. Armin Abedini, and Dr. Pedram Samadian for their guidance and help in material characterization and constant enthusiasm for my research. My appreciation also goes out to Dr. José Imbert for his support with the crash experiments, as well as Research Associates Amir Zhumagulov, Ryan George, and Kenneth Cheong for helping me with forming the crush specimens and conducting characterization tests. I also extend my gratitude to Eckhard Budziarek, Doug Hirst, and Tom Gawel for always being eager to help and keeping everyone safe in the lab.

Support and sponsorship from Honda R&D Americas, ArcelorMittal, Promatek Research Centre, as well as the Natural Sciences and Engineering Research Council, the Canada Research Chair Secretariat, the Canadian Foundation for Innovation, the Ontario Advanced Manufacturing Consortium, the Ontario Research Fund, and the Ontario Centres for Excellence are highly appreciated and recognized.

Thanks to the *hot stamping* boys Alireza Mohamadizadeh, Cale Peister, Cameron Tolton, and Matt Tummers for being excellent team workers. In addition, I acknowledge the occasional *Dyna* discussions at Molly's with Kaab Omer, Stan Lu, Edward Gutierrez, and Nicholas Aydemir. A shout-out also goes to Sante DiCecco, Hossein Pishyar, Jacqueline Noder, Raphael Boulis, Ruijian He, and Dylan Budnick for their friendship and encouragement in the office.

Lastly, I would like to thank my parents, Grace Shin and Thomas Lee, as well as my brother Michael Lee for their unconditional support.

Dedication

부모님께

(To my parents, Grace and Thomas)

Table of Contents

Author's Declaration ii
Abstract iii
Acknowledgements v
Dedication vi
List of Figures xi
List of Tables xxiv
List of Symbols xxvi
1.0 Introduction 1
1.1. Automotive Sheet Steel 3
1.1.1. Hot Stamping Process 5
1.1.2. Hot Stamping Process Parameters 7
1.1.1. Hot Stamping Steel Alloys 8
1.2. Material Modelling for Sheet Steel 10
1.2.1. Plasticity Response 10
1.2.2. Fracture Response 15
1.3. Crashworthiness and Axial Crush of Hot Stamped Steels 20
1.3.1. Axial Crush Experiments 21
1.3.2. Numerical Modelling of Axial Crush 23
1.3.3. Triggering Methods in Axial Crush 26
1.4. Crush Mechanics of Thin-Walled Structures 28
1.4.1. Crush Mechanics of multi-corner elements 29
1.4.2. Effective Crush Distance 34
1.4.3. Crushing of Square Tubes and Hat Channels 37
1.5. Summary of Previous Work and Scope of Thesis 41
2.0 Experimental Methods 42
2.1. Overview of Experimental Studies 42

2.1.1. Part 1: Baseline Study 44

2.1.2. Part 2: Fold Initiator Pattern Study 46

2.1.3. Part 3: Fold Initiator Spacing Study 49

2.2. Specimen Fabrication 51

2.2.1. Forming 51

2.2.2. Indenting 55

2.2.3. Spot Welding 59

2.2.4. Sandblasting 61

2.3. Dynamic Axial Crush Setup 63

2.4. Quasi-Static Axial Crush Setup 68

3.0 Numerical Models 69

3.1. Material Model for Hot Stamped Ductibor® 1000-AS 70

3.1.1. Constitutive Behaviour 72

3.1.2. Quasi-Static Hardening Response 72

3.1.3. Fracture Response 76

3.1.4. Spot Weld Response 82

3.2. Fold Initiator Treatment 84

3.2.1. Finite Element Mesh of Single Hat Section 84

3.2.2. Displacement Approach to Introduce Fold Initiators 85

3.2.3. Indentation Approach to Introduce Fold Initiators 85

3.3. Axial Crush Models 93

3.3.1. Dynamic Axial Crush Model 93

3.3.2. Quasi-static Axial Crush Model 99

4.0 Axial Crush Results and Discussion 100

4.1. Part 1: Crush Response of Baseline Specimens 101

4.1.1. Experimental Results 101

4.1.2. Numerical Results – Baseline Specimens 107

4.2. Part 2: Effect of Fold Initiator Pattern 109

4.2.1. Numerical Simulations of the Effect of Fold Initiator Pattern ... 109
4.2.2. Experimental Results – TCA and TF Initiator Patterns ... 120
4.3. Part 3: Effect of Fold Initiator Spacing ... 127
4.3.1. Experimental Results – Effect of Initiator Spacing ... 128
4.3.2. Numerical Results – Simulations of Effect of Initiator Spacing ... 133
4.4. Investigation of the Unstable 1.2 mm TF Cases ... 140
4.4.1. Effect of Section Concavity due to Flange Indentation ... 140
5.0 Development of Axial Crush Performance Metrics ... 144
5.1. Axial Crush Data Taken from Previous Research ... 145
5.2. Energy Absorption Performance Metric ... 149
5.2.1. Crush Energy Efficiency ... 150
5.3. Fracture Resistance Metric ... 153
5.3.1. Relative Bending Limit ... 154
5.4. Folding Stability Metric ... 160
5.4.1. Folding Transition Indicator ... 160
5.5. Performance Map and Benefit of Enhanced Fold Initiator Design ... 165
6.0 Conclusions and Recommendations ... 168
6.1. Conclusions ... 168
6.2. Recommendations ... 170
References ... 171
Appendix A. Solution Procedure for Superfolding Element Analysis ... 185
A.1. Perfectly Plastic Assumption ... 190
A.2. Hardening Assumption ... 190
A.3. Numerical Solution Procedure ... 192
Appendix B. MATLAB® Source Code for SE Analysis ... 197
B.1. Main Program ... 198
B.2. Newton-Raphson Function ... 200
B.3. Other Functions ... 203

B.3.1. Geometric Constant Function 203
B.3.2. Hardening Model Function 204
Appendix C. List of Alloys and Hardening Models for SE Analysis 206
Appendix D. Simplified Approximation of Relative Bending Limit 209
D.1. Approximate Solution for W_{SE} 209
D.2. Approximate Solution for $W_{v\text{-}bend}$ 210
D.2.1. Weak Work Hardening Assumption 210
D.2.2. Strong Work Hardening Assumption 212
Appendix E. High Strain Rate Tensile Test 215
Appendix F. FE Model Description and Results of Nakazima 50 mm Biaxial Dome Test 217
F.1. Boundary Condition 217
F.2. Material model and Mesh 218
F.3. Contact Algorithm 220
F.4. Results 221
F.4.1. Damage Contour Plot 221
F.4.2. Punch Force *vs.* Punch Height 222

List of Figures

Figure 1: Comparison of axial crash specimens, fabricated from the hot stamped steel grades: (a) Usibor® 1500-AS and (b) Ductibor® 500-AS. 2

Figure 2: Different steel grades in the BIW for 2016 Honda Civic, from Honda (2019). Tensile strength of the steels ranges from 270 MPa to 1500 MPa based on the location. 3

Figure 3: Illustration of vehicle structures (highlighted in blue) with different functions: (a) dent resistant components such as hoods (b) anti-intrusion components such as b-pillars and (c) energy absorption components such as front rails. The images are adapted from Hilfrich and Seidner (2008) 3

Figure 4: Comparison of various steel grades in tensile strength and elongation, adapted from Billur et al., (2015). The properties of ArcelorMittal hot stamping steel grades (after die-quenching) are shown including the main focus of the thesis, Ductibor® 1000-AS. 4

Figure 5: Illustration of (a) direct hot stamping and (b) indirect hot stamping processes, adapted from Karbasian and Tekkaya (2010) 6

Figure 6: CCT diagram for 22MnB5, adapted from Tekkaya et al. (2007) 6

Figure 7: Illustration of contact surface between blank and die at the microscopic level, adapted from George (2011) 7

Figure 8: Flow curve of water-cooled, die-quenched Usibor® 1500-AS by Bardelcik et al. (2012) and Ductibor® 500-AS by Samadian et al. (2018) and Abedini (2019) 13

Figure 9: Illustration of a continuum element with damage caused by microcracks (Lemaitre, 1985) 15

Figure 10: Example of a fracture surface (Basaran et al., 2010) 17

Figure 11: Fracture loci of Usibor® 1500-AS in five different quench conditions, adapted from Samadian et al. (2020). Experimental points were obtained from butterfly, hole expansion, plane strain tension dome, v-bend and biaxial tension dome tests. The dashed and solid lines represent fracture curves based on the plane strain tension dome and v-bend tests, respectively. 18

Figure 12: Effect of mesh refinement on equivalent plastic strain during plane strain simulation in LS-Dyna (Eller et al., 2014) 19

Figure 13: Mesh regularized fracture curves of martensitic 22MnB5 for three different element sizes (L), adapted from Eller et al. (2014) 20

Figure 14: Dynamic axial crush specimens of Usibor® 1500-AS under the fully martensitic condition, adapted from Omer et al. (2017b) 21

Figure 15: Four different quenched conditions of Usibor® 1500-AS specimens, adapted from Omer et al. (2017b) 22
Figure 16: Crush mode comparison of various IDH specimens, adapted from Omer et al. (2017b)... 22
Figure 17: Dynamic axial crush specimens from Peister (2019): (a) 1.2mm Ductibor® 500-AS and (b) 1.2mm TWB consisting of Ductibor® 500-AS welded to Usibor® 1500-AS 23
Figure 18: Examples of dynamic axial crush numerical models: (a) double hat channel with shell elements (b) polygonal column with shell elements and (c) square column with solid elements. All models were solved using the non-linear, explicit finite element code LS-Dyna (Livermore Software Technology Corporation, 2016). 24
Figure 19: Comparison of (a) a spot weld using a beam element (Park et al., 2018) and (b) a spot weld using eight hexagonal solid elements (Tummers, 2020). 25
Figure 20: Meso-scale modelling of spot weld nuggets, adapted from Chen *et al.* (2014). 25
Figure 21: Numerical model setup of front end module (left) and bolt connection between the battery base and side frame member, using constrained nodal rigid bodies (right), adapted from Tummers (2020) 26
Figure 22: Asymmetric (left) and symmetric (right) insertion of fold initiators near the top end of double hat channel crush specimens, adapted from Chen (2001) 27
Figure 23: Different forms of mechanical fold initiators: (a) corner notches on steel square tubes (b) beads for steel square tubes (c) machined dents for 6063 aluminum square tubes (d) machine grooves for mild steel circular tubes (e) holes for mild steel square tubes and (f) pulling strips for 6063 aluminum square tubes 27
Figure 24: Final deformed images of (a) axially crushed hydroformed aluminum alloy tubes (Williams *et al.,* 2010) and (b) non-hydroformed steel tubes (Abramowicz and Jones, 1984). Different repeating modes within each tube are highlighted in red. 29
Figure 25: Inextensional and extensional deformation of corner elements (Hayduk and Wierzbicki, 1984) 29
Figure 26: (a) Quasi-inextensional mode and (b) extensional mode of corner elements 30
Figure 27: (a) Quasi-inextensional mechanism and (b) extensional mechanism of corner elements .. 31
Figure 28: Illustration of: (a) superfolding element and (b) its folding mechanism 32
Figure 29: Progressive collapse of hat structure flange: (a) idealized folding where $\alpha f = \pi/2$ and (b) actual folding where $\alpha f \geq \pi/2$, adapted from Ohkubo et al. (1974) 35

Figure 30: Representation of fully crushed superfolding element by densely packed circles of equal size (Wierzbicki et al., 1992) 35
Figure 31: Progressive folding of square columns idealized as a flat sheet undergoing two subsequent bends with radius r and R, respectively (Abramowicz, 1983) 36
Figure 32: A typical force-displacement (F-D) curve of axial crush models. The crush force spikes after full consolidation. 36
Figure 33: Paper models of three collapse modes for axial crushing of square tubes (Abramowicz and Jones, 1984) 37
Figure 34: (a) Cross-section of a single top hat and (b) double top hat geometry. (c) Four SEs and a backing plate forming the single top hat profile and (d) Eight SEs forming the double top hat collapse profile (White et al., 1999). 38
Figure 35: Two collapse modes of double hat specimens: (a) rolling deformation of flange during progressive collapse and (b) in-plane deformation of plane leading to irregular folding¸ adapted from White and Jones (1999) 39
Figure 36: Flowchart outlining the experimental studies 42
Figure 37: Baseline fold initiator pattern in two configurations: (a) monolithic and (b) TWB. 44
Figure 38: Geometric parameters of (a) a hat channel cross-section and (b) a double hat channel. Dimensions are in millimeters. The entire perimeter of the cross-section, Z, is 200 mm for top hat and 400 mm for double hat geometry, respectively. 45
Figure 39: Illustration of different design variables considered in the fold initiator patterns 46
Figure 40. Schematic diagrams of the seven selected fold initiator patterns in a double hat channel. The red-highlighted patterns were chosen for dynamic sled tests 47
Figure 41: Illustration of pattern TF: isometric view (left) and side view (right). Flange and top fold initiators are collinear and facing towards the same direction. 48
Figure 42: Comparison of TF pattern (left) and TFO pattern (right). In TFO pattern, flange fold initiators are translated down with relative to top fold initiators by the half spacing, H 48
Figure 43: (a) a double hat channel modelled as 8 SEs and (b) a SE overlaid on pattern TF. 49
Figure 44: Five different fold initiator spacings considered: (a) 20 mm (b) 25 mm (c) 27.5 mm (d) 30 mm and (e) 35 mm. The sheet thicknesses considered are indicated as either white (1.2 mm) or grey (1.6 mm) above for each pattern. Inside the parenthesis are the corresponding specimen designations listed in the test matrix in Table 3. 50
Figure 45: Five stages of axial crush specimen fabrication in the thesis 51

Figure 46: Drawing of a pre-formed blank. All units are in mm. 52
Figure 47: Overview of forming setup, adapted from Peister (2019) 52
Figure 48: Illustration of a die set: (a) CAD and (b) actual image, adapted from Peister (2019)........ 53
Figure 49: Overview of a transfer system, adapted from Peister (2019) 54
Figure 50. Forming process flow of a hat channel rail, adapted from University of Waterloo Forming and Crash Lab (2018)... 55
Figure 51. Illustrations of pre-weld indentation (a) fixture (b) setup, and post-weld indentation (c) fixture and (d) setup. As-fabricated indentation fixtures are shown in (e) for pre-weld and (f) for post-weld. The (g) indenter punch geometry (h) and its as-fabricated condition is shown as well. 56
Figure 52: Illustration of inner bosses: (a) CAD and (b) as-fabricated... 57
Figure 53: Indentation setup, utilizing manual hydraulic press at the University of Waterloo Engineering Machine Shop 57
Figure 54: Illustration of in-plane distortion in baseline and TF specimens after indentation; and, sectional imprints at the impact-end for (c) baseline specimen and (d) TF specimen 58
Figure 55: Illustration of (a) the flange to flange width (b) its measurement results and (c) the draft angle and (d) its results for 1.2mm Baseline and TF specimens. Along the x-axis, the 0 mm position refers to the impact-end of the specimens.. 59
Figure 56: Images of spot weld (a) spacer (b) setup at the Promatek Research Centre 60
Figure 57: Spot weld drawing for the baseline pattern. 61
Figure 58: Spot weld drawing for the fold initiator pattern TF. *For all patterns*, the spot weld pitch for un-indented regions remained 25 mm while that of indented region was set equal to the fold initiator spacing, 2H. 61
Figure 59: Sandblasted top hat channels before spot welding. Flanges were protected with masking tape to retain the aluminum silicon coating for the subsequent spot weld operation........................... 62
Figure 60: Crash sled at the University of Waterloo for dynamic axial crash tests, adapted from Peister (2019).. 63
Figure 61: CAD geometry of a (a) clamp set designed by Omer *et al.* (2017b) and (b) clamp sets with rail, forming a “rail assembly” 64
Figure 62: Mounting plate with clamps at the (a) wall-end, (b) impact-end, and (c) entire rail assembly mounted to the fixed barrier wall. Three piezoelectric load cells measure the crush force. Honeycomb arrestors provide 165 mm free crush distance. 65

Figure 63: Dynamic axial crush test setup, highlighting various test equipment: (i) one Photron SA-4 high speed camera, (ii) two Photron AX-100 high speed cameras, (iii) various lighting sources, (iv) a laser trigger system, and (v) a laser displacement sensor. 66
Figure 64: Still initial images of the dynamic axial crush test specimen from (a) top view (b) left view, and (c) right view 66
Figure 65: Quasi-static axial crush test setup: (a) overview and (b) mounted specimen. 68
Figure 66: Flowchart illustrating the overall scope of the numerical models presented in this thesis. Two different approaches were considered to create the fold initiator patterns in the FE simulations. 70
Figure 67: Stress *vs.* strain responses of die-quenched Ductibor® 1000-AS from (a) uniaxial tensile test (with five repeats) and (b) shear test (with six repeats) performed by Abedini (2018).................72
Figure 68: Equivalent stress *vs.* equivalent plastic strain curve for Ductibor® 1000-AS due to Abedini (2018) based on tensile and shear data. 73
Figure 69: Measured and predicted flow stress vs. equivalent plastic strain for a range of strain rates (0.01 s^{-1}, 1 s^{-1}, 10 s^{-1}, 100 s^{-1} and 1000 s^{-1}) for die-quenched Ductibor® 1000-AS (solid curves). The symbols are from the fit using Equation (40). 74
Figure 70: Normalized stresses vs. strain rates for various strain rates. The normalization ratio was obtained with respect to the 0.01 s^{-1} UTS. Note that the strain rates deviate to some degree from their nominal values as the test results revealed lower rates than the nominal values (see Appendix E). ...75
Figure 71: Specimen geometries used for the fracture limit characterization tests of die-quenched Ductibor® 1000-AS (1.2mm sheet steel)..76
Figure 72: Plane stress fracture locus of the die-quenched Ductibor® 1000-AS sheet. The measured fracture and damage integrated strains in Table 9, excluding 5 mm Nakazima dome test, were used to calibrate the Bai and Wierzbicki (2008) fracture model, described in Equation (44), due to Abedini and Butcher (2020). 79
Figure 73: Predicted punch force vs. punch height response from Nakazima 50 mm dome biaxial tension simulation of the die-quenched Ductibor® 1000-AS: (a) without and (b) with regularization. The measured response by Samadian (2018) is overlaid with the predicted responses. The 0 mm punch height refers to the first point of contact between the punch and the specimen. 80
Figure 74: Regularization factor for calibrated fracture locus of die-quenched Ductibor® 1000-AS.81
Figure 75: Illustration of the finite element mesh used to model the single hat channel subjected to dynamic loading. The unclamped length was reduced to 375 mm for the quasi-static load cases. 84

Figure 76: Illustration of the displacement approach used to recreate the TF pattern in the FE model. 85
Figure 77: Illustrations of the workflow within the numerical models of the TF (Top-Flange) pattern indentation, using the indentation approach. Each fold initiator is indented one at a time. 86
Figure 78: Illustration of the indenting sequence taken within the numerical models of flange indentation. Numbers indicate the sequence from the first to last. 87
Figure 79: Illustration of the indentation model setup: (a) pre-weld and (b) post-weld 88
Figure 80: Close-up image of the mesh used for fixture and the indenter for the flange indentation model...88
Figure 81: Illustration of an indented zone to demonstrate the effect of the coarsening algorithm: (a) before and (b) after applying the coarsening algorithm...89
Figure 82: Constrained nodes for a springback analysis of a double hat channel, which follows the flange indentation simulation...90
Figure 83: Indented shapes of the 1.2 mm (left) and 1.6 mm (right) specimens (SP-D12-275 and SP-D16-300) in Part 2: (a) numerical models and (b) actual tested samples 91
Figure 84: The measurements of flange-to-flange width (see Figure 55 for definition of this measurement) taken from the indented numerical models and test specimens for (a) 1.2 mm (SP-D12-275) and (b) 1.6 mm (SP-D16-300) specimens. The x-axis origin corresponds to the impact-end of the specimens...92
Figure 85: Illustrations for (a) overview of axial crush model and (b) various clamps and bosses used in the axial crush tests. The double channel hat model is obtained from the previous fold initiator modeling stage, either using the "displacement approach" or the "indentation approach". 93
Figure 86. Illustration of mesh for (a) impactor plate, clamps and bosses at (b) impact end (c) and wall end. The inner shells were given a thickness of 4 mm and increased density to achieve the similar mass properties as the actual bosses, and showing the outer surfaces after accounting the shell thickness. 95
Figure 87: Illustration of bolt connection using a beam element, joined by either nodal rigid bodies or a node, strategically located at the geometric center of holes. (a) wall clamps and (b) impact clamps. 96
Figure 88: Illustration of the spot weld beam element tied to the quadrilateral elements at the rail flanges...98
Figure 89: Illustration of the tied interface between the element edges of the outer clamps to the fixed wall..98

Figure 90: Deformation history of the monolithic Ductibor® 1000-AS baseline specimen (repeat #1) under a dynamic sled test. The displacements in (a) to (f) refer to the crush distance, and the time is measured relative to the trigger of the data acquisition unit, shown in *Figure 63*. 102
Figure 91: Force vs. crush displacement (F-D) plot of the monolithic Ductibor® 1000-AS baseline specimen (repeat #1). Labels (a) to (f) are the displacements at which images in Figure 90 are taken. 102
Figure 92: Final deformed specimens: (a) hot-stamped monolithic Ductibor® 1000-AS and (b) hot-stamped TWB consisting of Ductibor® 1000-AS and Usibor® 1500-AS 103
Figure 93: Close up images of (a) hot-stamped monolithic Ductibor® 1000-AS and (b) hot-stamped TWB consisting of Ductibor® 1000-AS and Usibor® 1500-AS. The fracture locations in (a) are encircled in red. 103
Figure 94: Force vs. crush displacement (F-D) and absorbed energy vs. crush displacement (E-D) for Ductibor® 1000-AS monolithic baseline specimens. 104
Figure 95: Deformation history of a TWB baseline specimen (repeat #1) under a dynamic test. The displacement in (a) to (f) refers to the crush distance and the time is measured relative to the trigger of the data acquisition unit, shown in Figure 63. 105
Figure 96: Force vs. crush displacement (F-D) plot of the TWB baseline: (a) specimen repeat #1 and (b) the average of three repeats. Labels (a) to (f) correspond to the crush displacements at which images in Figure 95 are taken. 106
Figure 97: Observed and predicted deformation of the monolithic Ductibor® 1000-AS baseline pattern (repeat #1) at five different crush displacements from the experiment and the numerical model 107
Figure 98: Comparison of the measured and predicted force and energy absorption vs. crush displacement (F-D and E-D) for the monolithic Ductibor® 1000-AS baseline pattern 108
Figure 99: Contour plot of damage variable (D) at 250 mm crush distance 110
Figure 100. Bar chart showing initial peak forces for the numerical models shown in Figure 99 113
Figure 101: Bar charts showing predicted absorbed energy for all fold initiator patterns at: (a) 165mm and (b) 250mm crush distance, as well as the energy calculated using the Superfolding Element Analysis (see Appendix A for detailed solution) 114
Figure 102: Bar charts showing the predicted eroded energy of the parent metal for all fold initiator patterns at: (a) 165mm and (b) 250mm crush distance 114
Figure 103: A response map showing effect of deformation mode on the predicted eroded energy vs. absorbed energy for numerical patterns at 165 mm and 250 mm crush distance. A pictorial illustration is shown as an example for each deformation mode, listed. 115

Figure 104: Mid-cross-section (highlighted blue) images across the top face: (a) TF and (b) TFO at 250 mm crush displacement. Skipped fold initiators in the TFO pattern are circled in red. 116
Figure 105: Plots of (a) Force *vs.* crush displacement and (b) absorbed energy and eroded energy *vs.* crush displacement for the TF and TFO patterns 116
Figure 106: Predicted force *vs.* crush displacement (F-D) for the (a) TF pattern and (b) FCS pattern. Each encircled peak or valley corresponds to the crush displacement at which a collapse of a local fold is completed. 117
Figure 107: Side view images of the predicted TF pattern deformation, taken at the crush displacements corresponding to each peak of the F-D plot in Figure 106. 117
Figure 108: Comparison of $L2$ error calculated using for three progressively folded patterns, as well as an irregular folded pattern. 118
Figure 109: Images of (a) the prepared specimens prior to axial crush test and the final deformed shapes of three different patterns after the dynamic crush test: (b) BA, (c) TCA, and (d) TF. Minimum three repeats were tested for each pattern. 120
Figure 110: Measured responses of force *vs.* crush displacement (F-D) and energy *vs.* crush displacement (E-D) for three patterns: (a) BA, (b) TCA and (c) TF. The average response of the repeats is highlighted black. 121
Figure 111: Bar chart showing the average peak force for three fold initiator patterns. The error bands represent the scatter in the measured data (i.e. min/max) 122
Figure 112: Absorbed energy for three fold initiator patterns at (a) 165 mm and (b) 250 mm crush distance. The error bands represent the scatter in the measured data. SEA refers to the theoretical energy by the SE Analysis (Abramowicz and Wierzbicki, 1989) from Appendix A. 123
Figure 113: High-speed images of a TCA specimen (repeat #2) from the top view, which globally buckled. The crush distances (a) to (g) correspond to the local force peaks labelled in Figure 114. 124
Figure 114: Force vs. crush displacement plot of a TCA specimen (repeat #2), which globally buckled. 124
Figure 115: Still images of a TF specimen (repeat #3), which showed mixed folding and buckling. The crush distances (a) to (f) corresponds to the local peak forces labelled in Figure 116. 125
Figure 116: Force *vs.* crush displacement plot of TF specimen #3, which showed mixed folding and buckling...126

Figure 117: Final deformed shapes of 1.2mm specimens for the fold initiator spacing study. The SP-D12-200 specimen test was stopped at the early testing stage due to excessive out-of-plane buckling. 128
Figure 118: Final deformed images of the 1.6mm thick TF specimens with four different fold initiator spacings ($2Hindent$) ranging from (a) 20mm to (d) 35mm. The analytical folding wavelength ($2H$) obtained from the SE solution is 30 mm (see Appendix A), which corresponds to the most uniform folding in the specimens. 129
Figure 119: Force and absorbed energy *vs.* crush displacement for the 1.6mm TF crush specimens at four different initiator spacings: (a) 20 mm, (b) 25 mm, (c) 30 mm and (d) 35mm. The force peaks and valleys (symbols) are labelled for one sample for each initiator spacing to illustrate the crush displacements used to calculate the L_2 error using Equations (48) and (49). 130
Figure 120: The average measured absorbed energy plotted against the crush displacement for 1.6mm thick TF specimens of four different fold initiator spacings 131
Figure 121: Side view images of final deformed 1.6mm specimens with four different fold initiator spacing—(a) 20 mm, (b) 25 mm, (c) 30 mm and (d) 35 mm. Red zones indicate major fracture regions 132
Figure 122: Front view images of final deformed 1.6mm specimens with four different fold initiator spacing—(a) 20 mm, (b) 25 mm, (c) 30 mm and (d) 35 mm. Red zones indicate regions of fracture. 132
Figure 123: Still images taken from the quasi-static crush models of 1.2mm thick TF specimens, with fold initiator spacing ranging from (a) 20 mm to (c) 35 mm. 134
Figure 124: Predicted and actual deformed images at 230 mm crush displacement for the 1.2 mm axial crush specimens in Part 3 for the three different fold initiator spacings. Note that the experiment in (a) was interrupted prior to 230 mm crush displacement due to excessive lateral displacement. 135
Figure 125: Still images taken from the quasi-static crush models of 1.6mm thick TF specimens, with fold initiator spacing ranging from (a) 20 mm to (d) 35 mm. 136
Figure 126: Deformed images of the numerical models of 1.6 mm rails at 230 mm crush distance—each at different spacing ranging from (a) 20mm to (d) 35mm. 137
Figure 127: Force and absorbed energy *vs.* crush displacement for the 1.6 mm TF crush models (red lines) at four different initiator spacings: (a) 20 mm, (b) 25 mm, (c) 30 mm and (d) 35 mm. The measured (average) force and absorbed energy responses are overlaid as comparison (black lines). The

force peaks and valleys (symbols) in the numerical responses are labelled, whose crush displacements were used to calculate the L_2 error using Equations (48) and(49). 138
Figure 128: $L2$ errors for 1.6 mm rails of Part 3. Both numerical (yellow) and experimental (blue) results are shown here. 139
Figure 129: Final crushed, front view image of the TF rail from (a) the experiment (repeat #3), (b) the indented numerical model and (c) the displaced numerical model 141
Figure 130: Final crushed, side view image of the TF rail from (a) the experiment (repeat #3), (b) the indented numerical model and (c) the displaced numerical model. 141
Figure 131: High-speed, front view images of TF rail undergoing a dynamic sled test at three different crush displacements: (a) experiment (repeat #3) and its corresponding numerical models: (b) indented model and (c) displaced model. 142
Figure 132: Measured and predicted mean crush force of 1.2 mm monolithic axial crush specimens in Table 19 plotted against their reported UTS level by several authors in parentheses. The dotted lines represent polynomial lines of best fit. The experimental mean force was calculated using the free crush distance. The theoretical mean force was calculated using the SE Analysis (Wierzbicki and Abramowicz, 1983) whose solution procedure can be found in Appendix A. 149
Figure 133: Crush Energy Efficiency ($\eta crush$) for all of the steel grades in Table 19 plotted against their reported UTS levels by several authors in parentheses. 151
Figure 134: Crush Energy Efficiency ($\eta crush$) of the monolithic crush specimens in Table 19 plotted in terms of increasing UTS (left to right). As-tested images of each crush specimen are also shown above the bar chart. For brevity, only one thickness configuration for each material is shown (*e.g.* Ductibor® 1000-AS 1.2 mm). 152
Figure 135: Illustration of (a) Usibor® 1500-AS crushed specimen, showing fracture along the sidewall or topwall, which correspond to the (b) SE horizontal bending region and (c) v-bend test. αSE is the SE crush angle in unit of radian and θ is the VDA bend angle (VDA, 2010) in units of degrees (°). 153
Figure 136: Measured (a) bending moment evolution from v-bend tests on various materials by Noder and Butcher (2020) and Cheong (2019b). The following properties were calculated using the methodology developed by Noder *et al.* (2020): (b) Stress metric evolution (c) Plastic work evolution and (d) Plastic work at the onset of fracture, using a 5% drop in the stress metric criterion. 156

Figure 137: Bar chart of $\chi bend$ in the descending order, calculated using Equation (58) with two different hardening assumptions: (a) perfectly plastic assumption or (b) hardening assumption in Equation (56). The calibrated hardening models can be found in Appendix C. 158
Figure 138: Crush Energy Efficiency *vs.* Relative Bending Limit calculated using Equation (50) and (58). 159
Figure 139: Illustration of (a) asymmetric collapse of double hat column, modeled as 8 joined SE by White et al. (1999) and (b) the double hat cross-section with dimensions. The entire perimeter Z can be approximated as $Z \approx 2a + 2b + 4f$. Note that Z was taken as 400 mm for all double hat channels considered in the current thesis. 161
Figure 140: Illustration of (a) asymmetric collapse of single hat column, modeled as 4 joined SE and a backing plate by White et al. (1999) and (b) the single hat cross-section with dimensions shown. The entire perimeter Z can be approximated as $Z \approx 2a + 2b + 4f$. Images adapted from White et al. (1999). 163
Figure 141: Plot of deformation mode vs. Folding Transition Indicator ($\eta fold$). The legend is shown in the table. Note that $\eta fold$ for TWB specimens were calculated by assuming the specimen length (L) in Equations (67) and (70) to be the same as their reduced effective column length. 164
Figure 142: A 2D response map of Relative Bending Limit (χbend) *vs.* Folding Transition Indicator (ηfold) for the monolithic and TWB crush specimens for which material fracture data (v-bend) was available. 166
Figure 143: Modified plot of deformation mode *vs.* $\eta fold$. The black symbols are from Figure 141. The red and green symbols represent 1.2 mm and 1.6 mm Ductibor® 1000-AS specimens, respectively. The solid and open symbols represent the BA and TF patterns, respectively. 167
Figure 144: Side view images of the baseline and TF specimens from the dynamic experiments, at the crush displacement corresponding to initial peak force in F-D graphs. The corresponding times for the images taken are 0.078 s and 0.070 s for BA and TF, respectively, which are measured relative to the trigger of the data acquisition unit (see Figure 63). 167
Figure A.1: Illustration of the Superfolding Element and its constitutive surfaces 1 to 6. The surface elements from quasi-inextensional mode (white) and extensional mode (black) are coloured separately for distinguishment. 186
Figure A.2: Illustration of double hat cross-section modelled by eight (8) joined Superfolding Elements (White et al., 1999). Z refers to the entire mid-shell perimeter of the double hat cross-section, which is eight times the base length of the SE ($8 \times C$). 188

Figure A.3: Flow chart illustration of the Newton-Raphson method used in solving the SE analysis. The initial estimate used for H and r was 100, while the tolerances for both system variables were set as 0.01. 194
Figure A.4: Theoretical prediction of SE system variables: (a) toroidal radius (r) and (b) folding wavelength (2H) plotted against sheet thickness (t) for die-quenched Ductibor® 1000-AS. The predicted toroidal radius are 2.9 mm and 3.54 mm, while the folding wavelengths are 27.6 mm and 30.7 mm for 1.15 mm and 1.55 mm thick sheets, respectively. 195
Figure A.5: Theoretical prediction of SE system variables: (a) toroidal radius (r) and (b) folding wavelength (2H) plotted against sheet thickness (t) for six different steel alloys. $I1$, $I3$ were assumed as 0.567 and 1.173 in the solution, given $\varphi o = 42.5°$ (see Figure A.1) 195
Figure A.6: Theoretical prediction of mean crushing force (Pm) plotted against sheet thickness (t) for six different steel alloys, which is obtained from the SE analysis. 196
Figure D.1: θf vs. $Wv - bend/t2$ for all materials whose hardening exponent is below 0.2. Mild 270 steel grade, whose uniform elongation is 0.271 (Noder *et al.,* 2020), is excluded here. The dashed line represents a line of best fit. 211
Figure D.2: Relative Bending Limit ($\chi bend$) vs. $a1\theta f/K$ in Equation (D.9). The different levels of fracture severity are commented. The dotted line represents the linear line of best fit. 212
Figure D.3: Response plot of the predicted *vs.* measured v-bend plastic work, showing a good, linear correlation. The predicted v-bend plastic works for all materials are calculated using Equation (D.13) and (D.14) 213
Figure D.4: Different terms in Equation (D.15) plotted against the hardening exponent (n). 214
Figure E.1: Measured tensile stress *vs.* strain responses at nominal strain rate of (a) 1 s^{-1} (b) 10 s^{-1} (c) 100 s^{-1} high strain rate tensile tests and (d) Hopkinson bar test with 1000 s^{-1}. Five repeats were conducted for each test (Imbert and Zhumagulov, 2019). 215
Figure E.2: Measured strain rates for tensile tests at nominal strain rate of (a) 1 s^{-1} (b) 10 s^{-1} (c) 100 s^{-1} and (d) Hopkinson bar test with 1000 s^{-1}. Five repeats were conducted for each test. 216
Figure F.1: Numerical model for the Nakazima 50 mm dome simulations: (a) overall setup and (b) setup, highlighting shim. Quarter symmetry were imposed about x-y plane and y-z plane. 218
Figure F.2: Four different blank mesh sizes considered in the dome simulations: (a) 5.0 mm, (b) 2.5 mm, (c) 1.2 mm, and (d) 0.6 mm. The region between 60 mm and 75 mm radii was meshed finely. 219

Figure F.3: Damage (D) contour plot of the 50 mm blanks, whose element sizes range from (a) 5.0 mm to (d) 0.6 mm. The images are taken at the measured (average) limiting dome height, which is 24.0 mm, approximately, reported by Samadian (2018)..221
Figure F.4: Predicted punch force *vs.* punch height responses for Nakazima dome (50 mm) models of die-quenched Ductibor® 1000-AS: (a) numerical model without the lockbead and shim (b) model with lockbead and shim. The measured test results by Samadian (2018) are overlaid for comparison.....222

List of Tables

Table 1: Chemical composition (maximum weight %) of ArcelorMittal hot stamping steels, from ArcelorMittal (2021) 8

Table 2: Mechanical properties of ArcelorMittal hot stamping steels after hot stamping and paint baking, from ArcelorMittal (no date; 2016a; 2016b; 2016c; 2016d) 9

Table 3: Test matrices devised for the experimental studies. The length of the dynamic and quasi-static crush specimens are 500 mm and 375 mm, respectively. The detailed parametric aspects for each study are presented in Section 2.1.1 to 2.1.3. 43

Table 4: Spot weld schedule used for the hot-stamped Ductibor® 1000-AS rail specimens 60

Table 5: List of tasks and the corresponding researchers responsible for constitutive characterization of die-quenched Ductibor® 1000-AS. The highlighted tasks (in red) represent contributions of the author of this thesis. 71

Table 6: List of tasks and the corresponding researchers responsible for fracture locus calibration of Ductibor® 1000-AS. The highlighted tasks represent contributions of the author of this thesis. 71

Table 7: Calibrated constants for die-quenched Ductibor® 1000-AS using modified Hockett-Sherby equation (see Equation (39)) 73

Table 8: Calibrated constants for the die-quenched Ductibor® 1000-AS using the strain rate sensitive model given by Equation (40). 75

Table 9: List of idealized stress triaxiality and the measured average fracture strain (equivalent plastic strain) obtained from each fracture characterization test, and (the names of responsible researchers). For 50 mm dome test, stress triaxiality was estimated using Equation (41) to (43). Likewise, the fracture strain of 50 mm dome test was damage integrated by Butcher (2020) 77

Table 10: Calibrated constants for the die-quenched Ductibor® 1000-AS using the Bai-Wierzbicki (2008) fracture model given by Equation (44). 78

Table 11: GISSMO parameters used for the calibrated fracture locus of die-quenched Ductibor® 1000-AS 81

Table 12: Calibrated parameter for the spot weld model, *MAT_SPOTWELD_DA (Livermore Software Technology Corporation), by Tolton (2020). The spot weld diameter was assumed as 6.0 mm. 83

Table 13. LS-Dyna material models used in the axial crash model 97

Table 14: A list of LS-Dyna contact algorithms used in the dynamic axial crush model. 98

Table 15: Test matrix for baseline study (Part 1)....................101
Table 16: Test matrix for fold initiator pattern study. Two of the fold initiator patterns, TCS and FCS, which are designed to promote the symmetric folding mode (rather than the asymmetric folding mode), were assigned a higher fold initiator spacing (35 mm) in comparison to the rest of the patterns......109
Table 17: Classification of folding patterns into four groups of deformation modes and their pictorial illustrations. The solid line represents the top face edge, while the dotted line represents the flange edge when viewing at from the side. 112
Table 18: Summary of crush performance for three promising numerical patterns and the baseline. The final absorbed and eroded energy of each pattern are taken at 250 mm crush distance. 119
Table 19: Test matrix for Part 3. The visual illustrations of specimens listed here are shown in Figure 44. Also, all specimens have a length of 375 mm....................127
Table 20: List of dynamic axial crush results and test parameters from several previous studies (see citations in table). All specimens correspond to the baseline double hat channels (see Figure 38 for cross-section) except for the single top hat studied by Ohkubo et al. (1974). The hot-stamped Usibor® 1500-AS (fully-cooled condition), Ductibor® 500-AS and TWBs of these alloys were austenitized for minimum of 6 minutes and quenched in a water chilled-die with a temperature of approximately at 15 °C. Mean forces were calculated up to the free crush distance. The quasi-static specimens are represented by ‘Q’ in the impact velocity column....................146
Table 21: List of cross-section geometric parameters for crush specimens in Table 20, whose definitions are given in Figure 34. All of the results except for the mild steel are from the research work of Waterloo Forming and Crash research group (denoted as “University of Waterloo Materials”) and their specimens share the same geometry. Due to the presence of corner radii and obtuse draft angle of the double hat geometry, its dimension ‘a’ is approximated. 148
Table 22: Quasi-static hardening models and strain rate sensitivity functions for flow stress calculation of different materials. Note that all hot-stamping materials listed here were die-quenched at 13°C after heating in the oven above 930 for 6 minutes, minimum....................206
Table 23 List of energy equivalent flow stress in horizontal bending region of the SE (numbered 2 and 5 in Figure A.1), calculated using Equation (A.2.2) for the considered materials....................208
Table 24 List of LS-Dyna material models used in the Nakazima dome model 218
Table 25: A list of LS-Dyna contact keywords used for 50 mm Nakazima dome models. The Soft=2 algorithm (LSTC, 2016) was assigned to all contact incidents that involve the lock bead profile in the forming die and binder....................220

List of Symbols

Symbol	Description
$a, b, f, \emptyset$	Hat channel cross-sectional width, height, flange length and draft angle defined in Figure 34.
d	Crush distance
f_1, f_2	Residual functions used for the Newton-Raphson method in solving the Superfolding Element Analysis (Wierzbicki and Abramowicz, 1983; Abramowicz and Wierzbicki, 1989)
n, K	Hardening exponent, coefficient in the power-law equation
r	Toroidal radius of the Superfolding Element
t	Sheet thickness, excluding the thickness of Al-Si coating in the case of hot-stamped steel sheets
v_i	Initial impact velocity
v_m	Mean crush velocity, which is approximated as $v_m \approx {}^{v_i}/_{2}$ (White and Jones, 1999)
w	Width of V-bend specimens
A	Cross sectional area
A_1, A_2, A_3	SE analysis coefficients defined in Equations (A.15) and (A.17)
C	Entire base length of the Superfolding Element defined in Figure A.1
$C_1, \ldots, C_6$	Material constants in hardening models
D	Damage parameter
$D_1, \ldots, D_6$	Material constants in fracture models

E_1, ..., E_6	Internal energy absorbed in the various surface elements of Superfolding Element durnig its deformation
E_{exp}	Experimental absorbed crush energy
$E_{SE,int}$	Total internal energy absorbed during deformation of Superfolding Element
E_t	Tangent modulus
$2H$	Folding wavelength of the Superfolding Element (initial height between plastic hinges at top and bottom) defined in Figure A.1.
$2H_{indent}$	Fold initiator indent spacing
$2H_{i,peak}$, $2H_{i,valley}$	Crush distance at the i^{th} force peak or valley in the crush force *vs.* crush displacement plot
I_{yy}, I_{xx}	Area moment of inertia for the cross section, evaluated about the flange plane and the plane perpendicular to the flange plane
I_1, I_3, I_4, I_6	Integrals defined in Equations (A.10) to (A.13)
L	Initial length of the axial crush column
L_2	Least square error defined in (48)
M_p	Plastic bending moment of a sheet metal, predicted by Wang *et al.* (1993), as defined in Equation (D.12)
M_{v-bend}	Plastic bending moment in V-bend test specimens whose expression is given by Noder *et al.* (2020)
$M_{SE,1}$,..., $M_{SE,3}$	Plastic bending moment in the surface elements (1) to (3) of the Superfolding Element
$N_{SE,1}$	Uniaxial stress in the torozidoal zone, surface element (1), in the Superfolding Element
P_{SE}	Theoretical prediction of mean crushing force obtained by the Superfolding Element Analysis

R_g	Radius of gyration for single or double hat cross-section
R_i, R_n, R_0	Radius at the inner concave surface, neutral layer, and outer convex layer of a sheet metal
R_{SE}	Cylindrical radius of the horizontal bending zone in the Superfolding Element
$W_{SE,ext}$	External work applied in crushing the Superfolding Element
$W_{SE,bend}$	Theoretical prediction of the plastic bending energy in the horizontal bending zone of the Superfolding Element
$W_{v,bend}$	Measured plastic work in the V-bend specimen using Equation (52) due to Noder *et al.* (2020)
Z	Mid-shell perimeter of single or double hat cross section, which is approximated as $2a + 2b + 4f$
$\alpha_{SE,i}$, $\alpha_{SE,f}$, α_{SE}	Initial, final, and current crush angle of Superfolding Element defined in Figure A.1
$\bar{\alpha}$	Transition angle at which the deformation mode of Superfolding Element switches from the quasi-static inextensional mode to extensional mode.
δ_e	Effective crush distance
ε_1, ε_2	Major and minor true strain
$\varepsilon_{SE,1}$, …, $\varepsilon_{SE,3}$	Theoretical prediction of final plastic strain in outer surfaces of toroidal, horizontal and inclined bending zones, defined in Equations (A.2.4) and (A.2.5)
$\bar{\varepsilon}_f$	Effective (or equivalent) plastic fracture limit strain
$\bar{\varepsilon}_p$	Effective (or equivalent) plastic strain
$\dot{\varepsilon}$	Strain rate
$\dot{\varepsilon}_{avg}$, $\dot{\varepsilon}_0$	Average and reference strain rate
η	Stress triaxiality

η_{crush}	Crush energy efficiency defined in Equation (50)
η_{fold}	Folding Transition Indicator defined in Equation (67)
$\theta_i, \theta_f, \theta$	Initial, final, and current bend angle of the V-bend specimen defined in Figure 135c
μ	Friction coefficient
σ_{cr}^{col}	Critical column plastic buckling stress
σ_y	Yield strength
σ_{UTS}	Ultimate tensile strength
σ_{SE}	Predicted mean crushing stress obtained by the Superfolding Element Analysis
$\sigma_{SE,1}$,…, $\sigma_{SE,3}$	Energy equivalent plastic flow stress in surface element (1) to (3) of the Superfolding Element, defined in Equation (A.2.1) to (A.2.3)
$\bar{\sigma}$	Effective (or equivalent) plastic flow stress
χ_{bend}	Relative Bending Limit defined in Equation (58)
φ_o	Initial corner angle of the Superfolding Element defined in Figure A.1.

1.0 Introduction

In recent years, increasing concerns regarding automotive fuel efficiency and occupant safety have led to strict government regulations. For example, the Corporate Average Fuel Economy (CAFE) standards established by the National Highway Traffic Safety Administration (NHTSA) mandate increases in the minimum fuel efficiency of passenger cars from the 2016 level of 34.7 mpg to 42.4 mpg by 2025 (NHTSA, 2021). With such demands, the automotive industry has begun an unrelenting quest to reduce vehicle body weight, promoting the development of Ultra High Strength Steel (UHSS).

UHSS can be categorized into several groups. The cold formable 3rd generation steels, such as enhanced Dual Phase (DP) or Quench and Partition (Q&P) steels (Edmonds *et al.,* 2006), aim to retain both high strength and ductility at room temperature. Hot stamped steel, a focus of the current thesis, utilizes forming and quenching in a one-step process. The maximum tensile strength of hot stamped steels, such as Usibor® 2000-AS, exceeds 1800 MPa and allows a reduction in the sheet thickness and weight of structural sheet components while maintaining similar load carrying capacity (ArcelorMittal, 2016d).

However, hot stamped UHSS exhibits relatively low ductility, which stems from less ductile microstructures required to achieve ultra-high strength. The consequence can be limited folding stability and fracture resistance in axial crush loading due to the formation of brittle martensitic microstructures after quenching blanks from their austenitization temperature during forming in water-cooled dies (Mori *et al*., 2017; Omer, 2017a).

While the high tensile strength of hot stamped UHSS makes them ideal candidates for anti-intrusion structural components, which require high rigidity, their lower ductility can make them inappropriate for application in energy absorption components for vehicle frontal or rear body applications. In Figure 1, the evident case of parent metal fracture present in Usibor® 1500-AS is compared to that of stable folding present in the lower strength grade hot stamped steel, namely Ductibor® 500-AS.

(a) hot stamped Usibor® 1500-AS (Omer *et al.*, 2017b)

(b) hot stamped Ductibor® 500-AS (Peister, 2019)

Figure 1: Comparison of axial crash specimens, fabricated from the hot stamped steel grades: (a) Usibor® 1500-AS and (b) Ductibor® 500-AS.

A number of manufacturing methods exist to improve the folding stability of hot stamped UHSS structures, such as tailored in-die heating (IDH) (Omer *et al.*, 2017b). Such a method promotes phase transformation to softer microstructures; hence, increasing ductility by decreasing the cooling rate in regions of interest. Another method is to utilize tailor-welded blanks (TWB), which comprise UHSS on one side of the sheet and a more ductile material on the other side. To this end, newer grades of hot stamping alloys, such as Ductibor® 1000-AS, offer intermediate combinations of strength (1000 MPa) and ductility. Recent experience (Tummers, 2020) has suggested that such alloys can be used in frontal and rear energy absorbing structures; however, it has become evident that design tools are required to optimize the folding stability and avoid fracture of such alloys.

Motivated by these requirements, the current thesis aims to develop methods to design structures that promote stable folding and enhance the potential to use hot stamped UHSS in energy absorption structures through improved analysis and design methods. To meet this aim, the overall scope of the thesis consists of a multi-step approach. Axial crush experiments and supporting numerical models were developed that considered a hot stamped UHSS material, Ductibor® 1000-AS. Parametric studies were performed that considered a wide range of fold initiator patterns to ascertain their effect on progressive folding stability and fracture suppression. Next, analytical models of axial crush were applied to develop performance metrics to predict axial crush response in terms of folding stability, global buckling onset and fracture during tight bending within folds. These metrics were applied to a wide range of steel alloys with strengths ranging from 270-1500 MPa and represent a first step to the development of design guidelines for UHSS axial crush structures.

1.1. Automotive Sheet Steel

The decades-long pursuit of weight reduction has led to the emergence of lightweight materials in vehicle bodies such as aluminum and magnesium alloys, as well as carbon fiber composites. Nevertheless, modern automobile bodies still consist primarily of steel which makes up over 50% of total mass (Hovorun *et al.*, 2017). This predominance can be attributed to the exceptional strength and relative low cost of steel, which places steel as a top contender for stamped structural components. The strength levels of steels found in the vehicle body-in-white (BIW), however, vary significantly depending on the location, as demonstrated in Figure 2.

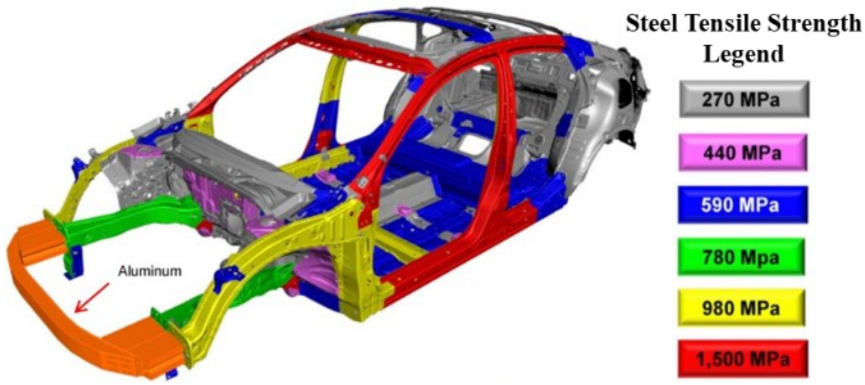

Figure 2: Different steel grades in the BIW for 2016 Honda Civic, from Honda (2019). Tensile strength of the steels ranges from 270 MPa to 1500 MPa based on the location.

Different components within an automotive structure serve different functions. Hence, the mechanical properties of materials inevitably vary across the vehicle body. In general, material selection for the vehicle structure considers three functions: dent resistance, anti-intrusion and energy absorption (Billur, 2019).

Figure 3: Illustration of vehicle structures (highlighted in blue) with different functions: (a) dent resistant components such as hoods (b) anti-intrusion components such as b-pillars and (c) energy absorption components such as front rails. The images are adapted from Hilfrich and Seidner (2008)

For dent resistant components in which shape retention is of concern, high yield strength is the desired material property. For anti-intrusion components, high ultimate tensile strength (UTS) is required to protect passengers in the event of a crash. Lastly, energy absorption components require both high UTS and high post uniform elongation because the area under the stress-strain curve determines the specific energy absorption (Billur, 2019).

Over the decades, steels have evolved to meet improved formability and mechanical properties. From mild steel to advanced high strength steel (AHSS), different UTS and uniform elongation levels are achieved by controlling alloying elements and heat treatments. Nowadays, the list of commonly found steels in the vehicle BIW may include, but is not limited to, mild steel, high strength low alloy (HSLA) steel, dual phase (DP) steel, transformation induced plasticity (TRIP) steel, hot stamping boron steel and 3rd generation (Gen 3) steel. These steels show a general trend of increasing strength as ductility (*i.e.* uniform elongation) decreases, as shown in Figure 4.

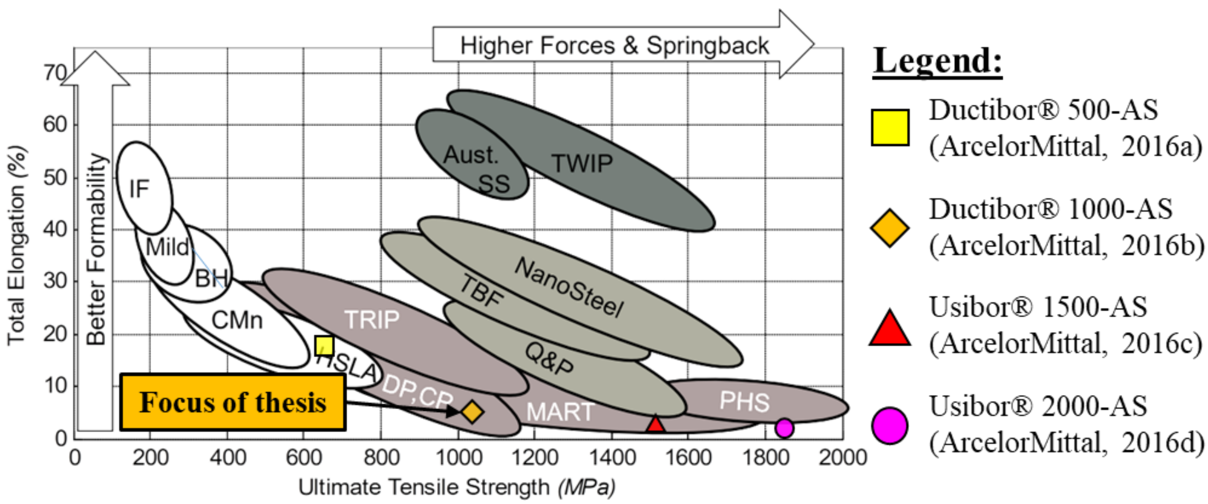

Figure 4: Comparison of various steel grades in tensile strength and elongation, adapted from Billur *et al.,* (2015). The properties of ArcelorMittal hot stamping steel grades (after die-quenching) are shown including the main focus of the thesis, Ductibor® 1000-AS.

Mild steels display a primarily ferritic microstructure, imparting a very high ductility, but sacrificing strength. HSLA steels are carbon-manganese steels with additional alloying elements such as vanadium and titanium. At a microstructural level, the strength of HSLA is attributed to precipitation hardening and grain refinement which improves strength but results in a total elongation as low as 16% (POSCO, 2014). The mechanical behaviour of dual phase (DP) steels is explained by the presence of martensite islands in a ferrite matrix (ArcelorMittal, 2019), resulting in strong work hardening and good ductility. TRIP steels, on the other hand, consist partially of retained austenite that undergoes gradual martensitic phase transformation when subject to plastic deformation (Li *et al.*, 2003). Because of the TRIP effect, the material generally exhibits higher work hardening and elongation compared to DP steels (Samek and Krizan, 2012); however, these steels have seen only limited commercial application due to high cost and poor weldability. Gen 3 steels were introduced to improve formability relative to previous generation AHSS. For example, Q&P steels undergo an interrupted quench stage to produce a microstructure with stabilized retained austenite and carbon-depleted martensite (Speer *et al.,* 2003). Finally, hot stamping steels, such as 22MnB5, have high formability during high temperature stamping and are capable of reaching a UTS above 1500 MPa through a fully martensitic transformation during the hot stamping process (Samek and Krizan, 2012). The advantages of hot stamping steels include reduced springback by holding the formed part in its final configuration (in-die) past the martensite finish temperature (Nakagawa *et al.*, 2018) and controlled ductility based on the quench rate (Samadian *et al.*, 2020). Ductibor® 1000-AS, a material of focus in the current thesis, also belongs to the family of hot stamping steels and offers a somewhat reduced strength but higher ductility after hot stamping than Usibor® 1500-AS. The following section discusses the manufacturing process and mechanical properties associated with hot stamping steel grades.

1.1.1. Hot Stamping Process

Hot stamping was first patented by a Swedish company for manufacturing lawnmower blades in 1977 (Karbasian and Tekkaya, 2010). The automotive industry eventually recognized the strong benefit in light-weighting, and the first vehicle to consist of hot stamped parts emerged in 1984 (Berglund, 2008). Since then, the usage of hot stamped components in vehicles has rapidly increased. VOLVO vehicles, for example, have increased the mass percentage of total BIW in XC90 models from 7% in 2003 to 40% in 2014, according to Mori *et al.* (2017). Today, the list of common hot stamped components includes bumpers, roof rails, A-pillars and B-pillars.

Modern hot stamping technology is broken down into two different methods: (i) direct hot stamping and (ii) indirect hot stamping, as illustrated in Figure 5. In the direct hot stamping method, the blank is heated in a furnace above the Ac_3-temperature of approximately 850°C (Merklein *et al.*, 2009). Once the blank is fully austenitized, it is quickly transferred to a die in which forming and quenching take place simultaneously. In order to ensure the required minimum cooling rate, water-cooled dies are used in the forming process (George, 2011). In the indirect method, the blank is cold stamped prior to the furnace stage, and the subsequent process follows the same steps.

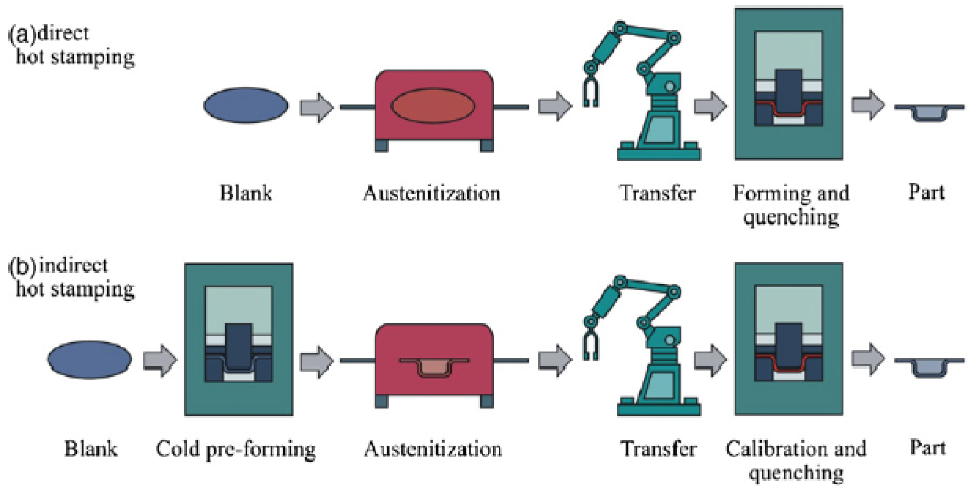

Figure 5: Illustration of (a) direct hot stamping and (b) indirect hot stamping processes, adapted from Karbasian and Tekkaya (2010)

The high strength of hot stamped components is mainly attributed to the martensite phase transformation during forming and in-die quenching that increases the flow stress of material (Karbasian and Tekkaya, 2010). For this reason, the cooling rate of the blank during the forming stage plays a crucial role. In order to predict the resulting microstructures for a given cooling rate, a continuous cooling temperature (CCT) diagram can be referenced, as shown in Figure 6. For 22MnB5 steel, which is the most commonly studied hot stamping alloy, the critical cooling rate to avoid the bainite and ferrite transformation is 27 K/s, according to Tekkaya *et al*. (2007).

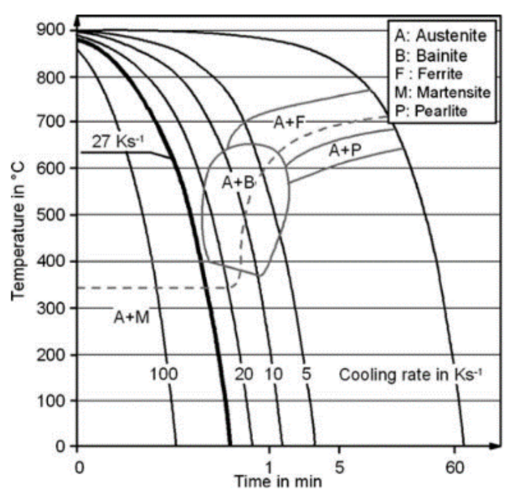

Figure 6: CCT diagram for 22MnB5, adapted from Tekkaya *et al.* (2007)

1.1.2. Hot Stamping Process Parameters

Understanding the key parameters controlling the rate of heat transfer between the workpiece and die, normally quantified by the heat transfer coefficient (HTC), is essential in controlling the cooling rate. For heat transfer between the tooling and blank during hot stamping, die tonnage or contact pressure govern the HTC (Shapiro, 2008). At the microscopic level, the surfaces of the blank and tool are not entirely in contact due to surface irregularities. Contact spots experience direct metal conduction, while the rest of the surface experiences radiative or conductive heat transfer through an air gap (see Figure 7). Since the thermal conductivity via direct metal conductance is significantly larger than that via an air gap or fluid-filled interstices, as noted by Fenech (1959), the majority of the heat transfer will occur at the contact points, and thus, HTC in during hot stamping is primarily governed by the area of spot contacts. In general, by increasing the die tonnage or contact pressure, surface asperities become more flattened, and the total area of contact increases, giving a rise in HTC.

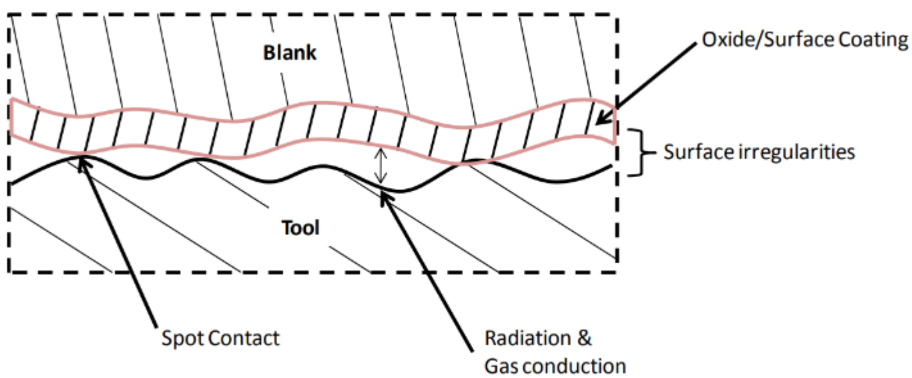

Figure 7: Illustration of contact surface between blank and die at the microscopic level, adapted from George (2011)

The significance of contact pressure in determining HTC was pointed out and studied by numerous authors (Merklein and Lechler, 2008; Salomonsson *et al.*, 2009; Oldenburg and Lindkvist, 2011; George *et al.*, 2012; Caron *et al.*, 2013; Omer *et al.,* 2020). Merklein and Lechler (2008) adopted an analytical approach in determining the HTC of Usibor® 1500-AS at different contact pressures. In that study, the temperature history of the blanks was measured during quenching and fit to theoretical heat transfer equations. Their results have shown that the averaged HTC approximately increased in a linear relationship from 700 W/m^{2}K to 3000 W/m^{2}K with varying contact pressure from 0 MPa to 40 MPa. Similarly, the experimental characterization by Omer *et al.* (2020) of HTC of Usibor® 1500-AS showed a linear relationship with the contact pressure from 0 to 30 MPa. On the other hand, Salomonsson *et al.* (2009) conducted an inverse analysis in determining HTC. The experimental setup was modelled in numerical simulation using LS-Dyna, and optimization analyses were conducted so that the measured temperature history of the blanks was reproduced in the model.

1.1.1. Hot Stamping Steel Alloys

Hot stamping steels are commonly referred to as boron steels. As the name suggests, such steels utilize boron as an alloying element for improved hardenability. The underlying mechanism has been characterized as the segregation of boron on the austenite grain boundary which results in suppression of ferrite nucleation (Taylor and Hansen, 1990; Taylor, 1992). As a result, more austenite remains at lower temperatures during quenching and is available for martensite formation.

The hot stamping steel considered in this research is Ductibor® 1000-AS, manufactured by ArcelorMittal. The carbon content of Ductibor® 1000-AS falls between the two other steel grades from the manufacturer, namely Usibor® 1500-AS and Ductibor® 500-AS, as shown in Table 1. The maximum boron content in Ductibor® 1000-AS is the same as Usibor® 1500-AS and Usibor® 2000-AS, which creates a *predominantly* martensitic microstructure after hot stamping, as reported by Samadian and Abedini (2020).

Table 1: **Chemical composition (maximum weight %) of ArcelorMittal hot stamping steels, from ArcelorMittal (2021)**

Material	C	B	Mn	P	S	Si	Cr	Al	Ti	Nb	N	Fe
Ductibor® 500-AS	0.08	0.001	1.70	0.030	0.01	0.35	0.2	0.06	0.09	0.1	0.01	remaining
Ductibor® 1000-AS	0.10	0.005	1.80	0.030	0.01	0.60	0.2	0.06	0.05	0.1	0.01	remaining
Usibor® 1500-AS	0.25	0.005	1.40	0.030	0.01	0.40	0.5	0.06	0.05	-	0.01	remaining
Usibor® 2000-AS	0.36	0.005	0.80	0.030	0.01	0.80	0.5	0.06	0.06	0.07	0.01	remaining

The mechanical properties of Ductibor® 1000-AS also fall between the two (of three) other steel grades, as shown in Table 2.

Table 2: Mechanical properties of ArcelorMittal hot stamping steels after hot stamping and paint baking, from ArcelorMittal (no date; 2016a; 2016b; 2016c; 2016d)

Material	Yield Strength (MPa)	Ultimate Tensile Strength (MPa)	Fracture Elongation	Bending Angle (°)
Ductibor® 500-AS	408	657	0.189	≥90
Ductibor® 1000-AS	849	1067	0.056	≥75
Usibor® 1500-AS	1141	1553	0.046	≥50
Usibor® 2000-AS	1462	1848	0.054	≥45

Usibor® 1500-AS belongs to a family of 22MnB5 alloys, with UTS above 1500 MPa. Several authors have extensively studied the flow and fracture behaviour of die-quenched 22MnB5 (Bardelcik *et al.*, 2012; ten Kortenaar, 2016; Östlund *et al.*, 2016, Samadian *et al.*, 2020). Among these researchers, Samadian *et al.* (2020) specifically investigated the effect of quench rate on the resultant microstructures. Fully austenitized samples were oil-, forced-air-, and air-cooled separately and yielded 100% martensite, a mixture of bainite and martensite and 100% bainite microstructures, respectively. The fracture *loci* and flow curves of the multi-phase (forced-air-cooled) microstructures were modelled through a mean field homogenization approach in which the macroscopic mechanical properties are calculated by statistical averaging of the phases present in the microstructure. On the other hand, Bardelcik *et al.* (2012) predicted the flow response of the multi-phase microstructure based on the measured Vickers hardness. Given the extensive past research on this alloy, 22MnB5 currently serves as the benchmark in the list of boron steels.

Ductibor® 500, on the other hand, exhibits a UTS up to 810 MPa, depending upon the quench rate, and substantially higher fracture elongation than Usibor® 1500-AS (Samadian *et al.*, 2018). The fracture behaviour of the alloy also has been studied by Samadian *et al.* (2019). Ductibor® 1000-AS carries a very little published literature on the characterization of constitutive and fracture behaviour to-date and is the topic of ongoing work by researchers at the University of Waterloo.

One approach to tailoring the local properties within a hot stamped component is achieved using a blank comprising different steel grades and gauges joined by a laser welding process. Such a blank is commonly referred to as a Tailor Welded Blank (TWB). The main advantage of TWBs is the weight reduction by strategically placing the higher strength or thicker gauge portion at BIW areas where structural stiffness is desired (Merklein *et al.,* 2014). In studying the potential applications of TWBs in vehicle structures, Múnera *et al*. (2008) demonstrated a 20 % weight-saving in a door ring comprising tailor welded Usibor® 1500-AS and Ductibor® 500-AS. Similarly, the numerical studies by Tummers (2020) demonstrated a 27.6% weight-saving in the front sub-assembly of a commercial SUV using tailor welded Ductibor® 1000-AS and Usibor® 1500-AS. The axial crush experiments by Peister *et al.* (2018) considered double hat channels comprising tailor-welded Ductibor® 500-AS and Usibor® 1500-AS. They reported a 12% increase in energy absorption compared to non-tailored channels composed entirely of Ductibor® 500-AS.

1.2. Material Modelling for Sheet Steel

In the vehicle design cycle, the development of a new material is followed by material modelling for finite element implementation within forming and crashworthiness simulations. In this section, different approaches in modelling the plasticity and fracture response of sheet steel are discussed. The discussion is tailored towards consideration of material characterization and modelling appropriate for a UHSS sheet.

1.2.1. Plasticity Response

Linear elasticity and infinitesimal strain assumptions have their merits in structural analysis for simplicity; yet, many challenging problems—such as metal forming or crash simulations—involve plasticity to a greater extent. For that reason, the automotive industry has a need for accurate plasticity modelling in finite element implementations.

In general, there are two approaches in modelling plasticity: physics-based approaches *versus* phenomenological-based approaches. The physics-based approach studies the movement of atoms and deformation of grains at the microscopic level, while the phenomenological approach mathematically models the measured material behaviour at the macroscopic or continuum level (Khan and Huang, 1995). Adopting a mesh size as small as the size of grains in polycrystalline is computationally costly in many industrial applications in which problems are usually simulated at the macroscopic scale. Hence, the phenomenological approach is usually adopted.

Phenomenological plasticity, at its core, is built upon three cornerstones: (i) the yield surface, which sets the boundary between the plastic and elastic deformation states (ii) the hardening law, which determines how the yield surface evolves following onset of yielding, and (iii) the flow rule, which relates the stress and plastic strain rate (Krabbenhoft, 2002).

1.2.1.1. Hardening Behaviour

In the physical description, hardening behaviour stems from the mechanism of dislocations. As more dislocations are generated during deformation, a higher amount of stress is required to sustain dislocation motion along slip planes (Bergström, 2015). Taylor (1934) was perhaps the first to physically describe the hardening behaviour of metals in terms of dislocation density:

$$\sigma_{flow} = \alpha G b \sqrt{\rho(\varepsilon)} \tag{1}$$

Where σ_{flow} is the flow stress, α is a hardening parameter, G is the shear modulus, b is the magnitude of the Burgers vector, ε is the true strain and ρ is the dislocation density.

As noted by van den Boogaard (2002), the key aspect in modelling work hardening lies in predicting the evolution of dislocation density, and authors including Bergström (1983) have developed models for predicting the dislocation evolution based on several mechanisms such as immobilization, remobilization and annihilation. While the remaining section focuses on phenomenological descriptions of work hardening, a detailed summary is presented by Bergström (2015).

Phenomenologically, the hardening rate $d\sigma_{flow}/d\varepsilon$ decreases continuously from a high value to zero for polycrystalline metals (van den Boogaard, 2002). Over the decades, many authors (Holloman, 1945; Voce, 1948; Zerilli and Armstrong, 1987) developed models to capture such saturation behaviour in various forms. One example is the model, developed by Hockett and Sherby (1975), that describes flow stress saturation at large strain under room temperature conditions using the following relationship

$$\sigma_{flow} = \sigma_{sat} - \exp\left(-\left(N\varepsilon_p\right)^m\right)\left(\sigma_{sat} - \sigma_y\right) \tag{2}$$

Where σ_{sat} is the saturation stress, ε_p is the equivalent plastic strain, σ_y is the yield strength and N and m are calibration coefficients, respectively.

In addition to the plastic strain, the flow stress of a metal is governed by other variables such as temperature and strain rate. To account for the effects of these variables, Johnson and Cook (1983) assumed a multiplicative form of three functions as follows:

$$\sigma_{flow} = \left[A + B\varepsilon_p^n \right] \left[1 + C \ln\left(\frac{\dot{\varepsilon}}{\dot{\varepsilon}_0} \right) \right] \left[1 - \left(\frac{T - T_0}{T_m - T_0} \right)^m \right] \tag{3}$$

The first function describes power law hardening with yield stress A and hardening parameters B and n. The second function accounts for the strain rate sensitivity through coefficient C and the reference strain rate $\dot{\varepsilon}_0$. Lastly, the temperature sensitivity is described by the third function with thermal softening coefficient m and reference temperature T_0 and melting temperature T_m. (Note that the parameter m has differing meanings in Equations (2) and (3).) Due to the multiplicative coupling assumption inherent in the Johnson-Cook model, it fails to capture complex material behaviour such as that of Al-7039, as reported by Gray *et al.* (1994). Nonetheless, the model is widely used for its simplicity and has been extended in different forms (Børvik *et al.*, 2001).

Phenomenological characterization of the hardening behaviour of hot stamped steels takes two steps: (1) conducting uniaxial tension testing until diffuse necking and (2) extrapolating the stress-strain data to account for large strain. Although the tensile data can be fitted in hardening models beyond the experimental range, such a method can cause a significant deviation in post necking behaviour based on the choice of model. A recent analytical method by Rahmaan *et al.* (2017) presents a solution in which one conducts a complementary coupon test that does not develop a necking instability such as simple shear and then extrapolates the tensile data using the stress ratio between shear stress (from the simple shear test) and equivalent stress (from the uniaxial tensile test). The ratio is obtained by plastic work equivalence analysis, and detailed description of this approach is provided by Rahmaan *et al.*, 2017. The extrapolated curve is fitted to hardening models with additional constraints such as the Considère criterion that equates the hardening rate to the true stress. Finally, the fitted model with the least error is selected.

The hardening behaviour of hot stamped steels varies significantly under different quench conditions. To perform tensile and simple shear tests on a broad range of as-quenched specimens is time-consuming and repetitive. For such problems, the Tailor Crash Models I and II (Bardelcik *et al.*, 2012; Bardelcik *et al.*, 2014) offer a convenient solution in which the flow stress is predicted by the measured Vickers hardness following quenching. The use of Vickers hardness was justified by the observed linear dependency with the area fraction of martensite, banitie and ferrite phases in the quenched specimens.

Figure 8 shows the hardening behaviour of Usibor® 1500-AS and Ductibor® 500-AS under a water-cooled, die-quenched condition. The Usibor® 1500-AS data was fitted to a Voce model and multiplied by an exponential-type strain rate sensitive function due to Børvik *et al.* (2001) by Bardelcik *et al.* (2012). The quasi-static hardening curve of Ductibor® 500-AS was modelled by Samadian *et al.* (2018) and modified to include strain rate sensitivity using the Johnson-Cook function by Abedini (2019).

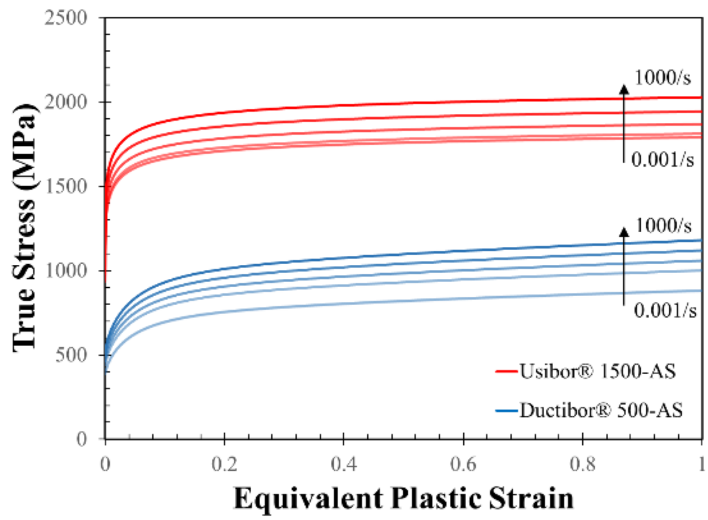

Figure 8: Flow curve of water-cooled, die-quenched Usibor® 1500-AS by Bardelcik *et al.* (2012) and Ductibor® 500-AS by Samadian *et al.* (2018) and Abedini (2019)

1.2.1.2. Yield Criterion

Due to the intrinsic properties of rolled sheets, some level of anisotropy is inevitable in sheet steels. Austenitizing at high temperatures, such as 950 °C, largely removes planar anisotropy for 22MnB5, as reported by Hu *et al.* (2017). For this reason, much research towards modelling hot stamped steel (Östlund, 2015; ten Kortenaar, 2016; Samadian *et al.*, 2020) assumes isotropic yield functions to this day. One of the earliest and most famous example of such isotropic yield criteria is due to von Mises (1913), with the following expression:

$$\sigma_{eq} = \sqrt{3J_2} = \frac{1}{\sqrt{2}}\left\{\left(\sigma_1 - \sigma_2\right)^2 + \left(\sigma_1 - \sigma_3\right)^2 + \left(\sigma_2 - \sigma_3\right)^2\right\}^{\frac{1}{2}} \tag{4}$$

Where J_2 is the second deviatoric stress invariant and σ_1, σ_2, σ_3 are the principal stresses.

Yield criteria often describe what is considered as a "yield surface" in principle stress space as a convenient approach to visualizing the material stress state resulting in plastic flow. A point in principle stress space can either be inside (elastic loading) or outside (plastic loading) the surface. However, the latter case is not physical since plastic loading is accompanied by distortion (hardening) of the yield surface such that the stress state remains on the expanding yield surface. In mathematical form, this condition can be expressed as

$$\sigma_{eq} - \bar{\sigma} = 0 \tag{5}$$

in which σ_{eq} is the equivalent stress, calculated by a yield criterion, and $\bar{\sigma}$ is the flow stress, obtained from a hardening response of materials.

1.2.1.3. Flow Rule

The last constituent of the phenomenological plasticity model is the flow rule. Like Hooke's law that relates strain increment to stress in the theory of elasticity, the flow rule relates plastic strain increment to stress in the theory of plasticity. In the flow rule, however, the direction of plastic strain increment is governed by a separate function known as the plastic potential ψ. Furthermore, its magnitude is calibrated by the plastic multiplier $d\lambda$ through the following relationship

$$d\boldsymbol{\varepsilon}_p = d\lambda \frac{\partial \psi}{\partial \boldsymbol{\sigma}} \tag{6}$$

The partial derivative term $\frac{\partial \psi}{\partial \boldsymbol{\sigma}}$ enforces the requirement that the yield surface will grow in the normal direction to the ψ function. In the associated flow rule (AFR), the plastic potential function is assumed to coincide with the yield function. In the case of the von Mises (1913) yield criterion, Equation (6) reduces to

$$d\boldsymbol{\varepsilon}_p = d\lambda \boldsymbol{N} \tag{7}$$

in which $\boldsymbol{N}$, the normal to the yield surface, becomes

$$\boldsymbol{N} = \frac{\partial \sigma_{eq}}{\partial \boldsymbol{\sigma}} \tag{8}$$

Equations (4) to (8) are examples of so-called "constitutive relations" in describing the plasticity behaviour of materials and are commonly solved computationally in finite element problems.

1.2.2. Fracture Response

In predicting the fracture response of ductile metals, three categories of models exist: (i) micro-mechanical damage models, (ii) Continuum Damage Models (CDM) and (iii) phenomenological models. In micromechanical damage models, the effect of void growth or coalescence at the microscale is incorporated into a constitutive relation. Such an example is the Gurson (1977) model, with the idea of narrowing the yield surface as the volume fraction of voids increases. In contrast, the two latter models aim to express the fracture response of a bulk material or "continuum" element at the macroscopic scale. In CDM, the interplay of such microscale defects is represented as a scalar variable, damage. As explained by Lemaitre (1985), the presence of microcracks in the continuum element with normal vector $\boldsymbol{n}$ gives damaged area S_D from the total cross-sectional area S, as shown in Figure 9.

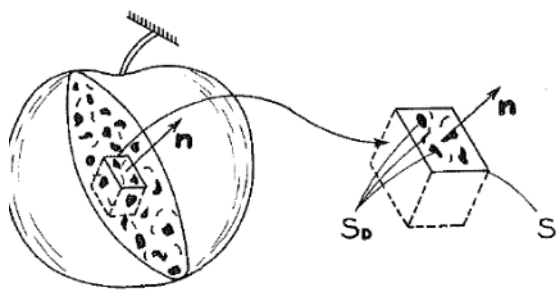

Figure 9: Illustration of a continuum element with damage caused by microcracks (Lemaitre, 1985)

A decrease in cross-sectional area corresponds to a reduced load-carrying capacity; hence, the effect of damage should increase. From this notion, the definition of damage is expressed below.

$$D = \frac{S_D}{S} \tag{9}$$

A value of damage equal to unity corresponds to the onset of failure. For damage below unity, the effective stress of the element under traction $\boldsymbol{T}$ is defined in terms of damage and Cauchy stress tensor ($\boldsymbol{\sigma} \cdot \boldsymbol{n} = \boldsymbol{T}$) by the following relation:

$$\bar{\boldsymbol{\sigma}} = \frac{\boldsymbol{\sigma}}{1-D} \tag{10}$$

In phenomenological models, fracture in a continuum element is perceived as a sudden event that occurs when the equivalent plastic strain, $\bar{\varepsilon}_p$, reaches the fracture strain, $\bar{\varepsilon}_f$, that is governed by the strain path or stress state (Abedini, 2018). The two key parameters in describing the stress state are stress triaxiality (η) and Lode angle (θ) whose expressions follow

$$\eta = \frac{\sigma_{hyd}}{\sigma_{eq}} = \frac{1/3I_1}{\sqrt{3J_2}} \tag{11}$$

$$\theta = \frac{1}{3}\cos^{-1}\left(\frac{3\sqrt{3}}{2}\frac{J_3}{J_2^{3/2}}\right) \tag{12}$$

Where σ_{hyd} is the hydrostatic stress, σ_{eq} is the von Mises equivalent stress, I_1 is the first stress invariant and J_2, J_3 are the second and third deviatoric stress invariants. The Lode angle θ is also related to the normalized Lode angle $\bar{\theta}$ or the Lode parameter ξ whose expressions follow

$$\bar{\theta} = 1 - \frac{6\theta}{\pi} = 1 - \frac{2}{\pi}\arccos\xi \tag{13}$$

$$\xi = \cos(3\theta) = \frac{3\sqrt{3}}{2}\frac{J_3}{J_2^{3/2}} \tag{14}$$

Early studies by several authors (McClintock, 1968; Rice and Tracey, 1969; Gurson, 1977; Tvergaard and Needleman, 1984; Johnson and Cook, 1985) all have shown the strong effect of stress triaxiality on ductile fracture. In particular, Rice and Tracey (1969) studied the growth of a spherical void in an infinite matrix subject to uniaxial tension and concluded the relationship with material constant α:

$$\frac{dR}{R} = \alpha \exp\left(\frac{3\sigma_m}{2\sigma_{eq}}\right) \tag{15}$$

Equation (15) was later visited by Hancock and Mackenzie (1976) to postulate that the failure strain shall be inversely proportional to the hole growth-rate and thus, the following relationship holds:

$$\bar{\varepsilon}_f = \alpha \exp\left(\frac{-3\sigma_m}{2\bar{\sigma}}\right) \tag{16}$$

Since then, the exponential dependency of stress triaxiality became a foundation for subsequent fracture models developed by Johnson and Cook (1985), Wierzbicki and Xue (2005) and Bai and Wierzbicki (2008).

Recent studies, however, further pointed out Lode angle-dependence on ductile fracture (Wierzbicki and Xue, 2005; Bai and Wierzbicki, 2010). One example that considers both parameters is the model developed by Bai and Wierzbicki (2008) in which fracture strain is assumed to have an exponential dependence on triaxiality and parabolic dependence on Lode angle:

$$\bar{\varepsilon}_f = \left[\frac{1}{2}\left(D_1 e^{-D_2\eta} + D_5 e^{-D_6\eta}\right) - D_3 e^{-D_4\eta}\right]\bar{\theta}^2 + \frac{1}{2}\left(D_1 e^{-D_2\eta} - D_5 e^{-D_6\eta}\right)\bar{\theta} + D_3 e^{-D_4\eta} \tag{17}$$

in which D_1 to D_6 are calibration constants. The above relationship gives rise to visualizing a fracture locus in 3D space, as shown in Figure 10.

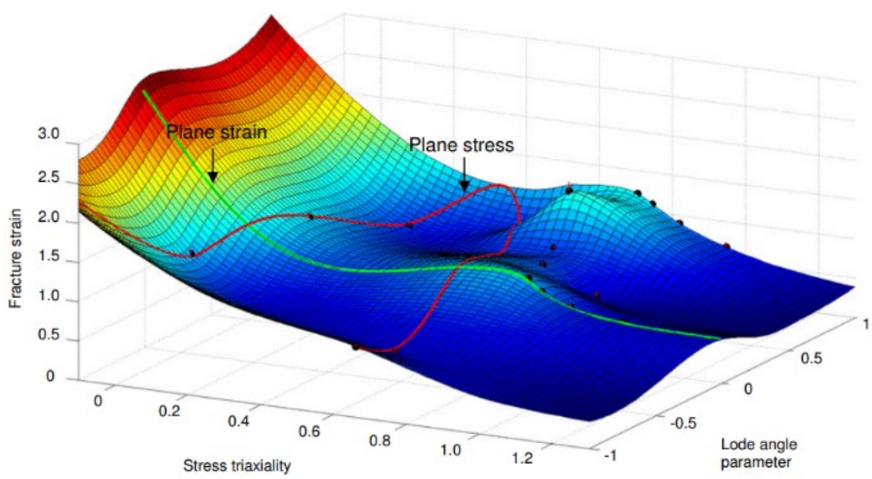

Figure 10: Example of a fracture surface (Basaran *et al.*, 2010)

For plane stress conditions, Wierzbicki and Xue (2005) showed that an additional relation holds between stress triaxiality and Lode parameter given by

$$\xi = -\frac{27}{2}\eta\left(\eta^2 - \frac{1}{3}\right) \tag{18}$$

Combining Equations (13) and (18) with Equation (17) results in direct dependence of fracture strain on triaxiality (for plane stress conditions) and generates a plane stress fracture *locus* that lines within the generalized fracture surface, as shown in Figure 10. Consequently, for sheet metal, for which a predominantly plane stress condition exists, fracture *loci* are often simplified into 2D curves expressed solely as a function of stress triaxiality. Typical examples of 2D fracture *loci* are shown in Figure 11 for different quenched conditions of Usibor® 1500-AS (Samadian *et al.*, 2020). To construct phenomenological fracture *loci*, fracture strains at various triaxial stress states are obtained by performing calibration tests. Such tests consist of, but are not limited, to shear, uniaxial tensile, plane strain dome or v-bend, and biaxial dome tests with different punch diameters.

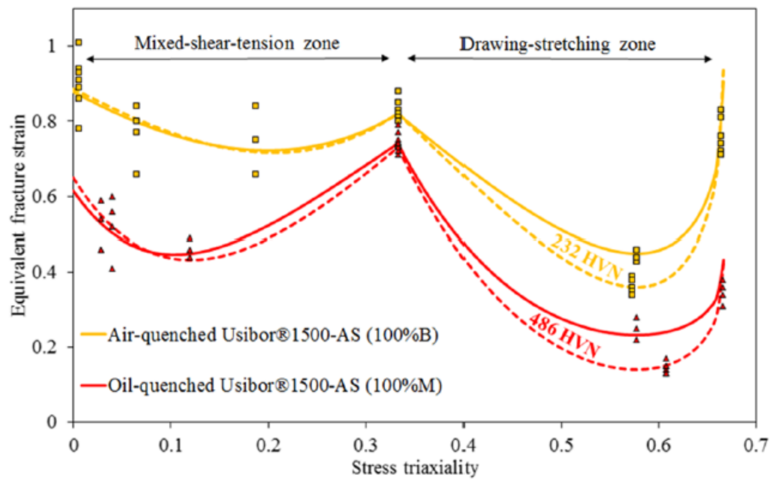

Figure 11: Fracture *loci* of Usibor® 1500-AS in two different quench conditions, adapted from Samadian *et al.* (2020). Experimental points were obtained from butterfly, hole expansion, plane strain tension dome, v-bend and biaxial tension dome tests. The dashed and solid lines represent fracture curves based on the plane strain tension dome and v-bend tests, respectively.

Unlike calibration tests, most problems in metal forming and crashworthiness involve severely nonlinear strain paths. In order to predict fracture in such problems, one solution is to utilize an incremental CDM approach such as the Generalized Incremental Stress State-dependent damage MOdel (GISSMO) developed by Neukamm *et al.* (2009). In the GISSMO approach, the incremental damage is described as:

$$dD = \frac{nD^{(1-\frac{1}{n})}}{\bar{\varepsilon}_f} d\bar{\varepsilon}_p \tag{19}$$

where dD is the incremental damage, $d\bar{\varepsilon}^p$ is the incremental plastic strain, n is the damage exponent to allow nonlinear accumulation and $\bar{\varepsilon}_f$ is the equivalent fracture strain, which can be obtained from the phenomenological fracture *locus*. When the damage reaches a value of unity, the corresponding element in finite element simulation is deemed to no longer possess load-carrying capacity. This damage treatment is available in commercial finite element software, such as in LS-Dyna (Livermore Software Technology Corporation, 2016) which was used in the current research, to trigger element deletion due to material fracture (*MAT_ADD_EROSION keyword).

Mesh (element) sizes also need to be taken into account in predicting fracture. Mesh convergence in the finite element method states that as the element size decreases, the solution converges (Fish and Belytschko, 2007); however, mesh convergence is often not achieved for fracture prediction. Consider the simulation of a plane strain dome in Figure 12 in which Eller *et al*. (2014) showed that equivalent plastic strain increases with decreasing element size. Since the phenomenological fracture strain remains constant for a given stress triaxiality, damage would accumulate faster with increasing equivalent plastic strain according to Equation (19). Thus, a smaller element would reach fracture sooner, which is not physical.

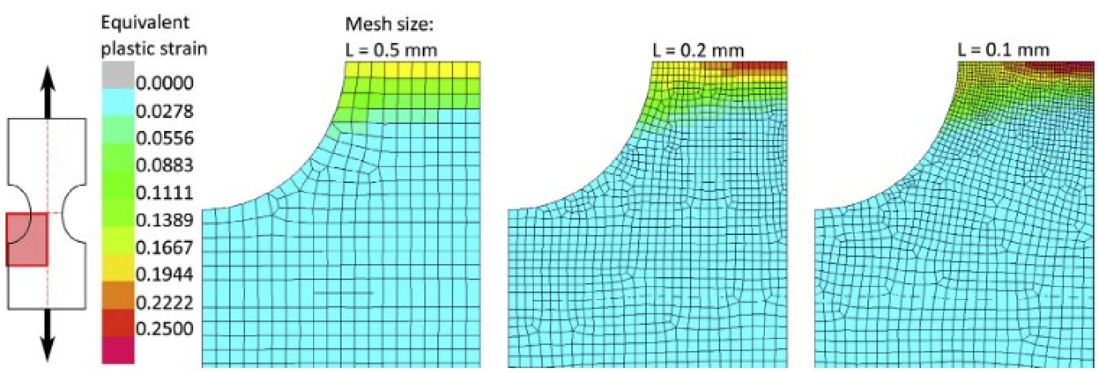

Figure 12: Effect of mesh refinement on equivalent plastic strain during plane strain simulation in LS-Dyna (Eller *et al.*, 2014)

One approach to account for or limit the effect of element size on fracture prediction is by performing mesh regularization. In the mesh regularization process, fracture calibration tests are numerically simulated with different element sizes within the actual coupon geometry. Then, the phenomenological fracture curve is scaled accordingly for each mesh size such that numerical response, such as the predicted limiting dome height or force-displacement at failure, matches that of the test results. Figure 13 shows an example of mesh-regularized fracture curves for fully martensitic 22MnB5.

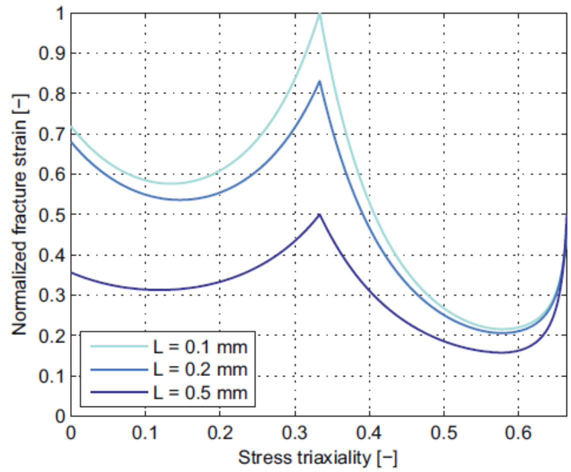

Figure 13: Mesh regularized fracture curves of martensitic 22MnB5 for three different element sizes (L), adapted from Eller *et al.* (2014)

1.3. Crashworthiness and Axial Crush of Hot Stamped Steels

The first record of documented crash experiments dates as far as back as 1924 with the aim of evaluating aircraft safety (Waldock, 1997). At that time, aerospace engineers were trying to minimize the risk of occupant injury through the design of the cockpit. The term crashworthiness emerged from the aerospace industry in the 1950s (Paluszny, 1992).

The concept of crashworthiness is equally important in the automotive industry. According to McGregor *et al.* (1993), a crashworthy vehicle serves three functions: (i) dissipate the kinetic energy of the impact in a controlled manner; (ii) minimize the force and acceleration to the occupants; and (iii) retain a survival space for occupants. For vehicle frontal or rear impact structures, the compliance of the first two functions is validated through axial crush tests. In particular, measurements of energy absorption and peak force assess the compliance with the first and second functions, respectively. The last function is usually achieved using high strength, "anti-intrusion" components that maintain occupant "survival space". These three metrics constitute the criteria used in vehicle crash safety design.

For every new material considered for application in automotive structures, its crashworthiness must be validated. The ideal axial crush test involves the actual vehicle components; however, new materials may present a challenge in the forming stage—resulting in new tools and processes. For this reason, simple geometric components such as square or hat channel tubes are often used to validate the crashworthiness of new materials in axial crush tests.

1.3.1. Axial Crush Experiments

There has been a significant amount work in studying the axial crush behaviour of hot stamped steel grades using double hat channel specimens. Omer *et al.* (2017b) studied the dynamic axial crush performance of Usibor® 1500-AS specimens under different in-die heated tailored quench conditions. The fully cooled (martensitic) specimens exhibited the greatest extent of fracture and spot weld failure, with little repeatability in deformation modes, as shown in Figure 14.

Figure 14: Dynamic axial crush specimens of Usibor® 1500-AS under the fully martensitic condition, adapted from Omer *et al.* (2017b)

In addition to the fully cooled (quenched) condition, three tailored quench conditions were obtained in which one-half of the die set was fully cooled while the tool in the other half (zone) was heated. Three heated conditions were considered with the die temperatures designated as single soft zone 400°C, single soft zone 700°C and graded soft zone, which was divided into 400°C and 700°C zones (see Figure 15).

The microstructures of the heated zones revealed bainite and ferrite phases with a larger amount of ferrite present in the single soft zone 700°C configuration. The axial crush results showed a clear trend of improved folding behaviour as the ductility of specimens improved, as shown in Figure 16.

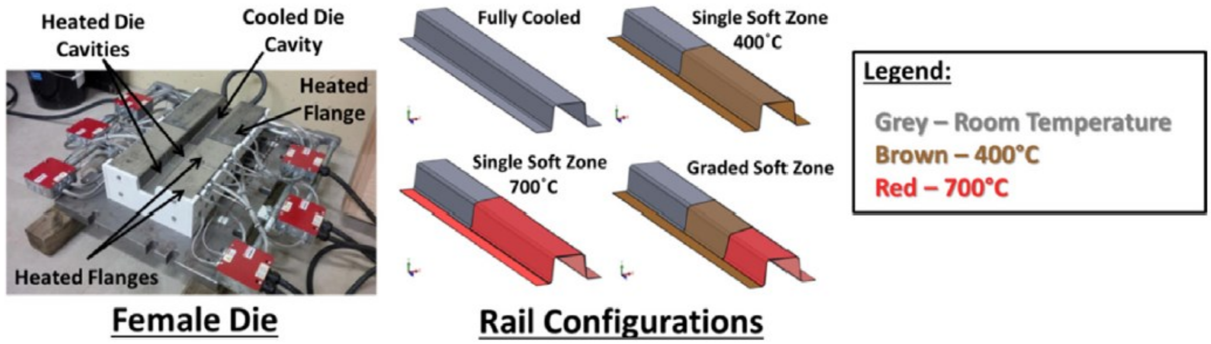

Figure 15: Four different quenched conditions of Usibor® 1500-AS specimens, adapted from Omer *et al.* (2017b)

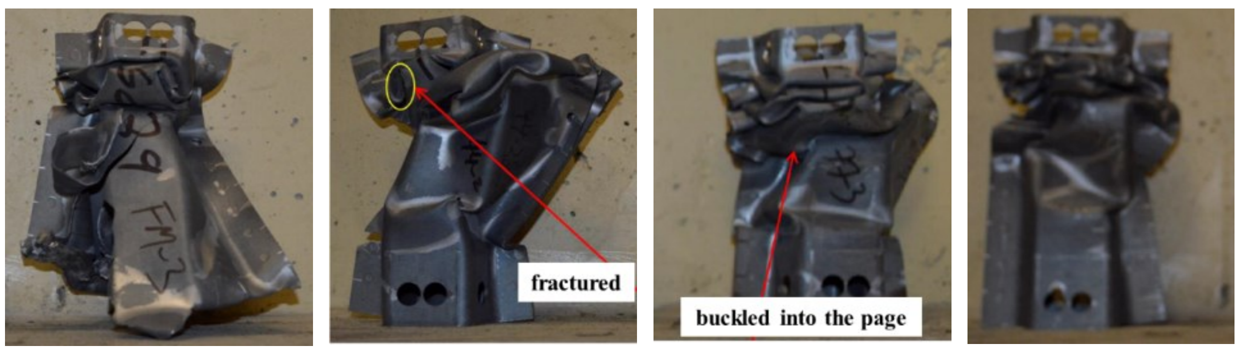

(a) fully cooled (b) single soft zone 400°C (c) single soft zone 700°C (d) graded soft zone

Figure 16: Crush mode comparison of various IDH specimens, adapted from Omer *et al.* (2017b)

Among all specimens, the graded soft zone exhibited the most consistent progressive folding mode with the least scatter in energy absorption. The presence of the two stronger regions was hypothesized to reduce the effective column length and reduce the global buckling tendency. However, the average absorbed energy of graded soft zone specimens (12.6 kJ) was lower than that of the fully cooled specimens (14.8 kJ) despite the extensive fracture of the fully cooled specimens.

Peister (2019) studied the crush performance of hot stamped axial crush specimens fabricated using both monolithic Ductibor® 500-AS and TWBs comprising Ductibor® 500-AS laser welded to Usibor® 1500-AS, as shown in Figure 17. The monolithic specimens did not exhibit parent metal fracture due to the high ductility of Ductibor® 500-AS. The specimens exhibited global buckling tendencies, however, after initial folding. The TWB specimens exhibited a stable folding mode without global buckling although some parent metal fracture initiated in the Usibor® 1500-AS region late in the crush experiment.

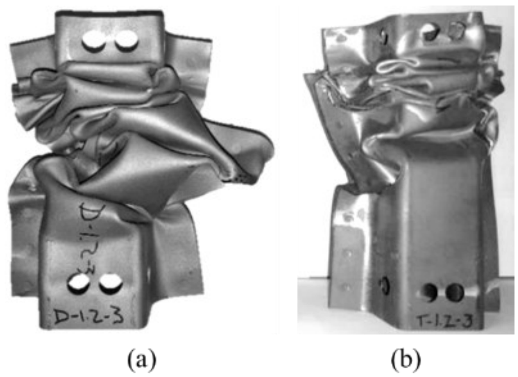

Figure 17: Dynamic axial crush specimens from Peister (2019): (a) 1.2mm Ductibor® 500-AS and (b) 1.2mm TWB consisting of Ductibor® 500-AS welded to Usibor® 1500-AS

1.3.2. Numerical Modelling of Axial Crush

Conducting full-scale crash tests is time-consuming and expensive. Consequently, the automotive industry relies on numerical modelling to predict vehicle crash behaviour and reduce the number of required crash tests. For boundary value problems whose time scale is less than a fraction of a second, the computational efficiency of explicit analysis, such as central difference methods (James *et al.*, 1985), provides advantage over implicit analysis, such as the Newmark method (Newmark, 1959), in solving the discretized form of the structural dynamic equilibrium equation,

$$\{\boldsymbol{F}(t)\} = [\boldsymbol{K}]\{\boldsymbol{d}\} + [\boldsymbol{M}]\{\ddot{\boldsymbol{d}}\} \tag{20}$$

where $\{\boldsymbol{F}\} = \sum_{e=1}^{N}\{\boldsymbol{f}^{(e)}\}$, $[\boldsymbol{K}] = \sum_{e=1}^{N}[\boldsymbol{k}^{(e)}]$ and $[\boldsymbol{M}] = \sum_{e=1}^{N}[\boldsymbol{m}^{(e)}]$ are the global force, stiffness and mass matrices, respectively. In either solution scheme, $[\boldsymbol{M}]^{-1}$ can be cheaply approximated by using a lumped mass matrix or more accurately by using a consistent mass matrix (Archer, 1965). Figure 18 shows various numerical models of dynamic axial crush using explicit solvers.

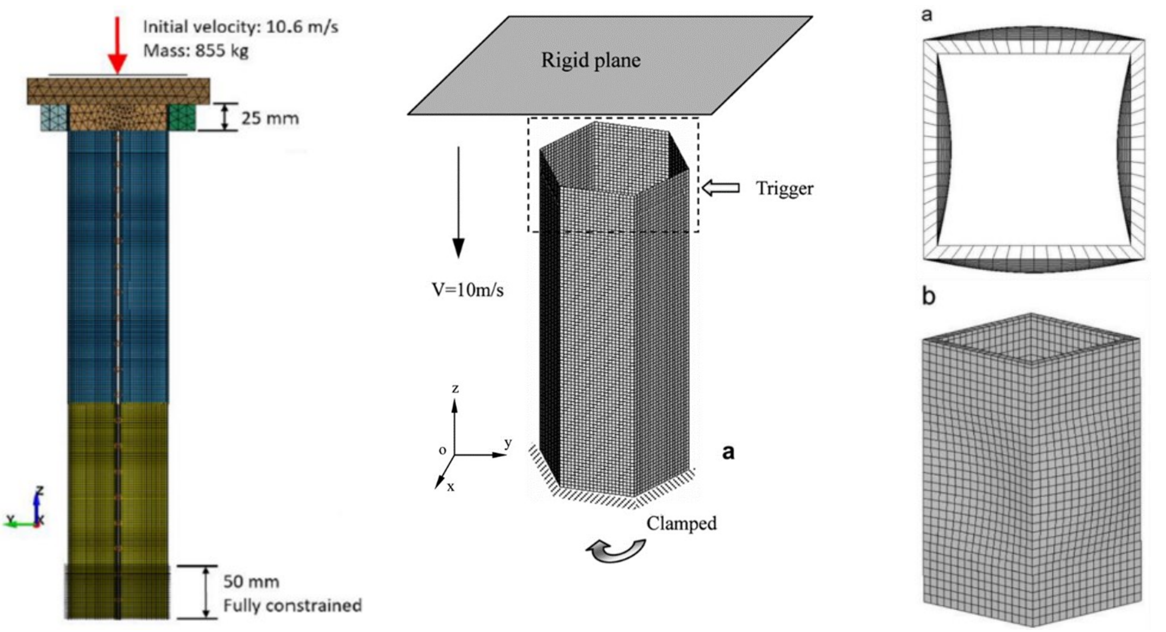

(a) double hat channel (Peister, 2019) | (b) polygonal column (Zhang and Huh, 2010) | (c) square column (Fyllingen *et al.*, 2010)

Figure 18: Examples of dynamic axial crush numerical models: (a) double hat channel with shell elements (b) polygonal column with shell elements and (c) square column with solid elements. All models were solved using the non-linear, explicit finite element code LS-Dyna (Livermore Software Technology Corporation, 2016).

For numerical problems whose total simulation time is much larger than the explicit time step, selective mass scaling is commonly adopted (Langseth *et al.,* 1999; Pan *et al*., 2006; Toksoy and Güden, 2010). The method artificially increases the density of elements who possess the lowest time step, thereby increasing the critical time step (Courant *et al*., 1928) and reducing computational cost.

Another approach to improve efficiency is time scaling in which the tool velocities (in metal forming) are increased. Although both methods introduce artificial dynamic effects and hence, require engineering judgement, several forming and crash studies (Santosa *et al.,* 2000; Lorenz and Haufe, 2008; Suresh and Regalla, 2014; Omer, 2014; Peister, 2019) have successfully demonstrated the accuracy of obtained numerical results.

A key aspect of modelling crash is the prediction of spot weld behavior since automotive structures commonly contain thousands of spot welds. For numerical simulation of spot welds, one common method in the literature is to utilize beam elements (Matzenmiller *et al.,* 1994; Dreas, 1988). Beams are created between two shell elements to transmit forces and moments. In contrast, a volume element-modelling approach has been studied to represent the spot weld nugget in 3D (Chen and Deng, 2000;

Xiang *et al*., 2006). Figure 19 demonstrates such an approach by Tummers (2020) in which a spot weld is modelled by eight hexahedral elements. Another important aspect, failure criteria, should also be added to account for failures in shear, bending and normal loads and considerable previous research has aimed to calibrate different failure models (Malcolm and Nutwell, 2007; O'Keeffe, 2018; Tolton, 2020).

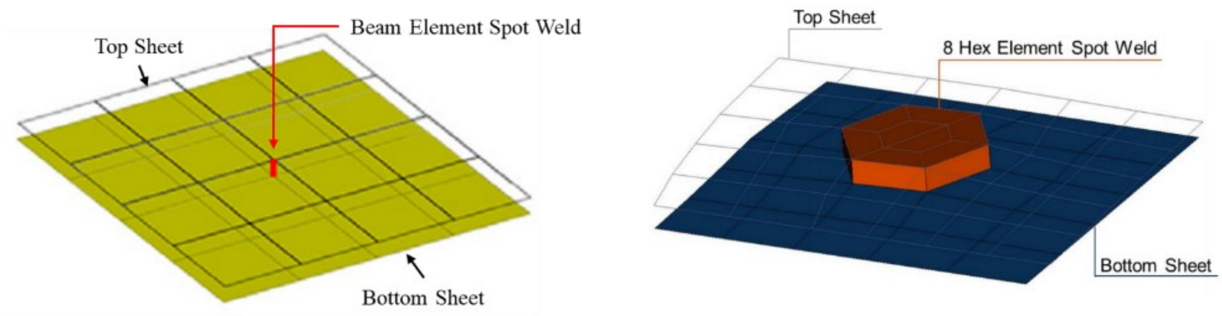

(a) Beam element (b) Hexahedral elements

Figure 19: Comparison of (a) a spot weld using a beam element (Park *et al.*, 2018) and (b) a spot weld using eight hexagonal solid elements (Tummers, 2020).

Recent studies by Chen *et al.* (2014) and Mohamadizadeh *et al.* (2020) have introduced an improved level of detail in weld failure modelling using a meso-scale approach. This approach utilizes fine solid elements, as shown in Figure 20, with the aim to capture the effect of local variations in weld microstructure on failure. For example, the elements across the Heat Affected Zone (HAZ) are assigned varying hardening curves based on the measured micro-Vickers Hardness (Chen *et al*., 2014). The principal challenge in utilizing such an approach in structural crash safety modelling is the high computation cost associated with such fine discretization of spot welds.

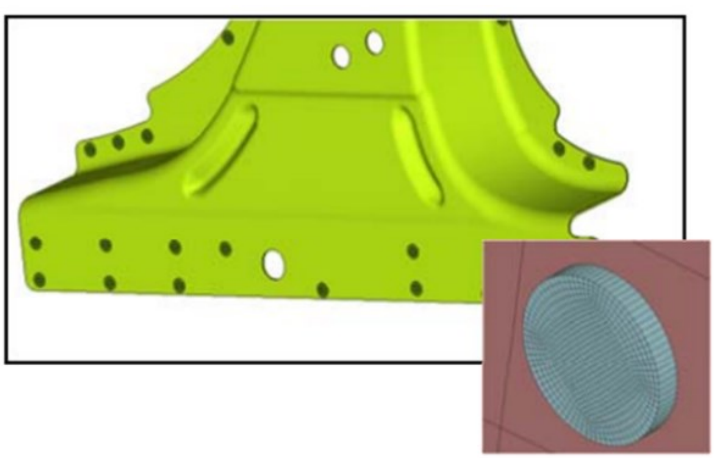

Figure 20: Meso-scale modelling of spot weld nuggets, adapted from Chen *et al.* (2014).

Tummers (2020) modelled the axial crush of a commercial SUV sub-assembly, which is referred to as the front end module, as shown in Figure 21. The front end module consisted of components such as the front bumper, side frame member, shock tower and shock tower support. The level of completeness and efforts in boundary condition modelling is demonstrated by several features including the wood attenuator modelled using solid elements, the load cells modelled as linear elastic beams and several bolted connections modelled as plastic beam elements with pre-tension due to bolt torque.

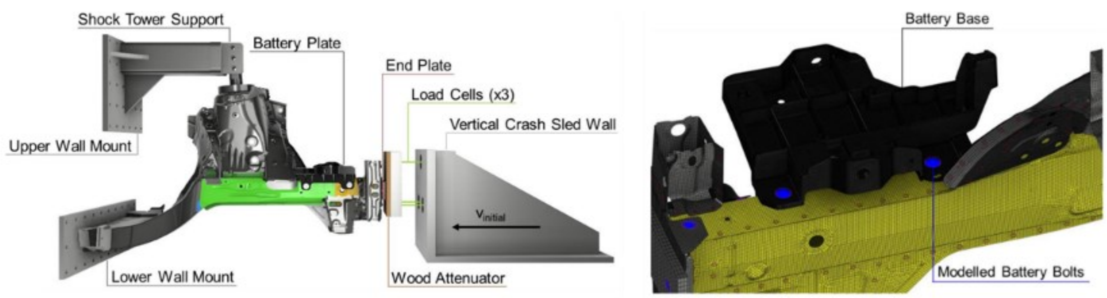

Figure 21: Numerical model setup of front end module (left) and bolt connection between the battery base and side frame member, using constrained nodal rigid bodies (right), adapted from Tummers (2020)

1.3.3. Triggering Methods in Axial Crush

Ideal axial crush structures are required to show good repeatability in the deformation mode; however, geometric defects or fracture-susceptible material behaviour can result in a lack of repeatability. One method to improve repeatability is to control fold initiation and mode of deformation by introducing triggering mechanisms. These mechanisms are sometimes referred to as fold initiators and are generally broken down into mechanical or thermal means of structural modification.

The most common method to produce mechanical fold initiators is by local indentation, as illustrated in Figure 22. Often, a row of two indents is inserted on opposite walls of the double hat specimens either asymmetrically (Chen, 2001) or symmetrically (Omer *et al.*, 2017b). Numerous axial crush studies of hot stamped steel (Omer *et al.*, 2017b; Peister, 2019; Tummers *et al.*, 2018) consistently adopted the symmetrical form; hence, this will be referred to as the “standard fold initiator trigger” to serve as a baseline comparison throughout the balance of this thesis.

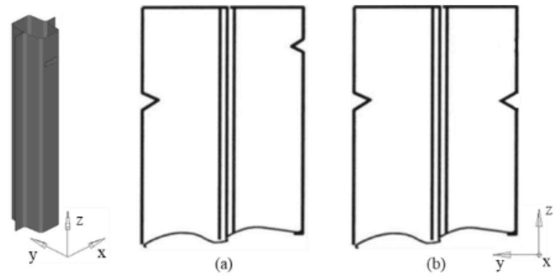

Figure 22: Asymmetric (left) and symmetric (right) insertion of fold initiators near the top end of double hat channel crush specimens, adapted from Chen (2001)

Other types of mechanical fold initiators take the forms of notches, beads, grooves, holes or pulling strips, as shown in Figure 23. Similar to indentation, studies of these fold initiators (Lee *et al.*, 1999; Witteman, 1999; Hosseinipour and Daneshi, 2003; Eren *et al.*, 2009; Zhang *et al.*, 2009) all showed a significant decrease in the initial peak force and more stable folding modes without much change in energy absorption, compared to specimens without fold initiators.

In contrast to mechanical triggering, "thermal triggering" induces change in the microstructure by localized heating. Local heating can introduce soft zones where hinge line formation could occur. Peixinho *et al.* (2012) introduced thermal triggers at various locations of AA6061-T5 aluminum square tubes by a laser treatment. The Vickers micro-hardness measurement confirmed the softening at the heated zones and the thermal triggers successfully assisted in fold formations at the heated locations. Similar to mechanical triggering, a significant decrease in peak force and a slight decrease in energy absorption were also observed in the thermal triggered specimens, compared to those without triggers.

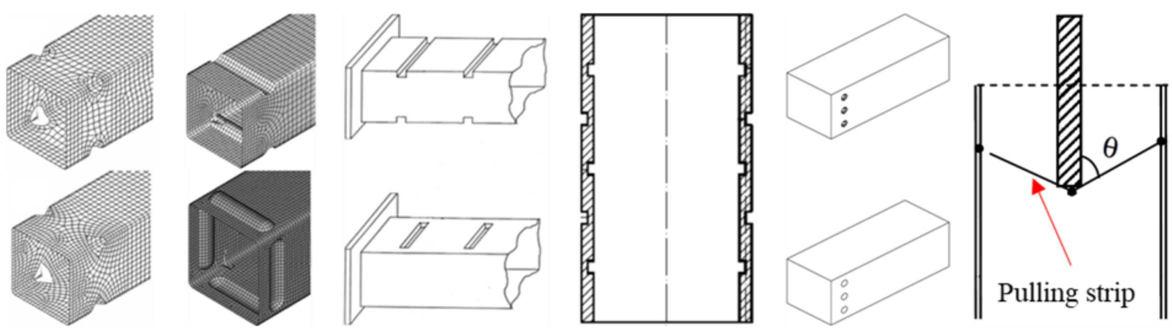

(a)	(b)	(c)	(d)	(e)	(f)
(Eren *et al.*, 2009)	(Eren *et al.*, 2009)	(Lee *et al.*, 1999)	(Hosseinipour and Daneshi, 2003)	(Witteman, 1999)	(Zhang *et al.*, 2009)

Figure 23: Different forms of mechanical fold initiators: (a) corner notches on steel square tubes (b) beads for steel square tubes (c) machined dents for 6063 aluminum square tubes (d) machine grooves for mild steel circular tubes (e) holes for mild steel square tubes and (f) pulling strips for 6063 aluminum square tubes

The effect of trigger spacing plays an important role in axial crush performance. Lee *et al.* (1999) varied the indent spacing along the length of rectangular aluminum crush tubes under quasi-static loading. The important finding was that specimens with trigger indents, introduced at the pre-estimated sites by elastic folding analysis, experienced a significant decrease in initial peak force and a slight decrease in absorbed energy compared to the specimens without or randomly distributed dents. Also, the effect of two different indent sizes, namely half indents and full indents, were studied. The specimens containing half indents absorbed higher energy than those with full indents due to an increase in the plastic work required for hinge line formation. The number of plastic hinges and overall deformation, however, did not vary between the two sizes.

Najafi and Rais-Rohani (2008, 2011) studied the effect of triggering location on square aluminum tubes that were 400 mm in length under dynamic loading. The specimens considered a symmetric trigger configuration, as in Figure 22b, but the location of the indents varied from 5mm to 30mm from the impact-end. The location was found to have a little effect on the peak force and absorbed energy.

All of the fold initiator studies mentioned in this section considered ductile materials such as low strength steel or aluminum alloys. No published literature to date has considered fold initiators within UHSS specimens. Secondly, these studies only considered a single pair of fold initiators, with little systematic study of fold initiator patterns and spacing. The findings of Lee *et al*. (1999) suggest that fold initiators should be placed at pre-estimated sites; however, the locations were estimated by elastic folding analysis whereas real axial crush problems exhibit plastic folding. The lack of relevant literature in developing an improved triggering methodology based on kinematic folding analysis signifies the novelty of the current research, which investigates the design of fold initiators, suitable for UHSS axial crush specimens, to promote stable folding.

1.4. Crush Mechanics of Thin-Walled Structures

Many analytical models (Reid and Reddy, 1986; Grzebieta, 1990; Xue, 2003; Ye *et al*., 2011) exist to predict the axial collapse response of different-shaped, thin-walled structures. The most notable models originate back to the work of Alexander (1960) on circular tubes and the work of Abramowicz and Wierzbicki (1989) on multi-corner tubes. In essence, these studies aimed to identify and isolate the repeating patterns within tubes undergoing axial crush (see Figure 24) based on observed experimental phenomena, break down the pattern into different regions of distinct deformation mode and calculate the dissipated energy associated with each region.

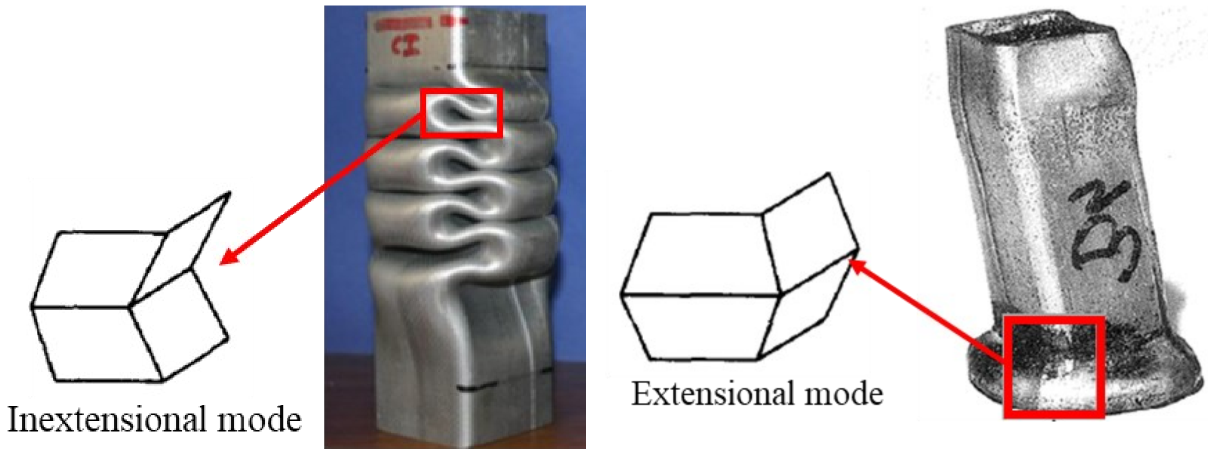

(a) aluminum square tube (b) mild steel square tube

Figure 24: Final deformed images of (a) axially crushed hydroformed aluminum alloy tubes (Williams *et al.,* 2010) and (b) non-hydroformed steel tubes (Abramowicz and Jones, 1984). Different repeating modes within each tube are highlighted in red.

1.4.1. Crush Mechanics of multi-corner elements

The work of Wierzbicki and Abramowicz (1983) and Abramowicz and Wierzbicki (1989) on multi-corner elements assumes two principal deformation paths that a corner element could take: extensional or inextensional, as shown in Figure 25.

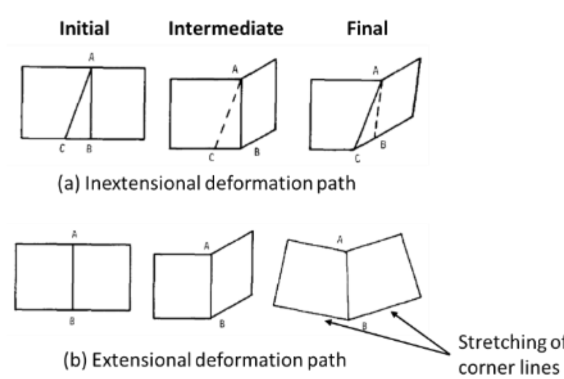

Figure 25: Inextensional and extensional deformation of corner elements (Hayduk and Wierzbicki, 1984)

In inextensional deformation, hinge lines such as AB in Figure 25a stay rotate and/or translate without change in length, imparting a rigid body motion to adjacent elements. On the other hand, the extensional deformation path consists of extending or "stretching" of hinge lines, resulting in shape distortion of adjacent elements. By considering the principle of minimum energy, the preferred mode of deformation would be inextensional because a considerably higher amount of energy is required for extensional deformation (*i.e.* bending vs. in-plane stretching). Physically though, some level of extension is inevitable to ensure material continuity, hence, making every inextensional deformation path virtually quasi-inextensional (Hayduk and Wierzbicki, 1984).

By observing repeated collapse patterns of corner elements in multi-corner tubes, Abramowicz and Wierzbicki (1989) presented two major folding modes, which are designated as quasi-inextensional and extensional modes.

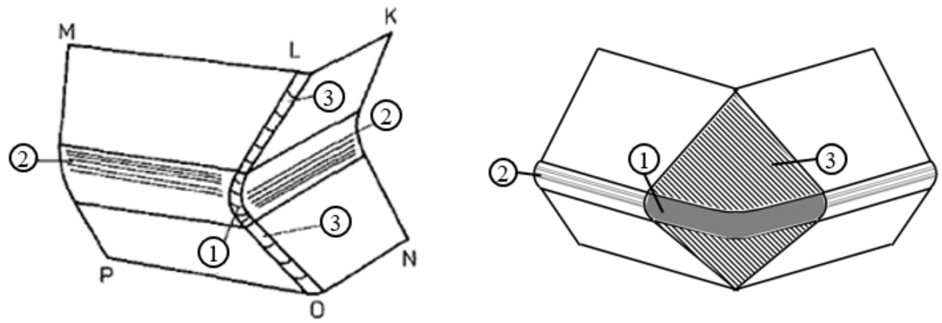

(a) Quasi-inextensional mode (Abramowicz and Wierzbicki, 1989)

(b) Extensional mode (Najafi and Rais-Rohani, 2011)

Figure 26: (a) Quasi-inextensional mode and (b) extensional mode of corner elements

These folding modes consist of several surface elements (numbered 1 to 3 in Figure 26), whose deformation mainly follows either inextensional or extensional paths. In the quasi-inextensional mode, one side deforms outward while the other deforms inward. As reflected by the name of this mode, it consists largely of inextensional elements with the exception of the one small toroidal surface (numbered 1 in Figure 26a). The extensional mode, however, consists of shape-distorted conical surfaces (numbered 3 in Figure 26b) as well as a toroidal surface (numbered 1 in Figure 26b). These deformation regions are portrayed with hinge lines to illustrate the kinematics of the crush mechanism in Figure 27.

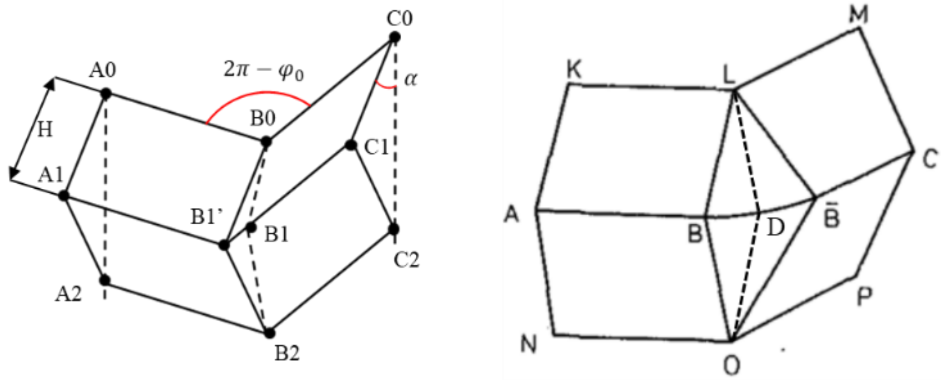

(a) Quasi-inextensional mechanism (Abramowicz and Jones, 1984)

(b) Extensional mechanism (Abramowicz and Wierzbicki, 1989)

Figure 27: (a) Quasi-inextensional mechanism and (b) extensional mechanism of corner elements

In the quasi-inextensional mechanism, lines A_iB_i and B_iC_i represent the horizontal plastic hinge lines. As the element crushes, A_0B_0 and B_0C_0 translate downward, and the initially vertical lines such as A_0A_1 and C_0C_1 become gradually inclined. Simultaneously, point B_1 moves to $B_1{}'$, and the material flows from left-side surfaces $A_0B_0B_1{}'A_1$ and $A_2B_2B_1{}'A_1$ to right-side surfaces $B_0C_0C_1B_1{}'$ and $B_2C_2C_1B_1{}'$, respectively, crossing inclined hinge lines B_0B_1' and $B_2B_1{}'$.

In the extensional mechanism, the initially straight line LDO splits into four inclined lines LB, $L\bar{B}$, *etc.*, and line $B\bar{B}$ stretches circumferentially. Consequently, conical surfaces $LB\bar{B}$ and $OB\bar{B}$ undergo large shape distortions and cause adjacent elements (once rectangular) to transform into a trapezoidal shape. In general, obtuse elements are controlled by the extensional deformation mode, while acute elements are controlled by the quasi-inextensional mode (Abramowicz, 2003).

Further experimental observations made by Abramowicz and Wierzbicki (1989) suggested co-existence of the quasi-inextensional mode and the extensional mode during the crushing process of columns. Motivated to capture the two folding modes in a more generalized mechanism, they presented a superfolding element (SE), which captures the quasi-inextensional mode and extensional mode in a series manner with angle parameter α as shown in Figure 28.

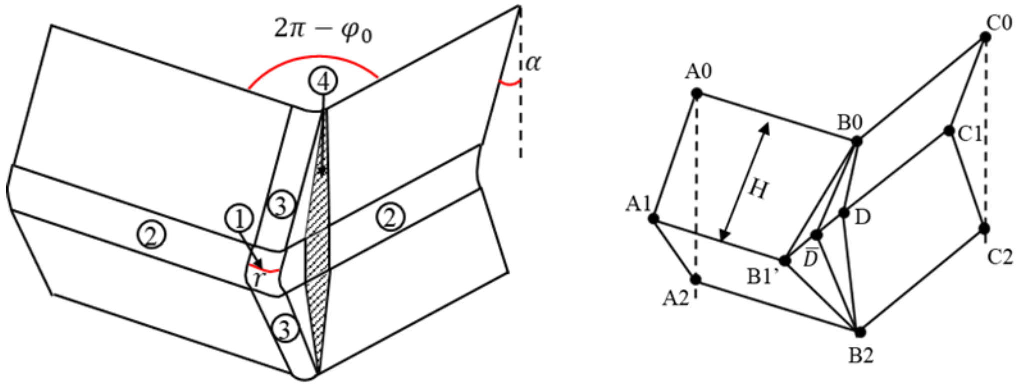

(a) Superfolding element (b) Folding mechanism

Figure 28: Illustration of: (a) superfolding element and (b) its folding mechanism

The parameter α, referred to herein as the crush angle, defines the stage of the crushing process. An uncrushed SE would have an initial height of 2H and its initial state can be expressed as $\alpha = 0$. Once the collapse begins, α increases from 0 and eventually reaches the terminal value of α_f. In a simplified kinematic analysis, the final state results in complete flattening and corresponds to $\alpha_f = \pi/2$. A transition angle $\bar{\alpha}$ is defined as the angle at which a change in mode takes place from quasi-inextensional to extensional mode. When $\bar{\alpha} = 0$, the superfolding element undergoes a purely extensional mode, while $\bar{\alpha} = \alpha_f$ gives a purely inextensional mode.

There are four different classifications of surface elements in the SE, as shown in Figure 28a. The first three groups are developed during the quasi-inextensional stage. Group 1 represents a toroidal surface with extensional deformation in the circumferential direction; group 2 represents cylindrical surfaces, which undergo bending without any extensional deformation; group 3 represents cylindrical surfaces that are bent around inclined hinge lines and undergo inextensional deformation. Lastly, group 4 represents conical surfaces developed during the second extensional stage. The unnumbered surfaces experience rigid body motion.

The mechanism of the SE follows that of the quasi-inextensional mode except when switching between modes takes place, as-inclined lines $B_0{B_1}'$ and $B_2{B_1}'$ become "locked" in place. Subsequently, the initially straight line B_0D and B_2D split into four lines $B_0\overline{D}$, $B_2\overline{D}$, *etc.*, and create conical surfaces $B_0D\overline{D}$ and $B_2D\overline{D}$.

The SE analysis (Abramowicz and Wierzbicki, 1989) begins with identifying the internal energy contribution from two different modes as below:

$$E_{\text{int}} = \int_0^{\bar{\alpha}} \dot{E}_{\text{int}} d\alpha + \int_{\bar{\alpha}}^{\alpha_f} \dot{E}_{\text{int}} d\alpha \tag{21}$$

Kinematically admissible velocity fields, which impose continuity in the velocity distribution over the structure except permissible discontinuity at plastic hinge lines (Lu and Yu, 2003), are assumed over the entire SE domain. Then, the velocity of each hinge line and the corresponding strain rates are found. The rate of internal energy dissipation ($\dot{E}_{int}$) in Equation (21) can now be expressed in terms of the strain rates present in the continuous (over the membranes) and discontinuous (at hinge lines) velocity fields, respectively.

$$\dot{E}_{\text{int}} = \int_S \left(M^{\alpha\beta} \dot{\kappa}_{\alpha\beta} + N^{\alpha\beta} \dot{\lambda}_{\alpha\beta} \right) dS + \sum_{i=1}^{n} \int_{L^i} M_o^i \dot{\theta}_i dl^i \tag{22}$$

where S denotes the mid shell of membranes and L represents the length of i^{th} plastic hinge line over the total number n. In the first integrand, $\dot{\kappa}$ and $\dot{\lambda}$ are the rate of rotation and rate of extension tensors, respectively. The corresponding conjugate generalized stress tensors are $M^{\alpha\beta}$ and $N^{\alpha\beta}$. In the second integrand, M_o^i and $\dot{\theta}_i$ represent the bending moment and rotation rate of the hinge line, respectively.

On the other hand, the external work applied to axially crush the element is represented by

$$W_{ext} = 2P_m H \tag{23}$$

where P_m is the mean crushing force over the crushing length $2H$. The analysis continues with the energy balance

$$W_{ext} = E_{\text{int}} \tag{24}$$

and the closed form solution for P_m is obtained. For simplicity, the subsequent solution procedure is omitted in this section and the reader is referred to Wierzbicki and Abramowicz (1983) for further details.

For perfectly plastic, square columns undergoing a purely quasi-inextensional crush mode, Wierzbicki and Abramowicz (1983) assumed that the element flattens to zero height and presented a final solution of Equation (24) as

$$P_m = 9.56\sigma_y t^{5/3} b^{1/3} \tag{25}$$

where σ_y is the yield strength of the material, t is the sheet thickness, and b is the side length of the square cross section.

One important conclusion drawn from Equation (25) is the ratio of internal energy. Wierzbicki and Abramowicz (1983) stated that the thickness term $t^{5/3}$ indicates that one-third of the dissipated energy is from the extensional collapse mechanism (*i.e.* the toroidal surface), while the remaining two-third stems from the other elements, which experience the inextensional mechanism (*i.e.* bending).

1.4.2. Effective Crush Distance

In the superfolding element analysis, its terminal stage, corresponding to complete consolidation of the folding cell, is defined by α_f, as shown in Equation (21). The simplified folding analysis assumes $\alpha_f = \pi/2$ and the element be completely flattened out. The effective crush distance, δ_{eff}, would be 2H in this case, neglecting the sheet wall thickness and using the following relation

$$\delta_{eff} = \delta_{ini} - \delta_f \tag{26}$$

where δ_{ini} and δ_f are the final and initial vertical length of the superfolding element, respectively.

A schematic comparison of idealized folding and more physical folding is shown in Figure 29. In actual collapse of thin-walled structures, complete flattening (see Figure 29a) does not occur due to the presence of finite radii of the toroidal elements (Wierzbicki and Abramowicz, 1983). The expected crush distance would be smaller and α_f will increase by a small amount, as shown in Figure 29b. Several authors (Ohkubo *et al.*, 1974; Abramowicz, 1983; Abramowicz and Jones, 1984; Abramowicz and Wierzbicki, 1989) reported this phenomenon based on experimental observation.

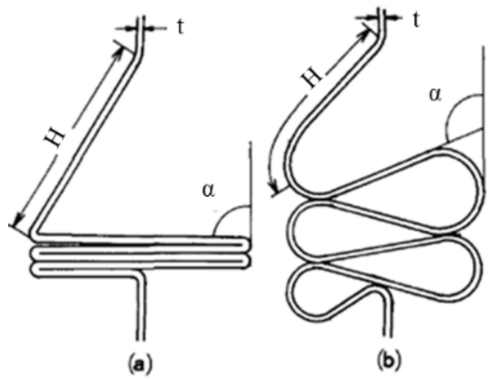

Figure 29: Progressive collapse of hat structure flange: (a) idealized folding where $\alpha_f = \pi/2$ and (b) actual folding where $\alpha_f \geq \pi/2$, adapted from Ohkubo *et al.* (1974)

There are several analytical approaches studied in determining the effective crush distance of different shaped structures. In the case of a cylindrical shell, Wierzbicki *et al.* (1992) represented a fully crushed SE by densely packed circles, as shown in Figure 30. If the size of the lobes are equal, the effective crush distance ratio $\delta_{eff}/2H$ reduces to 0.81.

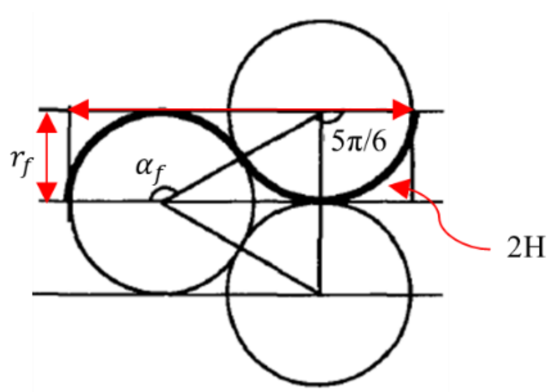

Figure 30: Representation of fully crushed superfolding element by densely packed circles of equal size (Wierzbicki *et al.*, 1992)

For square columns undergoing progressive folding, Abramowicz (1983) idealized the collapse as two subsequent bends about orthogonal axes with radius r and R. In the first bend, the maximum height is 2r whereas that in second bending is 2r + 2R as shown in Figure 31.

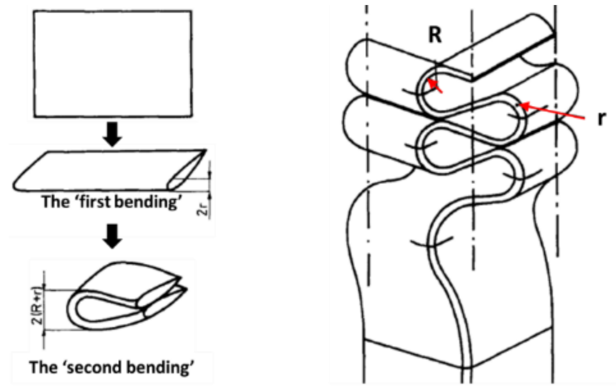

Figure 31: Progressive folding of square columns idealized as a flat sheet undergoing two subsequent bends with radius r and R, respectively (Abramowicz, 1983)

From this analysis, the final crush distance can be obtained by solving the maximum height of the first and second bends. The subsequent analysis treated each bend as a beam buckling problem with plastic flow concentrated at the center zone and the rest of the beam as a rigid zone. The effective crush distance ratio $\delta_{eff}/2H$ was calculated as 0.7, approximately. The later experimental work of Abramowicz and Jones (1984) confirmed the ratio as 0.73 for quasi-inextensional elements and 0.77 for extensional elements.

Another way to measure the effective crush distance in axial crush is by observing the force-displacement curve. As noted by Najafi (2009), the structure would require a substantial increase in the crush force after full consolidation. The onset of such an event would correspond to δ_{eff} and measured by the point of force spike in the curve, as shown in Figure 32.

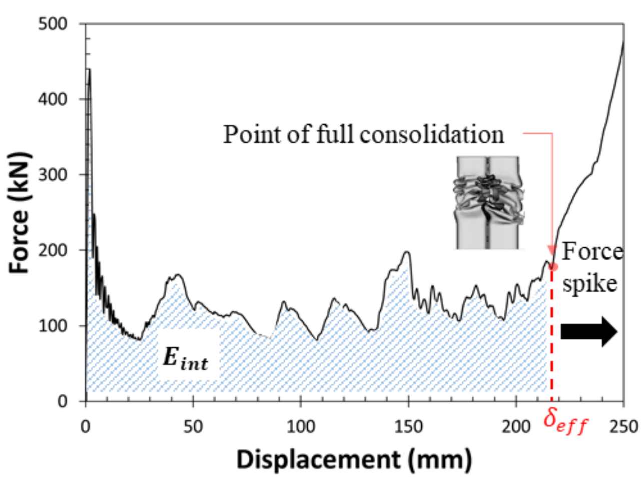

Figure 32: A typical force-displacement (F-D) curve of axial crush models. The crush force spikes after full consolidation.

1.4.3. Crushing of Square Tubes and Hat Channels

For axial crushing of square tubes, Abramowicz and Jones (1984, 1986) conducted a series of tests and observed three different collapse modes, as shown in Figure 33.

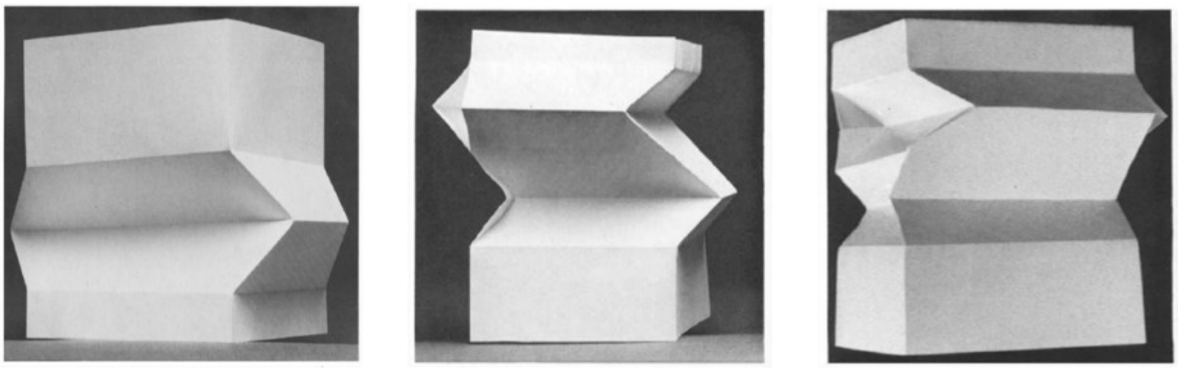

(a) Symmetric mode (b) Asymmetric mixed mode A (c) Asymmetric mixed mode B

Figure 33: Paper models of three collapse modes for axial crushing of square tubes (Abramowicz and Jones, 1984)

They identified that each mode can be assembled by different combinations of quasi-inextensional and extensional elements. For example, the symmetric mode consists of four quasi-inextensional elements over one folding wavelength (2H). The crush mean force would be the same as Equation (25), but Abramowicz and Jones (1986) considered a physical effective crush ratio of 0.73, which gave

$$P_m = 13.06\sigma_y t^{5/3} b^{1/3} \tag{27}$$

In contrast, the asymmetric mixed mode A consists of six quasi-inextensional and two extensional elements, while the mode B consists of seven quasi-inextensional and one extensional elements over two folding wavelengths (4H). The energy balance analyses gave

$$P_m = 10.73\sigma_y t^{5/3} b^{1/3} + 0.79\sigma_y t^{4/3} b^{2/3} + 0.51\sigma_y t^2 \tag{28}$$

and

$$P_m = 11.48\sigma_y t^{5/3} b^{1/3} + 0.44\sigma_y t^{4/3} b^{2/3} + 0.26\sigma_y t^2 \tag{29}$$

for modes A and B, respectively.

Although Equations (27) to (29) are different expressions, they give similar results over the practical range of b/t ratio (Ma, 2011). Another key finding was that what gives rises to the event of one mode than the other is the loading case (*i.e.* static *vs.* dynamic) and the ratio of sidewall length to thickness (b/t).

Motivated to expand theoretical work to consider top hat and double hat cross sections, White *et al.* (1999) predicted the mean crushing force by identifying that top hat and double hat cross sections consist of four and eight, SEs undergoing quasi-inextensional modes, respectively, as shown in Figure 34. The top hat section consists of an additional rectangular backing plate that undergoes pure bending.

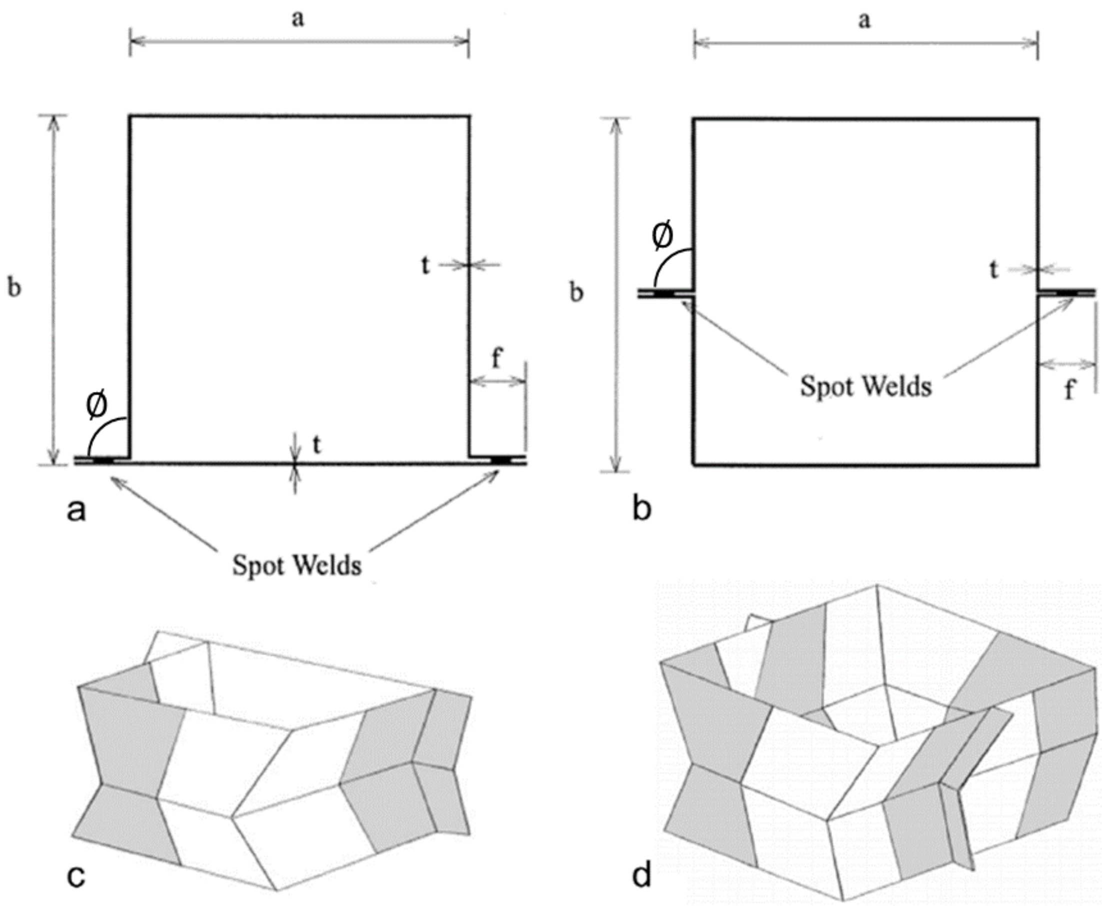

Figure 34: (a) Cross-section of a single top hat and (b) double top hat geometry. (c) Four SEs and a backing plate forming the single top hat profile and (d) Eight SEs forming the double top hat collapse profile (White *et al.*, 1999).

The predicted mean force equation for the top hat section was

$$P_m = 8.22\sigma_y t^{5/3} Z^{1/3} \tag{30}$$

and for the double hat section was

$$P_m = 13.05\sigma_y t^{5/3} Z^{1/3} \tag{31}$$

in which Z is the middle surface perimeter of the cross-section, which can be approximated as $2a + 2b + 4f$, as illustrated in Figure 34.

Their analytical prediction was validated in an experimental study with several design parameters consisting of the column length and flange size (White and Jones, 1999). The key observation was that rolling deformation of the flange is crucial in promoting progressive collapse (see Figure 35a), and in-plane deformation of the flange leads to irregular folding in the double hat channel (see Figure 35b).

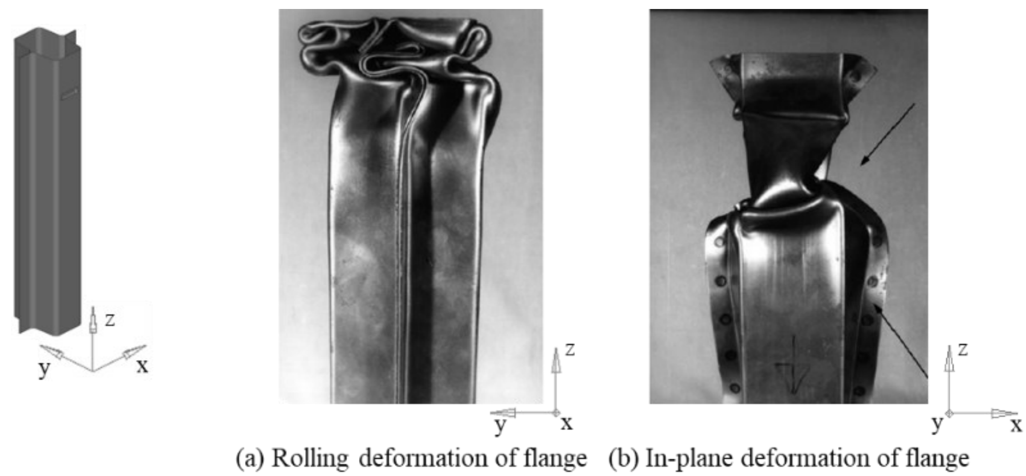

Figure 35: Two collapse modes of double hat specimens: (a) rolling deformation of flange during progressive collapse and (b) in-plane deformation of plane leading to irregular folding¸ adapted from White and Jones (1999)

Although a reasonable agreement in the mean force was shown between the experiential and theoretical results using Equation (30) and (31), a major shortcoming of the theoretical analysis was apparent: the SE analysis assumed progressive collapse mode while physical axial crush tests revealed other modes such as Euler buckling or irregular folding, as shown in Figure 35b.

Several sources of in-plane deformation of the flange were identified as asymmetry of spot weld positions in the specimens and a short flange length (f), giving a low stability ratio. Interestingly, irregular folding specimens often exhibited simultaneous lobe formation at the top–end and bottom-end of specimens. Concluding remarks on the design insights were that (1) single hat structures exhibit a more stable progressive collapse than double hat structures and (2) collapse stability generally improved as the flange length increased.

The analyses on rectangular or hat channels introduced so far were made under the perfectly plastic assumption. To consider the material strain hardening effect in the energy balance analysis, White *et al.* (1999) assumed a power law for the stress-strain relationship

$$\frac{\sigma(\varepsilon)}{\sigma_u} = \left(\frac{\varepsilon}{\varepsilon_u}\right)^n \tag{32}$$

in which σ_u is the UTS, ε_u is the ultimate tensile strain (the strain at UTS) and n is the strain hardening exponent. For mild steel with $\varepsilon_u = 0.3$ and $n = 0.1$, the predicted mean force was

$$P_m = 8.89\sigma_u t^{1.71} Z^{0.29} \tag{33}$$

for the top hat section and

$$P_m = 13.05\sigma_u t^{1.71} Z^{0.29} \tag{34}$$

for the double hat section. An alternative approach to consider the strain hardening effect was suggested by Santosa *et al.* (2000) to adopt an energy equivalent flow stress σ_o in the following form

$$\sigma_0 = \sqrt{\frac{\sigma_y \sigma_u}{1+n}} \tag{35}$$

Lastly, the theoretical work was expanded to predict mean force P_m^d under dynamic axial crush, accounting for material strain rate sensitivity, by White and Jones (1999) using the Cowper-Symonds relation as follows

$$\frac{P_m^d}{P_m} = 1 + \left(\frac{\dot{\varepsilon}_{av}}{D}\right)^{1/\rho} \tag{36}$$

in which $\dot{\varepsilon}_{av}$ is the average strain rate in the Superfolding element and D, ρ are material constants.

1.5. Summary of Previous Work and Scope of Thesis

The preceding literature review shows that a considerable effort has been expended on the analysis of the crush mechanics of thin-walled structures undergoing progressive folding, as well as the axial crush performance of hot stamped components. While crush components made of low strength, high ductility steel alloys predominantly showed progressive or irregular folding, it is evident that those fabricated with fully quenched 1500 MPa hot stamped grades, for example, instead exhibited fracture or global buckling. Much of this unstable crush response can be attributed to the low ductility of parent metal.

Prior studies have examined the folding stability of crush components, but have not considered the systematic optimization of fold initiator patterns nor has the effect of fracture on folding stability of crush structures been examined in a rigorous manner.

This thesis addresses these deficits in the literature by systematically investigating the effect of fold initiator pattern and spacing on the folding stability of hot stamped Ductibor® 1000-AS axial crush rails. The thesis also addresses the development of metrics that can predict axial crush performance in terms of three criteria: energy absorption, extent of fracture, and deformation mode, which are characterized in terms of three performance metrics: “Crush Energy Efficiency”, “Relative Bending Limit” and “Folding Transition Indicator”, respectively. To this end, a wider range of steel grades are considered, in addition to Ductibor® 1000-AS, drawing on axial crush results taken from the literature for strengths in the range 270-1500 MPa.

Accordingly, the remainder of the thesis presents research undertaken to address these objectives and is organized as follows. Chapter 2 presents the experimental testing program, including the methods used for specimen preparation, the test setup for the dynamic and quasi-static axial crush experiments, and the test matrices capturing the scope of the experiments. Chapter 3 presents the numerical models developed herein to simulate the axial crush experiments. The results obtained from the numerical models and axial crush experiments considering Ductibor® 1000-AS are presented in Chapter 4, while Chapter 5 presents the development of the axial crush performance metrics. Lastly, Chapter 6 presents conclusions stemming from this research and recommendations for future work.

2.0 Experimental Methods

This chapter presents the experimental methods used in this research, including specimen fabrication and test setup. Three sets of axial crush experiments were performed, and the corresponding test matrices for each, referred to as Parts 1, 2 and 3, are presented. The chapter is organized as follows. Section 2.1 presents an overview of the experimental program and the scope of each part of the testing program. Section 2.2 describes the methods used to manufacture and indent the axial crush specimens. Lastly, Sections 2.3 and 2.4 describe the test setup for the dynamic and quasi-static axial crush experiments.

2.1. Overview of Experimental Studies

A three-part experimental program, each comprising a set of axial crush experiments, is employed. The interrelationship between each part (*i.e.* study) is illustrated in the flowchart in Figure 36. The corresponding test matrices are shown in Table 3, which summarizes the test conditions.

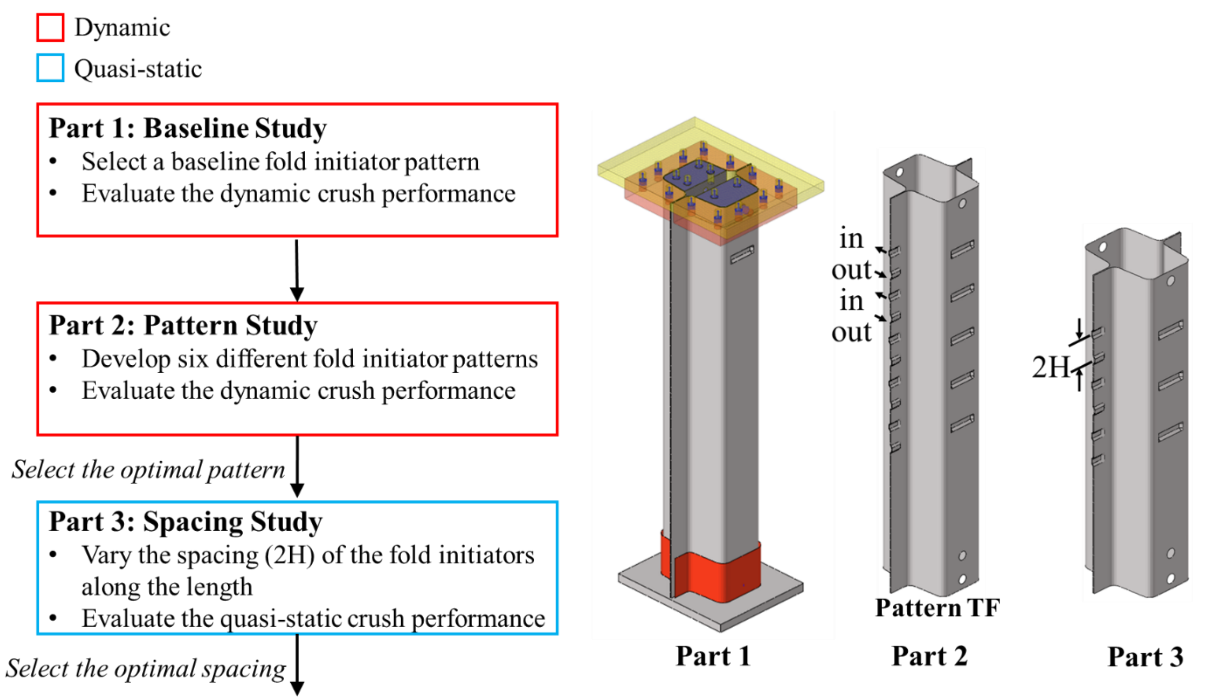

Figure 36: Flowchart outlining the experimental studies

As shown in the flowchart, the program entails a sequential progression of fold initiator designs. In Part 1, the specimen geometry to be used throughout the thesis is established as a baseline pattern, corresponding to the "standard" trigger configuration (introduced in Section 1.3.3). In Part 2, several kinds of repeating fold initiator patterns are introduced in the specimen. One of the results stemming from Part 2 is a unique fold initiator pattern, namely pattern TF, in which the fold initiators are strategically located on the faces of the double hat channel to improve on the baseline crush performance. Based on pattern TF, Part 3 investigated the effect of fold initiator spacing on folding stability. In particular, the initiator spacing is varied in a parametric fashion, and the resulting crush stability was compared to that corresponding to the analytically predicted folding wavelength using the methodology of Abramowicz and Wierzbicki (1989). Sections 2.1.1 to 2.1.3 detail each aspect of the fold initiator patterns.

Table 3: Test matrices devised for the experimental studies. The length of the dynamic and quasi-static crush specimens are 500 mm and 375 mm, respectively. The detailed parametric aspects for each study are presented in Section 2.1.1 to 2.1.3.

Specimen Designation	Numerical (N) Experimental (E)		Dynamic (D) Quasi-Static (Q)		Thickness (mm)		Fold Initiator Spacing, 2H (mm)				
					1.2	1.6	20	25	27.5	30	35
Part 1. Baseline Study											
BA	**N**	**E**	**D**		✓				-		
BA_TWB	**N**	**E**	**D**		✓				-		
Part 2. Fold Initiator Pattern Study											
TCS	**N**		**D**		✓						✓
TCA	**N**	**E**	**D**		✓			✓			
FCS	**N**		**D**		✓						✓
FCA	**N**		**D**		✓			✓			
TF	**N**	**E**	**D**		✓			✓			
TFO	**N**		**D**		✓			✓			
Part 3. Fold Initiator Spacing Study											
SP-D12-200	**N**	**E**		**Q**	✓		✓				
SP-D12-275	**N**	**E**		**Q**	✓				✓		
SP-D12-350	**N**	**E**		**Q**	✓						✓
SP-D16-200	**N**	**E**		**Q**		✓	✓				
SP-D16-250	**N**	**E**		**Q**		✓		✓			
SP-D16-300	**N**	**E**		**Q**		✓				✓	
SP-D16-350	**N**	**E**		**Q**		✓					✓

Note that the experiments in Parts 1 and 2 considered dynamic (impact) loading in view of the crash nature of the application. In Part 3, quasi-static loading was considered in order to improve the quality of imaging and data acquisition and also to prevent clouds of Al-Si dust, ejected from the specimen surface, from obscuring the folding patterns. Furthermore, the specimen length in Part 3 was reduced to 375 mm to reduce the likelihood of global buckling.

2.1.1. Part 1: Baseline Study

For the purposes of this study, the "Baseline" specimen is considered to be a double hat channel in which two fold initiators are inserted, one on each top face of two opposing channel sections, positioned in a symmetrical fashion, located 70 mm from the impact end as shown in Figure 37a. In addition to the Baseline specimens, a number of TWB samples, shown in Figure 37b, were tested. Note that the major focus of this research was on the monolithic Ductibor® 1000-AS samples and only a limited number of tests were performed on TWB samples.

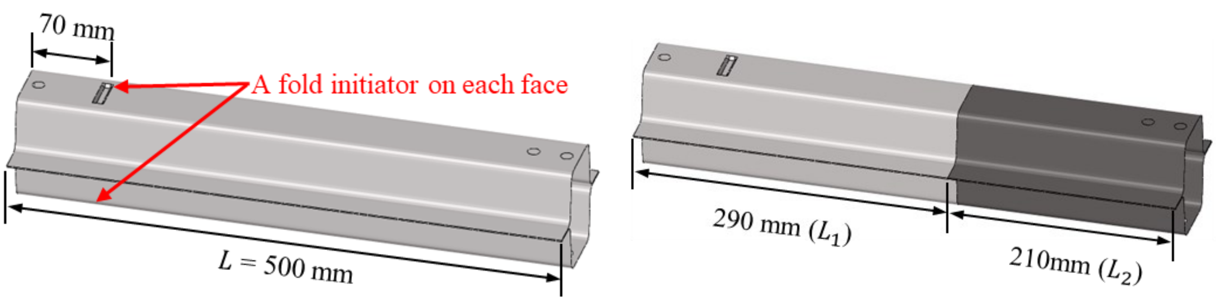

(a) Monolithic configuration (b) TWB configuration

Figure 37: Baseline fold initiator pattern in two configurations: (a) monolithic and (b) TWB.

The cross-sectional geometry shown in Figure 38 was common to all of the current experiments, as well as previous axial crush studies on hot stamping steels by Omer *et al.* (2017b) and Peister (2019).

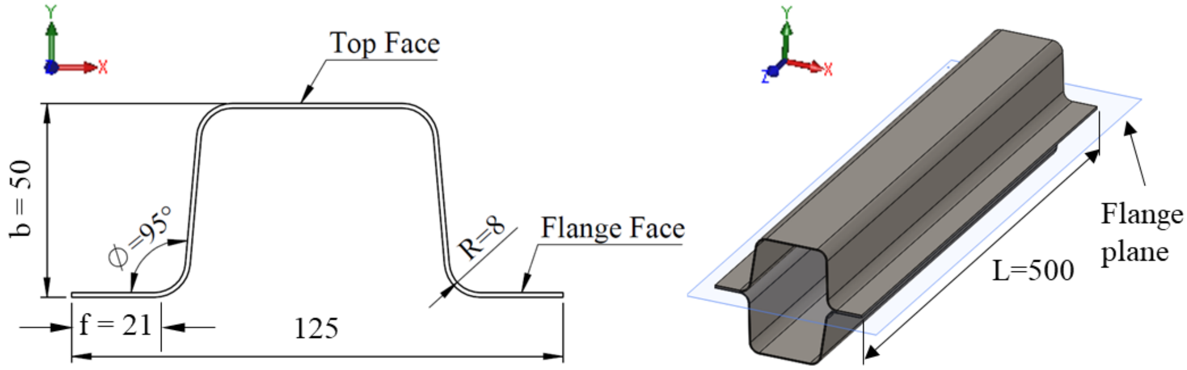

(a) Hat channel cross section (b) Double hat channel

Figure 38: Geometric parameters of (a) a hat channel cross-section and (b) a double hat channel. Dimensions are in millimeters. The entire perimeter of the cross-section, Z, is 200 mm for top hat and 400 mm for double hat geometry, respectively.

The height (b) and flange length (f) of the specimens are defined in the cross-sectional view, while the length (L) refers to the longest dimension along the axis. The top face refers to the face furthest from the flanges in the cross-section, while the flange face is shown in Figure 38a. For convenience, a "rail" refers to a spot-welded double hat channel specimen assembly.

2.1.2. Part 2: Fold Initiator Pattern Study

Figure 39 shows the set of five design variables considered in the fold initiator patterns: (i) location (top face *vs.* flange face); (ii) sequence (consecutive *vs.* non-consecutive); (iii) symmetric *vs.* non-symmetric; (iv) in *vs.* out; and (v) spacing of the fold initiators.

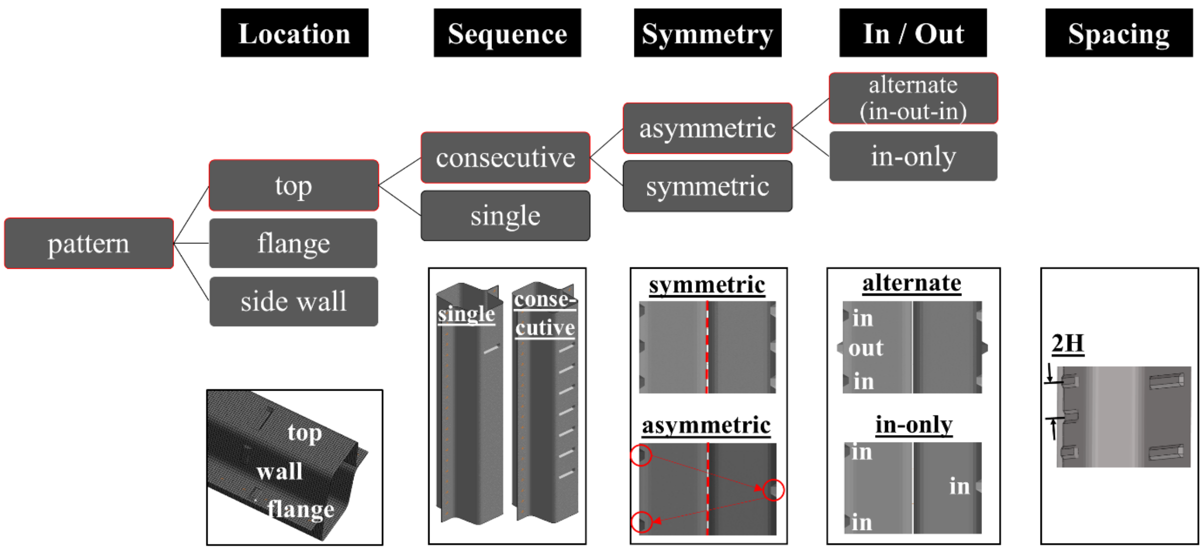

Figure 39: Illustration of different design variables considered in the fold initiator patterns

After considering different combinations, a total of six fold initiator patterns were selected and compared to the baseline pattern, as shown in Figure 40. In patterns TCA (Top-Consecutive-Asymmetric) and TCS (Top-Consecutive-Symmetric), fold initiators were added along the top face in a symmetric or asymmetric arrangement in an attempt to invoke the symmetric mode and the asymmetric mode of the SE pattern, as can be seen in Figure 24. Additionally, fold initiators were considered on the flange face. For FCA (Flange-Consecutive-Asymmetric) and FCS (Flange-Consecutive-Symmetric), fold initiators were added on the flanges only in a symmetric or asymmetric arrangement.

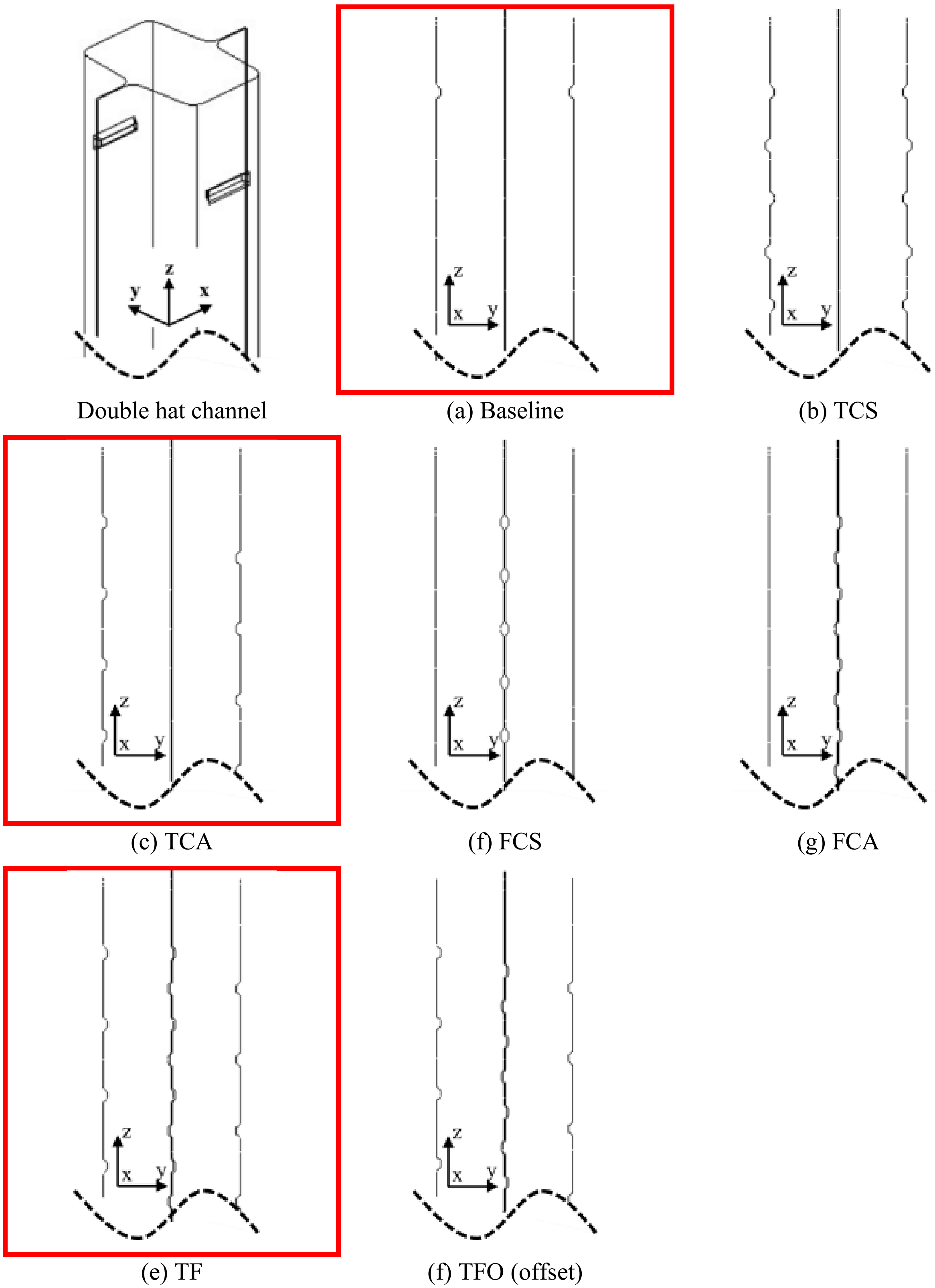

Figure 40. Schematic diagrams of the seven selected fold initiator patterns in a double hat channel. The red-highlighted patterns were chosen for dynamic sled tests.

In addition to placing initiators on just the top face or flange, the TF (Top-Flange) pattern is introduced, which resembles a combination of the TCA and FCA patterns. In this pattern, the flange fold initiators and top fold initiators from the TCA and FCA patterns were merged in a collinear arrangement, with the corresponding flange and top face initiators facing towards the same direction, as shown in Figure 41.

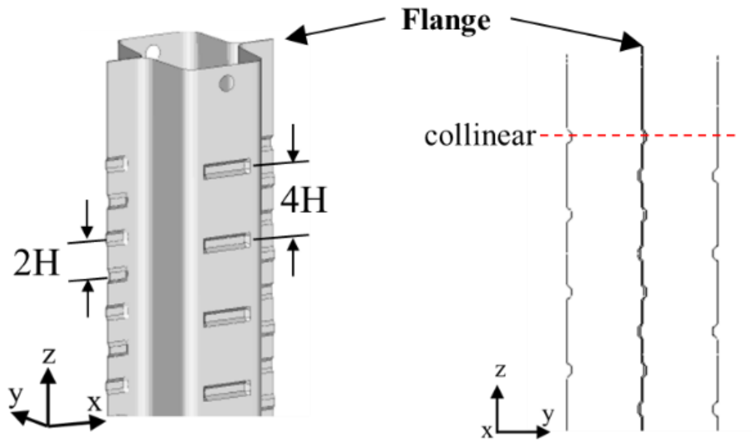

Figure 41: Illustration of pattern TF: isometric view (left) and side view (right). Flange and top fold initiators are collinear and facing towards the same direction.

To investigate the effect of the alignment of the flange and top fold initiators on the crush performance, an additional pattern, TFO (Top-Flange-Offset), was created in which the flange fold initiators were offset from the top face fold initiators by a one-half spacing, H, as shown in Figure 42.

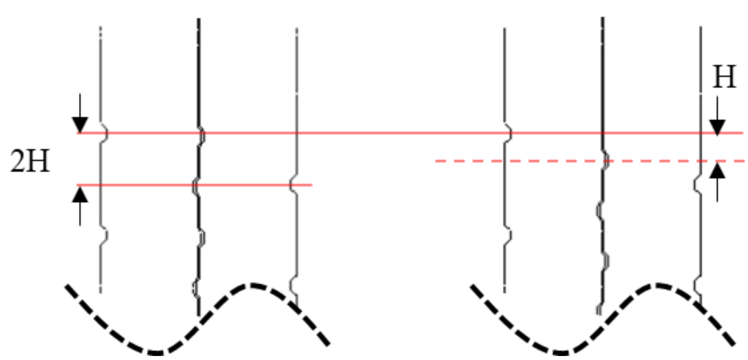

Figure 42: Comparison of TF pattern (left) and TFO pattern (right). In TFO pattern, flange fold initiators are translated down with relative to top fold initiators by the half spacing, *H*

It is important to note that the fold initiator spacing ($2H$) of all patterns, except for the TCS and FCS patterns, were set at 25 mm as a reference. This value is close to the analytical solution using the SE equations, as discussed in Section 2.1.3. Additionally, all fold initiator patterns begin 70 mm away from the impact end and run down along the length up to 300 mm, approximately. Note that an internal boss and external clamp assembly is mounted at the impact end of the rail and has the effect of clamping the first 25 mm of the rail, as described in Section 2.3.

2.1.3. Part 3: Fold Initiator Spacing Study

In selecting a fold initiator spacing, there may exist an "optimal" value that would result in the most stable progressive folding. Such conjecture gave motivation to search for an analytical solution for the optimal spacing. Figure 43b shows the Superfolding Element due to White *et al.* (1999) overlaid on pattern TF, undergoing the asymmetric folding mode. By assuming that the asymmetric folding mode in the double hat channel can be modelled as an assembly of eight Superfolding Elements (see Figure 43a), a critical inference can be made: the height of the SE ($2H$) is one-half of the span from a top fold initiator to the next one ($4H$). Similarly, the flange fold initiator spacing would be equal to the height of the SE. Such an observation implies that the analytical solution, $2H$, from the SE analysis may be the optimal spacing value, that is, the wavelength at which fold lines form and crush in the most stable fashion. To this end, the flange initiator pattern aligns with the serpentine folding sequence that the flange experiences during this asymmetric folding mode.

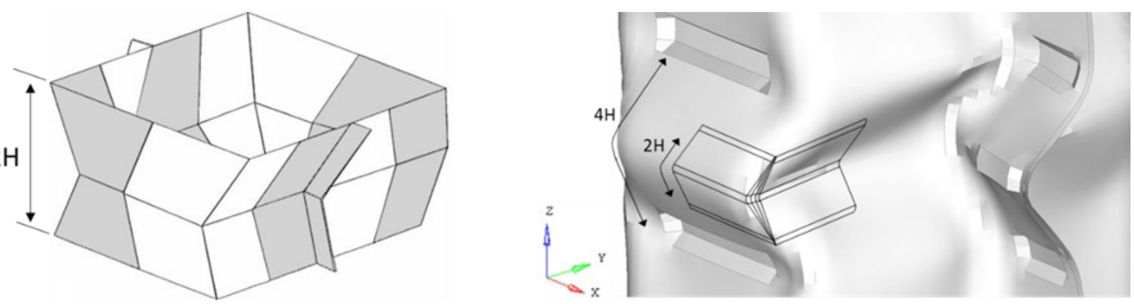

(a) Asymmetric folding of double hat channel (White *et al.,* 1999)

(b) Superfolding Element overlaid on pattern TF

Figure 43: (a) a double hat channel modelled as 8 SEs and (b) a SE overlaid on pattern TF.

The following hypothesis was considered:

A TF pattern—with its fold initiator spacing equal to the SE wavelength—will result in the most stable progressive folding. As the fold initiator spacing deviates from the SE wavelength (too coarse or too narrow), the pattern will result in an unstable folding.

The solutions to the SE wavelength are given by Equation (37) (White *et al.*, 1999), which relates the half-folding wavelength (H) and the sheet thickness (t) as follows:

$$\frac{H}{t} = 0.247\left(\frac{Z}{t}\right)^{2/3} \tag{37}$$

in which Z is the double hat cross-section perimeter (note that $Z \approx 400$ mm for all double hat sections considered in this research). The solution procedure of the SE analysis is provided in Appendix A.

The folding wavelength ($2H$) from Equation (37), which corresponds to the SE flange initiator spacing, was calculated to be 27.5 mm and 30 mm for the 1.2 mm and 1.6 mm thickness specimens, respectively. To examine the effect of initiator spacing, crush tubes with initiator spacings in the range from 20 mm to 35 mm were considered, as shown in Figure 44. For consistency, the number of fold initiators was kept as 3 per top face and 6 per flange face, and the first fold initiator was placed 70 mm away from the impact end.

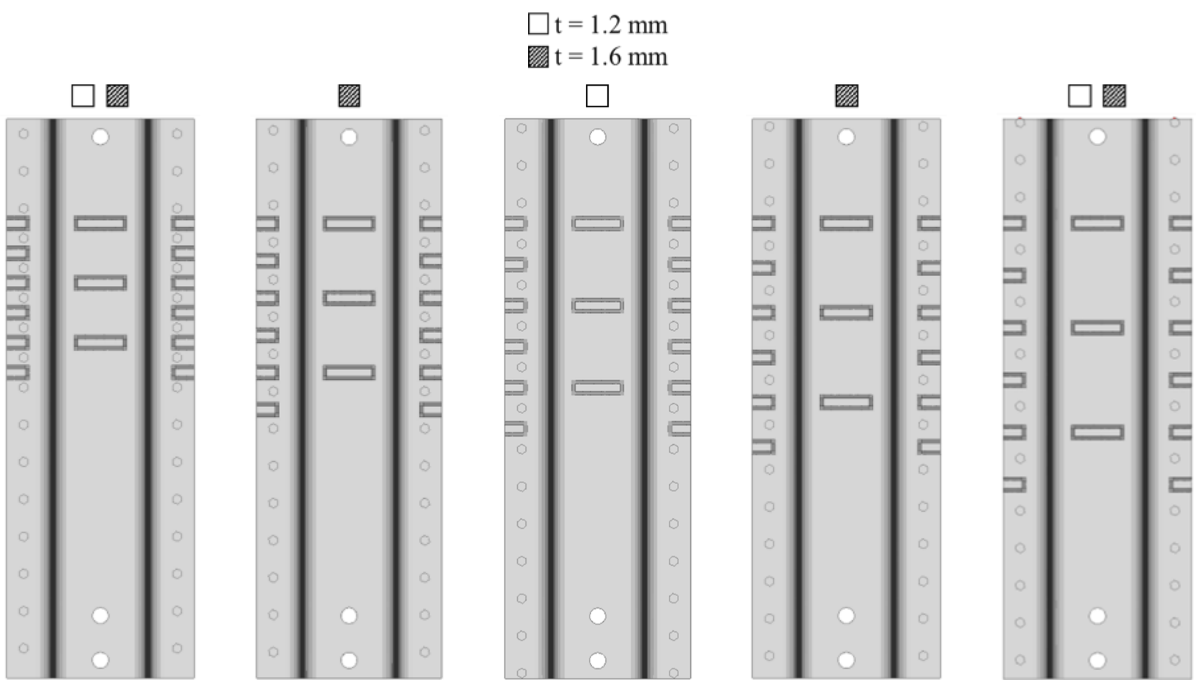

(a) 20 mm (SP-D12-200 / SP-D16-200)

(b) 25 mm (SP-D16-250)

(c) 27.5 mm (SP-D12-275)

(d) 30 mm (SP-D16-300)

(e) 35 mm (SP-D12-350 / SP-D16-350)

Figure 44: Five different fold initiator spacings considered: (a) 20 mm (b) 25 mm (c) 27.5 mm (d) 30 mm and (e) 35 mm. The sheet thicknesses considered are indicated as either white (1.2 mm) or grey (1.6 mm) above for each pattern. Inside the parenthesis are the corresponding specimen designations listed in the test matrix in Table 3.

2.2. Specimen Fabrication

The process for specimen fabrication follows five major stages: forming, pre-weld indentation, spot-welding and post-welding indentation, as shown in Figure 45. The fold initiators are strategically located at the top and flange faces. For convenience, the top face was indented prior to spot-welding (termed pre-weld indentation). The flange face, on the other hand, was indented after the spot welding.

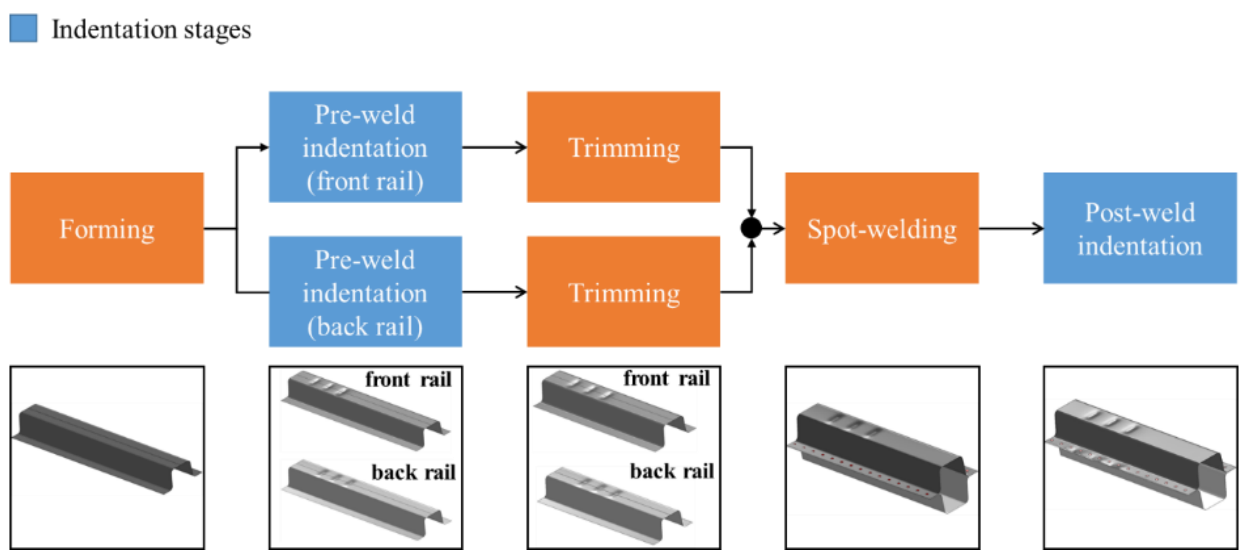

Figure 45: Five stages of axial crush specimen fabrication in the thesis

2.2.1. Forming

The forming process used to produce the hat channels was developed by Omer (2017b) and Peister (2019) in axial crush studies concerning Usibor® 1500-AS and Ductibor® 500-AS. Hence, the same equipment and procedure were used in the current work. The dimensions of a blank prior to forming are shown in Figure 46. These blanks were water-jet cut with two tabs remaining at each end to serve as locating holes for die pins in the transfer stage.

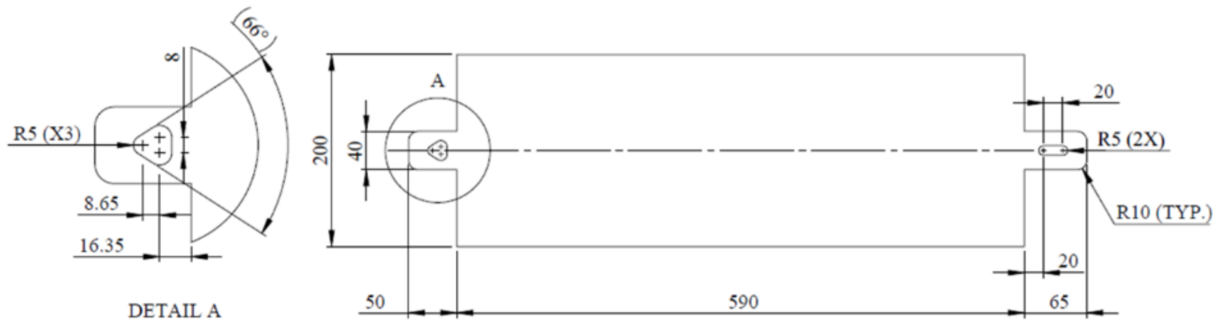

Figure 46: Drawing of a pre-formed blank. All units are in mm.

2.2.1.1. Die Set, Press, Furnace, and Transfer System

The overall forming set up consists of (i) a press, whose platen descends with an upper die; (ii) a die set, which is installed in the press; (iii) a furnace, which heats the blank; and (iv) a transfer system which moves the blank in and out of the furnace and places it in the tool, as shown in Figure 47. Additionally, the setup features a safety guard and a light curtain system programmed to stop the press stroke upon sensing entry into the press area.

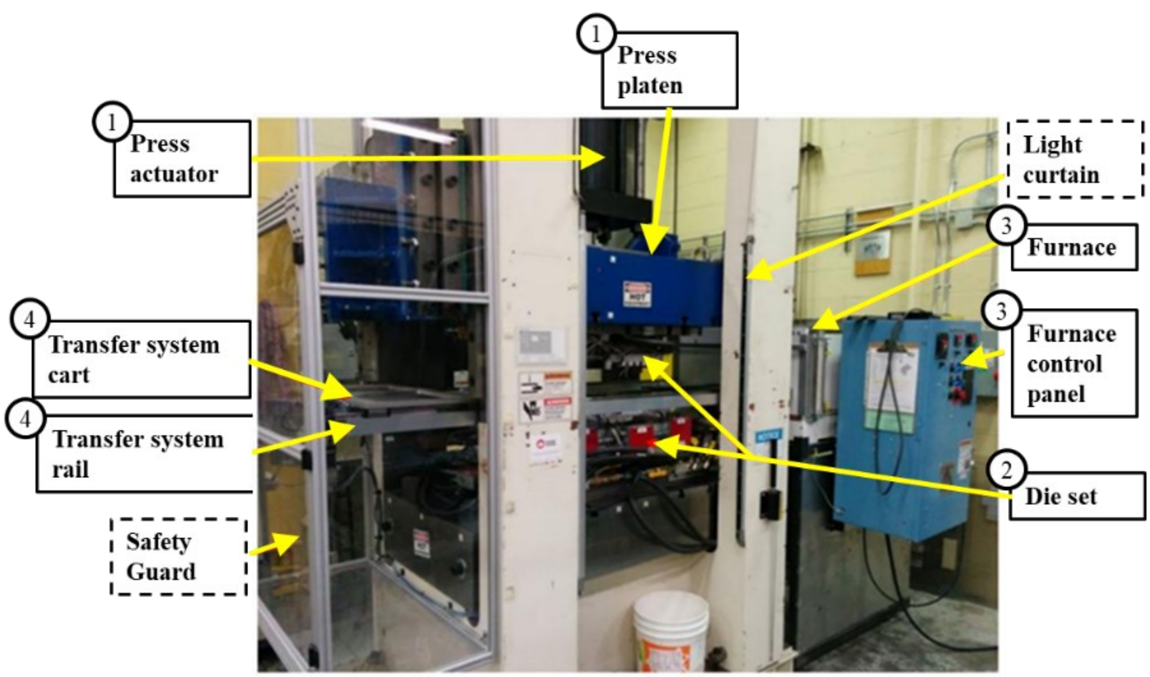

Figure 47: Overview of forming setup, adapted from Peister (2019)

The hydraulic press is manufactured by Macrodyne Technologies Inc. and incorporates an actuator, which provides a maximum force of 125 tons and a platen velocity up to 250 mm/s to which an upper die is mounted. The die set, designed by George (2012), includes an upper die, a lower binder and a punch with two locating pins. To rapidly cool blanks, water channels run inside the upper die and the punch, as shown in Figure 48.

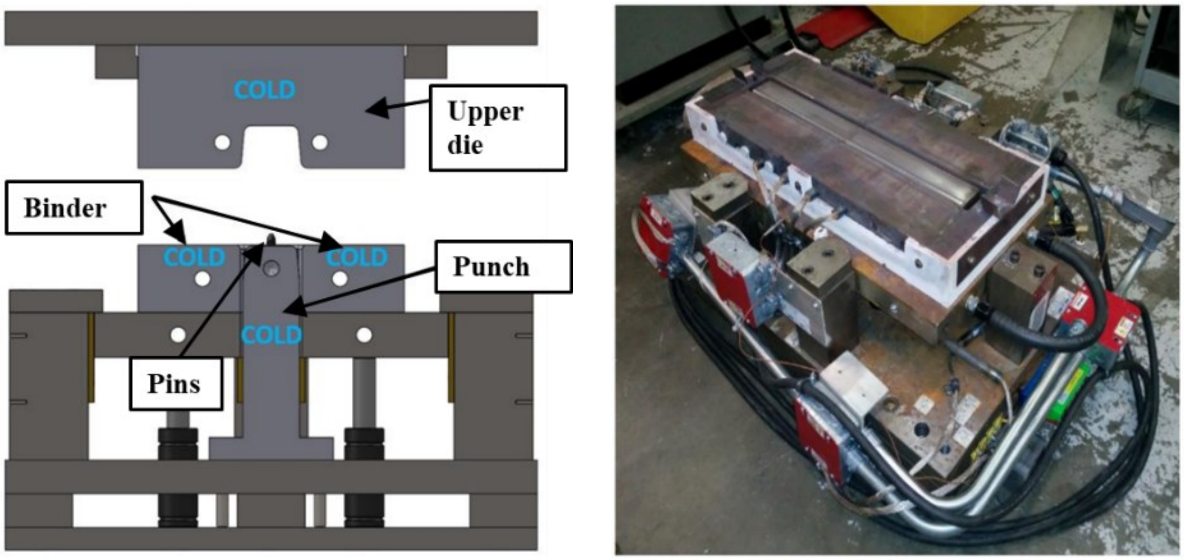

(a) CAD geometry of the die set (b) actual image of the die set

Figure 48: Illustration of a die set: (a) CAD and (b) actual image, adapted from Peister (2019)

During the forming stroke, the punch remains stationary and the upper die descends with the press. Four nitrogen-filled springs below the binder provide a total resistive force of 23.5 kN upon contact with the upper die.

The furnace is manufactured by Deltech Inc. and installed directly adjacent to the press. There are six electric elements inside the furnace with a total heating capacity of 18kW. The elements are spread over three control compartments—front, middle, and rear—which allow uniform heat distribution. The furnace door opens and closes by a foot pedal or automatically through a programming sequence.

The pneumatic transfer system was designed by ACRP Ltd. and is shown in Figure 49. Two guide rails are installed on the parallel sides of the press. A transfer cart features linear bearings which slide along the rails. The ceramic gripper is placed at the end of the cart to grip and hold onto a blank during the transfer stage.

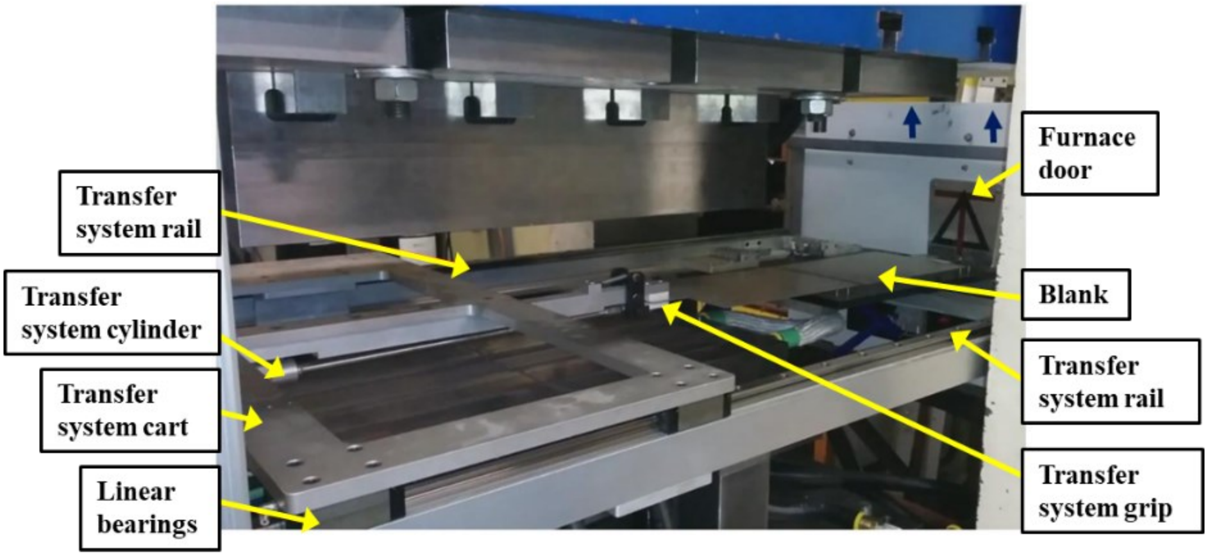

Figure 49: Overview of a transfer system, adapted from Peister (2019)

2.2.1.2. Process

By utilizing the above forming tools, the hot stamping process occurs over four main stages, shown in Figure 50:

1. The blank is austenitized in the oven at 930°C for 7 minutes.
2. The transfer system pulls the blank out of the oven and drops it on the lower binder. The locating pins on the binder align the heated blank in the correct position.
3. The upper die descends and forms the rail.
4. Once the die reaches its maximum displacement, the press is held for additional 10 seconds to quench the blank. Then, the tool opens.

Afterwards, the operator manually retrieves the hot-stamped rail with two long needle nose pliers.

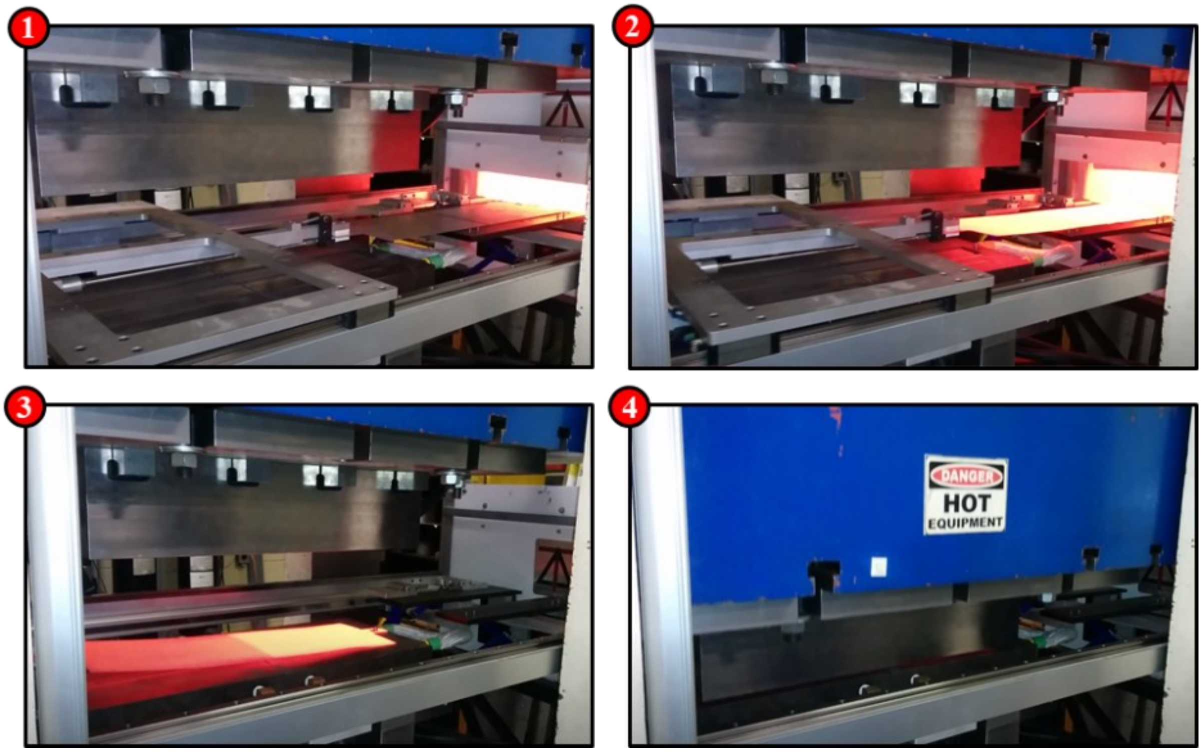

Figure 50. Forming process flow of a hat channel rail, adapted from University of Waterloo Forming and Crash Lab (2018).

2.2.2. Indenting

New indenter fixtures were designed to account for the large number of fold initiators to be formed and improve repeatability of the fold initiator locations. Figure 51a shows the fixture for top-face indentation, consisting of an aluminum base, a top boss and heat-treated H13 indenter punch and indenter inserts. The indenter punch measures 25 mm x 10 mm with a 5 mm spherical tip (see Figure 51g). The insert keeps the specimen profile from collapsing under the indenter load. Additionally, a 7 mm gauge block was placed between the inserts to control the depth of all fold initiators. Two toggle clamps were mounted on the base to secure the specimens. Figure 51c shows the fixture for flange face indentation in which the two side bosses are used, without the toggle clamps. The side bosses are designed to keep the rails from rotating about their axis across the length.

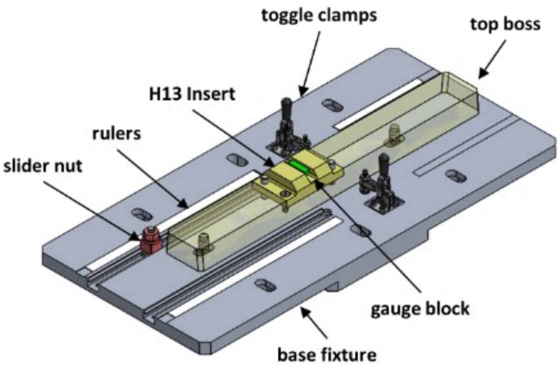

(a) pre-weld indentation fixture

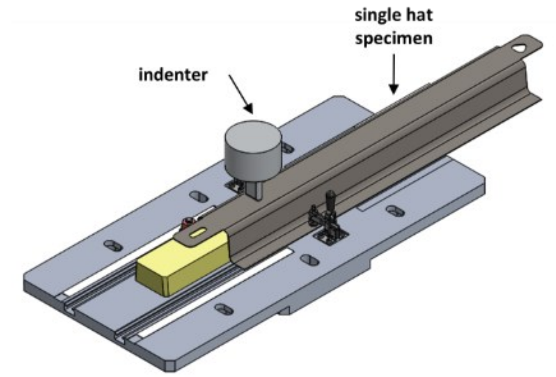

(b) pre-weld indentation setup

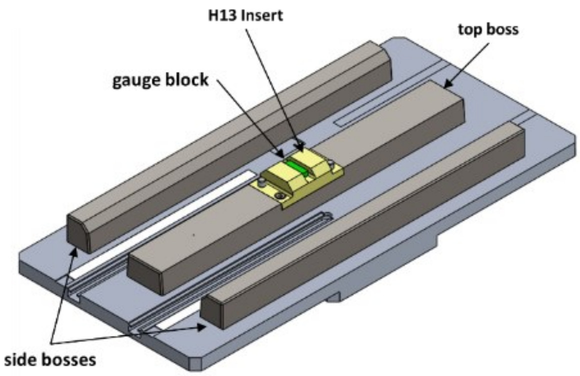

(c) post-weld indentation fixture

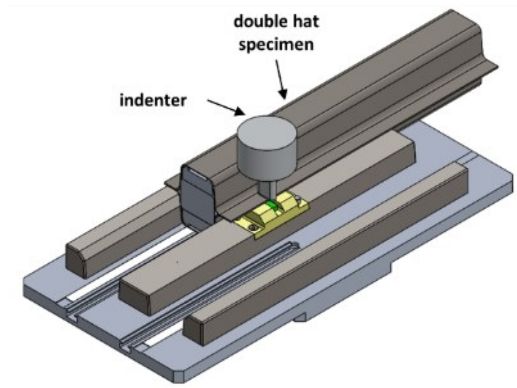

(d) post-weld indentation setup

(e) pre-weld fixture (as-fabricated)

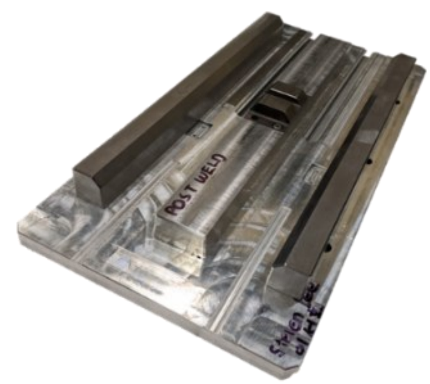

(f) post-weld fixture (as-fabricated)

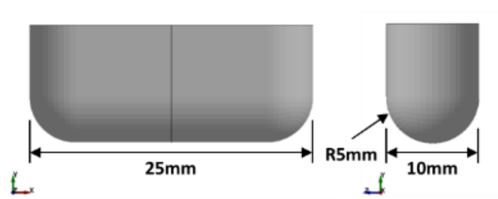

(g) geometry of indenter punch

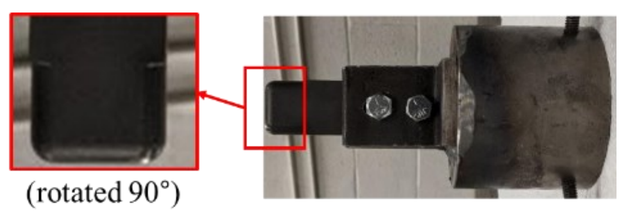

(h) indenter punch (as-fabricated)

Figure 51. Illustrations of pre-weld indentation (a) fixture (b) setup, and post-weld indentation (c) fixture and (d) setup. As-fabricated indentation fixtures are shown in (e) for pre-weld and (f) for post-weld. The (g) indenter punch geometry (h) and its as-fabricated condition is shown as well.

Other parts used for indentation were inner bosses, as shown in Figure 52. These inner bosses were fit inside the rails in attempt to minimize the distortion of the rails during the indenting process.

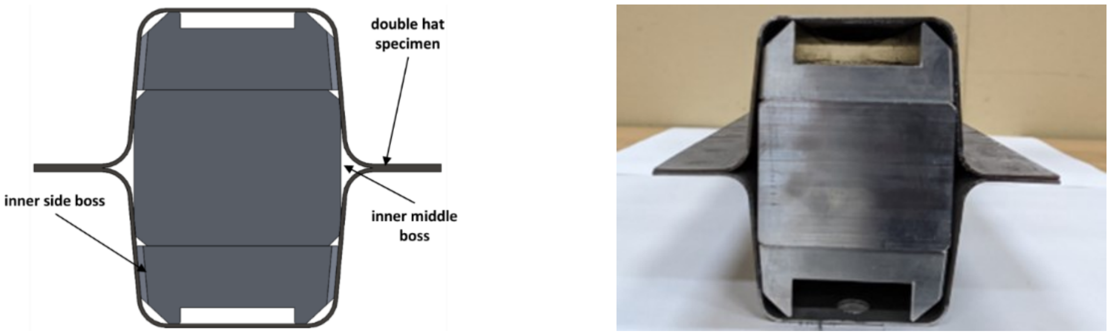

(a) CAD geometry of inner bosses (b) Fabricated inner bosses

Figure 52: Illustration of inner bosses: (a) CAD and (b) as-fabricated

The indenting operation utilizes a manual hand press at the University of Waterloo Engineering Machine Shop, as shown in Figure 53. The fixture is installed on the press base and secured by two C-clamps at the front and the back. The pump handle allows the descent of the indenter. Once the indenter is in contact with the rail, the increase in pressure is read from the pressure gauge. The pressures at the desired depth (3 mm) of fold initiators were recorded and consistently used for all indenting operations.

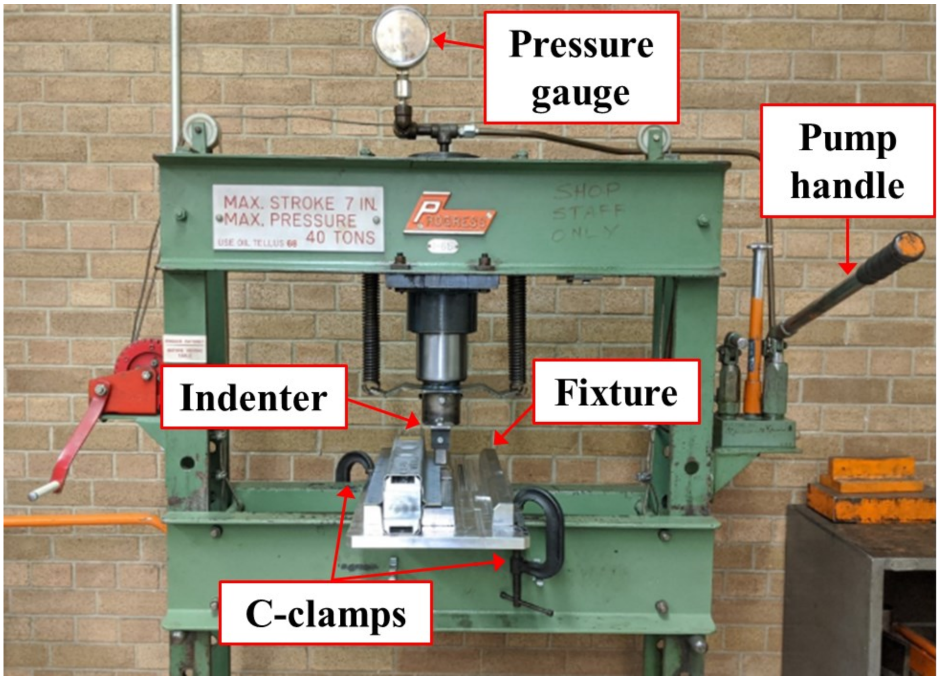

Figure 53: Indentation setup, utilizing manual hydraulic press at the University of Waterloo Engineering Machine Shop

One significant challenge that arose from the indenting process was distortion of rail cross-sections, which became more severe in thinner rails with multiple fold initiators. Figure 54 shows the baseline and TF pattern specimens (each using 1.2 mm thick sheets) after the indenting process and their imprints at the impact-end to demonstrate this phenomenon. While indenting the top face caused a minor geometric change, indenting the flange face caused a severe in-plane deformation that resulted in a “concave” shape. As such, the draft angle of the rail cross-section was affected, as shown in the imprints.

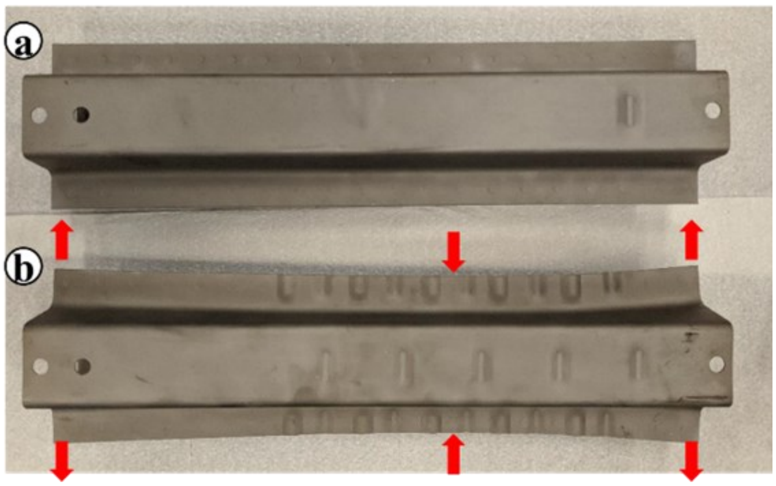

(a) baseline pattern (b) TF pattern

(c) baseline imprint (d) TF pattern imprint

Figure 54: Illustration of in-plane distortion in baseline and TF specimens after indentation; and, sectional imprints at the impact-end for (c) baseline specimen and (d) TF specimen

To measure the distortion severity, (i) the width spanning from one flange to the other and (ii) the draft angle were measured along the length using a Vernier caliper and a protractor, as shown in Figure 55a and Figure 55c. The two measurement results from 1.2mm thickness specimens in Figure 55b and Figure 55d show their variation up to 12% and 13%, respectively, from the nominal values. Although the distortion effect was still present for rails with 1.6 mm thickness, it was less severe than for the 1.2 mm rails.

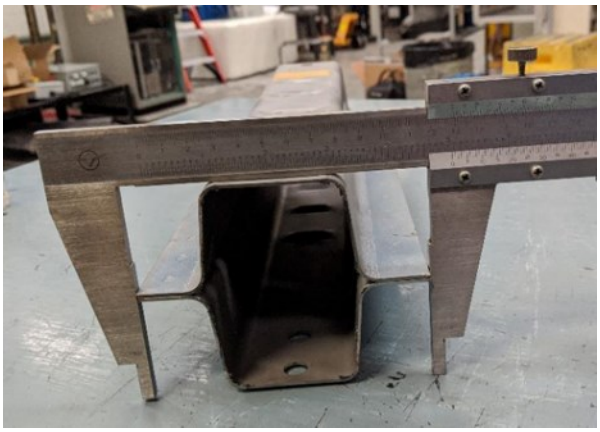

(a) flange to flange width of a rail

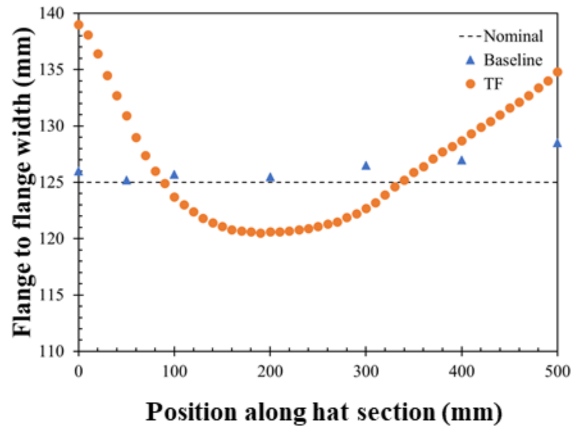

(b) flange to flange width measurement results

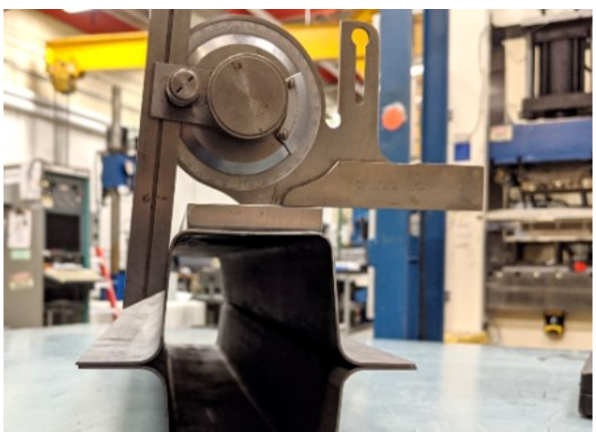

(c) draft angle of a rail

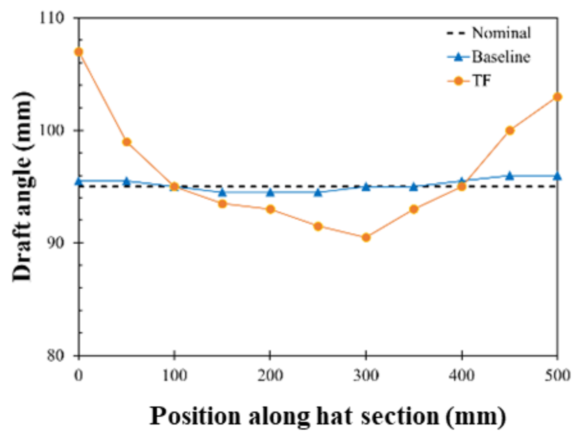

(d) draft angle measurement results

Figure 55: Illustration of (a) the flange to flange width (b) its measurement results and (c) the draft angle and (d) its results for 1.2mm Baseline and TF specimens. Along the x-axis, the 0 mm position refers to the impact-end of the specimens.

2.2.3. Spot Welding

The spot welding process was performed at the Promatek Research Centre, one of the research project sponsors. To establish the proper location of spot welds, a spacer was fabricated from Mica insulation material, as shown in Figure 56a. The spacer features linearly arrayed holes and sits on the specimen flange with the spring clamps. Because the spot weld spacing also varies according to the fold initiator spacing, multiple spacers with the appropriate spacings were fabricated. The aluminum-silicon (Al-Si) coating remained intact on the flanges prior to welding, meaning the flanges were left in the as-hot-stamped condition and not sandblasted up to this stage of specimen fabrication.

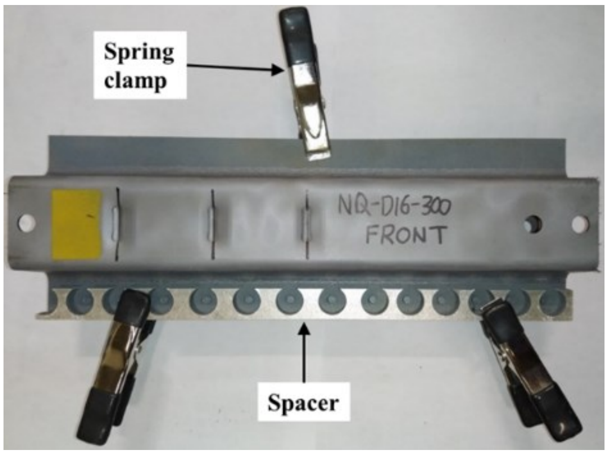

(a) Spacer

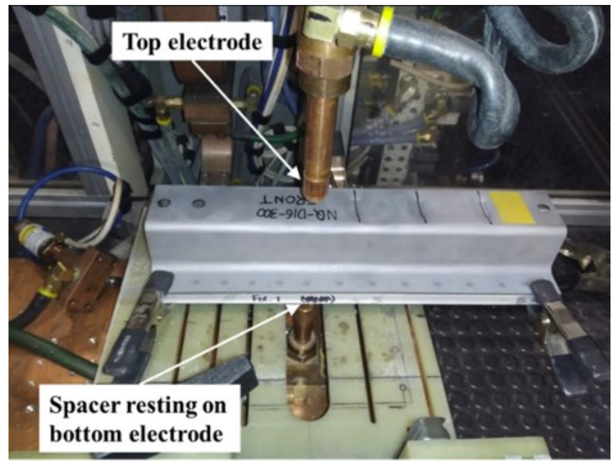

(b) Spot-weld setup

Figure 56: Images of spot weld (a) spacer (b) setup at the Promatek Research Centre

The spot weld schedule for the hot-stamped Ductibor® 1000-AS specimens was provided by Mohamadizadeh (2018), and is shown in Table 4. The electrode tip diameter used in the process is 6 mm.

Table 4: Spot weld schedule used for the hot-stamped Ductibor® 1000-AS rail specimens

Thickness (mm)	Pre-pulse		Weld		Force (kN)
	Time (ms)	Curent (kA)	Time (ms)	Curent (kA)	
1.2	33	8	400	7	3.5
1.6	33	10	400	7	4

Two key parameters are the spot weld-pitch and location relative to the fold initiators. Figure 57 and Figure 58 show the spot weld drawings for the baseline and TF pattern specimens, respectively. The spot weld pitch for the baseline rail configuration specimen was selected as 25 mm, which was consistent with the studies by Omer (2017b) and Peister (2019), as illustrated in Figure 57. *For all other patterns* (*e.g.* TF), the spot weld pitch was set equal to the fold initiator spacing ($2H$), which varies between 20 mm to 35 mm in Part 3. Moreover, the spot welds in the indented region were placed halfway between adjacent pairs of flange fold initiators (see Figure 58). This approach was adopted because it provided the largest flat region for spot welding. In addition, the resulting spot weld was located away from the tight fold region, thereby reducing bending strains experienced by the spot weld, at least for configurations that exhibited stable folding. Further optimization of the spot weld spacing and location was judged outside of the thesis scope.

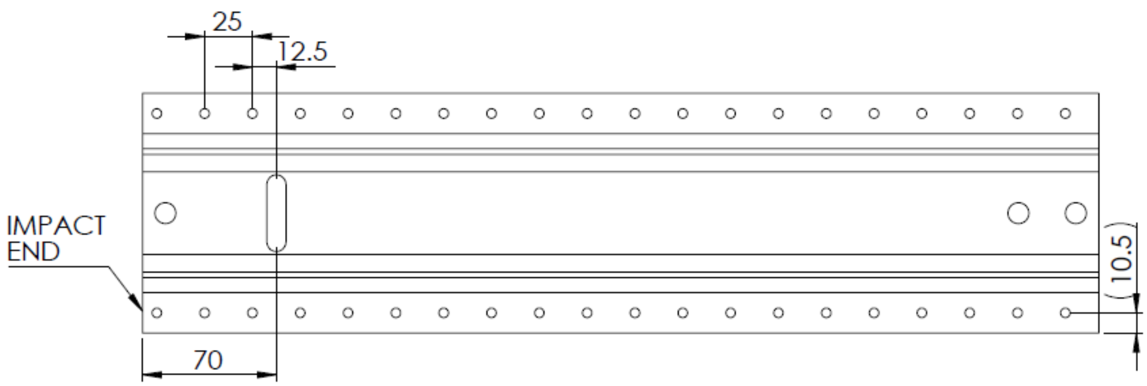

Figure 57: Spot weld drawing for the baseline pattern.

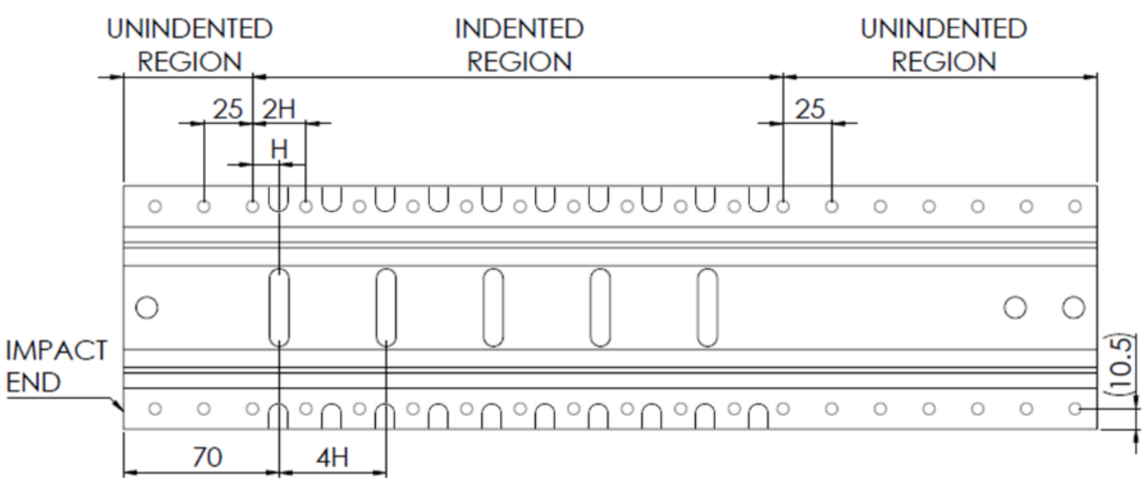

Figure 58: Spot weld drawing for the fold initiator pattern TF. *For all patterns*, the spot weld pitch for un-indented regions remained 25 mm while that of indented region was set equal to the fold initiator spacing, 2H.

2.2.4. Sandblasting

Specimens were also sandblasted twice to remove the aluminum-silicon (Al-Si) coating, as shown in Figure 59. Removal of the coating reduces the formation of dust clouds due to loss of the coating during impact which would otherwise obscure video recordings during testing. The inner surface of the top hats was first sandblasted prior to spot welding, while the outer surfaces of the welded rails were sandblasted after welding. When sandblasting the inner surface of the top hats, the flange regions were covered with masking tape to protect the coating. This approach is consistent with hot-stamping industrial practice in which the Al-Si coating is left on hot stamped sheets prior to spot welding.

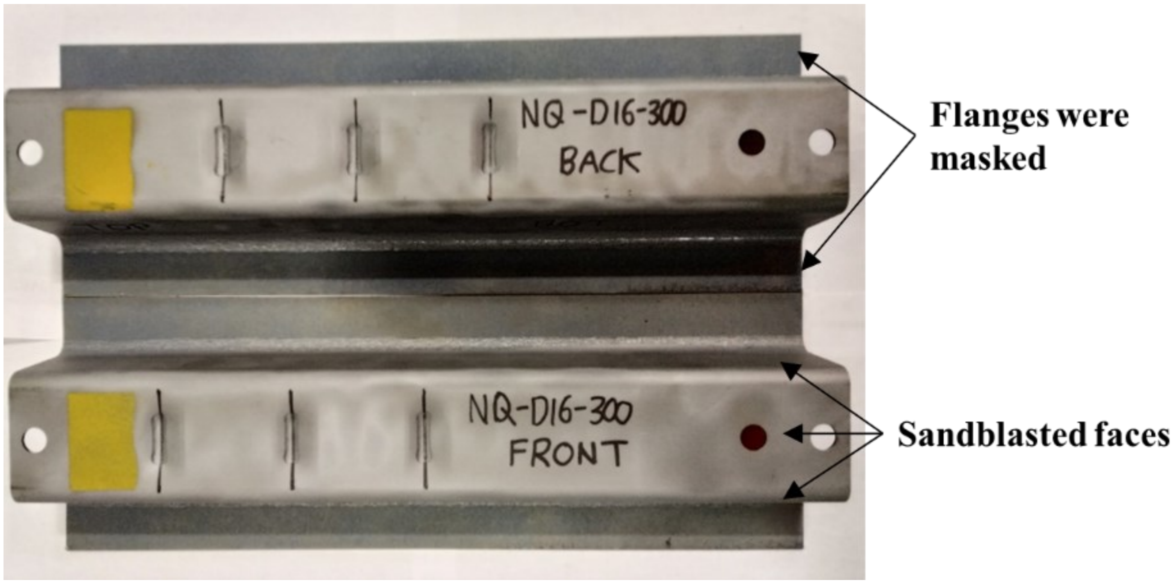

Figure 59: Sandblasted top hat channels before spot welding. Flanges were protected with masking tape to retain the aluminum silicon coating for the subsequent spot weld operation.

2.3. Dynamic Axial Crush Setup

The dynamic axial crush tests were conducted using a Seattle Safety D780-3.7 crash sled at the University of Waterloo Structural Crashworthiness Sled Facility (Figure 60). The crash sled features two onboard accelerometers, and is propelled by a pneumatic system in which a rope attached to the sled is pulled by a piston. The movement of the piston relies on the compressed air release from a reservoir, which allows a maximum initial velocity of 91 km/hr. For all dynamic tests considered in the thesis, an impact velocity of 10.6 m/s and a sled mass of 855 kg were used.

Figure 60: Crash sled at the University of Waterloo for dynamic axial crash tests, adapted from Peister (2019)

To mount the specimens to the barrier wall, custom fixtures, designed by Omer *et al.* (2017b), were used, as shown in Figure 61. The mounting fixtures consist of two inner bosses and two outer clamps that feature holes or slots to mount the rail specimen in a consistent position with regard to the sled. The bosses and clamps at the wall are 50 mm in length (L), while those at the impact-end are 25 mm.

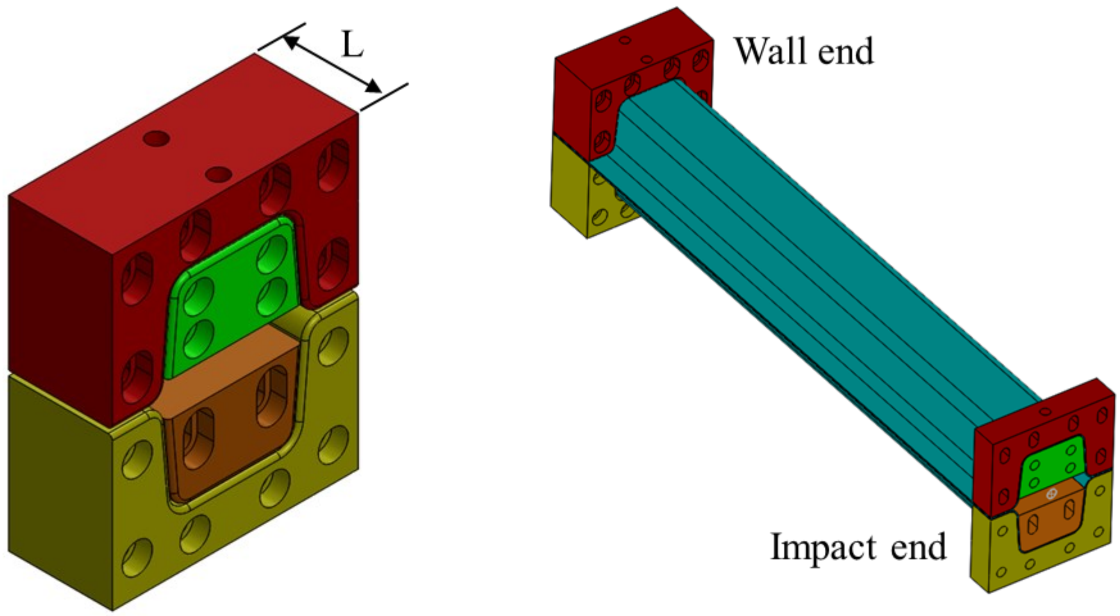

(a) clamp set (b) clamp sets

Figure 61: CAD geometry of a (a) clamp set designed by Omer *et al.* (2017b) and (b) clamp sets with rail, forming a "rail assembly"

The bosses and clamps are mounted to a steel plate using M8 bolts, as shown in Figure 62. To avoid metal-to-metal contact with the sled and dampen the vibration upon the impact, the impact plate is faced with a 19 mm (¾ inch) thick sheet of plywood. Once the rail is clamped to the impact plate, the rail assembly was mounted to a supporting plate.

On the fixed barrier wall, three 120kN Kistler 9731B piezoelectric load cells are attached in a triangular pattern to measure the crush force, (see Figure 62c). Additionally, two stacks of honeycomb arrestors were mounted on each side of the rail to stop a crash sled. The honeycomb arrestors are made of Plascore 5056 aluminum cells with a crush strength of 3.7 MPa (535 psi). The dimensions of the first and second stacks were 140 mm x 140 mm x 170 mm and 160 mm x 160 mm x 195 mm, respectively. The stacked honeycomb arrestors were mounted on the wall such that there is "free crush distance" of 165 mm, which corresponds to the distance traveled by the sled from the moment of its impact with the crush specimen up to the engagement of the honeycomb arrestors.

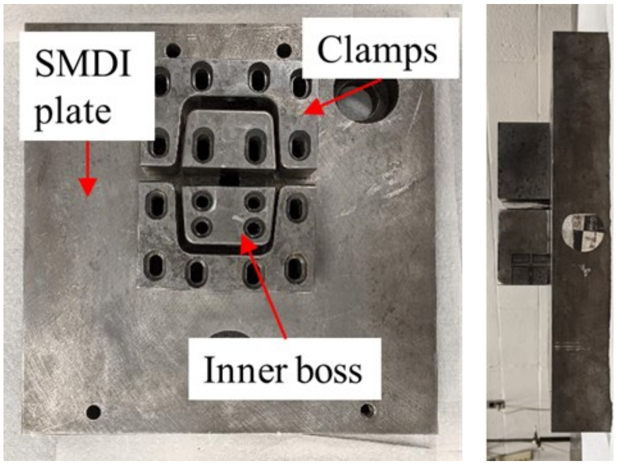

(a) Clamp and bosses at wall-end

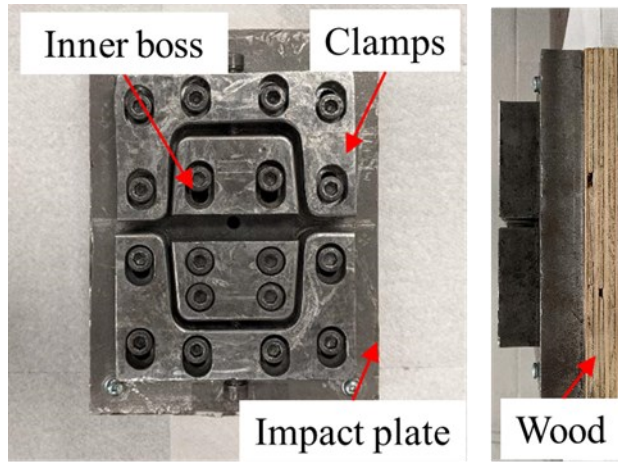

(b) Clamp and bosses at impact-end

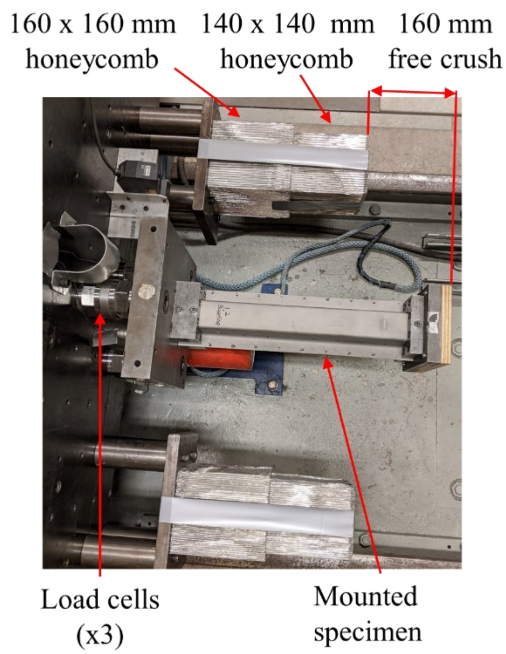

(c) rail assembly mounted to a barrier wall

Figure 62: Mounting plate with clamps at the (a) wall-end, (b) impact-end, and (c) entire rail assembly mounted to the fixed barrier wall. Three piezoelectric load cells measure the crush force. Honeycomb arrestors provide 165 mm free crush distance.

Figure 63 illustrates the lighting and camera setup for dynamic crush tests. One Photron SA-4 high-speed camera and two Photron AX-100 high-speed cameras were mounted directly above and next to the rail assembly to capture images at 5000 frames per second. To illuminate the rail assembly, two large lighting sources were placed at a far distance, in addition to a small lighting source placed directly below the specimen. Still images obtained from each camera during setup are shown in Figure 64.

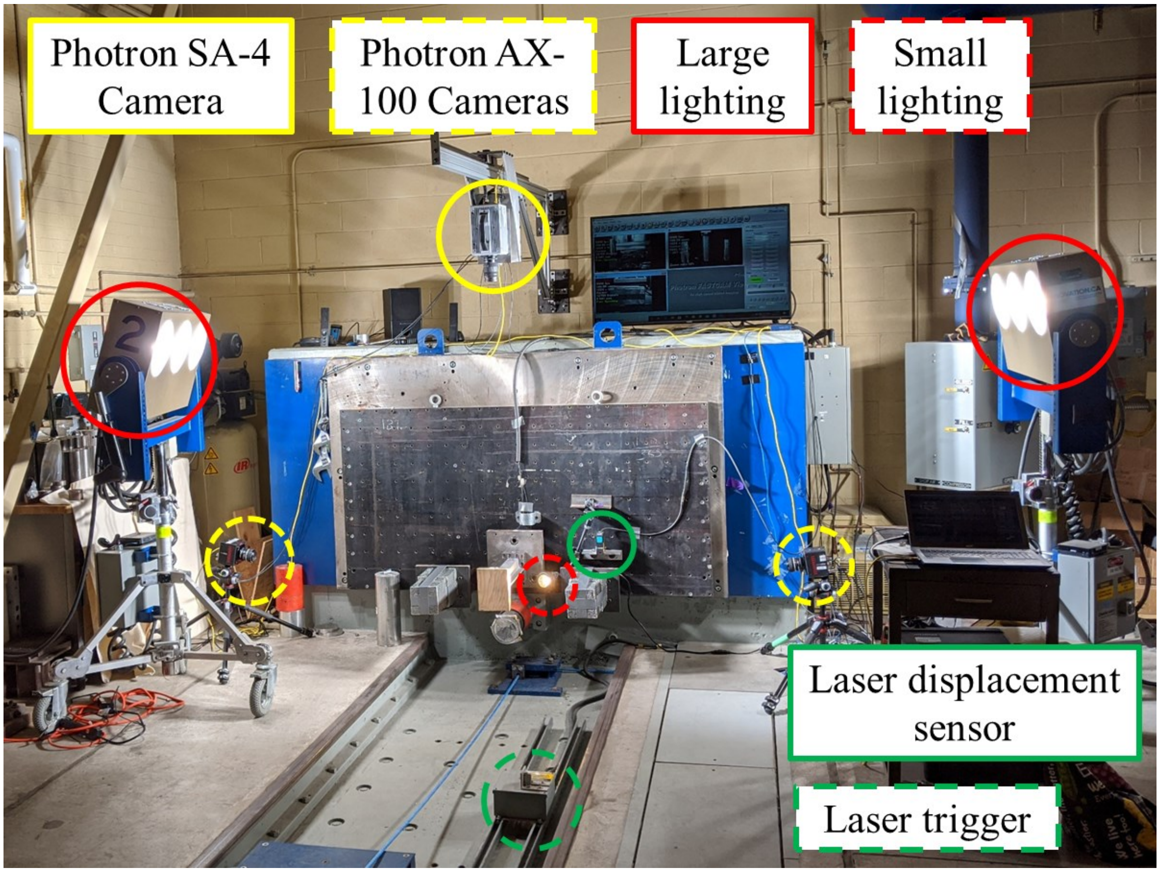

Figure 63: Dynamic axial crush test setup, highlighting various test equipment: (i) one Photron SA-4 high speed camera, (ii) two Photron AX-100 high speed cameras, (iii) various lighting sources, (iv) a laser trigger system, and (v) a laser displacement sensor.

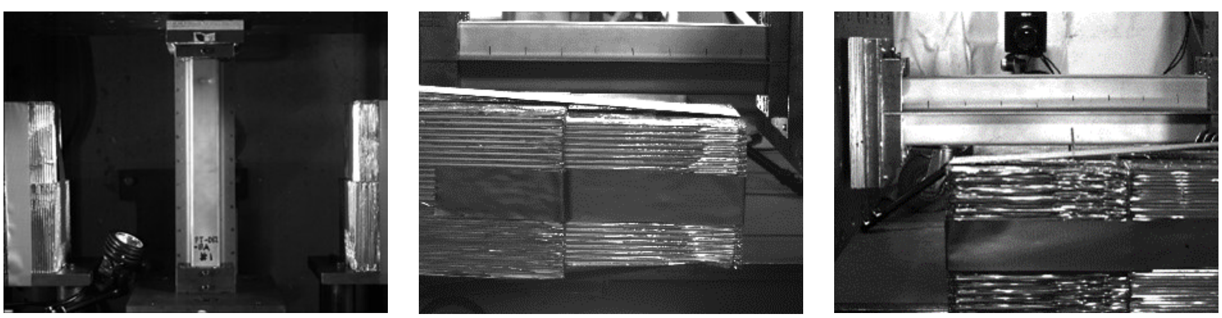

(a) top view (b) left view (c) right view

Figure 64: Still initial images of the dynamic axial crush test specimen from (a) top view (b) left view, and (c) right view

The data acquired during dynamic crush tests includes crush load, sled displacement, and sled deceleration. The crush load is measured by the three piezoelectric load cells sampled at 10,000 Hz (data points per second), while the sled deceleration is measured by the two onboard accelerometers at the same frequency. The load data from each cell is summed to calculate a total resultant load, while the sled displacement is calculated using the initial velocity and double integrating the measured deceleration. A Keyence LK 507 laser displacement sensor is placed on the barrier wall as a redundant measurement of sled displacement. Initiation of the data logging and camera image acquisition is accomplished by a laser trigger system, activated by the sled, which sends a signal to the data acquisition unit (DAC) and camera controller PC. The data logging duration was set for a 1-second interval, to begin 0.5 seconds before the sensor detects the sled.

The measured crush force (F) and crush displacement (d) were plotted against each other to develop the crush force *vs.* crush displacement plot (**F-D**), and the absorbed energy (E) was calculated using the relation

$$E = \int F \mathrm{d}d \tag{38}$$

which was numerically integrated using the trapezoidal rule.

2.4. Quasi-Static Axial Crush Setup

Figure 65 illustrates the quasi-static axial crush test setup, utilizing a hydraulic test frame with a load capacity and a displacement span of 496 kN and 250 mm, respectively. An MTS Flex Test SE controller controls the actuator displacement. Crush force and displacement data are obtained by a data acquisition board, which interfaces with the LabVIEW program on a PC.

A rail assembly was fixed on the frame bed by two forged steel step clamps encircled in Figure 65. Two video cameras were used to capture the front and the side view of a specimen. To illuminate the specimen, four small lighting sources were carefully placed nearby.

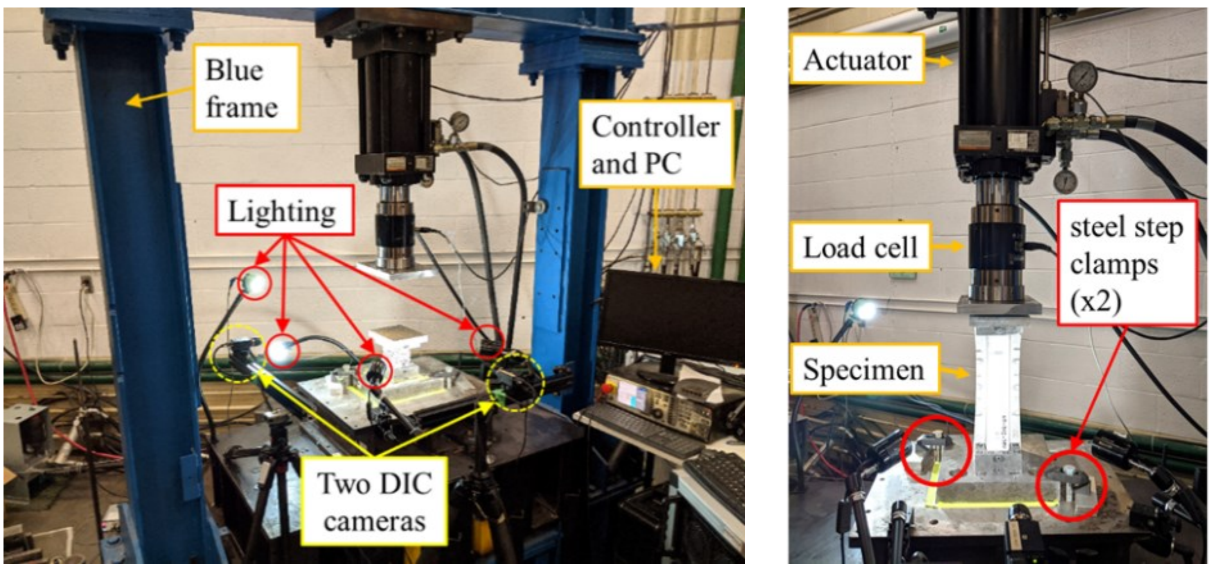

(a) Overview (b) Mounted specimen

Figure 65: Quasi-static axial crush test setup: (a) overview and (b) mounted specimen.

By utilizing this test setup, quasi-static axial crush tests were conducted in three steps: (i) the press cylinder was brought down close to the specimen, leaving a few millimeter gap; (ii) a customized LabVIEW program was executed to move the press down for 230 mm at a constant velocity of 0.3 mm/s; and lastly, (iii) the Vic-Snap program was executed to record data and videos at 1 Hz.

3.0 Numerical Models

A key aspect of the research work was the development of numerical models to simulate the quasi-static and dynamic axial crush experiments. The chapter is organized into three sections that present three primary aspects of the modeling scope: (i) development of a material model capturing the constitutive behaviour of Ductibor® 1000-AS sheet in the hot-stamped condition; (ii) development of finite element (FE) models that simulate the indentation process used to form the fold initiators; and lastly, (iii) FE models of the axial crush tests.

The flow chart in Figure 66 illustrates the overall scope of numerical models developed as part of the thesis activity. The material model aims to describe two main mechanical responses, which are the constitutive (stress-strain) and fracture limit response. To this end, numerous researchers contributed to the characterization of these properties, as detailed in Section 3.1. Modelling of the fold initiator patterns is described in Section 3.2. Two different modeling approaches are considered to reproduce the indented geometry in the specimens by either displacing the nodes at the desired locations of hat channel mesh or numerically simulating the indentation processes. The actual axial crush models are described in Sections 3.3. Here, the various axial crush rails (detailed in the previous chapter) are subjected to either a dynamic or quasi-static loading condition at 10.6 m/s or 0.00035 m/s initial impact velocity or constant velocity, respectively.

Note that all the finite element models presented in this thesis were developed using the commercial FE code LS-Dyna version 9.2 (Livermore Software Technology Corporation, 2016).

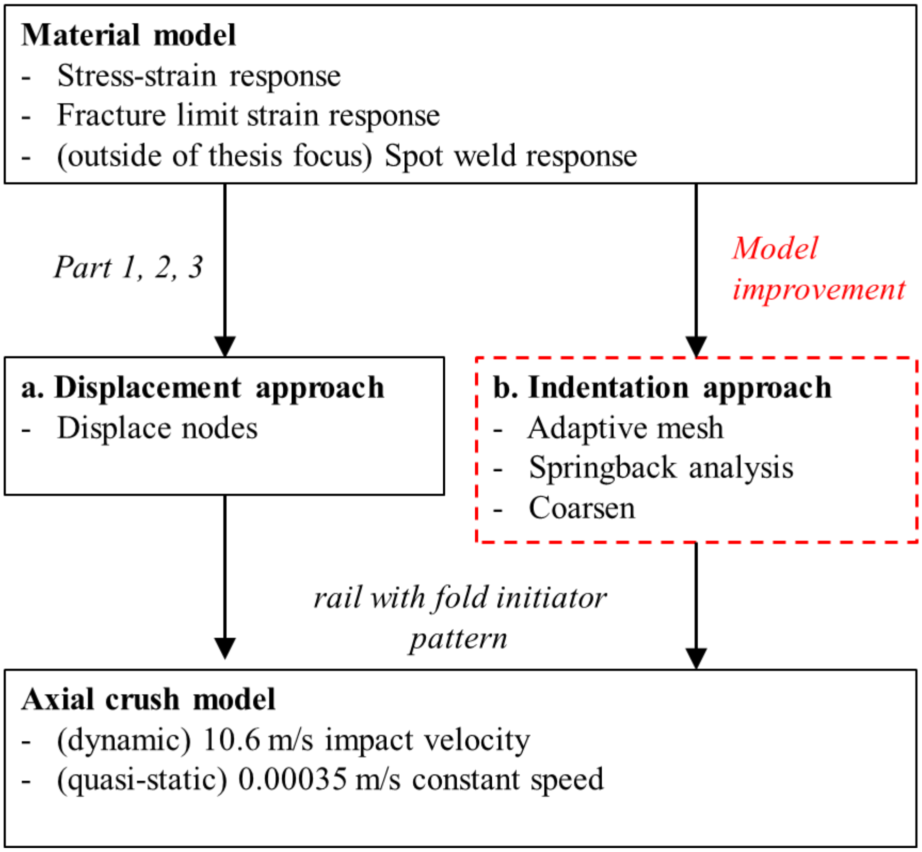

Figure 66: Flowchart illustrating the overall scope of the numerical models presented in this thesis. Two different approaches were considered to create the fold initiator patterns in the FE simulations.

3.1. Material Model for Hot Stamped Ductibor® 1000-AS

The material model used for the Ductibor® 1000-AS sheet in the hot stamped condition was developed as part of a larger collaborative research project at the University of Waterloo that was sponsored by Honda R&D Americas, Promatek Research Centre, and ArcelorMittal. The data presented in the balance of this section, comprising measured constitutive (stress-strain) response, rate sensitivity and fracture limit strains, stems from a number of as yet unpublished research studies undertaken within the project team, as documented in the following.

To provide readers an overview of the project scope from a material characterization perspective and to properly cite the source of the data, Table 5 and Table 6 list the various characterization tasks and the corresponding investigator(s). The tasks highlighted in red represent those undertaken in part by the author of this thesis, which consisted of (i) fitting the experimental stress-strain curve into a hardening model and (ii) conducting finite element mesh regularization of the fracture locus.

Table 5: List of tasks and the corresponding researchers responsible for constitutive characterization of die-quenched Ductibor® 1000-AS. The highlighted tasks (in red) represent contributions of the author of this thesis.

Task	Apparatus	Author
1. Quasi-static Constitutive Characterization Tests & Modeling		
Quasi-static tensile test Quasi-static shear test	MTS Criterion Model 45 Tensile Frame	Abedini (2018)
High strain extrapolation	-	
Hardening model fitting	-	Abedini and Lee (2019)
2. Strain Rate Sensitive Constitutive Characterization Tests & Modeling		
High strain rate tensile test (1, 10, 100s^{-1})	Hydraulic Intermediate Strain Rate Apparatus	Zhumagulov and Imbert (2018)
Hopkinson bar test (1000s^{-1})	Tensile Split Hopkinson Bar Apparatus	
Strain rate sensitive hardening model fitting	-	Abedini and Lee (2019)

Table 6: List of tasks and the corresponding researchers responsible for fracture *locus* calibration of Ductibor® 1000-AS. The highlighted tasks represent contributions of the author of this thesis.

Task	Apparatus	Author
1. Fracture Characterization Tests		
Mini shear test	Hydraulic Instron Model 1331 Tensile Apparatus	Abedini (2018)
Hole expansion test	MTS Formability Press	Samadian (2018)
V-bend test	Inverted VDA238-100 Bend Test Apparatus	Cheong (2019)
50 mm Nakazima dome test	MTS Formability Press	Samadian (2018)
5 mm Equi-biaxial dome test	MTS Formability Press	Cheong (2019)
2. Fracture *Locus* Calibration & Mesh Regularisation		
Fracture locus calibration	-	Abedini and Butcher (2020)
Modeling 50mm Nakazima dome test	-	Lee (2020)
Finite element mesh regularization	-	Lee (2020)

3.1.1. Constitutive Behaviour

For the purposes of the current work, the hot-stamped Ductibor® 1000-AS was assumed to obey the von Mises (1913) yield criterion with isotropic hardening response.

The Al-Si coating thickness on each face of the sheet was taken as 0.025 mm, as reported by Samadian *et al.* (2020). Because the Al-Si coating is brittle and has significantly less load-carrying capacity than the parent metal, the total coating thickness of 0.05 mm was subtracted from the nominal sheet thickness, such that a net thickness of 1.15 mm and 1.55 mm was considered in the models for the 1.2 and 1.6 mm sheet, respectively.

3.1.2. Quasi-Static Hardening Response

The constitutive model for as-hot stamped Ductibor® 1000-AS was developed using uniaxial and shear stress-strain data acquired by Abedini (2018). Figure 67 shows the stress-strain curves obtained from tensile and mini shear tests, using testing methodologies similar to that reported by Abedini *et al.* (2018). These quasi-static tests were conducted at an equivalent strain rate of 0.01 s^{-1}.

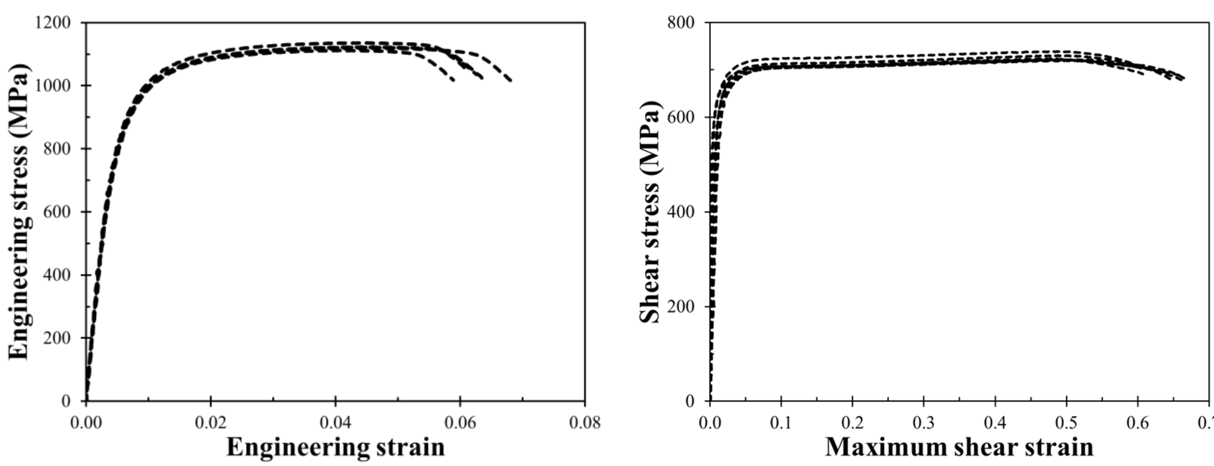

(a) Tensile test (b) Shear test

Figure 67: Stress *vs.* strain responses of die-quenched Ductibor® 1000-AS from (a) uniaxial tensile test (with five repeats) and (b) shear test (with six repeats) performed by Abedini (2018)

The uniaxial tensile uniform elongation (UE) of this material is quite low, only 0.04, as seen in Figure 67a. As a result, the measured shear stress-strain data was used by Abedini (2018) to extend the effective stress-strain response to larger strain levels (Figure 67b) using the work-equivalence method developed by Rahmaan *et al.* (2017). The resulting effective stress *versus* effective plastic strain response is shown in Figure 68.

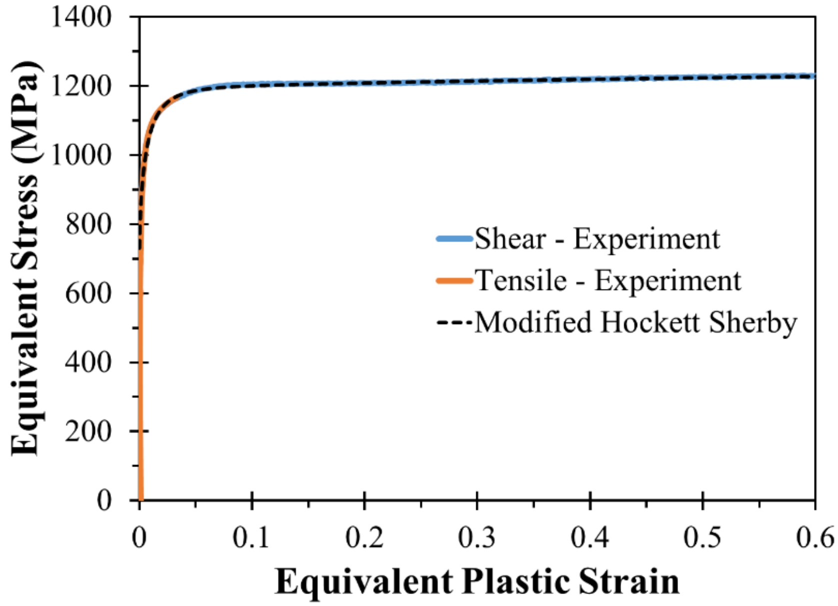

Figure 68: Equivalent stress *vs.* equivalent plastic strain curve for Ductibor® 1000-AS, extended to larger strain levels by Abedini (2018) based on tensile and shear data.

The measured quasi-static hardening response in Figure 68 was fit to a modified form of Hockett-Sherby (1975) equation due to Noder and Butcher (2019):

$$\bar{\sigma} = C_1 - (C_1 - C_2)\exp\left(-C_3\left(\bar{\varepsilon}_p\right)^{C_4}\right) + C_5\sqrt{\bar{\varepsilon}_p} \tag{39}$$

in which C_1 to C_5 are calibration parameters, $\bar{\varepsilon}_p$ is the equivalent strain and $\bar{\sigma}$ is the flow stress. The fitting was performed as part of the current work using a custom MATLAB script provided by Butcher (2019). The calibrated constants and the mean square error (R-sq) are listed in Table 7.

Table 7: Calibrated constants for die-quenched Ductibor® 1000-AS using modified Hockett-Sherby equation (see Equation (39))

C_1	C_2	C_3	C_4	C_5	R-sq
1183.57	731.55	29.37	0.67	57.84	0.992

3.1.2.1. Strain Rate Effects

Elevated strain rate tensile testing was performed on this alloy by Imbert and Zhumagulov (2018) to account for the effect of strain rate on flow stress. This data was acquired using the tensile Split-Hopkinson bar apparatus (1000 s^{-1}) and hydraulic intermediate strain rate apparatus (1-100 s^{-1}) at the University of Waterloo, using the methodologies documented by Rahmaan (2015). The measured data is shown in Figure 69 as solid lines with the quasi-static curve at 0.01 s^{-1}, shown in Figure 68 using the shear extrapolation technique. Overall, a moderate strain rate sensitivity is exhibited by the die-quenched Ductibor® 1000-AS sheet steel.

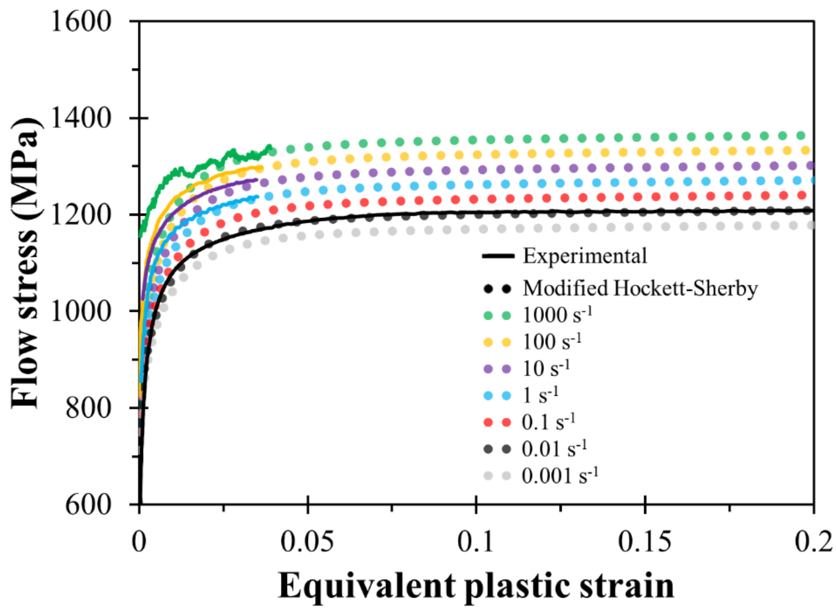

Figure 69: Measured and predicted flow stress *vs.* equivalent plastic strain for a range of strain rates (0.01 s^{-1}, 1 s^{-1}, 10 s^{-1}, 100 s^{-1} and 1000 s^{-1}) for die-quenched Ductibor® 1000-AS (solid curves). The symbols are from the fit using Equation (40).

In order to account for this material rate effect, a logarithmic strain rate sensitivity term, first proposed by Johnson and Cook (1983), was introduced to Equation (39), which assumes a multiplicative coupling or scaling of the quasi-static stress-strain response:

$$\bar{\sigma} = \left[C_1 - (C_1 - C_2)\exp\left(-C_3 \left(\bar{\varepsilon}_p \right)^{C_4} \right) + C_5 \sqrt{\bar{\varepsilon}_p} \right] \left[1 + C_6 \ln\left(\frac{\dot{\varepsilon}}{\dot{\varepsilon}_0} \right) \right] \tag{40}$$

Here, $\dot{\varepsilon}_O$ is a reference strain rate (taken as 0.01 s^{-1}), and $\dot{\varepsilon}$ is the actual strain rate. C_6 is a strain-rate calibration constant that was determined using the data shown in Figure 70 in which the flow stress at a strain of 0.04 is plotted as function of strain rate (log-plot). The flow stress at each strain rate is normalized by the flow stress at the reference strain rate of 0.01 s^{-1}. The strain-rate calibration constant (C_6) was determined by a linear line of best fit of the normalized stress *versus* log-strain rate data. The resulting values for all of the material parameters in Equation (40) are listed in Table 8. Figure 69 also shows the predicted stress-strain response using Equation (40) for strain rate in the range 0.001 s^{-1} to 1000 s^{-1}. The predicted curves are shown to agree well with the measured tensile results.

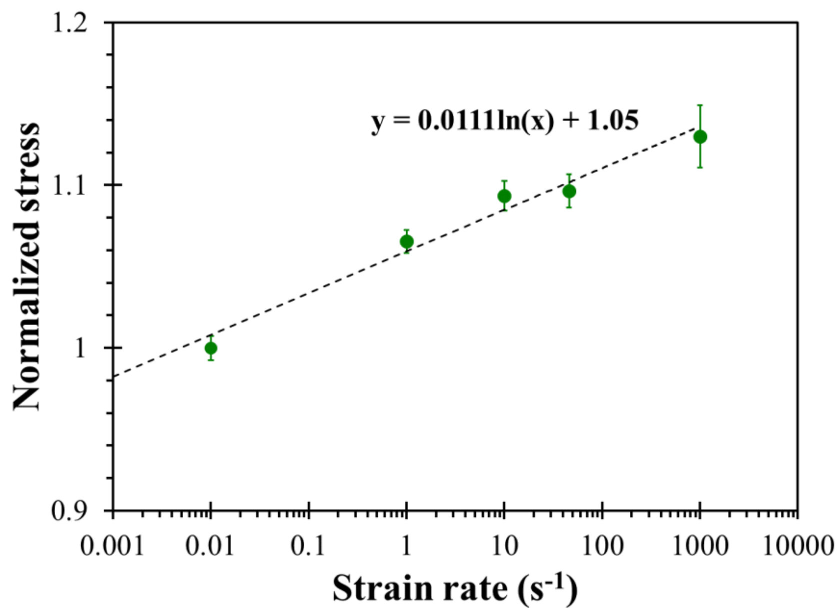

Figure 70: Normalized stresses *vs.* strain rates for various strain rates. The normalization ratio was obtained with respect to the 0.01 s^{-1} UTS. Note that the strain rates deviate to some degree from their nominal values as the test results revealed lower rates than the nominal values (see Appendix E).

Table 8: Calibrated constants for the die-quenched Ductibor® 1000-AS using the strain rate sensitive model given by Equation (40).

C_1 (MPa)	C_2 (MPa)	C_3	C_4	C_5 (MPa)	C_6	$\dot{\varepsilon}_O$ (s^{-1})
1183.57	731.55	29.37	0.67	57.84	0.011	0.01

Lastly, the predicted strain rate sensitive flow stress response in Figure 69 is taken as an input to a pre-existing elasto-plastic material model in LS-Dyna (*MAT_PIECEWISE_LINEAR_PLASTICITY, MAT 24).

3.1.3. Fracture Response

To characterize the fracture response of as-hot stamped Ductibor® 1000-AS, fracture limit strains under different strain paths were obtained by five characterization tests using the specimen geometries shown in Figure 71. These tests consist of the simple shear test, hole expansion test, V-bend test, 50 mm Nakazima dome biaxial tension and 5 mm dome equi-biaxial tension tests. The equivalent fracture limit strain obtained from each test is listed in Table 9 with sources for each result. The testing methodologies used are similar to those reported by Samadian *et al.* (2020).

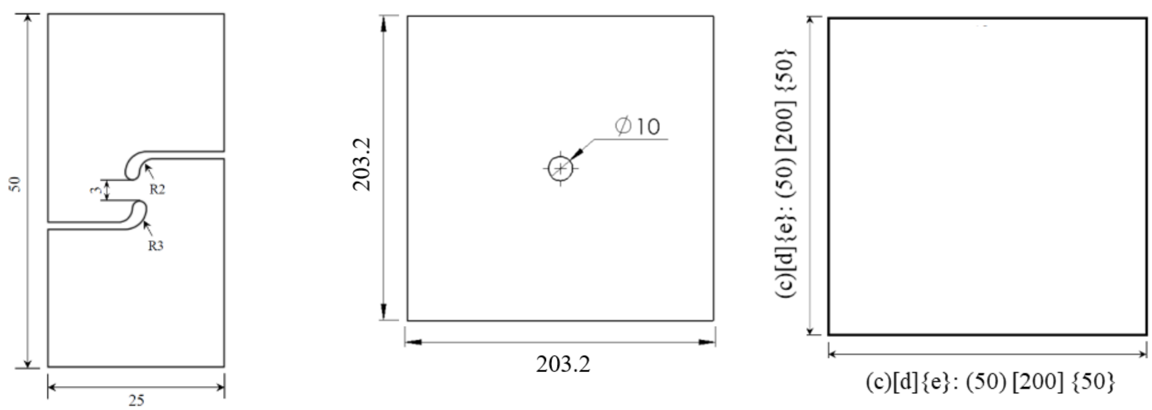

(a) simple shear (Peirs *et al.,* 2012)

(b) hole expansion (ISO, 2017)

(c) V-bend (VDA, 2017)

(d) 50mm dome Nakazima biaxial (Nakazima *et al.,* 1968)

(e) 5mm dome equi-biaxial (Cheong, 2019a)

Figure 71: Specimen geometries used for the fracture limit characterization tests of die-quenched Ductibor® 1000-AS (1.2mm sheet steel)

Table 9: List of idealized stress triaxiality and the measured average fracture strain (equivalent plastic strain) obtained from each fracture characterization test, and (the names of responsible researchers). For 50 mm dome test, stress triaxiality was estimated using Equation (41) to (43). Likewise, the fracture strain of 50 mm dome test was *damage integrated* by Butcher (2020)

Fracture limit characterization test (performed by)		Idealized or [averaged] stress triaxiality, η	Measured or [damage integrated] fracture strain $\bar{\varepsilon}_f$
simple shear	(Abedini, 2018)	0.0000	0.75
hole expansion	(Samadian, 2018)	0.3333	0.79
V-bend	(Cheong, 2019)	0.5774	0.67
50 mm Nakazima dome biaxial tension	(Samadian, 2018)	[0.6580]	0.53 [0.79]
5 mm dome biaxial tension	(Cheong, 2019)	0.6666	1.31

In Table 9, the stress triaxiality for each test is nominal, meaning that the path of continuum traveled in stress triaxiality *vs.* equivalent plastic strain ($\eta\ vs.\ \bar{\varepsilon}_p$) domain is linear (and vertical), except for the 50 mm biaxial Nakazima dome test. The measured 50 mm dome test data rather showed a strong nonlinear stress triaxiality-equivalent plastic strain path. As a result, its stress triaxiality was estimated by the following relations (Jia and Bai, 2016) that are derived with the plane stress and von Mises yield criterion assumptions

$$\eta = \frac{\beta + 1}{3\sqrt{\beta^2 - \beta + 1}} \tag{41}$$

$$\beta = \frac{2\alpha + 1}{2 + \alpha} \tag{42}$$

in which β is a function of α, which is the ratio of major strain increment ($\Delta\varepsilon_1$) and minor strain increment ($\Delta\varepsilon_2$)

$$\alpha = \frac{\Delta\varepsilon_2}{\Delta\varepsilon_1} \tag{43}$$

The fracture limit strain for each test was determined from the measured strain components at the onset of fracture, corresponding to the last image obtained by DIC techniques before visual cracking was observed. Non-linear strain path effects on the fracture *loci* (except for those from the 50 mm Nakazima dome biaxial tension test) were not taken into account in the current work.

The measured (and damage-integrated) fracture limit strains and triaxiality values in Table 9 were used to calibrate the Bai-Wierzbicki (2007) fracture model in Equation (44). The calibration was performed by Abedini and Butcher (2020), who excluded the 5 mm (sharp radius) dome test data, to obtain a fit to the plane-stress fracture *locus* in the following form:

$$\bar{\varepsilon}_f = \left[\frac{1}{2}\left(D_1 e^{-D_2\eta} + D_5 e^{-D_6\eta}\right) - D_3 e^{-D_4\eta}\right]\bar{\theta}^2 + \frac{1}{2}\left(D_1 e^{-D_2\eta} - D_5 e^{-D_6\eta}\right)\bar{\theta} + D_3 e^{-D_4\eta} \tag{44}$$

$$\bar{\theta} = 1 - \frac{6\theta}{\pi} = 1 - \frac{2}{\pi}\arccos\xi \tag{45}$$

where D_1 to D_6 are calibration parameters, η is the stress triaxiality, $\bar{\theta}$ is the normalized Lode angle defined due to Bai and Wierzbicki (2008) which is related to the Lode angle (θ) or the third deviatoric stress invariant (ξ). The resulting values for all of the material parameters in Equation (44) are listed in Table 10.

Table 10: Calibrated constants for the die-quenched Ductibor® 1000-AS using the Bai-Wierzbicki (2008) fracture model given by Equation (44).

D_1	D_2	D_3	D_4	D_5	D_6
0.7051	0.0493	0.7013	-0.3869	0.8300	-0.7276

The calibrated fracture *locus* in terms of von Mises effective fracture strain *versus* stress triaxiality is plotted in Figure 72.

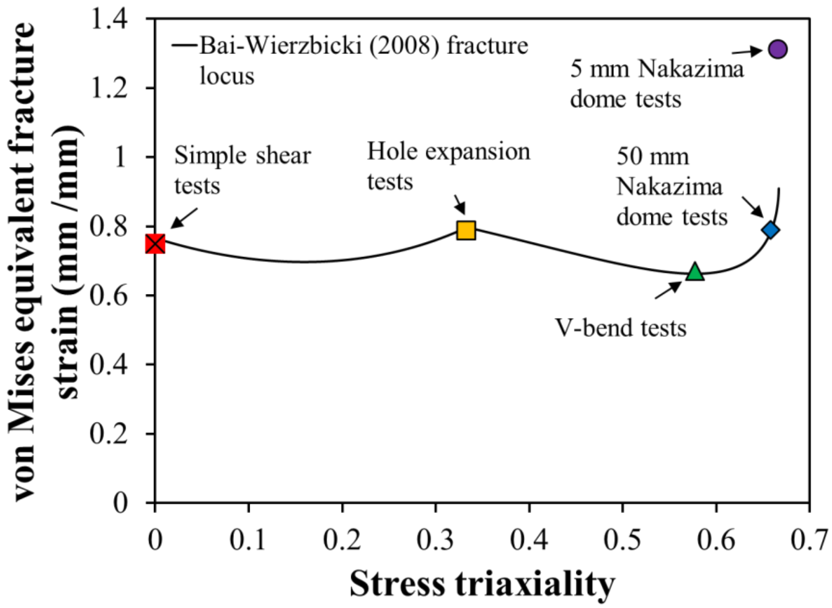

Figure 72: Plane stress fracture *locus* of the die-quenched Ductibor® 1000-AS sheet. The measured fracture and *damage integrated* strains in Table 9, excluding 5 mm Nakazima dome test, were used to calibrate the Bai and Wierzbicki (2008) fracture model, described in Equation (44), due to Abedini and Butcher (2020).

3.1.3.1. Mesh Regularization

It should be noted that the calibrated fracture *locus* is not immediately applicable to the finite element analysis due to the prevalence of finite element mesh sensitivity. In general, the predicted fracture strains in necking zones of a forming model can be significantly different based on the element size, as demonstrated by Eller *et al.* (2014). As a result, a process known as 'mesh regularization' was performed to account for the effect of element size on fracture prediction.

In the mesh regularization process herein, the 50 mm dome Nakazima biaxial tension test by Samadian (2018) was numerically modeled with four different element sizes within the blank mesh, 0.6 mm, 1.2 mm, 2.5 mm and 5.0 mm. In each model, a scaling factor was applied to the calibrated fracture *locus* (Figure 72 and Table 10) such that each predicted limiting dome height at failure matches that in the experiments. One important aspect considered in the numerical modeling of the Nakazima dome test was incorporating the die lock-bead geometry used in the test. Without the lock-bead, the correlation between the measured and the predicted responses in the punch load *vs.* punch height worsened significantly. The details of the Nakazima model setup are documented in Appendix F for brevity.

The predicted punch load *vs.* punch height response for each element size after applying the regularization is overlaid with the measured punch load *vs.* punch height response in Figure 73(b). Also shown in the figure is the punch load *vs.* punch height response with the as-calibrated fracture *locus* without regularization Figure 73(a). The applied scaling factor or regularization factor for each element size is shown in Figure 74.

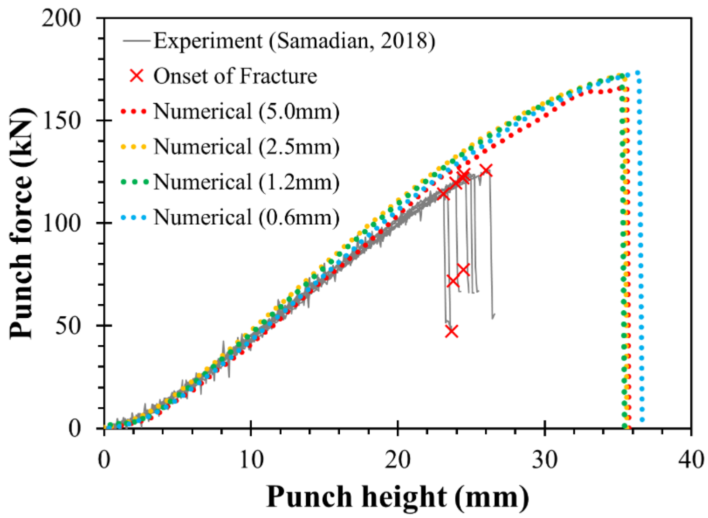

(a) without regularization

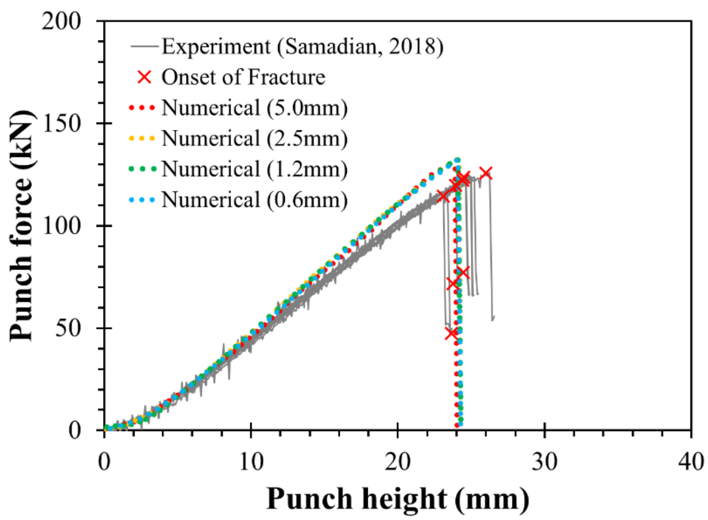

(b) with regularization

Figure 73: Predicted punch force *vs.* punch height response from Nakazima 50 mm dome biaxial tension simulation of the die-quenched Ductibor® 1000-AS: (a) without and (b) with regularization. The measured response by Samadian (2018) is overlaid with the predicted responses. The 0 mm punch height refers to the first point of contact between the punch and the specimen.

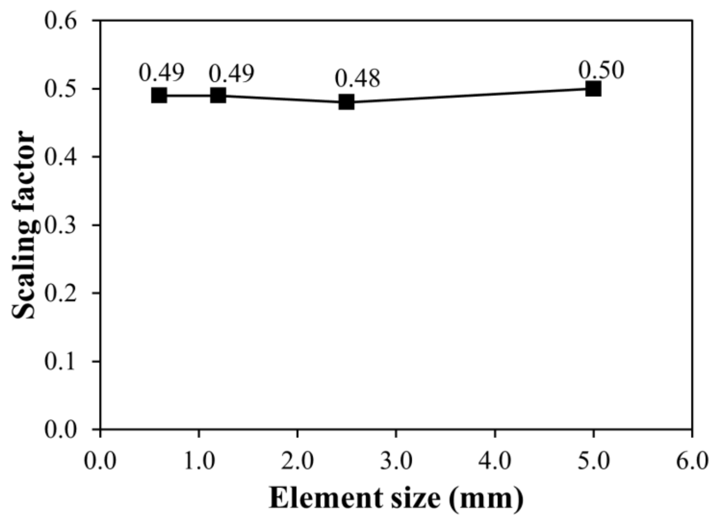

Figure 74: Regularization factor for calibrated fracture *locus* of die-quenched Ductibor® 1000-AS.

An interesting observation in Figure 74 is that the regularization factors are insensitive to the element sizes in the Nakazima 50 mm dome simulations, unlike the regularization factors for die-quenched Usibor® 1500-AS reported by Omer *et al.* (2017b). Lastly, the calibrated fracture locus in Figure 72 and the regularization factors in Figure 74 are taken as an input to the pre-existing GISSMO model in LS-Dyna (*MAT_ADD_EROSION). The additional parameters used for the GISSMO are listed in Table 11.

Table 11: GISSMO parameters used for the calibrated fracture locus of die-quenched Ductibor® 1000-AS

NUMFIP	ECRIT	DMGEXP	DCRIT	FADEXP	SHRF	BIAXF
-70	0	2	1	2	1	0

Mesh regularization may lead to excessive damage accumulation in the shell elements under compression (*i.e.* $\eta < 0$) since the scale factors would be applied to the entire fracture locus (*i.e.* $\eta < 2/3$). To avoid this, the shear regularization factor “SHRF” in *MAT_ADD_EROSION was set to 1, which prevents the compression (and shear) region of fracture *locus* from being scaled (Livermore Software Technology Corporation). The biaxial regularization factor “BIAXF” was set to 0 so that the rest of the region in fracture locus (*i.e.* $0 < \eta < 2/3$) is scaled.

3.1.4. Spot Weld Response

The material model adopted for the Ductibor® 1000-AS spot welds is documented in this section. All of the experiments and calibration work was performed by Tolton (2020) whose thesis topic is dedicated to spot welds. The spot weld model is named *MAT_SPOTWELD_DA, provided from the LS-Dyna material library (Livermore Software Technology Corporation, 2016), and consists of a spot weld failure model defined as

$$f = \left(\frac{\sigma_n}{\sigma_n^F}\right)^{m_n} + \left(\frac{\sigma_b}{\sigma_b^F}\right)^{m_b} + \left(\frac{\tau}{\tau^F}\right)^{m_T} - 1 \tag{46}$$

in which f is a failure parameter, and σ_n^F, σ_b^F , τ^F are the normal, bending, shear strengths and σ_n, σ_b , τ are the normal, bending, shear stresses. The failure parameter (f) of unity represents the onset of spot weld failure, upon which the damage parameter (D) begins to accumulate *via*

$$D = \frac{G_{\text{used}}}{2GFAD} \tag{47}$$

and G_{used} is the internal work done by the spot weld element after the failure (*i.e.* f reaches 1), and GFAD is the fading energy parameter. Damage parameter D should not be confused with f, since the former represents the accumulated rupture of spot welds *once the failure initiates*. Spot weld elements can only be deleted once D reaches a value of unity.

In Equation (47), GFAD also deserves particular attention because it controls the load-carrying capacity after the failure, which would otherwise result in an instant element deletion. The load supported by the spot weld is decreased by a scale factor of $1 - D$ (Livermore Software Technology Corporation, 2016). Thus, a higher value of GFAD would correspond to a lower damage accumulation (due to Equation (47)), which in turn, would result in a higher scale factor (Livermore Software Technology Corporation, 2016). The calibrated parameters described in Equations (46) and (47) are listed in Table 12 for the die-quenched Ductibor® 1000-AS. Note that the onset of bending failure in the spot welds was not calibrated by Tolton (2020) and was suppressed by assigning a high value to the bending strength parameters.

Table 12: Calibrated parameter for the spot weld model, *MAT_SPOTWELD_DA (Livermore Software Technology Corporation), by Tolton (2020). The spot weld diameter was assumed as 6.0 mm.

Sheet thickness (mm)	Normal strength (MPa)	Bending strength (MPa)	Shear strength (MPa)	Normal exponent	Bending exponent	Shear exponent	GFAD
1.2	235	1.00×10^{14}	800	1	1.00×10^{14}	1	192
1.6	435	1.00×10^{14}	875	1	1.00×10^{14}	1	120

3.2. Fold Initiator Treatment

In introducing the fold initiator patterns within the FE models, two different modeling approaches were considered, termed the "displacement approach" and "indentation approach". In the displacement approach models, the nodes of the double hat mesh at the appropriate locations were displaced by 3 mm, which is the fold initiator depth during the indentation processes. In the indentation approach, the fold initiator patterns were modeled by simulating the top and flange indentation processes undertaken during the specimen fabrication. These approaches are detailed in the following.

It is important to note that the majority of the numerical models utilized the displacement approach to introduce the fold initiators. The indentation approach was considered as an alternative to simulate some of the Part 2 and 3 experiments in an effort to account for significant distortion of the crush rails that incorporated multiple fold initiators.

3.2.1. Finite Element Mesh of Single Hat Section

The main input to the numerical models for creating fold initiator patterns is a discretized FE mesh of the single hat section. As shown in Figure 75, the single hat section mesh consists of uniform 2.5 mm quadrilateral elements. The length of the single hat section mesh is 500 mm for all dynamic crush models used to simulate the experiments in Parts 1 and 2 of the test matrix. For the quasi-static crush models in Part 3 of the experiments, the length of the single hat channel was reduced to 375 mm to reduce the likelihood of global buckling.

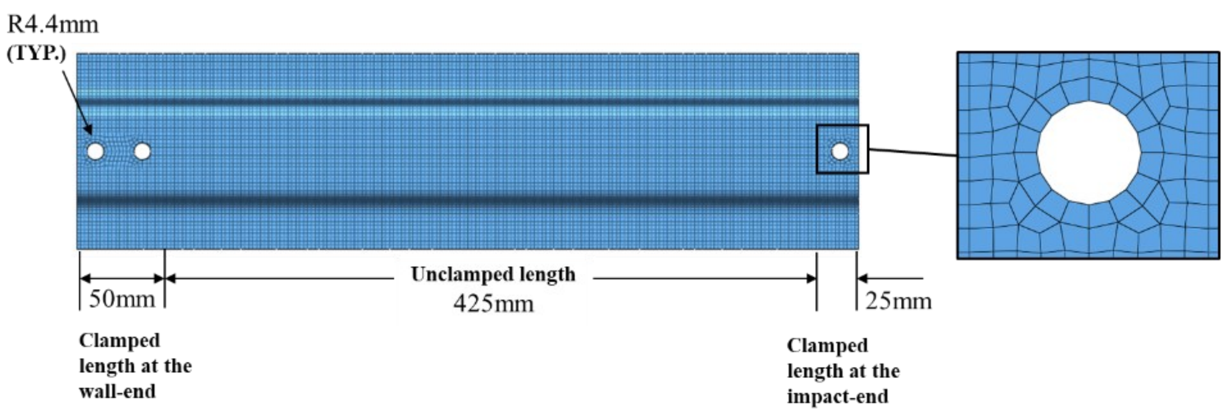

Figure 75: Illustration of the finite element mesh used to model the single hat channel subjected to dynamic loading. The unclamped length was reduced to 375 mm for the quasi-static load cases.

3.2.2. Displacement Approach to Introduce Fold Initiators

To illustrate the displacement approach in which nodes were simply translated to introduce fold initiators without modelling the resulting strains and stresses, the FE mesh for the TF fold initiator pattern is shown in Figure 76. The nodes at the locations corresponding to the fold initiators are displaced in the y-direction by 3 mm, which is the depth of the initiators in the experiments.

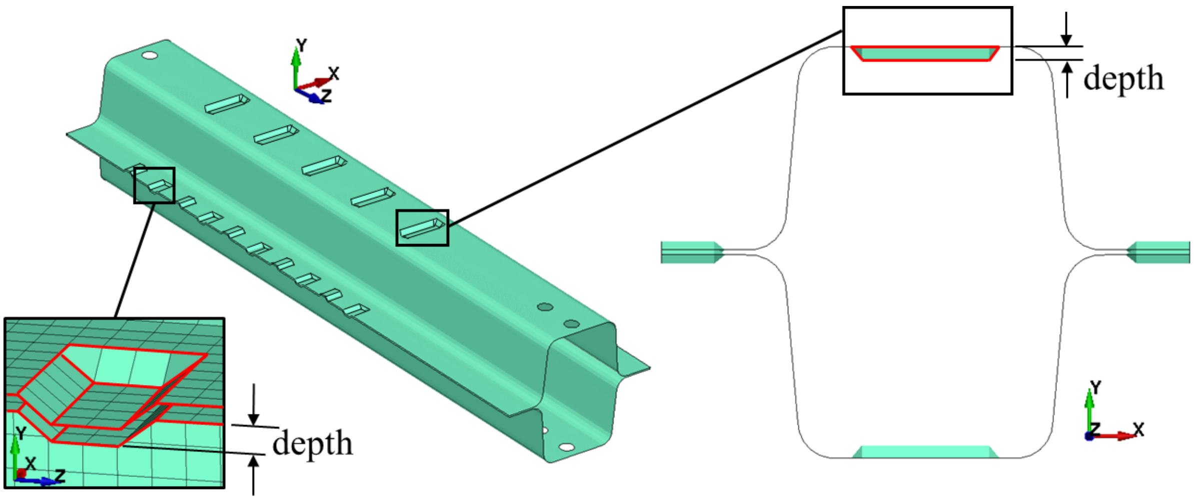

Figure 76: Illustration of the displacement approach used to recreate the TF pattern in the FE model.

3.2.3. Indentation Approach to Introduce Fold Initiators

The indentation approach simulates the plastic deformation process used to form the fold initiators in the flanges and/or top face of the channel sections, essentially mimicking the physical process adopted in the experiments. The indentation approach is considerably more complicated and requires meshing of the indentor tooling (described in Section 2.2.2) and modelling the indentation of each fold initiator, as described in this section of the thesis. The process of modeling indentation follows the specimen fabrication process with the following three steps:

1. Top fold initiators are indented on two single hat channel models, separately.
2. The two single hat models from Step 1 are joined by spot weld elements to form a double hat channel model
3. For patterns with flange initiator patterns, the initiators are indented on the double hat model as was done in the physical sample preparation.

To demonstrate the steps above, Figure 77 illustrates the workflow adopted within the numerical models of the TF (Top-Flange) pattern indentation in which the top face is first indented and the flange fold initiators after the hat sections are joined. A critical distinction between the top and flange indentation model is the half-symmetry about the y-z plane assumed for the top initiators, while the full geometry is modelled while simulating the flange initiator indentation process. In this case, the half-symmetry models were reflected after the top face indentation but before the flange indentation.

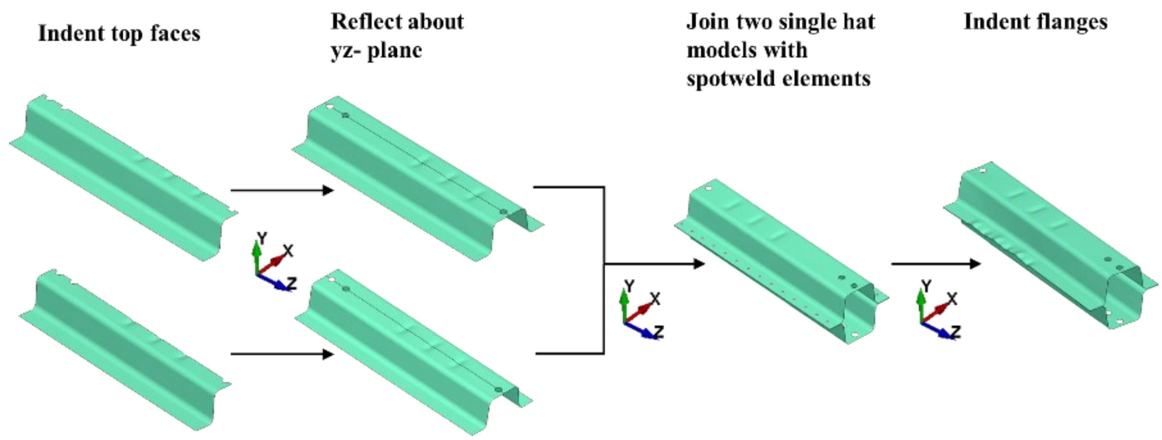

Figure 77: Illustrations of the workflow within the numerical models of the TF (Top-Flange) pattern indentation, using the indentation approach. Each fold initiator is indented one at a time.

The fold initiators were indented one at a time, meaning one indentation simulation forms one fold initiator. After each simulation, the single or double hat models were translated in the z-direction by twice the targeted fold initiator spacing (4H). During flange indentation, fold initiators were formed on one flange at a time (as illustrated in Figure 78) to reproduce the actual sequence taken during preparation of the physical specimens. As a result, after one flange was completely indented, the double hat models were rotated about the y-axis and then the z-axis after which the fold initiators were formed on the next flange.

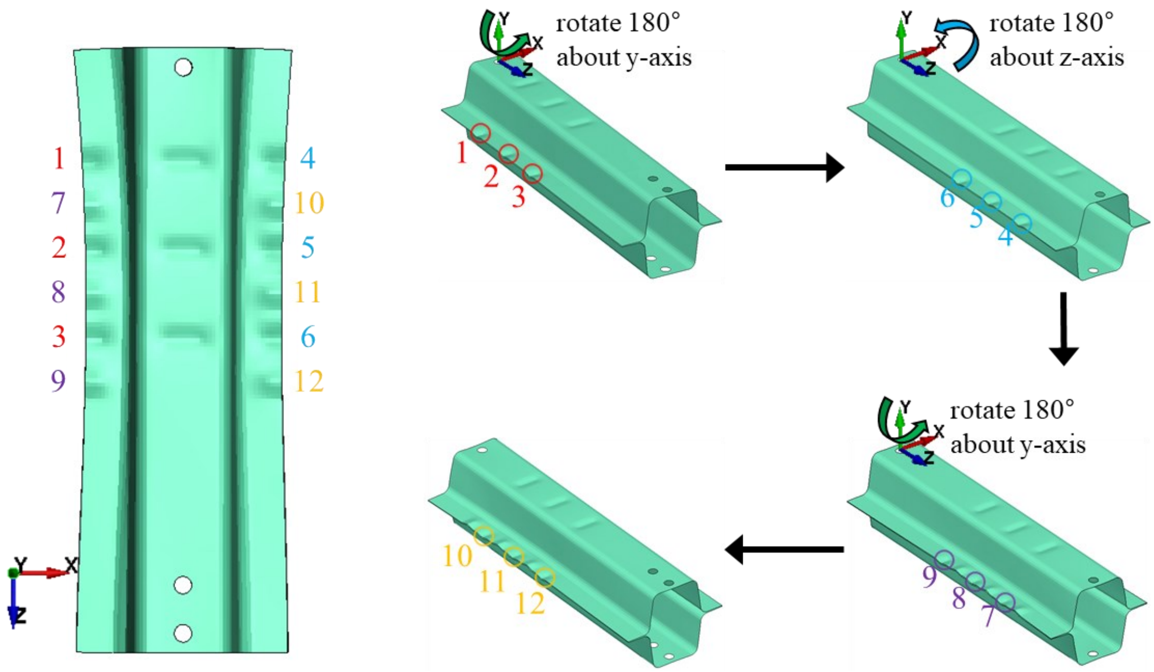

Figure 78: Illustration of the indenting sequence taken within the numerical models of flange indentation. Numbers indicate the sequence from the first to last.

As noted, this process is quite laborious and it is noted that a far more effective approach would be to incorporate the initiator geometry within the hot stamping tooling. Moreover, the excessive distortion observed in the specimens incorporating numerous fold initiators (Figure 54) would be significantly reduced by forming the initiators within the hot stamping tool. Unfortunately, the high cost of fabricating hot stamping tooling capturing all of the initiator patterns and spacings was prohibitive and the current manual indentation process was adopted in the experiments. The main purpose of the indention approach models was to assess the effect of the local thinning, work hardening and distortion due to the indentation process on the axial crush response of the rail assemblies.

3.2.3.1. Indentation Model Setup and Boundary Conditions

All the numerical simulations of indentation were performed using the static implicit formulation within LS-Dyna (Livermore Software Technology Corporation, 2016). Figure 79 illustrates the numerical model setup for top and flange indentation. Both setups consist of a fixture and an indenter. Additionally, the top indentation setup consists of a toggle clamp used to constrain the single hat specimens.

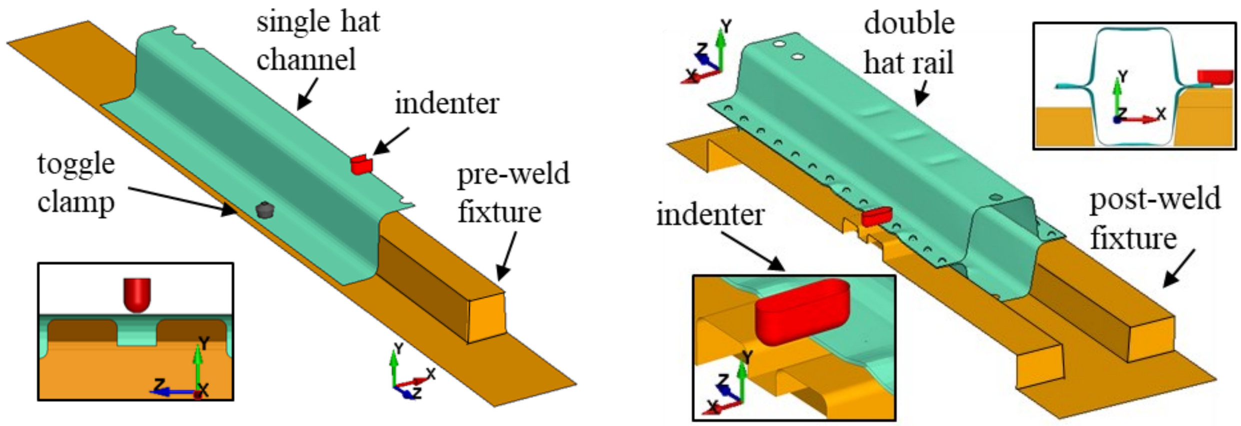

(a) Pre-weld (top) indentation model setup (b) Post-weld (flange) indentation model setup

Figure 79: Illustration of the indentation model setup: (a) pre-weld and (b) post-weld

All tools are modelled as rigid parts with quadrilateral shell elements to discretize the tool surfaces. The element size used for the fixtures and indenter was an order of magnitude smaller than the initial element size of a hat channel, as shown in Figure 80.

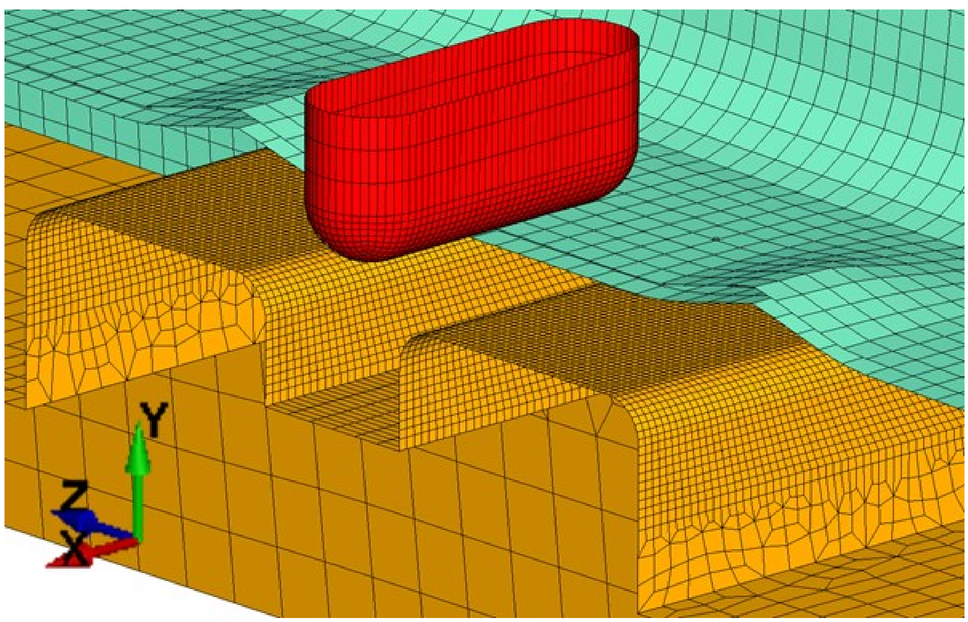

Figure 80: Close-up image of the mesh used for fixture and the indenter for the flange indentation model

The fixtures are fully constrained in all degrees of freedom and the indenter was prescribed a sinusoidal velocity profile capturing the indentation motion. The hat channels were assigned a gravitational load and the clamp was given a constant force of 250 N, which represents the actual clamping force.

A surface-to-surface, penalty-based contact algorithm was defined between the hat channels and tooling components, with a friction coefficient of 0.4.

3.2.3.2. Adaptive Mesh, Coarsening, and Springback for the Indentation Approach Models

The hat channels in the indentation approach were meshed with an initial element size of 2.5 mm; however, an adaptive mesh refinement algorithm was utilized in LS-Dyna. The algorithm refines those elements for which the total angle change between adjacent element edges exceeds 20°. A refinement level of three was used, meaning the smallest element size was 0.625 mm. Once the indentation stage was completed, the refined elements were combined using a coarsening algorithm in LS-Dyna to re-establish the nominal element size of 2.5 mm. To illustrate the refinement-coarsening process, Figure 81 shows one of the indented zones in a hat channel model following indentation as well as following application of the coarsening algorithm. Mesh coarsening was used to improve crash simulation run time and to keep the element size consistent with industrial crash safety practice.

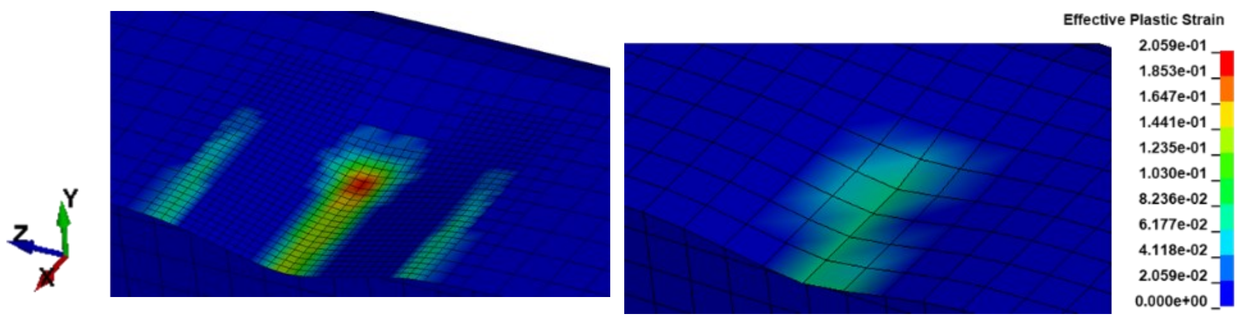

(a) before applying the coarsening algorithm (b) after applying the coarsening algorithm

Figure 81: Illustration of an indented zone to demonstrate the effect of the coarsening algorithm: (a) before and (b) after applying the coarsening algorithm.

After simulating indentation, all tools were removed and a springback analysis was performed on the indented hat models. In the springback analysis, a number of nodes adjacent to the potential datum locations in the hat model (*e.g.* the locating holes) were chosen and boundary constraints were applied to eliminate rigid body modes, as shown in Figure 82.

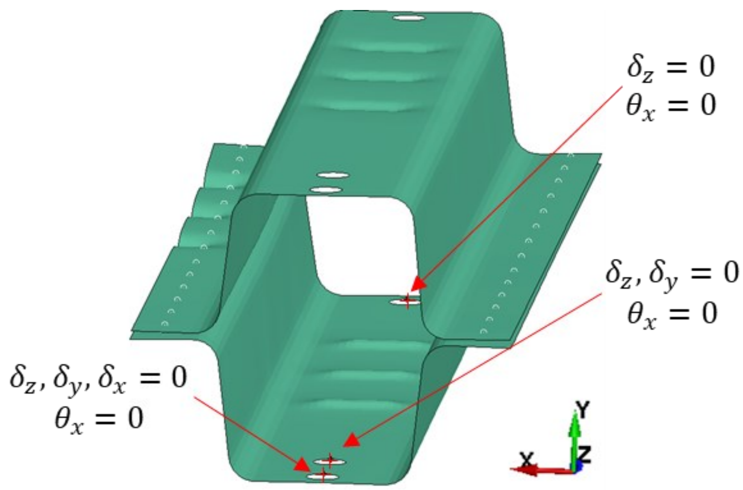

Figure 82: Constrained nodes for a springback analysis of a double hat channel, which follows the flange indentation simulation

It is important to note that in the indentation approach, the effect of the previous forming history (*e.g.* damage variable, effective plastic strain, residual stress and thinning) was taken into account by utilizing the *INTERFACE_SPRINGBACK keyword in the LS-Dyna software. This keyword creates a file named "dynain" which contains the forming history variables after each simulation. The dynain file was used to initialize each subsequent indentation simulation and, finally, the axial crush simulation.

3.2.3.3. Validation of the Indentation Approach Models

One important phenomenon observed during indentation was the significant geometric distortion of the flanges, as shown in Figure 54. The indentation models should closely replicate the same effect; hence, the model results must be validated. For that reason, Figure 83 shows two indented specimens from Part 3 of the tests matrix (SP-D12-275 and SP-D16-300) and their numerical counterparts developed by the indentation approach. Overall, the models well reproduced the concave shape of the flanges and the smooth, continuous surfaces at the fold initiator regions.

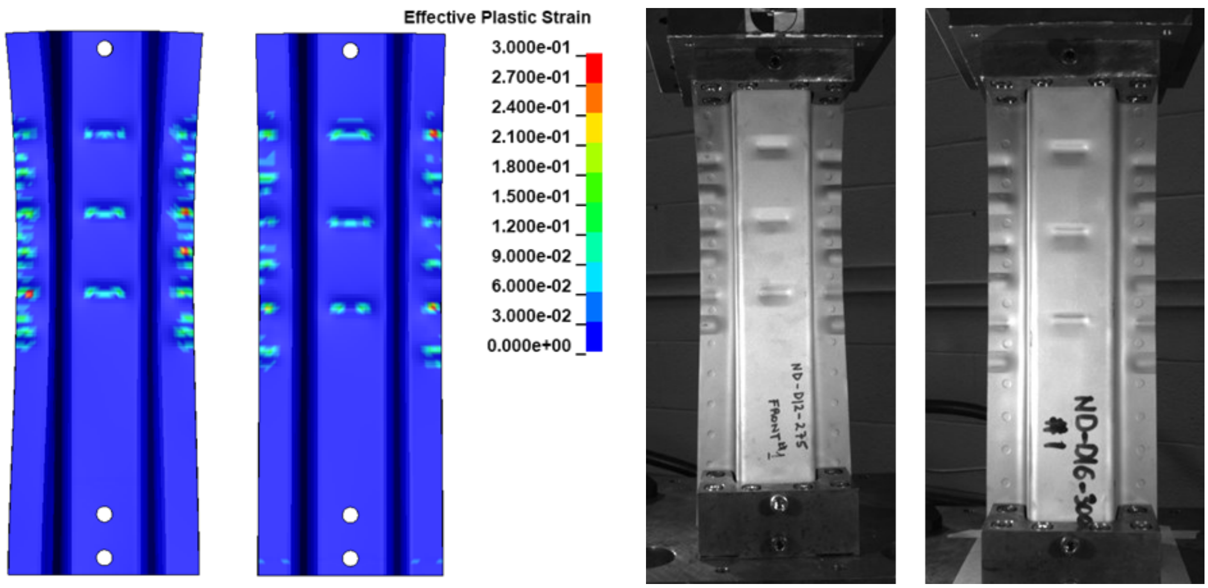

(a) Indented model (b) Test specimens

Figure 83: Indented shapes of the 1.2 mm (left) and 1.6 mm (right) specimens (SP-D12-275 and SP-D16-300) in Part 2: (a) numerical models and (b) actual tested samples

To quantify the accuracy of the indenter models in predicting the geometric distortion, the flange-to-flange widths (see Figure 55 for definition of this measurement) were taken from the indented models and plotted against the measured values from the test specimens, as shown in Figure 84. Both the 1.2 mm and 1.6 mm model predictions of flange-to-flange width are in very good agreement with the measured values. The indented 1.2 mm model (left) slightly over predicted the draw-in of the flange with a maximum error of 1.6 % (on the total flange-to-flange width) while the 1.6 mm model (right) under-predicted with the maximum error of 0.84 %.

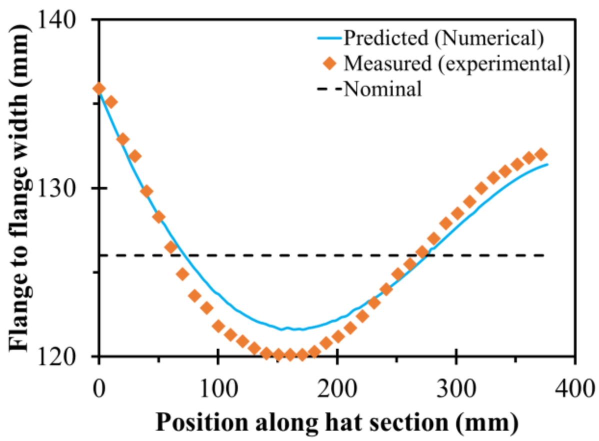

(a) 1.2mm

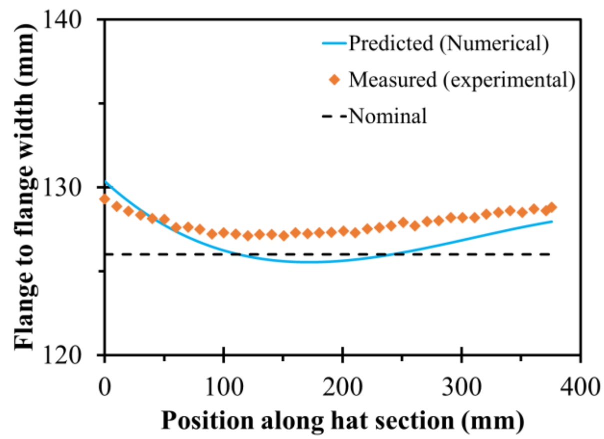

(b) 1.6mm

Figure 84: The measurements of flange-to-flange width (see Figure 55 for definition of this measurement) taken from the indented numerical models and test specimens for (a) 1.2 mm (SP-D12-275) and (b) 1.6 mm (SP-D16-300) specimens. The x-axis origin corresponds to the impact-end of the specimens.

3.3. Axial Crush Models

3.3.1. Dynamic Axial Crush Model

In this section, the numerical model setup for the dynamic axial crush simulations is described. All axial crush simulations were performed using the explicit, dynamic time integration formulation in the LS-Dyna software (Livermore Software Technology Corporation, 2016). In the pre-processing stage, Altair Hypermesh and LS-PrePost were utilized for meshing the geometry and assigning the boundary conditions, respectively. Note that the quasi-static models used the same meshing and boundary conditions as the dynamic models, with changes to account for the displacement-controlled loading (as opposed to impact) and time scale, as detailed in Section 3.3.2.

3.3.1.1. Boundary Conditions

An overview of the axial crush model is shown in Figure 85. The model consists of a double hat channel, with fold initiators introduced using either the displacement or indentation approach, the impact sled, and various clamps and bosses.

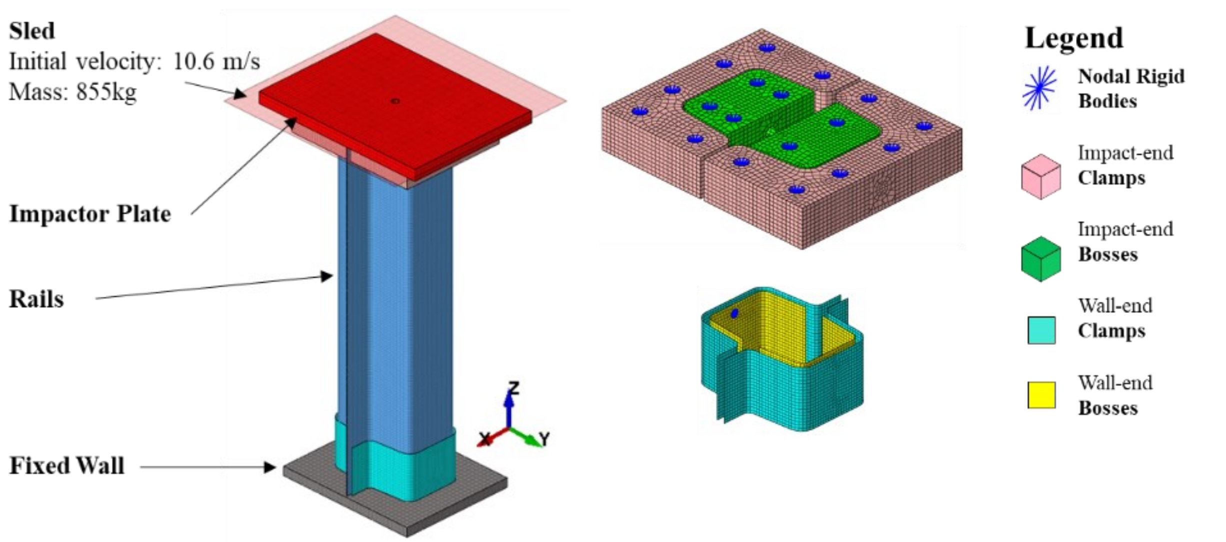

(a) Overview of Axial Crash Model (b) Clamps

Figure 85: Illustrations for (a) overview of axial crush model and (b) various clamps and bosses used in the axial crush tests. The double channel hat model is obtained from the previous fold initiator modeling stage, either using the "displacement approach" or the "indentation approach".

Two boundary conditions were introduced in the model. Firstly, the crash sled was assigned a mass of 855 kg and an initial velocity of 10.6 m/s using the *PART_INERTIA keyword. Secondly, the nodes of the fixed barrier wall were constrained in all six degrees of freedom. The resultant crush force is obtained by the total reaction force of the fixed nodes by utilizing the *DATABASE_SPCFORC keyword.

3.3.1.2. Mesh, Element Formulation

Plate, Clamp and Boss

A major effort of the modelling work was meshing the various fixture components, as shown in Figure 86. All fixtures were meshed with first-order brick elements except for the clamps and bosses at the wall end. The wall-end clamps were meshed with rigid, shell elements. On the other hand, the wall-end bosses were meshed with fully integrated, first-order elastic, shell elements with seven through-thickness integration points (highlighted in Figure 86). The neighboring elements around the holes were meshed in a cylindrical pattern about the geometric centres.

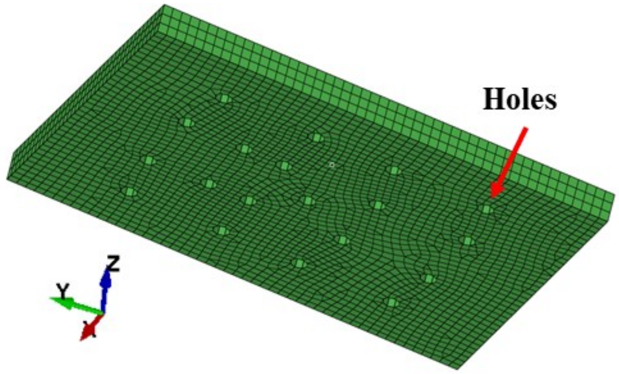

(a) Impactor plate

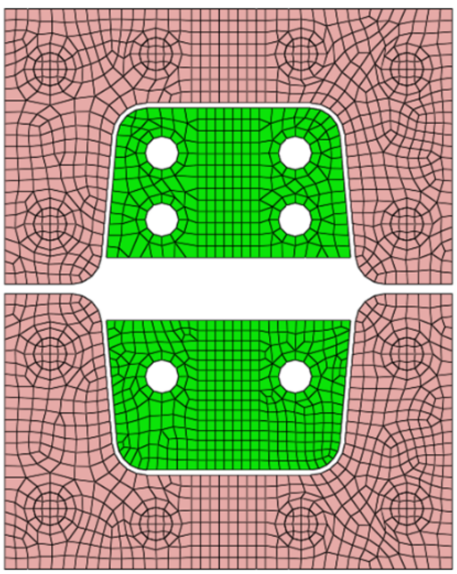

(b) clamps and bosses (impact-end)

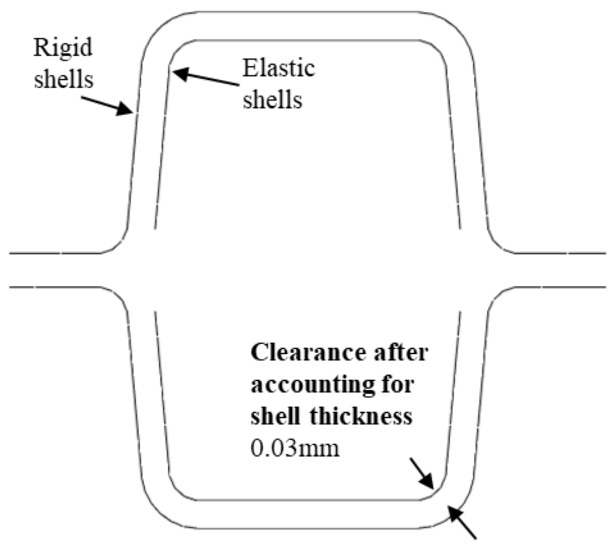

(c) Clamps and bosses (wall-end)

Figure 86. Illustration of mesh for (a) impactor plate, clamps and bosses at (b) impact end (c) and wall end. The inner shells were given a thickness of 4 mm and increased density to achieve the similar mass properties as the actual bosses, and showing the outer surfaces after accounting the shell thickness.

Bolts and Spot welds

The joining methods used in the mounting fixtures in the experimental setup are bolts used to tighten the bosses and clamps. One common approach in simplifying the meshing effort is utilizing beam elements to simulate the bolts. To demonstrate this, Figure 87 illustrates one of the bolts modeled as a beam element between the clamps and bosses at the wall-end (Figure 87c) and another at the impact-end (Figure 87b). The ends of the beam element coincide with either a nodal rigid body (Figure 87b) or a node that is strategically located at the geometric centre of the bolt holes (Figure 87c).

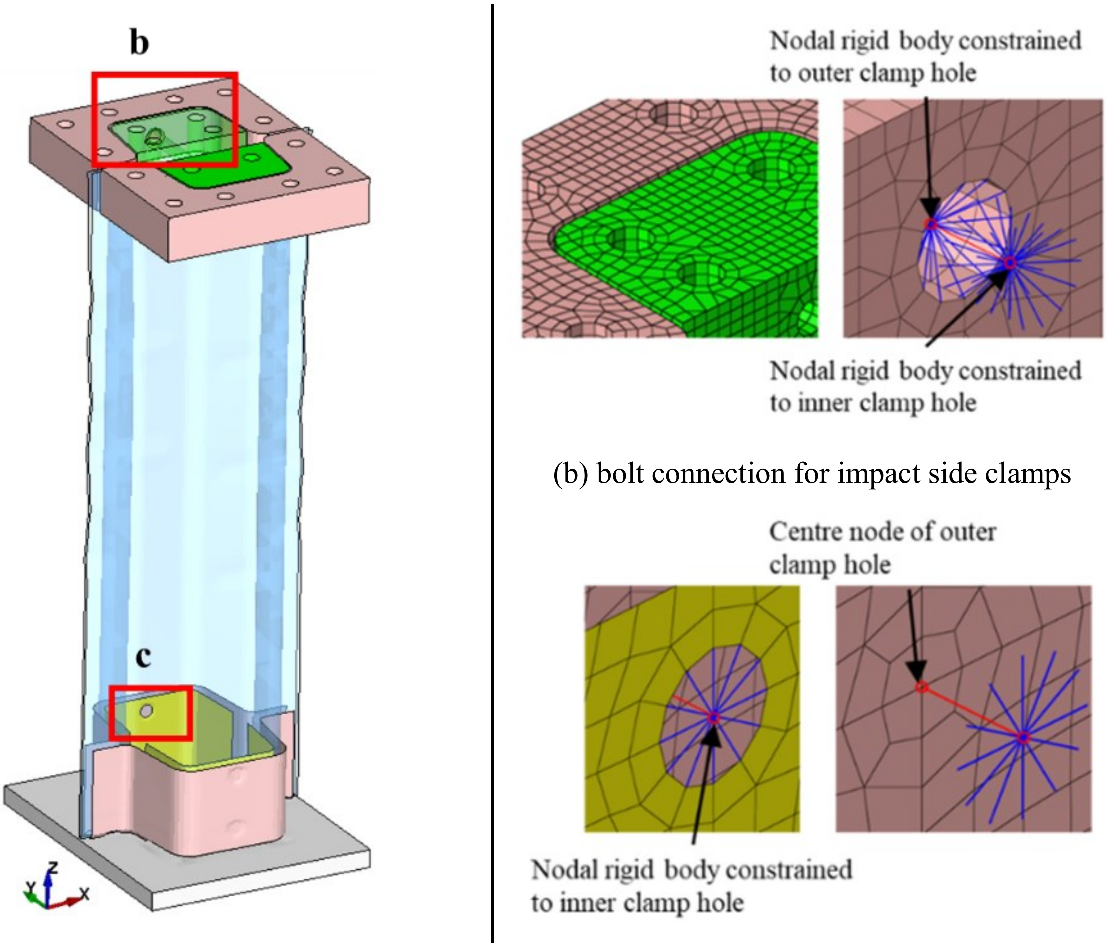

(a) overview

(b) bolt connection for impact side clamps

(c) bolt connection for wall side clamps

Figure 87: Illustration of bolt connection using a beam element, joined by either nodal rigid bodies or a node, strategically located at the geometric center of holes. (a) wall clamps and (b) impact clamps.

Similarly, 16 bolts were modelled as beam elements to join the clamps to the impactor plate. All bolts were assigned an estimated pre-tension of 24.9 kN by utilizing the *INITIAL_AXIAL_FORCE _BEAM keyword.

The spot welds used to join the two hat sections were modeled as eight hexagonal elements by utilizing the *CONTROL_SPOTWELD_BEAM keyword card. This keyword allows each spot weld to be modeled as a beam element, which then converts to a group of hexagonal elements at the beginning of the simulation.

3.3.1.3. Material Models

The material models used in the different components within the experiment are listed in Table 13. Given the primarily elastic response of the mounting fixtures and sled, the impactor plate and the barrier wall are modeled as rigid materials and all of the clamps are modeled as elastic (except for the outer clamps at the wall-end).

Table 13: LS-Dyna material models used in the axial crash model

	Part	Material Model
1	Rail	PIECEWISE_LINEAR_ PLASTICITY
2	Sled	RIGID
3	Impactor Plate	RIGID
4	Outer Clamps - Wall	RIGID
5	Inner Clamps - Wall	ELASTIC
6	Outer Clamps - Impact	ELASTIC
7	Inner Clamps - Impact	ELASTIC
8	Wall	ELASTIC
9	Spot weld	SPOTWELD_ DAIMLERCHRYSLER
10	Bolts	SPOTWELD

3.3.1.4. Contact Algorithms

All contact algorithms used in the numerical models are penalty function-based and are listed in Table 14. The *TIED_SHELL_EDGE_TO_SURFACE_OFFSET contact algorithm was used to tie the two main interfaces that exist in the rail assembly. The first interface was between the nodes of the spot weld beam elements (slave) and the elements of the rail flanges (master), as shown in Figure 88. The second interface was between the element edges of the outer clamps—that are adjacent to the barrier wall—and the closest solid elements of the barrier wall. To demonstrate this, Figure 89 highlights the tied interface in red. Lastly, the *AUTOMATIC_SINGLE_SURFACE contact algorithm deserves particular attention because its slave and master are left unassigned. By definition, this algorithm checks for and enforces contact between all components within the model, including self-contact of the folding crush rail. For all contact definitions, a constant friction coefficient of 0.4 was assigned.

Table 14: A list of LS-Dyna contact algorithms used in the dynamic axial crush model.

	Slave	Master	Contact Type
1	Spotwelds	Rail	TIED_SHELL_EDGE_TO_SURFACE_OFFSET
2	Wall Outer Clamps	Wall	TIED_SHELL_EDGE_TO_SURFACE_OFFSET
3	-	-	AUTOMATIC_SINGLE_SURFACE

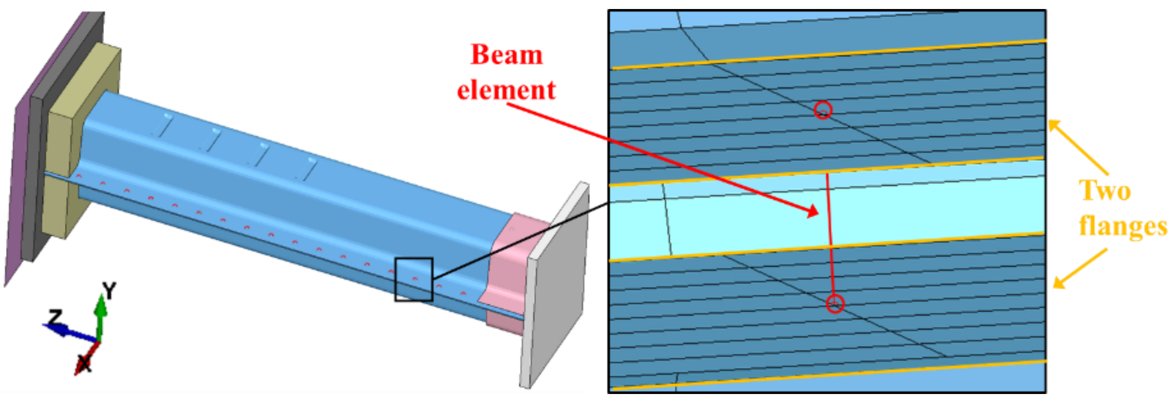

Figure 88: Illustration of the spot weld beam element tied to the quadrilateral elements at the rail flanges.

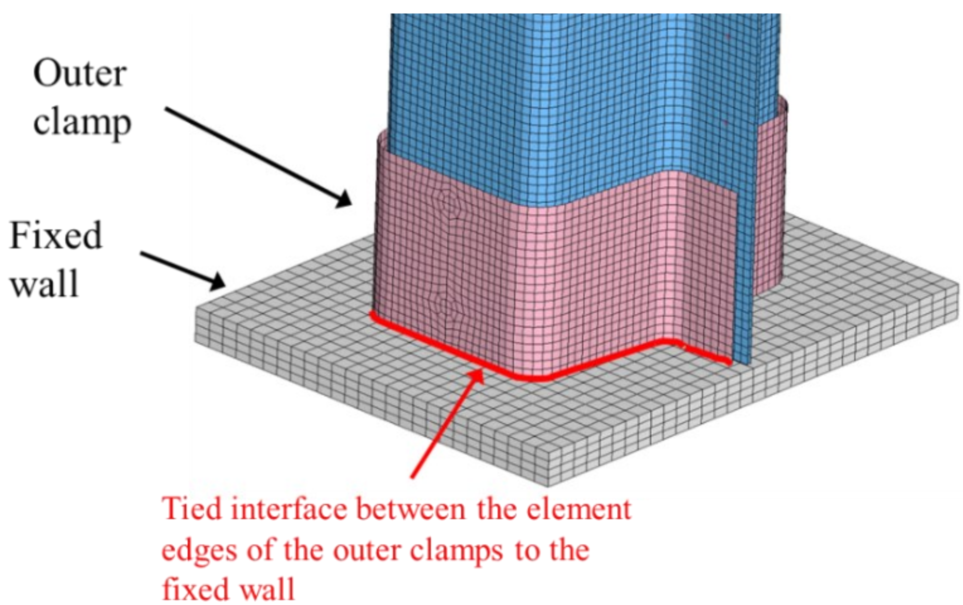

Figure 89: Illustration of the tied interface between the element edges of the outer clamps to the fixed wall

3.3.2. Quasi-static Axial Crush Model

The boundary conditions, mesh configurations, and contact algorithms on the quasi-static models were the same as those in dynamic crush models with a few minor differences. Firstly, the length of the rail was reduced from 500 mm to 375 mm, as was adopted in the quasi-static experiments to reduce the likelihood of buckling. Secondly, a constant velocity was applied at the end of the crush rail instead of the impact load. An artificially high velocity of 350 mm/s was adopted, which is 1000 times the loading rate in the experiment (0.35 mm/s). The elevated loading rate was applied to reduce the simulation time in the dynamic explicit method, which otherwise would be orders of magnitude larger than the explicit time step size. This method, however, introduces artificial strain rate effects. To offset these effects, the rate dependency of the stress-strain response was adjusted to account for the time scaling by a factor of 1000.

4.0 Axial Crush Results and Discussion

This chapter presents the results from the axial crush rail experiments and the corresponding numerical predictions, broken down into three sections, each dedicated to the results of Parts 1 to 3 of the experimental program, as detailed in the test matrix in Table 3 and flowchart illustrating the testing program in Figure 36. To provide readers with an understanding of the interrelationship between each part of the study, the roadmap of the experimental program is summarized as follows.

Part 1. The crush performance of the baseline specimen is established

a. Experimentally with the dynamic sled tests; and,
b. Numerically with the dynamic axial crush model.

Part 2. To improve on the baseline performance, a unique fold initiator pattern—namely pattern TF (Top-Flange)—is selected after

a. Numerically evaluating the crush performance of six different fold initiator patterns, and
b. Experimentally validating two potential candidate patterns.

Part 3. To further optimize the crush stability of the TF pattern, the fold initiator spacing is parametrically varied, and the crush results for each spacing are compared to that corresponding to analytically predicted folding wavelength using the methodology of Abramowicz and Wierzbicki (1989)

a. Numerically; and,
b. Experimentally.

.

4.1. Part 1: Crush Response of Baseline Specimens

In this section, the crush response of the baseline specimens is presented. Table 15 shows the test matrix for the baseline experiments in which BA designates monolithic Ductibor® 1000-AS, while BA_TWB refers to the Ductibor® 1000-AS and Usibor® 1500-AS TWB samples. The baseline specimens are 500 mm long, while the TWB specimens consist of a 210 mm long Usibor® 1500-AS section welded to a 290 mm long Ductibor® 1000-AS section. Note that only 1.2 mm thick specimens were considered for these baseline experiments. The results of the TWB specimens are included in this section for comparison purposes, although the focus of the thesis is primarily on monolithic Ductibor® 1000-AS.

Table 15: Test matrix for baseline study (Part 1)

Specimen Designation	Numerical (N) Experimental (E)		Dynamic (D) Quasi-Static (Q)	Thickness (mm)		Fold Initiator Spacing, 2H (mm)				
				1.2	1.6	20	25	27.5	30	35
BA	**N**	**E**	**D**	✓				-		
BA_TWB	**N**	**E**	**D**	✓				-		

4.1.1. Experimental Results

4.1.1.1. Monolithic Baseline Experiments

Figure 90 shows high-speed video images taken during a dynamic experiment on a monolithic baseline specimen, while Figure 91 shows the corresponding crush force *vs.* crush displacement response. From the images, it is apparent that the BA specimen first undergoes progressive folding during the early stages of impact. The formation of the first three folds corresponds to the local peaks, (a) - (c) in Figure 91, in the force *vs.* displacement (**F-D**) plot. However, upon the third fold formation, a hinge forms near the fixed-end, and global buckling takes over as the major deformation mode. As the buckling progresses, the force steadily decreases. Subsequently, the bottom hinge evolves to a fold, and the force reaches the next local peak, (d). At this point, the buckling mode switches back to local folding at the fixed-end. The last two local peaks, (e) and (f) at 232 mm and 257 mm crush displacement, correspond to the subsequent fold formations at the bottom.

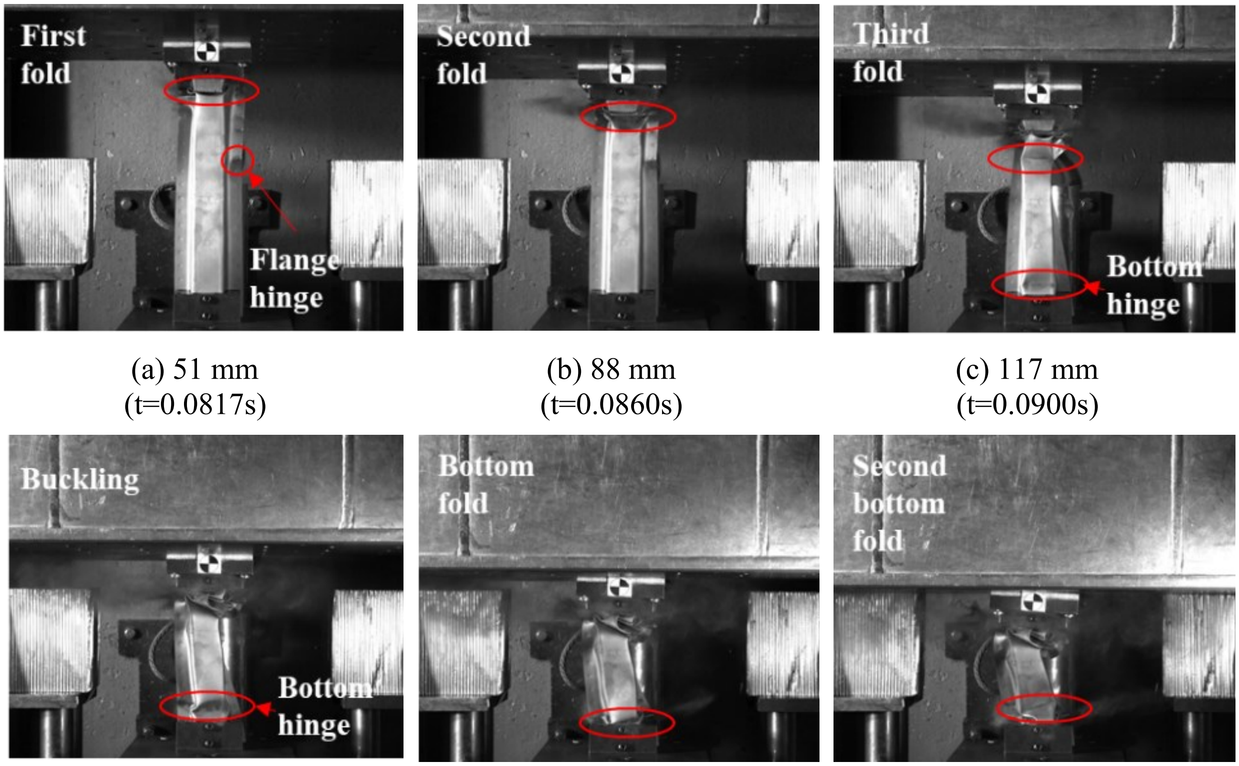

(a) 51 mm (t=0.0817s)

(b) 88 mm (t=0.0860s)

(c) 117 mm (t=0.0900s)

(d) 196 mm (t=0.9980s)

(e) 232 mm (t=0.1056s)

(f) 257 mm (t=0.1098s)

Figure 90: Deformation history of the monolithic Ductibor® 1000-AS baseline specimen (repeat #1) under a dynamic sled test. The displacements in (a) to (f) refer to the crush distance, and the time is measured relative to the trigger of the data acquisition unit, shown in Figure *63*.

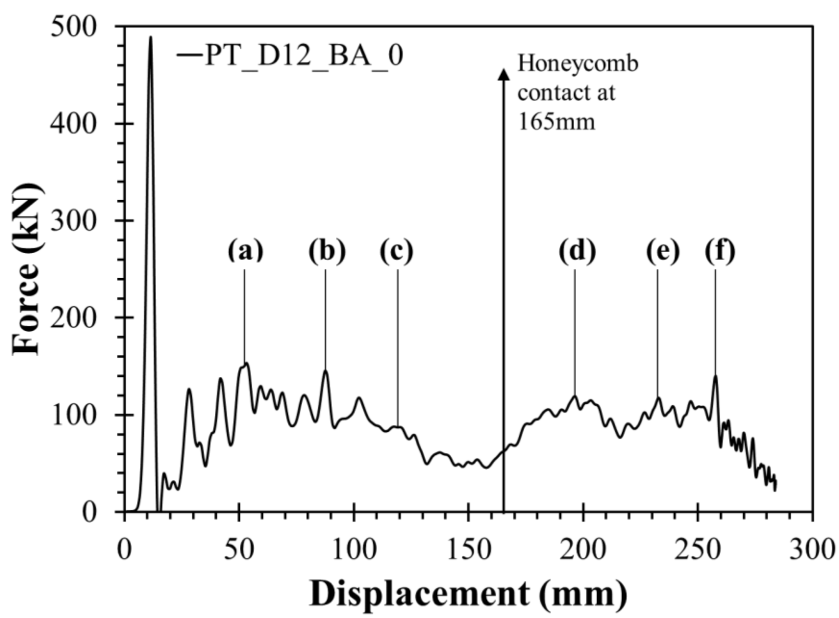

Figure 91: Force *vs.* crush displacement (F-D) plot of the monolithic Ductibor® 1000-AS baseline specimen (repeat #1). Labels (a) to (f) are the displacements at which images in Figure 90 are taken.

Figure 92a shows the final deformed specimens from the three repeat experiments using the baseline pattern. The three specimens show considerable variation due to the variable nature of the global buckling mode. For the most part, regions of cracking were mainly observed at the sidewall and the inclined radii, as highlighted in Figure 93a. A few spot weld failures were observed at the folding region, as also seen in Figure 93a.

(a) Monolithic (Ductibor® 1000-AS) (b) TWB (Ductibor® 1000-AS and Usibor® 1500-AS)

Figure 92: Final deformed specimens: (a) hot-stamped monolithic Ductibor® 1000-AS and (b) hot-stamped TWB consisting of Ductibor® 1000-AS and Usibor® 1500-AS

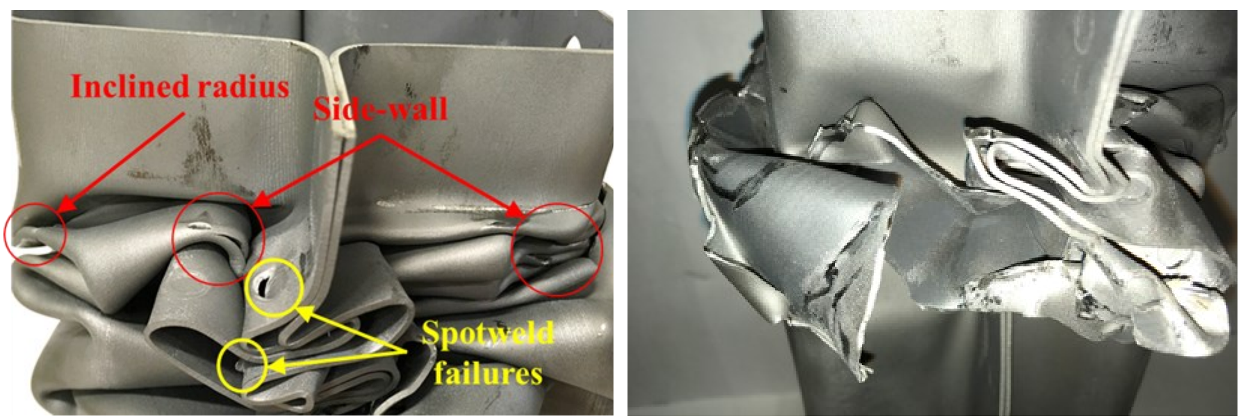

(a) Monolithic (Ductibor® 1000-AS) (b) TWB (Ductibor® 1000-AS and Usibor® 1500-AS)

Figure 93: Close up images of (a) hot-stamped monolithic Ductibor® 1000-AS and (b) hot-stamped TWB consisting of Ductibor® 1000-AS and Usibor® 1500-AS. The fracture locations in (a) are encircled in red.

Figure 94 shows the crush force and absorbed energy experienced by each specimen and their average, plotted against the crush displacement. Each follows a close trend up to 75 mm of crush displacement, after which the responses diverge. Such divergence is likely a reflection of randomness in the folding initiation, which leads to varying crush displacements at which point buckling takes over instead of folding. For the same reason, the peak force shows a 12% variation. Nonetheless, the absorbed energy of each repeat shows very little scatter. The measured average (and the sample standard deviation) of the peak force and absorbed energy at 165 mm crush distance are 448 (± 37) kN and 14.4 (± 0.2) kJ, respectively.

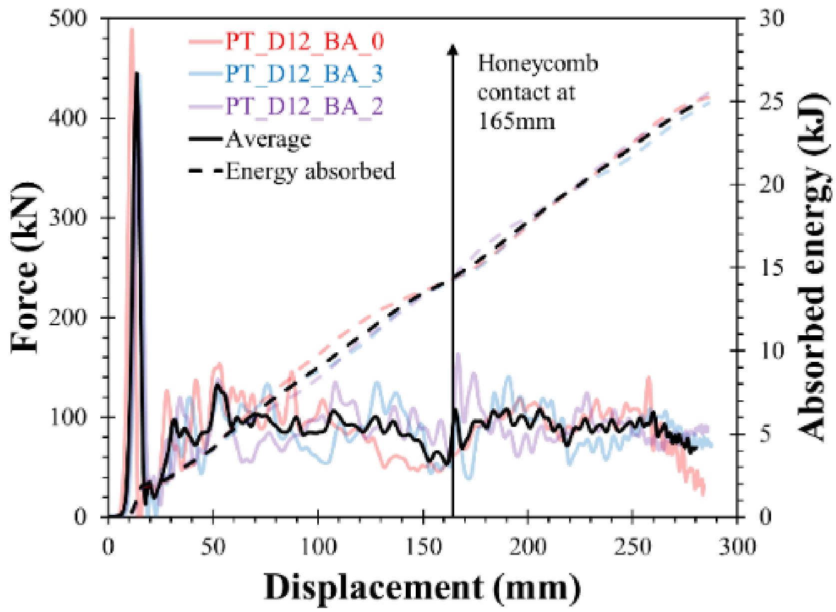

Figure 94: Force *vs.* crush displacement (F-D) and absorbed energy *vs.* crush displacement (E-D) for Ductibor® 1000-AS monolithic baseline specimens.

4.1.1.2. TWB Experiments

Figure 95(a)-(f) shows high-speed video images taken during a dynamic experiment on a TWB baseline specimen, while Figure 96 shows the corresponding force *vs.* crush displacement plot. The TWB specimen undergoes regular folding up to about 70 mm crush displacement (b). However, beyond this displacement, a flange pulls inwards away from the fold region at the crush displacement (c), and a hinge forms at the TWB weld-line at crush displacement in (d). The top fold and the bottom hinge act like two fixed-ends, causing the sample to fold irregularly. The aftermath reveals a large extent of tearing around the surfaces at the folded region, as shown in Figure 93b. The measured average of the peak force and absorbed energy at 165 mm crush distance for the TWB specimens are 450 (±21) kN and 15.0 (±1.0) kJ, respectively, which only differ from those of the monolithic specimens by 2 kN and 0.6 kJ.

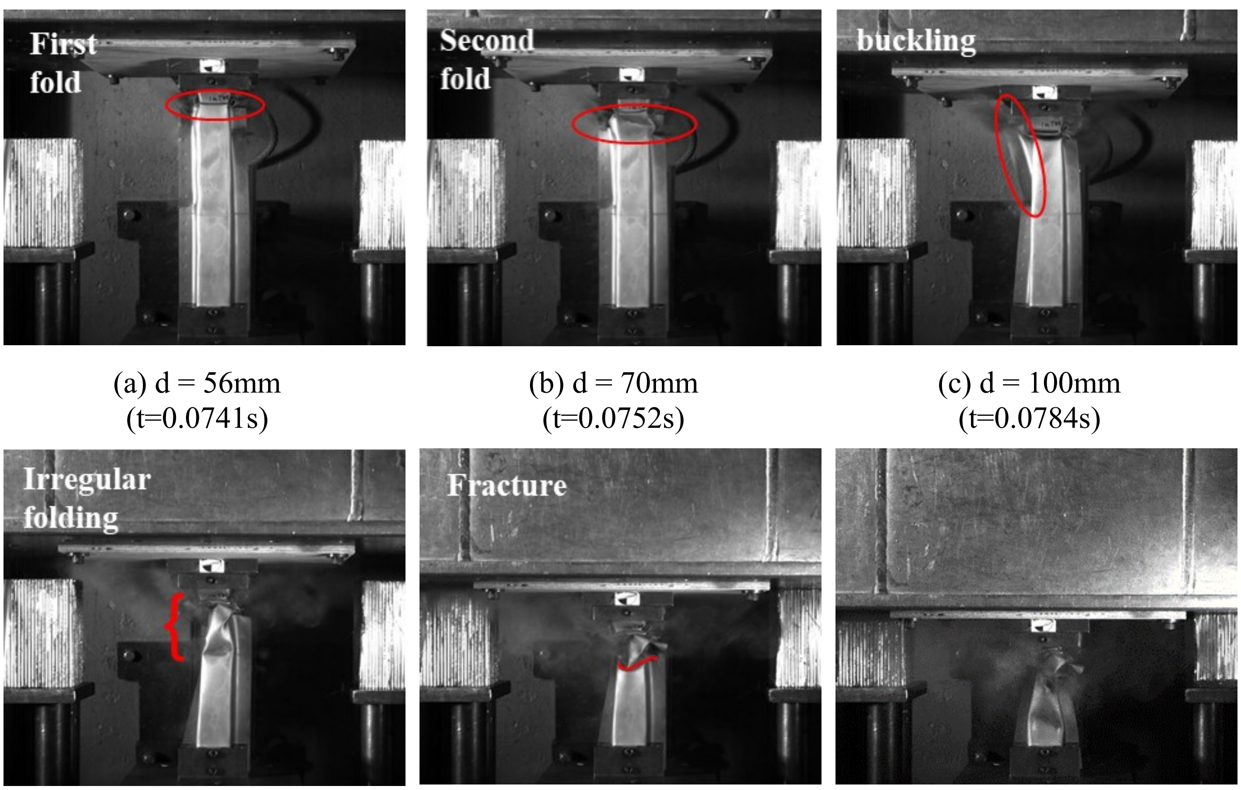

(a) d = 56mm (t=0.0741s)

(b) d = 70mm (t=0.0752s)

(c) d = 100mm (t=0.0784s)

(d) d = 142mm (t=0.0884s)

(e) d = 214mm (t=0.0917s)

(f) d = 260mm (t=0.1052s)

Figure 95: Deformation history of a TWB baseline specimen (repeat #1) under a dynamic test. The displacement in (a) to (f) refers to the crush distance and the time is measured relative to the trigger of the data acquisition unit, shown in Figure 63.

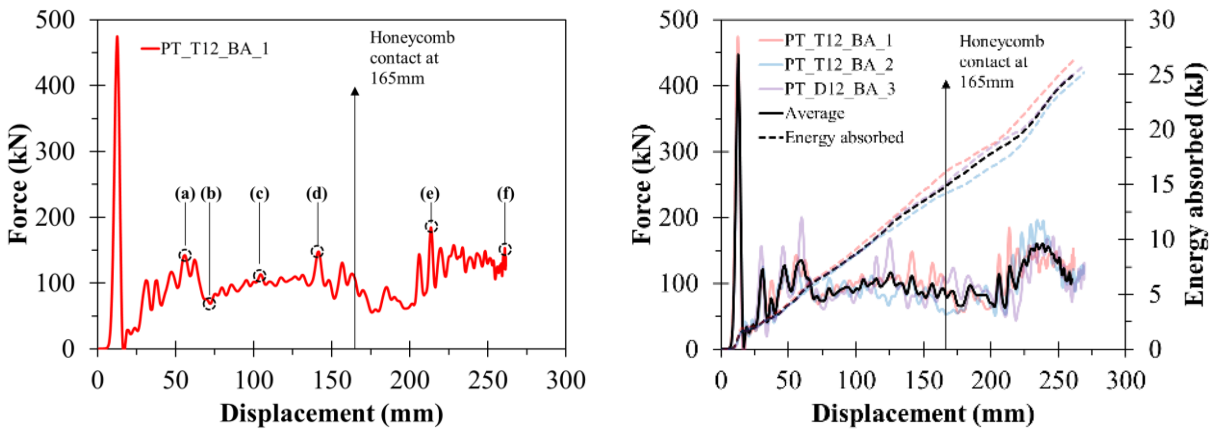

(a) TWB repeat #1 (b) TWB average

Figure 96: Force *vs.* crush displacement (F-D) plot of the TWB baseline: (a) specimen repeat #1 and (b) the average of three repeats. Labels (a) to (f) correspond to the crush displacements at which images in Figure 95 are taken.

Figure 92(b) shows the final deformed configuration of the TWB specimens next to the monolithic samples in Figure 92(a). Unlike the monolithic samples, the TWB specimens folded irregularly in the later stages of deformation after initially undergoing progressive folding. The lack of global buckling in the TWBs likely results from the shortening of the effective crush distance, as discussed by Omer *et al.* (2017b). Given the much higher strength of the Usibor® 1500-AS zone, the operative column length would reduce to that of the softer Ductibor® 1000-AS zone. As such, the likelihood of global buckling decreases, and folding becomes more prevalent. Another important difference in the TWB samples is the visual extent of cracking. In view of the localized fracture on the monolithic specimens, the TWBs showed extensive tears all around the faces, as shown in Figure 93b. The greater extent of tearing in the TWB specimens may be due to a combined loading of bending and shear during the lobe formation (hence, the term "irregular" folding). From the comparison, one could deduce that deformation mode affects fracture severity and *vice versa*.

4.1.2. Numerical Results – Baseline Specimens

Figure 97 shows high-speed video images of a baseline specimen and the corresponding numerical predictions of deformed shape at five different crush displacements. Good accord is demonstrated between the numerical and experimental results in capturing the initial folding, transition to global buckling, and final fold formation at the bottom-end (see Figure 97e). The major difference is that the experimental specimen reveals three progressive folds before the onset of global buckling, whereas the numerical prediction shows only two folds, indicating that the model predicts earlier onset of global buckling at around 150 mm crush displacement. Such a difference is likely due to the randomness of fold initiation as well as geometric defects in the specimen (*e.g.* variation in spot weld locations).

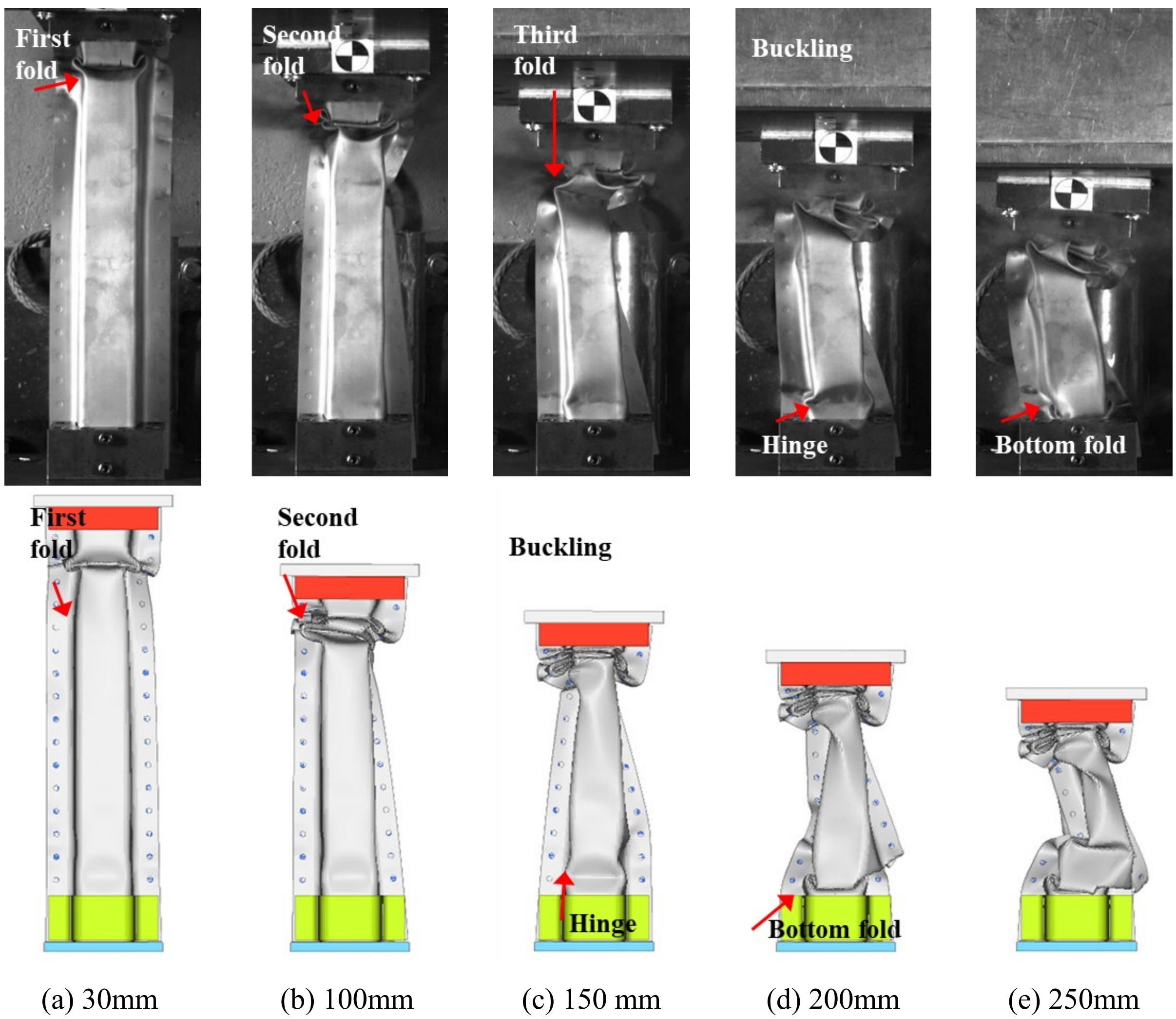

Figure 97: Observed and predicted deformation of the monolithic Ductibor® 1000-AS baseline pattern (repeat #1) at five different crush displacements from the experiment and the numerical model

Figure 98 shows the corresponding crush force *vs.* crush displacement responses from the experiments and numerical predictions for the monolithic baseline pattern. Good correlation is shown up to 140 mm crush displacement, at which point the predicted force begins to diverge due to the earlier onset of buckling. Nonetheless, the model reasonably predicts the absorbed energy at 165 mm (16.7 kJ) and 250 mm (23.2 kJ) crush displacement with 16.0 % and 4.0 % error, respectively.

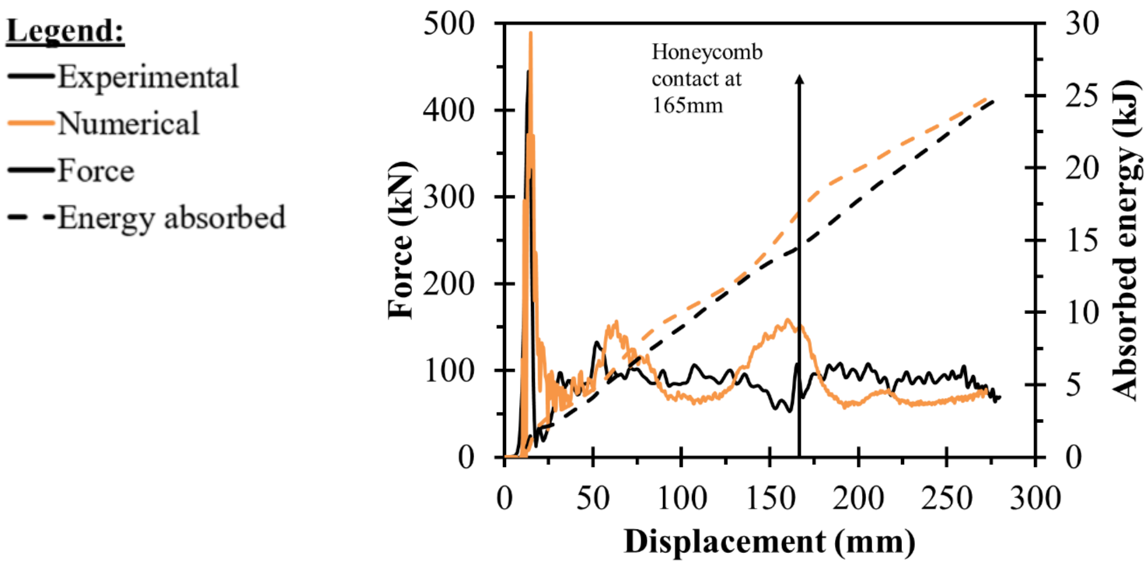

Figure 98: Comparison of the measured and predicted force and energy absorption *vs.* crush displacement (F-D and E-D) for the monolithic Ductibor® 1000-AS baseline pattern

4.2. Part 2: Effect of Fold Initiator Pattern

This section presents the experimental and numerical results from Part 2 of the test matrix, considering the effect of the fold initiator pattern on the crush response of the monolithic Ductibor® 1000-AS crush rails. Table 16 shows the test matrix for this part of the work, which considers six distinct fold initiator patterns, while schematics of the patterns are shown in Figure 40.

Table 16: Test matrix for fold initiator pattern study. Two of the fold initiator patterns, TCS and FCS, which are designed to promote the symmetric folding mode (rather than the asymmetric folding mode), were assigned a higher fold initiator spacing (35 mm) in comparison to the rest of the patterns.

Specimen Designation	Numerical (N) Experimental (E)		Dynamic (D) Quasi-Static (Q)	Thickness (mm)		Fold Initiator Spacing, 2H (mm)				
				1.2	1.6	20	25	27.5	30	35
2. Fold Initiator Pattern Study										
TCS	**N**		**D**	✓						✓
TCA	**N**	**E**	**D**	✓			✓			
FCS	**N**		**D**	✓						✓
FCA	**N**		**D**	✓			✓			
TF	**N**	**E**	**D**	✓			✓			
TFO	**N**		**D**	✓			✓			

4.2.1. Numerical Simulations of the Effect of Fold Initiator Pattern

Figure 99 shows the predicted deformed geometry from the dynamic crush models at 250 mm crush displacement. Also shown in the figure are contours of the damage variable (D) to visualize the extent of fracture. The damage variable, due to GISSMO (Neukamm *et al.*, 2009), is calculated using Equation (19) in terms of the accumulated plastic strain. The elements for which 70% or more integration points (including all the through-thickness and in-plane points) reach values of D equal to unity (coloured red in Figure 99), are considered to have fractured and are deleted. They are shown in the plots in order to visualize the extent of fracture.

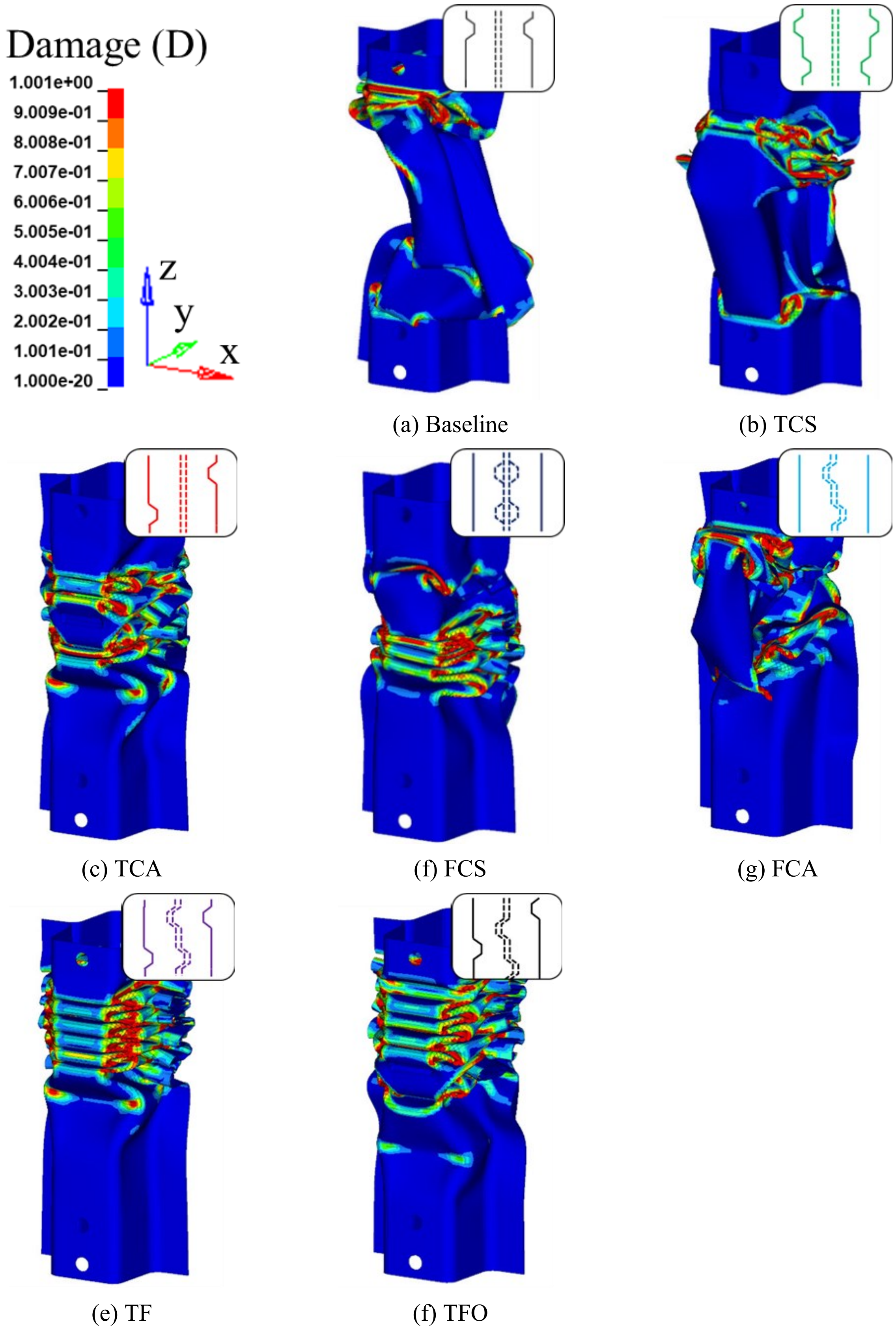

Figure 99: Contour plot of damage variable (D) at 250 mm crush distance

The numerical models of the different fold initiator patterns predicted a range of deformation modes, as seen in Figure 99. The predicted deformation modes can be categorized into four groups, listed here in increasing order of collapse stability, defined as follows:

(i) ***Global buckling*** refers to an Euler-type global buckling, in which one or two folds are often formed at the impact-end of a specimen before buckling occurs.

(ii) ***Mixed buckling and folding*** is a mixed mode response between folding and buckling. Herein, the major distinction from global buckling is defined by the short length of the buckling zone relative to the specimen length.

(iii) ***Irregular folding*** is a folding mode in which folds form successively after one another. However, the folds lack geometric uniformity or regularity.

(iv) ***Progressive folding*** refers to a folding mode in which uniform folds form successively, one after another.

Table 17 shows a summary list of fold initiator patterns, each categorized based on its deformation mode. The pictorial illustration of each pattern taken from its y-z plane cross-section (see Table 17d) is shown next to its acronym designation. Group (i) consists of the baseline and pattern TCS, which buckled in the plane of the flange as well as out of the flange plane. Group (ii) consists of pattern FCA, which buckled after making two successive folds. Pattern FCS belong to Group (iii), displaying irregular folding with some flange fold initiators remaining untriggered. Lastly, patterns TCA, TFO, and TF all showed progressive folding, although the TCA and TFO cases skipped one of the top fold initiators, displaying lower folding stability than the TF case.

Table 17: Classification of folding patterns into four groups of deformation modes and their pictorial illustrations. The solid line represents the top face edge, while the dotted line represents the flange edge when viewing at from the side.

(a) Deformation Mode	(b) Pattern (Acronym designation)	(c) Pictorial illustration	(d) The reference view at which the illustration was taken
(i) global buckling	**BA** (Baseline)	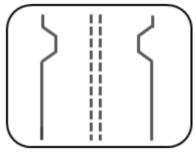	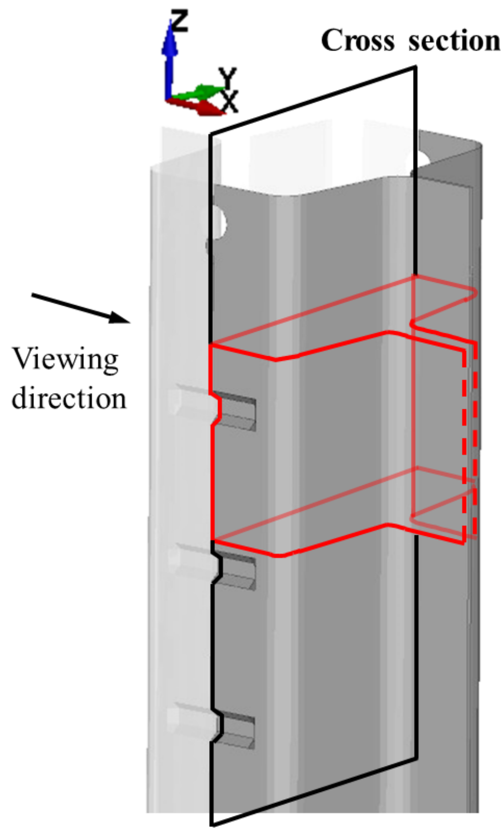 (Example: TCA)
	TCS (Top-Consecutive-Symmetric)	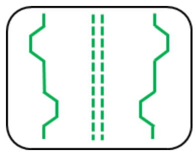	
(ii) mixed buckling and folding	**FCA** (Flange-Consecutive-Asymmetric)	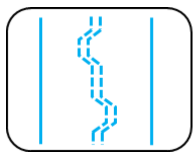	
(iii) irregular folding	**FCS** (Flange-Consecutive-Symmetric)	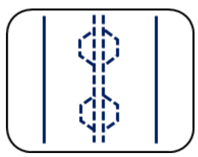	
(iv) progressive folding	**TCA** (Top-Consecutive-Asymmetric)	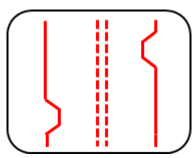	
	TF (Top-Flange)	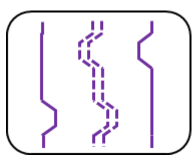	
	TFO (Top-Flange-Offset)	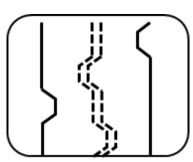	

Figure 100 shows the initial peak force for the numerical models shown in Figure 99. All patterns showed decreased peak force relative to the baseline peak force (489 kN), to varying degrees. The peak forces of those who only have fold initiators on either the flange or top face were marginally lower by a maximum 9.0% relative to the baseline. The TF and TFO patterns, on the other hand, with initiators on the flange and faces, showed a significant decrease in the peak force by 21% and 20% relative to the baseline, respectively.

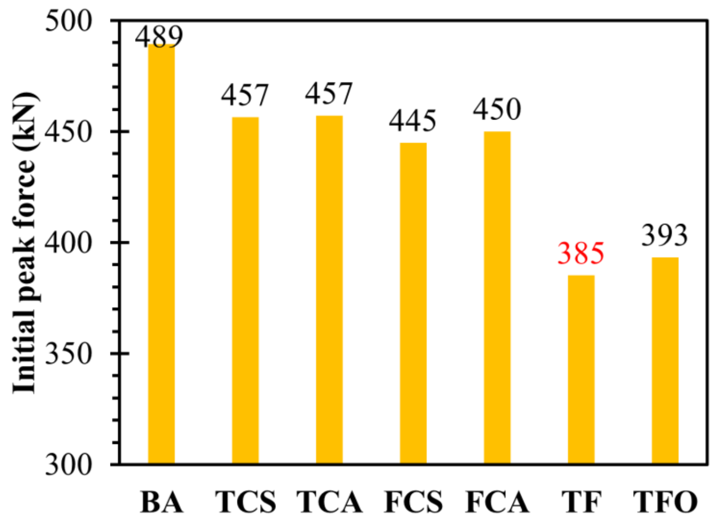

Figure 100. Bar chart showing initial peak forces for the numerical models shown in Figure 99

The predicted absorbed energy for each fold initiator pattern at 165 mm and 250 mm crush distance is shown in Figure 101. The theoretical energy obtained using the Superfolding Element Analysis (Abramowicz and Wierzbikci, 1989) in Appendix A is also shown for reference. With respect to the baseline, a marginal difference (up to 6.7%) in the absorbed energy at 165 mm crush distance is shown for all patterns. At 250 mm crush distance, all patterns showed an increase in the absorbed energy relative to the baseline pattern, with the TCA pattern showing the largest increase by 2.8 kJ (12%). The TF and TFO patterns showed an increase in the absorbed energy at 250 mm crush distance relative to the baseline by 2.1 kJ (8.8%) and 2.6 kJ (11%), respectively.

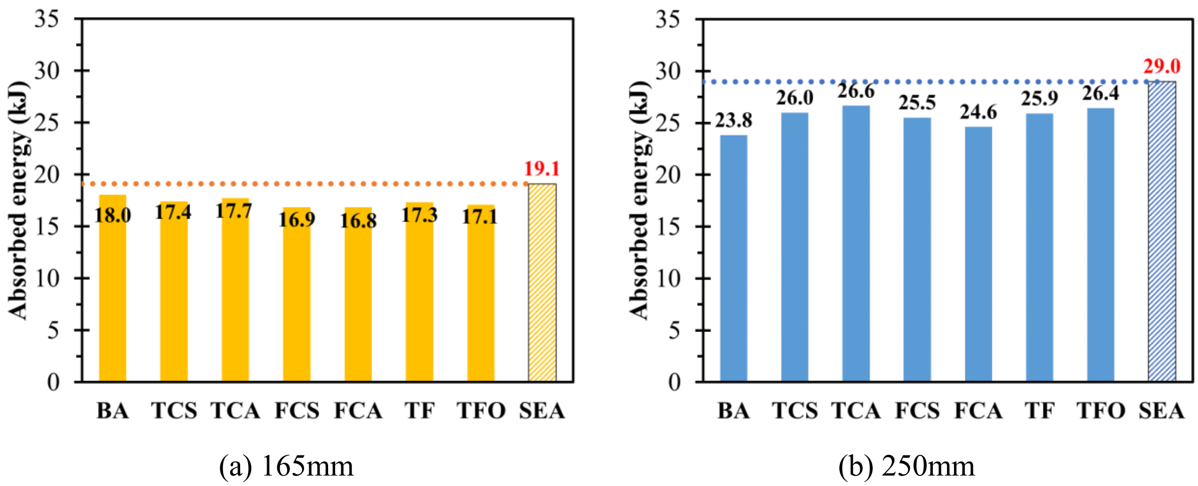

Figure 101: Bar charts showing predicted absorbed energy for all fold initiator patterns at: (a) 165mm and (b) 250mm crush distance, as well as the energy calculated using the Superfolding Element Analysis (see Appendix A for detailed solution)

To examine the extent of fracture, Figure 102 shows the predicted "eroded internal energy" at crush displacements of 165 and 250 mm. The eroded internal energy represents the internal energy associated with elements that were deleted upon meeting the GISSMO fracture criterion. Higher values of eroded energy indicate a greater extent of element deletion due to fracture; thus, eroded internal energy can be used as an indicator to predict the level of fracture in the parent metal. In Figure 102, the TCA model shows the lowest eroded energy relative to the baseline model by 0.9 kJ (60%) at 250 mm crush distance, which is indicative of a lesser extent of fracture. The TF and TFO patterns showed slightly higher eroded energy than the TCA pattern by 0.2 kJ and 0.4 kJ, respectively.

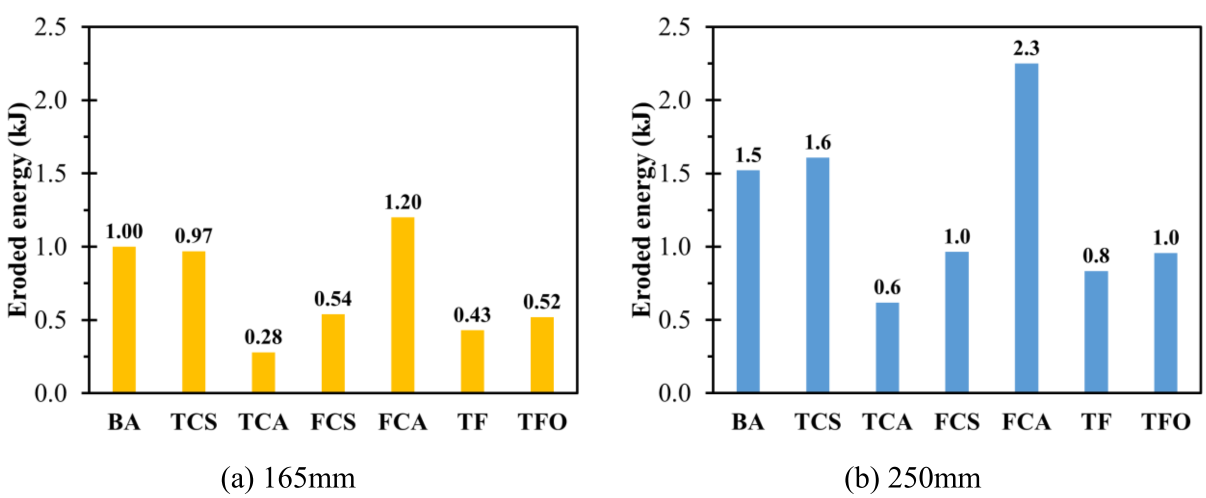

Figure 102: Bar charts showing the predicted eroded energy of the parent metal for all fold initiator patterns at: (a) 165mm and (b) 250mm crush distance

Figure 103 shows a response map in which the predicted eroded energy is plotted against the predicted absorbed energy for all fold initiator patterns. There is a clear trend that the patterns that folded progressively or irregularly show a significantly lower amount of eroded energy than those who showed mixed folding and buckling or primarily global buckling. In reference to the damage contour plot in Figure 99, the small amount of eroded energy in the patterns showing stable folding is due to the limited extent of damage, primarily within the tight radius zones (*e.g.* zones corresponding to horizontal or inclined bending zones in the SE). Interestingly, all modes show a similar level of absorbed energy at 250 mm, which suggests that the final absorbed energy is weakly dependent on the fold initiator design, for the loading cases and the material strength considered.

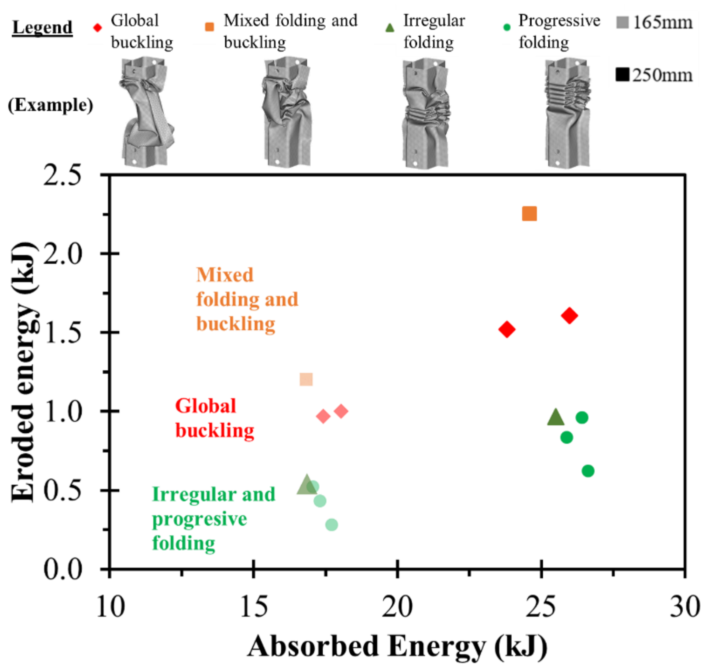

Figure 103: A response map showing effect of deformation mode on the predicted eroded energy *vs.* absorbed energy for numerical patterns at 165 mm and 250 mm crush distance. A pictorial illustration is shown as an example for each deformation mode, listed.

4.2.1.1. Effect of Fold Initiator Offset (Flange Versus Face Offset)

Figure 104 shows predicted mid-cross-section images of the deformed TF and TFO patterns at 250 mm crush distance. One major difference in the two cross-sections is that the TFO pattern results in less uniform folds than the TF pattern. Close examination of the TFO folds reveals that many of the fold initiators are facing upwards, some remaining untriggered. The other major difference is that the folds in the TFO pattern skipped the last fold initiator, located at the right bottom (see Figure 104).

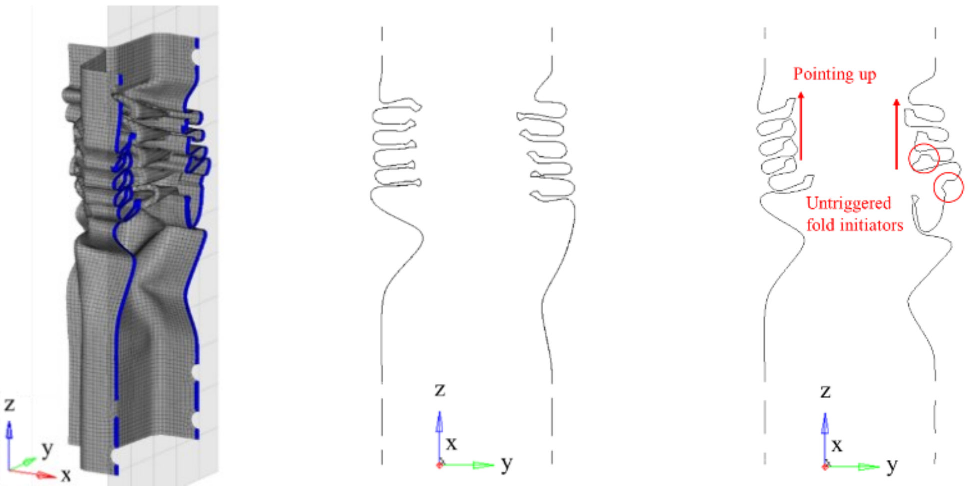

Cross-section (a) TF (b) TFO

Figure 104: Mid-cross-section (highlighted blue) images across the top face: (a) TF and (b) TFO at 250 mm crush displacement. Skipped fold initiators in the TFO pattern are circled in red.

Figure 105 shows the predicted crush force, absorbed energy, and eroded energy plotted against the crush distance for the TF and TFO patterns. In the **F-D** plot, the TF pattern generally exhibits higher peaks and lower valleys than for the TFO case, showing a more distinctive oscillation. The absorbed energy shows very little difference between the two, but the TF pattern results in a somewhat lower eroded energy than the TFO pattern, with a reduction of 0.2 kJ (17%) at 250 mm crush distance. The reduction in predicted eroded energy suggests that the offset could potentially result in more cracking.

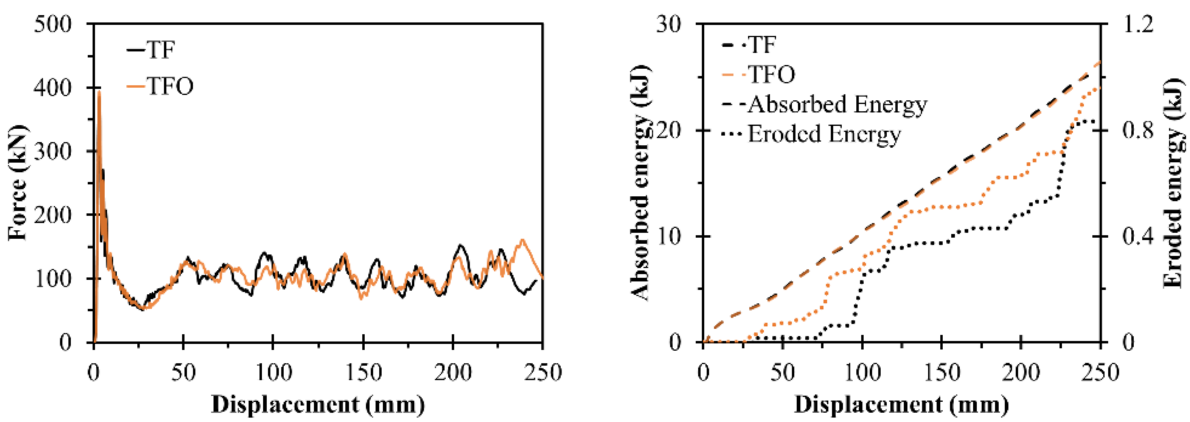

(a) Force *vs.* displacement

(b) Absrobed energy and eroded energy *vs.* displacement

Figure 105: Plots of (a) Force *vs.* crush displacement and (b) absorbed energy and eroded energy *vs.* crush displacement for the TF and TFO patterns

4.2.1.2. Folding Stability

A close look at the predicted **F-D** plot of pattern TF in Figure 106a reveals six force peaks (a) to (f) and five valleys (g) to (k) excluding the initial peak and valley, up to honeycomb contact. The crush displacement at each peak or valley corresponds to the event at which a local fold completely collapses and contacts the previously consolidated fold, as shown in the deformed images in Figure 107. Also shown in Figure 106b is the **F-D** plot of pattern FCS, which folded irregularly. Following the nomenclature introduced in the Superfolding Element Analysis (Abramowicz and Wierzbicki, 1989) in Appendix A, the distance from one peak to the next corresponds to the folding wavelength (2H).

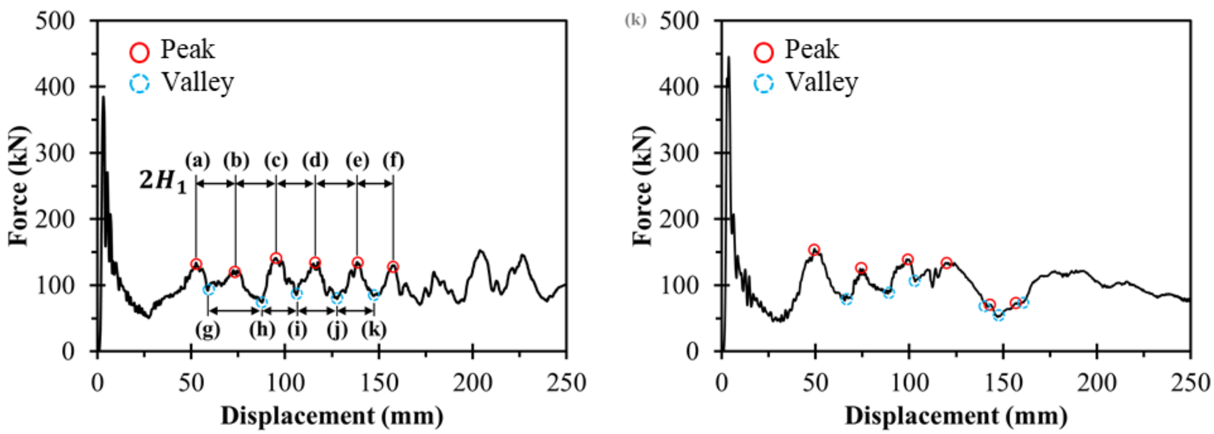

(a) TF (b) FCS

Figure 106: Predicted force *vs.* crush displacement (F-D) for the (a) TF pattern and (b) FCS pattern. Each encircled peak or valley corresponds to the crush displacement at which a collapse of a local fold is completed.

(a) 52 mm (b) 72 mm (c) 95 mm (d) 115 mm (e) 138 mm (f) 159 mm

Figure 107: Side view images of the predicted TF pattern deformation, taken at the crush displacements corresponding to each peak of the F-D plot in Figure 106.

To investigate the relationship between the degree of the folding regularity and that of the periodicity observed in the crush force-displacement (**F-D**) response, a new metric called the least squares error (L_2) is formulated as follows

$$L_2 = \sqrt{\sum_{i=2}^{n}\left[\left(2H_{indent} - 2H_{i,peak}\right)^2 + \left(2H_{indent} - 2H_{i,valley}\right)^2\right]} \quad (48)$$

$$2H_i = d_{i+1} - d_i \quad (49)$$

where $2H_{indent}$ is the fold initiator spacing, $2H_{i,peak}$ is the folding wavelength obtained from **F-D** plot by subtracting the crush distance at the i^{th} peak (d_i) from the next peak (d_{i+1}), and n is the total number of folds prior to the honeycomb contact, excluding the first fold that occurs regardless of the folding mode (the first fold occurs even in the monolithic baseline specimen that globally-buckled, as shown in Figure 97a).

A low value for L_2 (low error) would mean that the actual folding wavelengths are close to the fold initiator spacing and, thus, indicates that all fold initiators were triggered as intended. On the contrary, a high L_2 would mean that the actual folding wavelengths vary from the fold initiator spacing, likely caused by one or more untriggered initiators. Such phenomena would cause geometric irregularity of the folds, which are observed in the irregular folding or mixed folding and buckling. To demonstrate this point, Figure 108 shows L_2 errors calculated for three progressively folded patterns, as well as one irregular folded pattern using Equations (48) and (49). Remarkably, the L_2 values well reflect the folding stability observed in these patterns. For patterns that buckled, the L_2 values were not calculated.

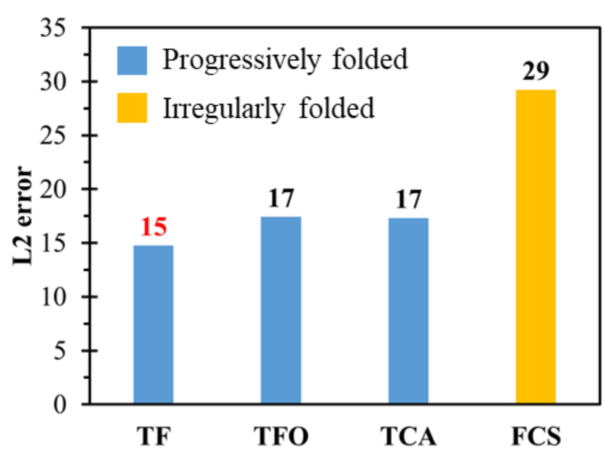

Figure 108: Comparison of L_2 error calculated using for three progressively folded patterns, as well as an irregular folded pattern.

A summary of the predicted crush performance for three progressively folded patterns (TCA, TF, TFO), along with that of the baseline pattern, is given in Table 18. Also shown in the table are the L_2 errors calculated for these patterns. The other parameters taken as indicative of the predicted performance are the final absorbed energy and eroded internal energy and initial peak force. The predicted values that indicate the best performance among the three patterns are highlighted in green. It is observed that the TCA pattern scored the best in two performance criteria, with the highest absorbed energy and lowest eroded energy at 250 mm crush distance. The TF pattern also scored the best in two performance criteria, with the lowest peak force and lowest L_2 error. From the comparison, the TCA and TF patterns were selected for experimental validation.

Table 18: Summary of crush performance for three promising numerical patterns and the baseline. The final absorbed and eroded energy of each pattern are taken at 250 mm crush distance.

Patterns	Baseline	TCA	TF	TFO
Deformation mode	global buckling	progressive folding	progressive folding	progressive folding
Absorbed energy (kJ)	23.8	26.6	25.9	26.4
Eroded energy (kJ)	2	0.6	0.8	1
Peak force (kN)	489	457	385	393
L2 error (mm)	-	17	15	17

4.2.2. Experimental Results – TCA and TF Initiator Patterns

Figure 109 shows the final deformed specimens from the repeat experiments for the TCA (c) and TF (d) patterns. Also shown in the figure are the three as-tested baseline repeat specimens (b), as well as a double hat channel section prior to testing for each pattern (a). The three specimens for the TCA and TF cases show a significant degree of variation. The TCA experiments resulted in one specimen that progressively folded and two that globally buckled. The TF specimens all underwent different modes of deformation, one progressive folding, one irregularly folding, and one exhibiting mixed folding and buckling with a severe number of spot weld failures. As discussed in the following sections, the tendency to global buckling in the experiments (that was not seen in the models presented in Section 4.2.1), can be attributed to the initial geometric distortion caused by the fold initiator indentation process (see Figure 54a). Nonetheless, the TF pattern revealed a significant improvement in the folding stability since two of the specimens underwent either progressive or irregular folding.

(a) prepared specimens prior to axial crush test

(b) BA (Baseline)

(c) TCA

(d) TF

Figure 109: Images of (a) the prepared specimens prior to axial crush test and the final deformed shapes of three different patterns after the dynamic crush test: (b) BA, (c) TCA, and (d) TF. Minimum three repeats were tested for each pattern.

The measured crush force and absorbed energy for the three patterns are plotted against the crush displacement in Figure 110, with the coloured lines representing each repeat and the black line representing the average for each pattern. For both the TCA and TF patterns, the repeat curves follow a close trend up to 100 mm crush displacement, at which point they begin to separate as the buckling or irregular folding mode overtakes the response.

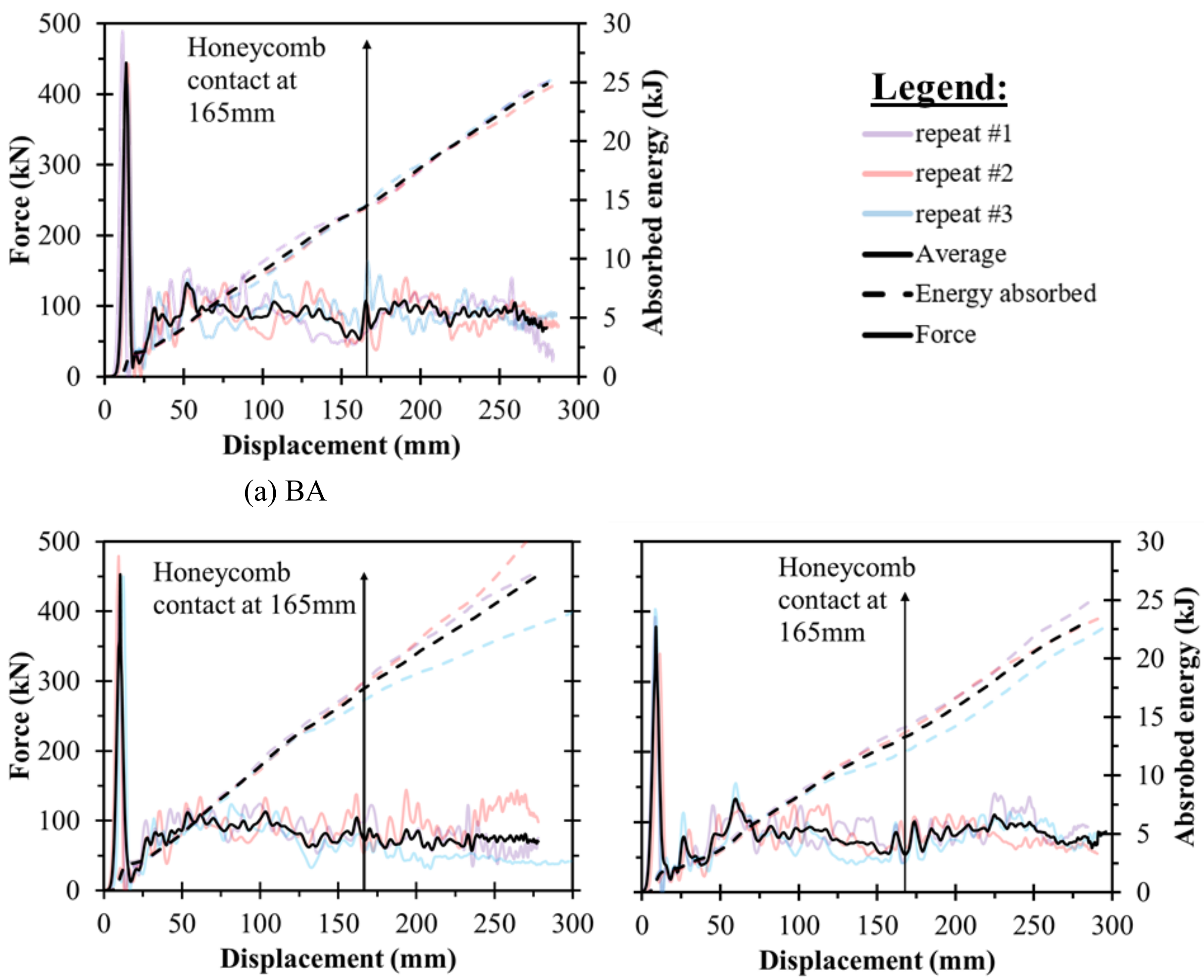

(a) BA

(b) TCA

(c) TF

Figure 110: Measured responses of force *vs.* crush displacement (F-D) and energy *vs.* crush displacement (E-D) for three patterns: (a) BA, (b) TCA and (c) TF. The average response of the repeats is highlighted black.

Figure 111 shows a chart of average peak forces for three patterns from the dynamic crush tests. The average peak force (and the standard deviation) for the TCA and TF patterns were 454 (±20) kN and 380 (±29) kN. The peak force for the TF pattern was considerably lower than the average peak force (479 kN) of the baseline pattern.

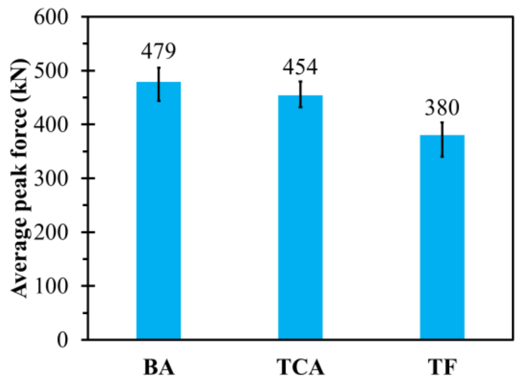

Figure 111: Bar chart showing the average peak force for three fold initiator patterns. The error bands represent the scatter in the measured data (*i.e.* min/max)

The average absorbed energy for each pattern at 165 mm and 250 mm crush distance is shown in Figure 112. The theoretical energy obtained by the Superfolding Element Analysis (Abramowicz and Wierzbicki, 1989) in Appendix A is shown as a dotted line. At 165 mm crush distance, the average absorbed energy of TCA and TF are 14.4 (±0.4) kJ and 13.1 (±0.6) kJ, which are 0.3 kJ and 1.6 kJ less than the baseline. At 250 mm crush distance, the average absorbed energy of TCA and TF are 20.7 (±0.6) kJ and 20.6 (±0.9) kJ, or 5.5 and 5.9% less than the baseline, respectively. The decrease in the absorbed energy in the TCA and TF patterns may be due to the fold initiators, which decrease the plastic work required for hinge line formation. In addition to the size or depth of fold initiators, which were shown to affect the absorbed energy (Lee *et al.,* 1999), the preceding results show that the total number of fold initiators could slightly alter the final absorbed energy in axial crush. In view of the Superfolding element theory (Abramowicz and Wierzbicki, 1989), the indented fold initiator imposes a curved surface at the horizontal hinge line location, which otherwise would be flat. Such geometric change in the SE could be viewed as an increase in the starting crush angle ($i.e.\ \alpha_o > 0$). If one assumes that the final angle of the SE remains the same, the range of total crush angle will decrease, resulting in the lower crush energy.

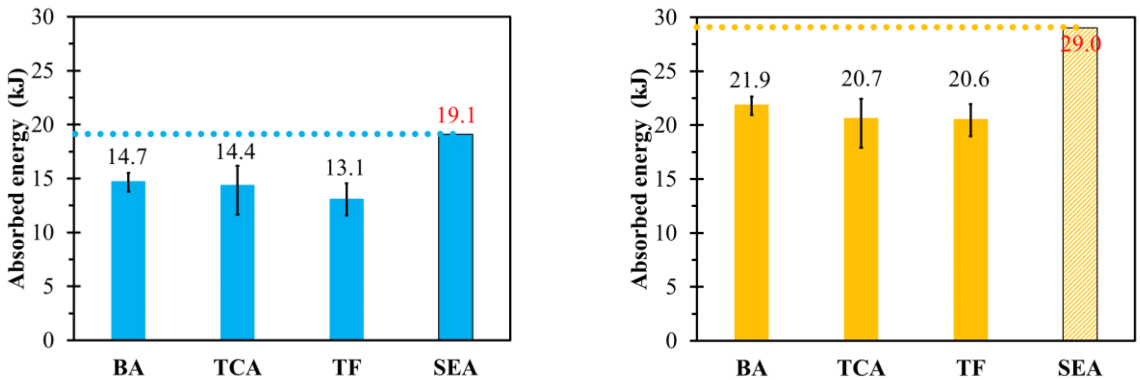

(a) Absorbed energy at 165 mm (b) Absorbed energy at 250 mm

Figure 112: Absorbed energy for three fold initiator patterns at (a) 165 mm and (b) 250 mm crush distance. The error bands represent the scatter in the measured data. SEA refers to the theoretical energy by the SE Analysis (Abramowicz and Wierzbicki, 1989) from Appendix A.

To further understand the unstable buckling onset observed in these specimens, the following sections more closely examine the repeat cases of global buckling and mixed folding / buckling in the TCA and TF patterns, respectively.

4.2.2.1. Assessment of Unstable Mode in Pattern TCA

Figure 113 shows high-speed images taken from the dynamic test of a TCA specimen (repeat #2) that globally buckled. The force *vs.* crush displacement curve for this case is shown in Figure 114. At 7 mm crush distance (a), the crush force reaches its initial peak and an irregular wrinkle appears on the left flange and sidewall. The flange wrinkle evolves to a fold at a crush distance of 30 mm (b) and causes the flange to draw towards the center. In contrast, the right flange remains relatively undeformed, promoting instability which becomes more evident at a crush distance of 63 mm (c). The instability leads to "skipping" of the subsequent fold initiators, and the bottom fold initiator is activated instead. The bottom fold acts like a pinned-end joint, and global buckling ensues in crush distances (e) and (f).

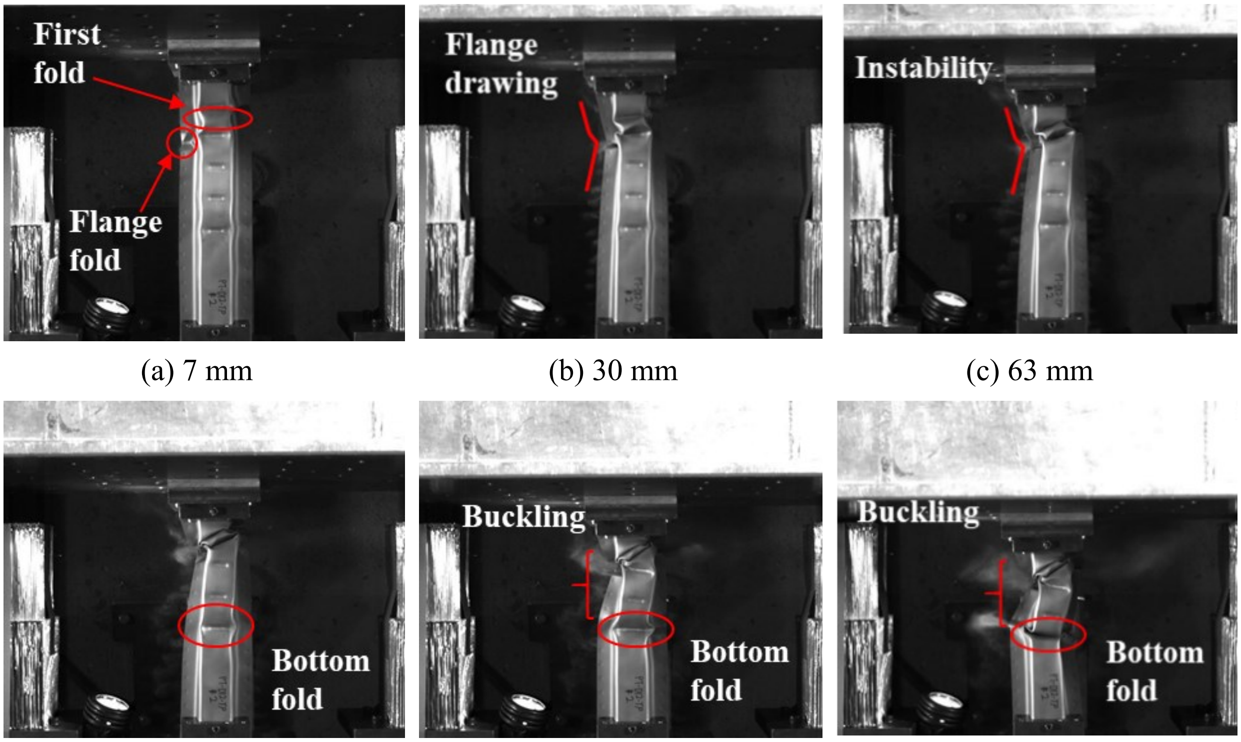

(a) 7 mm (b) 30 mm (c) 63 mm

(d) 97 mm (e) 118 m (f) 135mm

Figure 113: High-speed images of a TCA specimen (repeat #2) from the top view, which globally buckled. The crush distances (a) to (g) correspond to the local force peaks labelled in Figure 114.

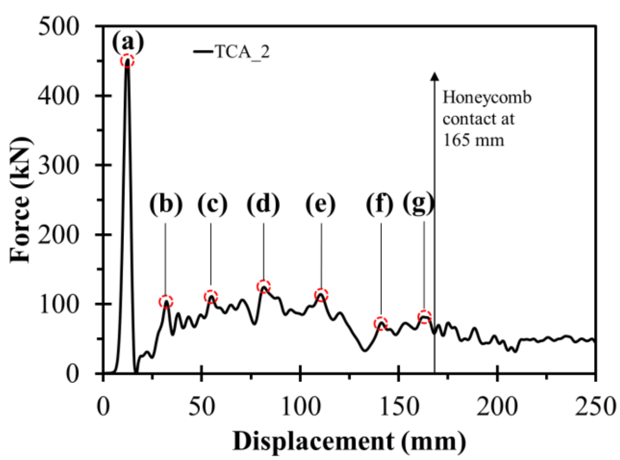

Figure 114: Force *vs.* crush displacement plot of a TCA specimen (repeat #2), which globally buckled.

Note that the absence of flange fold initiators in the TCA pattern likely resulted in the irregular wrinkling phenomenon, which highlights the potential stability gain by adding the flange initiators.

4.2.2.2. Assessment of Unstable Mode in Pattern TF

Figure 115 shows the high-speed images of a TF specimen (repeat #3) that exhibited mixed folding and buckling. Images (a) to (f) correspond to the crush distances at the local force peaks (circled) in the **F-D** plot of Figure 116. In comparison to the previous TCA specimen (repeat #2) that globally buckled, the 3rd repeat of TF pattern exhibits a more pronounced concave shape at a crush displacement of 60 mm (b). As the next fold forms, the left flange fold initiators are skipped, and irregular folding can be seen at a crush displacement of 84 mm (c). The irregular folding is followed by an extensive unzipping failure of the spot welds on the left flange at (e).

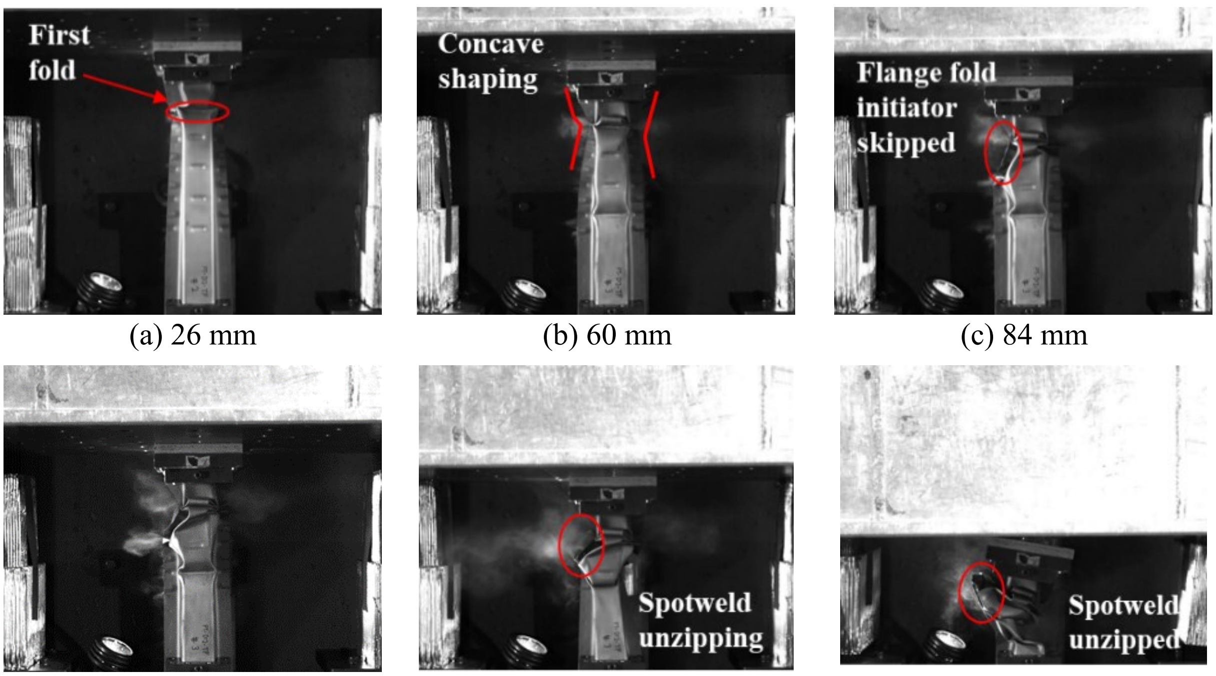

(a) 26 mm (b) 60 mm (c) 84 mm

(d) 104 mm (e) 161 mm (f) 250 mm

Figure 115: Still images of a TF specimen (repeat #3), which showed mixed folding and buckling. The crush distances (a) to (f) corresponds to the local peak forces labelled in Figure 116.

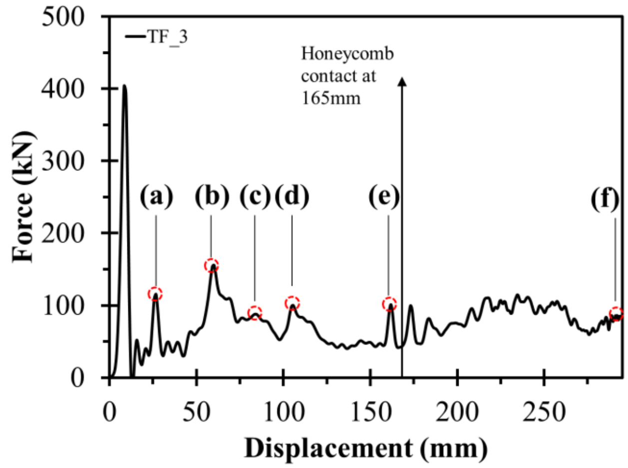

Figure 116: Force *vs.* crush displacement plot of TF specimen #3, which showed mixed folding and buckling.

To summarize, the observed crush responses of both the TCA and TF patterns showed a wide variation in their folding modes. However, despite the buckling tendency in the TF pattern (attributed to the distortion resulting from the flange indentation process), its repeat cases showed a progressive or irregular folding mode rather than the global buckling mode, that was exhibited by Pattern TCA. These experimental results point to the significance of an improved fold initiator pattern in controlling the deformation mode in axial crush columns. Furthermore, the improvement in the folding stability was shown by adding the flange fold initiators. For this reason, Pattern TF was selected for the subsequent study that centers around the effect of fold initiator spacing.

4.3. Part 3: Effect of Fold Initiator Spacing

The objective of Part 3 of the experiments is to investigate the effect of fold initiator spacing $(2H_{indent})$ on crush stability, both in terms of promoting regular, stable folding and avoidance of fracture. This study was undertaken in a parametric fashion in which the fold initiator spacing $(2H_{indent})$ was varied from 20 mm to 35 mm, as shown in Table 19. The specimens all share the TF fold initiator pattern that was demonstrated to provide the most stable folding behavior in Part 2. A key focus was to compare the folding wavelength (2H) predicted by the Superfolding Analysis due to Abramowicz and Wierzbicki (1983) to the most optimal spacing found in the numerical and experimental parametric studies. By following the solution procedure in Appendix A, the predicted folding wavelengths for the 1.2 mm and 1.6 mm thick double hat channels are 27.5 mm and 30 mm, respectively, so the ranges of initiator spacing outlined in Table 19 bracket these two values. Note also that the 25 mm spacing for the 1.2 mm hat section was already tested in Part 2 of this study.

Table 19: Test matrix for Part 3. The visual illustrations of specimens listed here are shown in Figure 44. Also, all specimens have a length of 375 mm.

Specimen Designation	Numerical N)	Experimental (E)	Dynamic (D) Quasi-Static (Q)	Thickness (mm)		Fold Initiator Spacing, 2H (mm)				
				1.2	1.6	20	25	27.5	30	35
3. Fold Initiator Spacing Study										
SP-D12-200	**N**	**E**	**Q**	✓		✓				
SP-D12-275	**N**	**E**	**Q**	✓				✓		
SP-D12-350	**N**	**E**	**Q**	✓						✓
SP-D16-200	**N**	**E**	**Q**		✓	✓				
SP-D16-250	**N**	**E**	**Q**		✓		✓			
SP-D16-300	**N**	**E**	**Q**		✓				✓	
SP-D16-350	**N**	**E**	**Q**		✓					✓

In view of the tendency towards global buckling observed in Part 2, hat sections with 1.6 mm thickness were considered, in addition to the 1.2 mm thickness examined in Part 2. For the same reason, the length of the specimens was reduced to 375 mm from 500 mm. This set of experiments was performed under quasi-static loading to eliminate dynamic effects (*e.g.* high-frequency oscillations) in the load-displacement measurements and to remove the effect of Al-Si dust ejected from the hot stamped specimens, which obscures imaging of the folding behavior.

4.3.1. Experimental Results – Effect of Initiator Spacing

4.3.1.1. 1.2mm Specimens

The as-tested shapes of the 1.2 mm thick specimens for three initiator spacings, 20 mm 27.5 mm, and 35 mm, are shown in Figure 117. All three specimens exhibited global buckling from the very early stage of axial crush. Furthermore, all fold initiators remained untriggered, with the exception of the first top fold initiator.

These results further demonstrate the effect of the flanges distortion, as seen in the dynamic TF specimen (repeat #3 in Figure 115). During the quasi-static experiments, the flanges rapidly drew into a concave shape promoting buckling (the quasi-static images are omitted here for brevity).

(a) 20 mm (SP-D12-200)	(b) 27.5 mm (SP-D12-275)	(c) 35 mm (SP-D12-350)

Figure 117: Final deformed shapes of 1.2mm specimens for the fold initiator spacing study. The SP-D12-200 specimen test was stopped at the early testing stage due to excessive out-of-plane buckling.

4.3.1.2. 1.6mm Specimens

The final deformed shapes of the complete set of crushed 1.6 mm thick specimens are shown in Figure 118. The corresponding measured force-displacement (**F-D**), and the energy absorption *versus* crush displacement (**E-D**) data are shown in Figure 119. The images reveal that the specimens with an initiator spacing equal to the SE analytical folding wavelength (30 mm) exhibit the most uniform final folding pattern. In the force-displacement curves, the folding uniformity is manifested by repeating load oscillation between consistent peaks and valleys. The specimens with 20 mm and 35 mm spacing, which differ the most from the Superfolding Element analysis spacing of 30 mm, show irregular folds and, in some cases, incipient mixed folding and buckling. The 25 mm spacing specimens show regular fold formation, but with inclination of what should ideally be horizontal folds (b), relative to that seen for the 30 mm folds (c), for example.

(a) 20 mm (SP-D16-200)

(b) 25 mm (SP-D16-250)

(c) 30 mm (SP-D16-300)

(d) 35 mm (SP-D16-350)

Figure 118: Final deformed images of the 1.6mm thick TF specimens with four different fold initiator spacings ($2H_{indent}$) ranging from (a) 20 mm to (d) 35 mm. The analytical folding wavelength ($2H$) obtained from the SE solution is 30 mm (see Appendix A), which corresponds to the most uniform folding in the specimens.

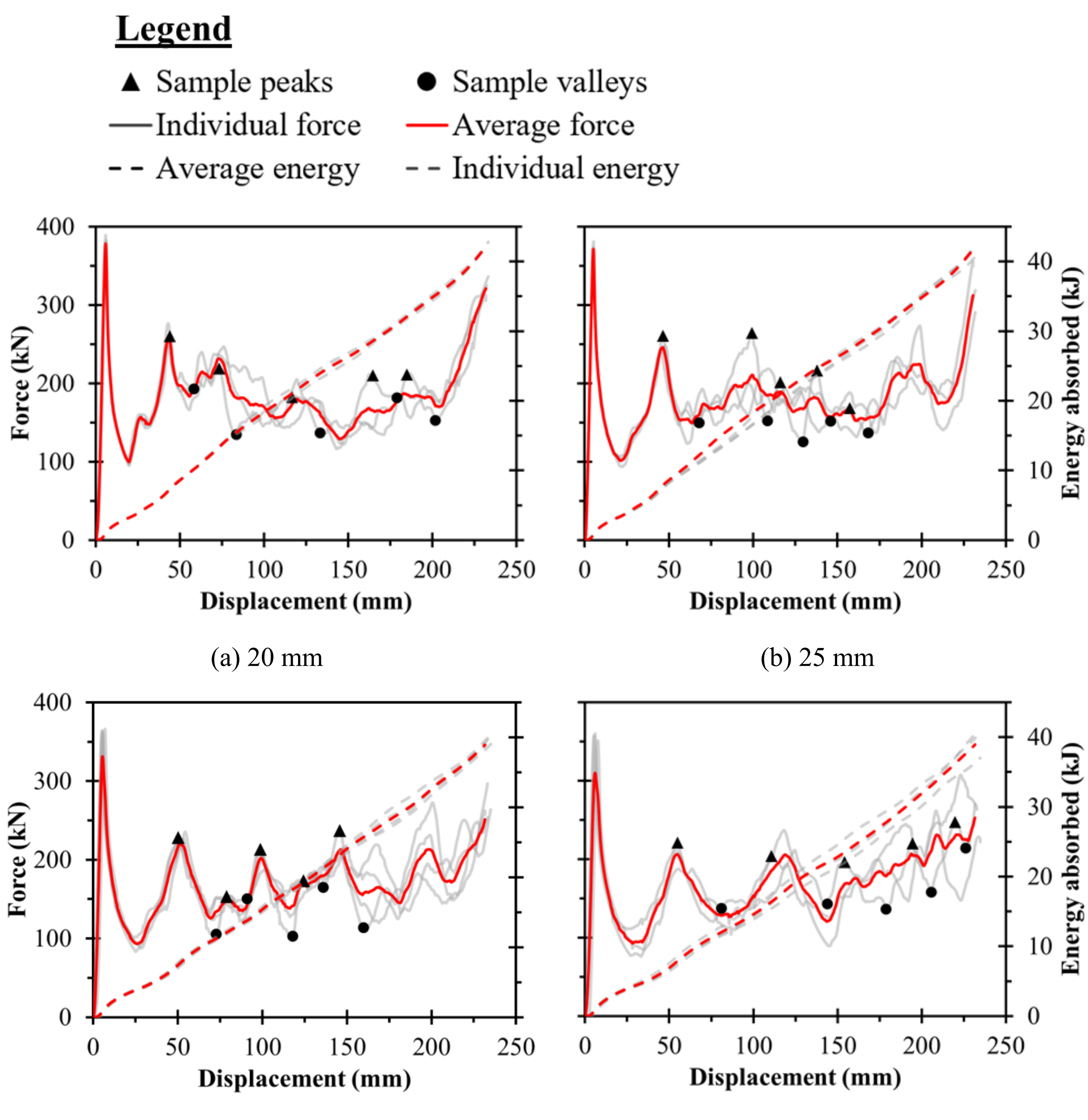

(a) 20 mm (b) 25 mm

(c) 30 mm (d) 35 mm

Figure 119: Force and absorbed energy *vs.* crush displacement for the 1.6mm TF crush specimens at four different initiator spacings: (a) 20 mm, (b) 25 mm, (c) 30 mm and (d) 35 mm. The force peaks and valleys (symbols) are labelled for one sample for each initiator spacing to illustrate the crush displacements used to calculate the L_2 error using Equations (48) and (49).

Figure 120 serves to compare the measured (average) absorbed energy *vs.* crush displacement for each fold initiator spacing. The difference in absorbed energy is relatively small (with a maximum of difference 7.5 % at 230 mm crush distance), despite the significant differences in folding uniformity. The ranking based on the average absorbed energy from the highest to the lowest is as follows: 20 mm, 25 mm, 30 mm, and 35 mm. It is interesting that the ranking does not correlate to types of deformation modes but rather strictly to the spacing values. One possible explanation is due to the variations in the consolidation crush distance, the point at which the crush force substantially increases in the **F-D** plot, although this ranking still holds for crush distances below the point of final consolidation. From Figure 119, the measured average consolidation distances for the four configurations are 205 mm, 215 mm, and 225 mm for the 20 mm, 25 mm and 30 mm spacing specimens, respectively. The specimens with 35 mm spacing did not reach the full consolidation point over the tested crush distance of 230 mm. A specimen with shorter consolidation distance would result in a higher absorbed energy onward from that point due to the subsequent increase in crush force.

The measured average peak forces of the four configurations are 384 (±4.1) kN, 375 (±3.8) kN, 365 (±1.3) kN, 355 (±2.6) kN for the four initiator spacings, ranging from 20 mm to 35 mm. The ranking of the measured peak forces also shows a strong correlation to the spacing.

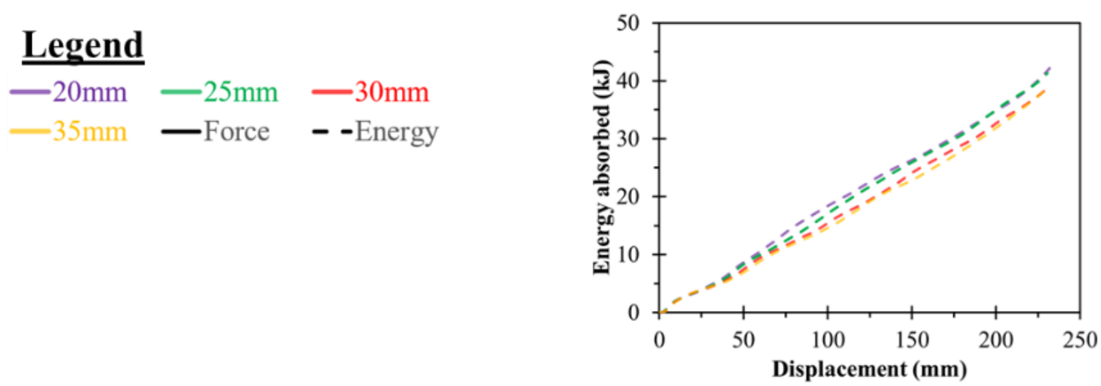

Figure 120: The average measured absorbed energy plotted against the crush displacement for 1.6mm thick TF specimens of four different fold initiator spacings

The visual extent of cracking in the 1.6 mm samples is shown in Figure 121 and Figure 122, which are taken from a side view and top view of as-tested specimens for each spacing (20 mm to 35 mm). In the 25 mm and 30 mm specimens, cracks are only observed on the sidewalls, as highlighted in the figure. In the 20 mm specimens, the cracks are rather randomly distributed and appear on the sharp radii of the irregular folds. Lastly, the 35 mm specimens did not show visible indications of fracture.

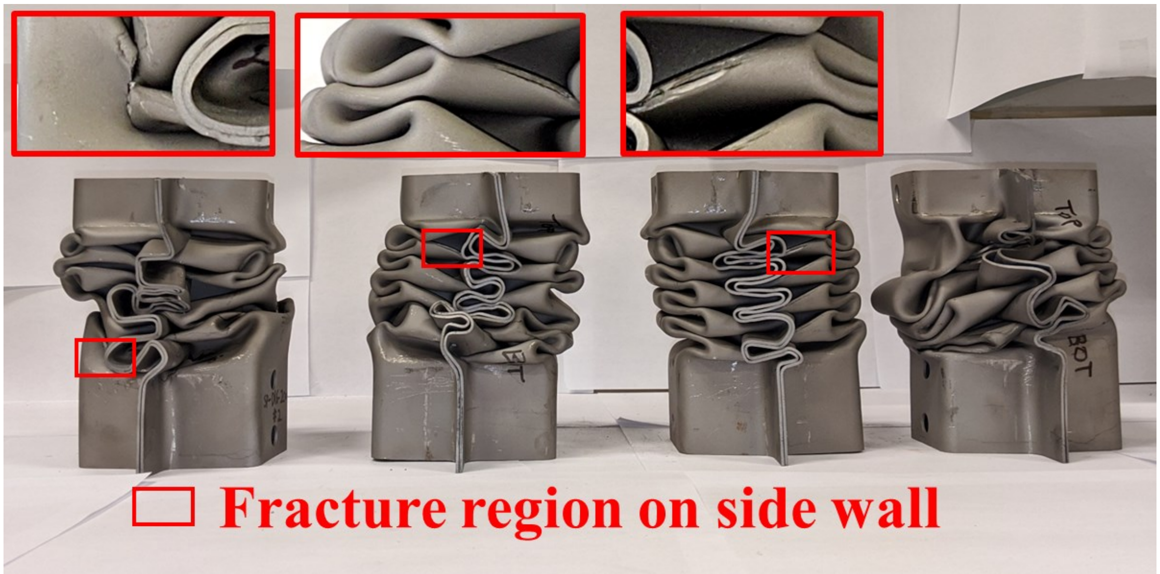

(a) 20mm (SP-D16-200) | (b) 25mm (SP-D16-250) | (c) 30mm (SP-D16-300) | (d) 35mm (SP-D16-350)

Figure 121: Side view images of final deformed 1.6mm specimens with four different fold initiator spacing—(a) 20 mm, (b) 25 mm, (c) 30 mm and (d) 35 mm. Red zones indicate major fracture regions

(a) 20mm (SP-D16-200) | (b) 25mm (SP-D16-250) | (c) 30mm (SP-D16-300) | (d) 35mm (SP-D16-350)

Figure 122: Front view images of final deformed 1.6mm specimens with four different fold initiator spacing—(a) 20 mm, (b) 25 mm, (c) 30 mm and (d) 35 mm. Red zones indicate regions of fracture.

4.3.2. Numerical Results – Simulations of Effect of Initiator Spacing

In this section, the quasi-static axial crush model predictions for the specimens in Part 3 of the experimental program are presented. These models consider both the 1.2 mm and 1.6 mm TF pattern with a column length of 375 mm. Fold initiator spacings in the range from 20 mm to 35 mm were considered (see Figure 44 for visual illustration).

4.3.2.1. Numerical Predictions for 1.2mm Specimens

Predictions of the folding progression for the 1.2 mm axial crush rails are in Figure 123. These images reveal that the 20 mm model irregularly folded while the 27.5 mm and 35 mm models progressively folded. Furthermore, the irregular folding mode in the 20 mm model is accompanied by the skipping of both top and flange fold initiators. For the 27.5 mm and 35 mm models, all fold initiators were triggered, but their folding sequences differ from the experimental responses. Specifically, the folding sequence of the 27.5 mm model from the first to last followed the 3rd fold initiator, bottom un-indented zone, 2nd and 1st fold initiators, while that of 35 mm model followed the 2nd, 1st, and 3rd fold initiators.

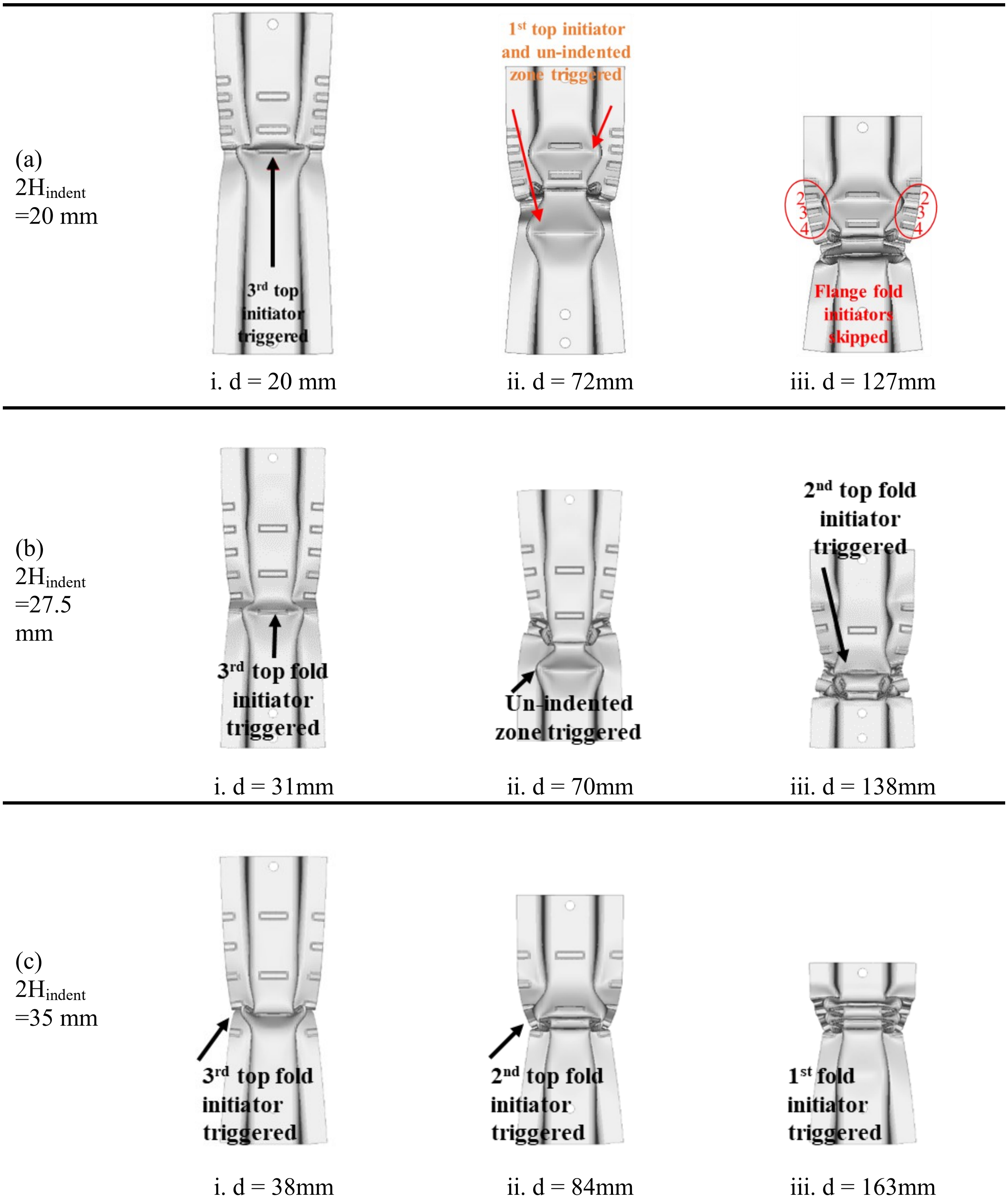

Figure 123: Still images taken from the quasi-static crush models of 1.2mm thick TF specimens, with fold initiator spacing ranging from (a) 20 mm to (c) 35 mm.

A comparison of the predicted and observed deformed shapes of the 1.2 mm axial crush rails at 230 mm crush distance are shown in Figure 124. It is evident from the figure that none of the models were able to predict the onset of global buckling that was evident in the experiments. Instead, the model predicted either irregularly folding, as with the 20 mm spacing, or progressively folding in the 27.5 mm and 35 mm spacing cases. Further examination of the causes of this discrepancy is provided in Section 4.4.

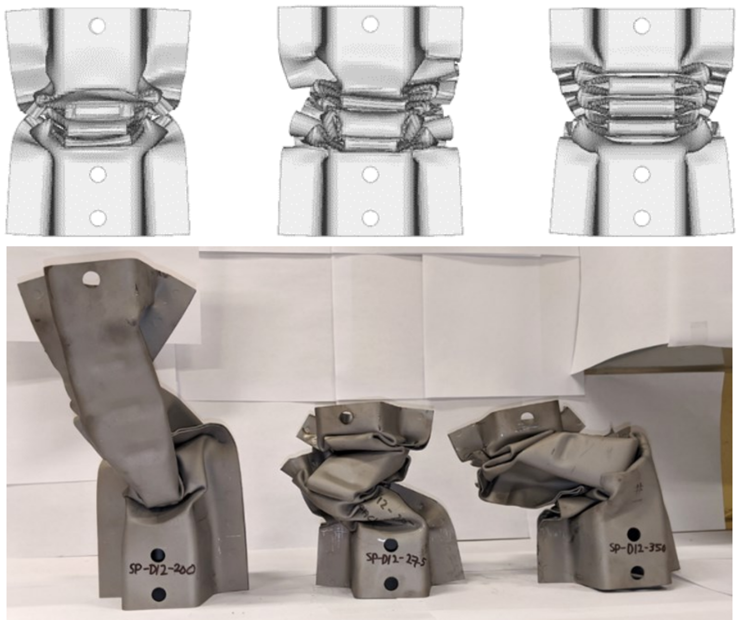

(a) 20 mm (SP-D12-200) (b) 27.5 mm (SP-D12-275) (c) 35 mm (SP-D12-350)

Figure 124: Predicted and actual deformed images at 230 mm crush displacement for the 1.2 mm axial crush specimens in Part 3 for the three different fold initiator spacings. Note that the experiment in (a) was interrupted prior to 230 mm crush displacement due to excessive lateral displacement.

4.3.2.2. Numerical Predictions for 1.6mm Specimens

Predictions of the folding progression for the 1.6 mm axial crush rails are in the Figure 125. These images reveal that the 20 mm model irregularly folded, while the rest of the models progressively folded, as observed in the experiment. Furthermore, the irregular folding mode in the 20 mm model is accompanied by the skipping of both top and flange fold initiators. As for the ranking of fold uniformity, 30 mm model showed the most uniform cases, followed by 25 mm and 35 mm models, as observed in the experiments.

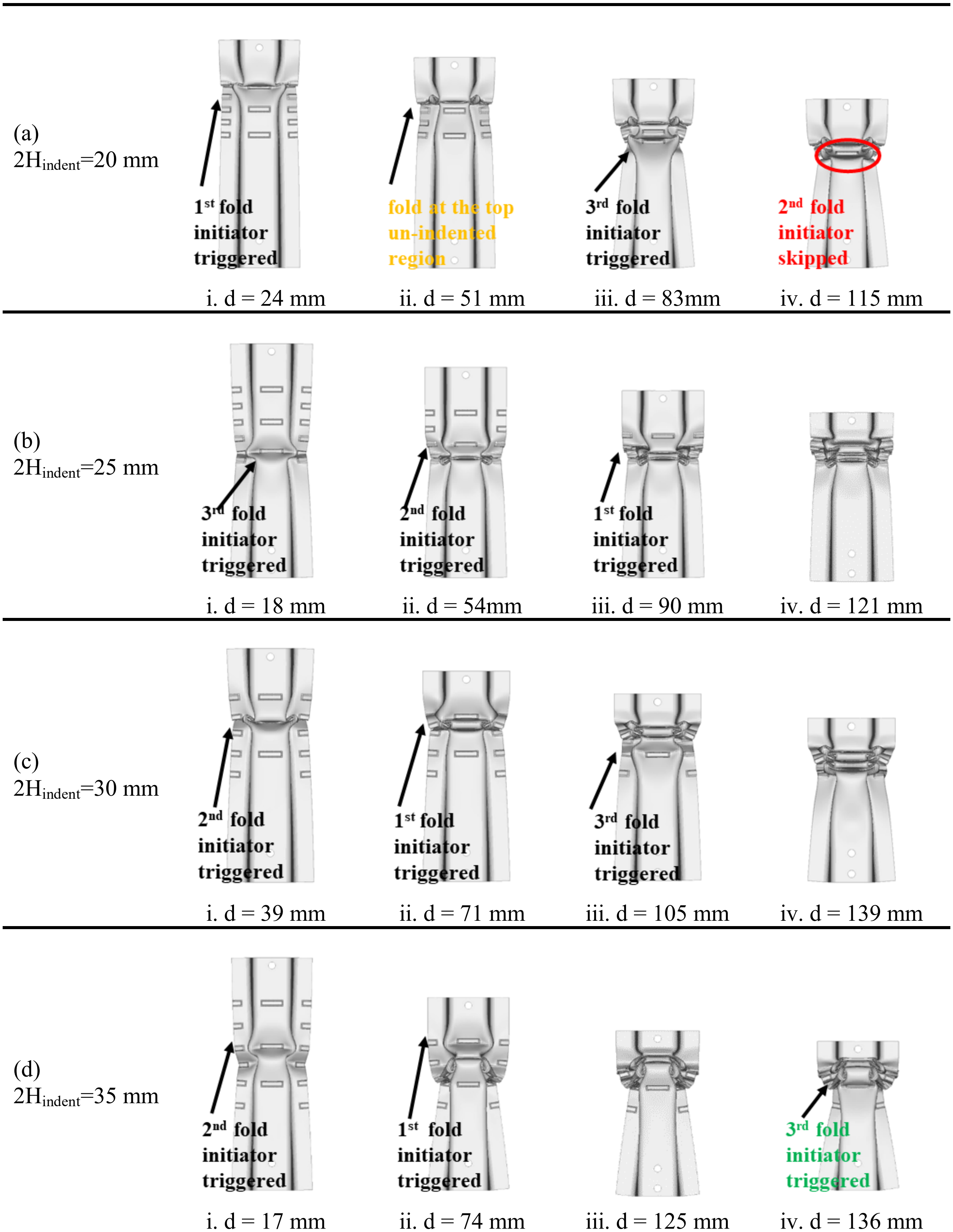

Figure 125: Still images taken from the quasi-static crush models of 1.6mm thick TF specimens, with fold initiator spacing ranging from (a) 20 mm to (d) 35 mm.

The final deformed images of the 1.6 mm axial crush models and experiments at 230 mm crush distance are shown in Figure 126. Overall, the predicted results for initiator spacings show good agreement with the crushed test specimens, except for the 20 mm model that shows more uniform folds than the as-tested specimens. This observation is evidenced by a strong symmetry between the left and right flange that is not seen in the as-tested rails.

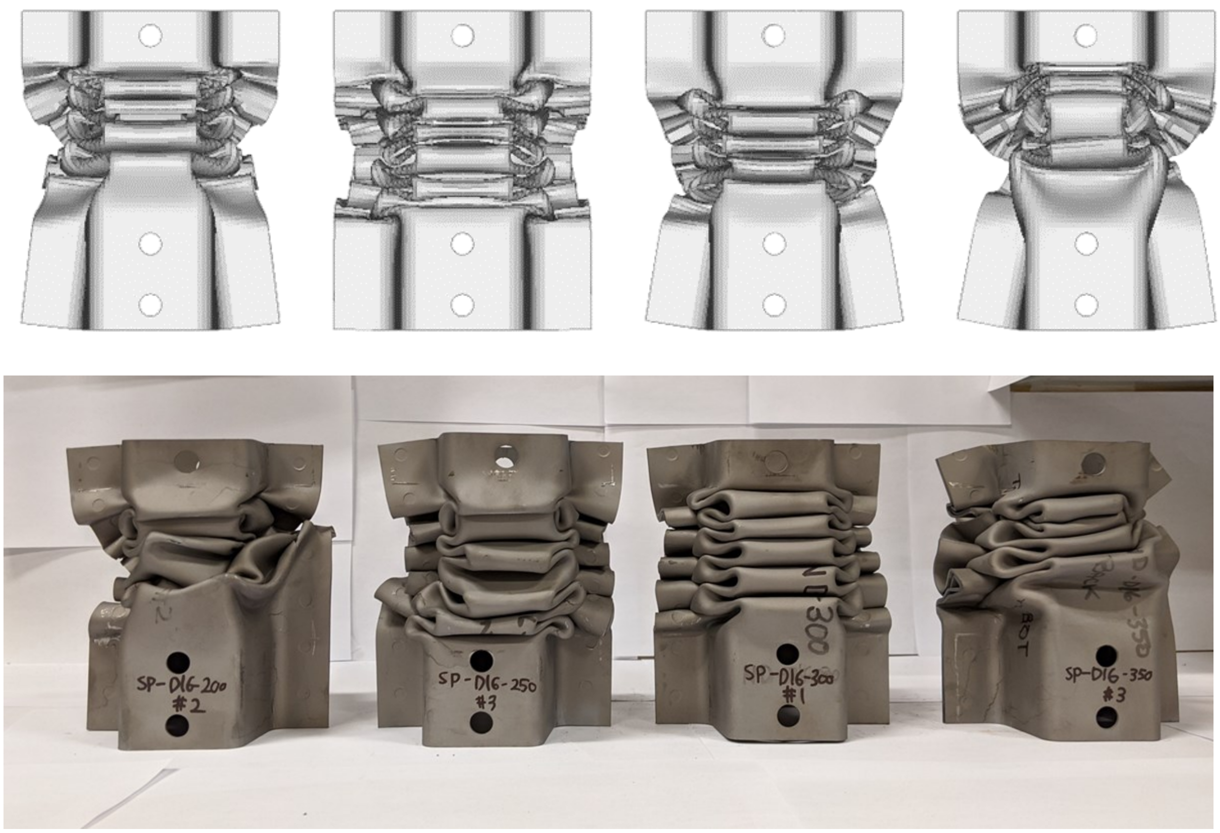

(a) 20mm (b) 25mm (c) 30mm (d) 35mm

Figure 126: Deformed images of the numerical models of 1.6 mm rails at 230 mm crush distance—each at different spacing ranging from (a) 20mm to (d) 35mm.

The predicted crush force and absorbed energy response for each 1.6 mm quasi-static crush model with different spacing are plotted against the crush displacement, as shown in Figure 127. For comparison, the measured average force and absorbed energy responses of the experimental counterparts from are also plotted in the figure. The force peaks and valleys whose corresponding crush displacements were selected for calculation of the L_2 error prediction are labeled as triangular or circular markers.

Overall, the predicted force and energy *vs.* displacement show good agreement with the measured results, except for the 20 mm spacing configuration. This was likely caused by the asymmetry of the folds in the 20 mm specimens that the model was not able to predict.

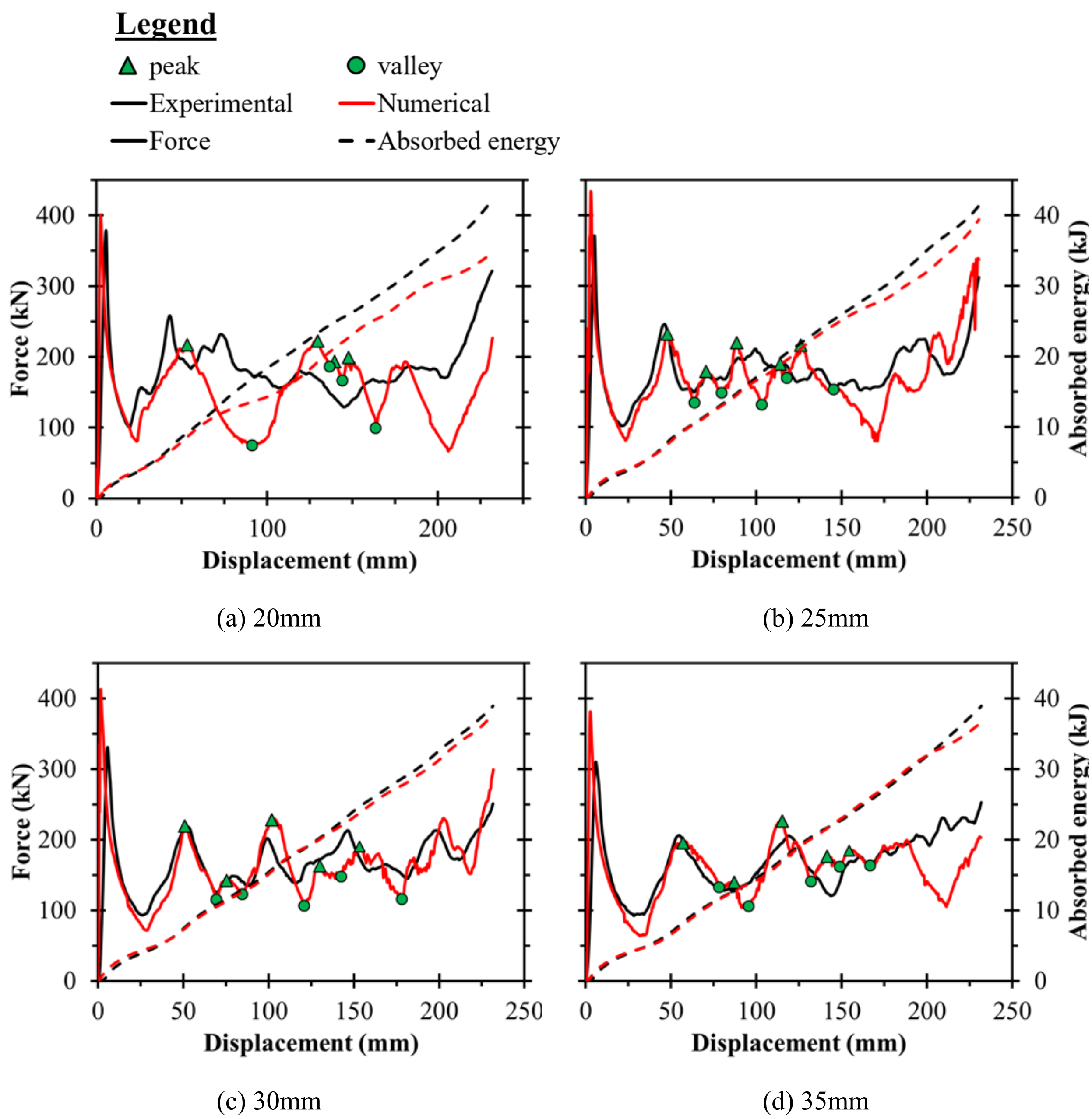

Figure 127: Force and absorbed energy *vs.* crush displacement for the 1.6 mm TF crush models (red lines) at four different initiator spacings: (a) 20 mm, (b) 25 mm, (c) 30 mm and (d) 35 mm. The measured (average) force and absorbed energy responses are overlaid as comparison (black lines). The force peaks and valleys (symbols) in the numerical responses are labelled, whose crush displacements were used to calculate the L_2 error using Equations (48) and(49).

The trends for folding uniformity in the 1.6 mm models and the experiments are examined in terms of the L_2 errors, as shown in Figure 128. The general trend in the L_2 error with respect to the fold initiator spacing is remarkably reflective of the visual trend in the fold uniformity of the model prediction and experimental responses. The uniformity of the folds in both the models and experiments can be ranked in order from the most uniform to the last uniform as 30 mm, 25 mm, 35 mm, 20 mm which corresponds directly to the ranking of the L_2 error from the lowest to the highest.

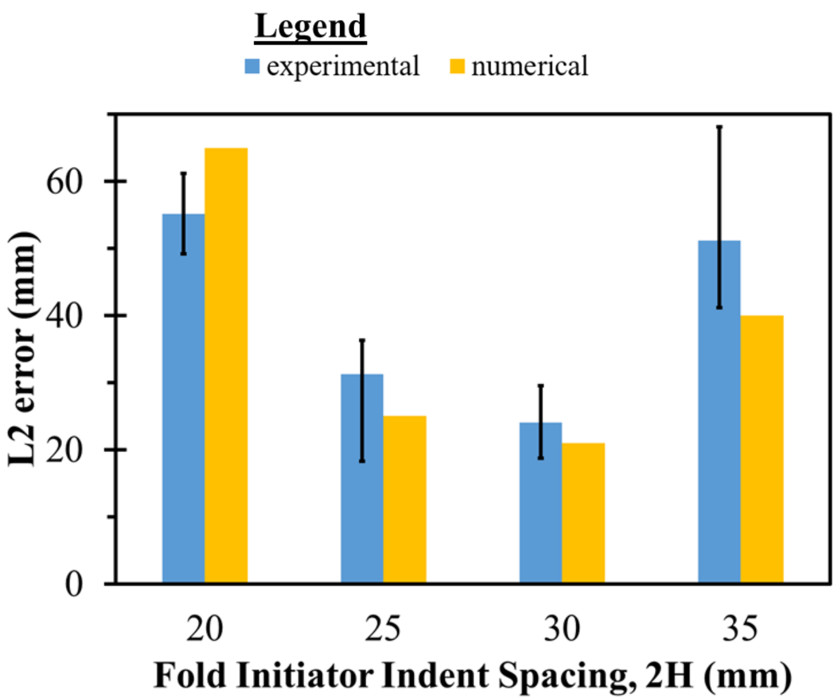

Figure 128: L_2 errors for 1.6 mm rails of Part 3. Both numerical (yellow) and experimental (blue) results are shown here.

4.4. Investigation of the Unstable 1.2 mm TF Cases

The previous section demonstrated a significant effect of the fold initiator design and the spacing on the axial crush performance. In particular, the results from Part 2 suggest that the TF pattern showed the most improved folding stability in comparison to the baseline pattern. However, the thinner (1.2 mm) TF specimens showed one case of mixed folding and buckling in the dynamic sled test (Part 2) and consistent cases of global buckling in the quasi-static tests (Part 3). To further examine these instabilities, the current section examines the role of the cross-section distortion introduced by the flange indentations (Figure 54) on the onset of buckling. Other factors potentially inducing buckling would include the slenderness ratio of the double hat specimen; this aspect of folding stability is examined in detail in Chapter 5 of this thesis.

4.4.1. Effect of Section Concavity due to Flange Indentation

To demonstrate the increased likelihood of global buckling due to the section concavity, the distorted geometry of the TF specimens was recreated in the numerical model by simulating the physical indentation process (as described in Section 3.2.3), after which the distorted column was loaded under dynamic crush conditions. To avoid confusion with the previous models, the new model that incorporates the indentation effects is referred to as the "indented model." On the other hand, the previous models whose fold initiator patterns were recreated by simply displacing the nodes are referred to as the "displaced models." For the purposes of the current discussion, the dynamic TF specimen from Part 2 is revisited here.

The final crushed images of the TF specimen (repeat #3) from the indented model and the experiment are shown in Figure 129 (front view) and Figure 130 (side view), along with those from the displaced model. Remarkably, the final image of the indented model shows a close resemblance to the tested specimen in terms of the buckling mode and spot weld unzipping phenomenon, respectively. As shown earlier, the displaced model, instead, shows a stable, progressive folding. The stark contrast between these two predictions highlights the importance of choice in the modeling approach for creating fold initiators in pattern TF.

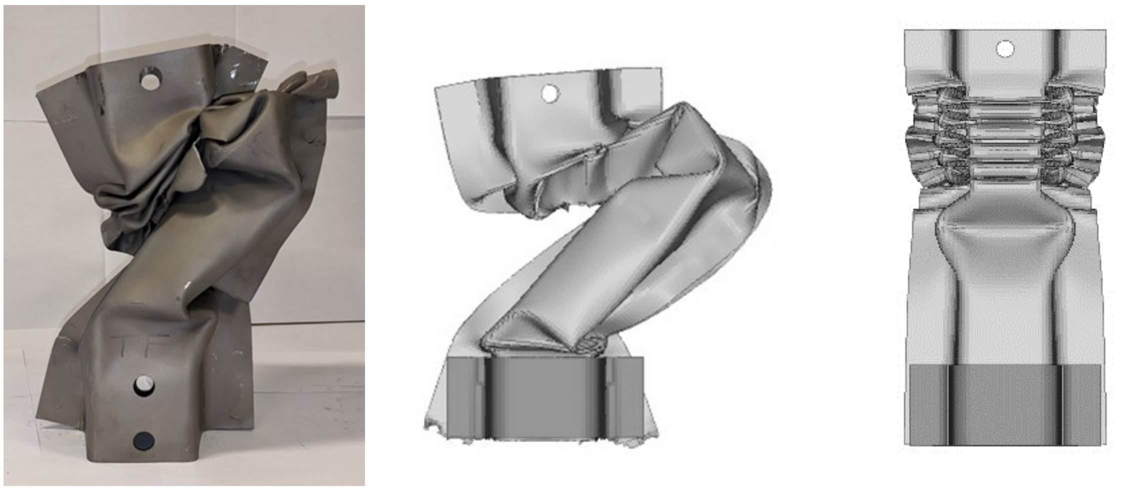

(a) experiment (TF repeat #3) | (b) indented model | (c) displaced model

Figure 129: Final crushed, front view image of the TF rail from (a) the experiment (repeat #3), (b) the indented numerical model and (c) the displaced numerical model

(a) experiment (TF repeat #3) | (b) indented model | (c) displaced model

Figure 130: Final crushed, side view image of the TF rail from (a) the experiment (repeat #3), (b) the indented numerical model and (c) the displaced numerical model.

The still images of TF rail from the three different sources discussed above (experiment, indented model, and displaced model) are shown in Figure 131. Overall, the indented model demonstrates a good correlation with the experiment in capturing the initial fold formation at 60 mm crush displacement and the transition to buckling at 130 mm crush displacement, as shown in Figure 131.

(a) Experiment

(b) Indented model

(c) Displaced model

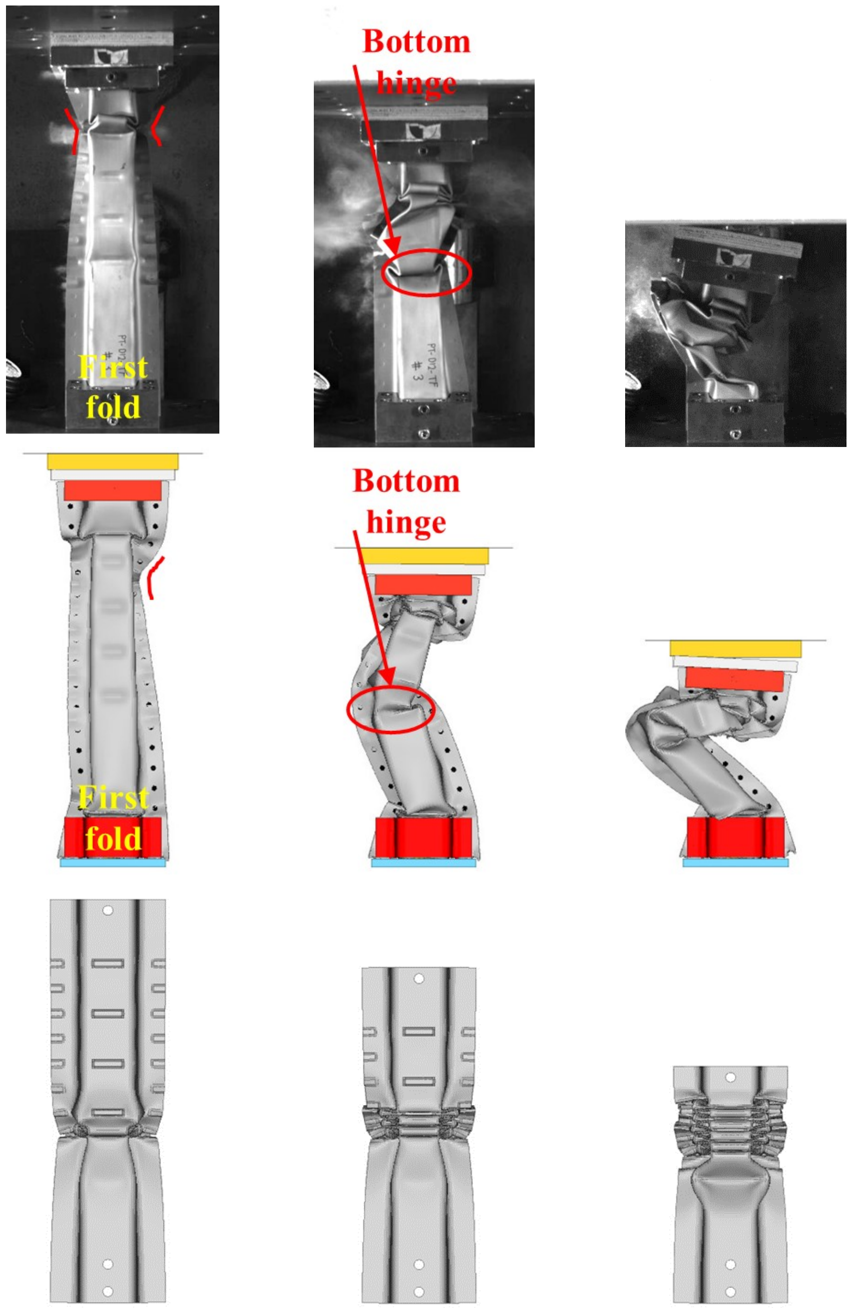

i. 60mm ii. 130mm iii. 250mm

Figure 131: High-speed, front view images of TF rail undergoing a dynamic sled test at three different crush displacements: (a) experiment (repeat #3) and its corresponding numerical models: (b) indented model and (c) displaced model.

In summary, the effect of the geometric distortion in the indented model clearly destabilized the predicted mechanical response. The initial inwards drawing of the flanges is seen to intensify as the first fold forms (Figure 131i), which causes the folding process to skip some of the intermediate fold initiators. The last fold initiator activates (see Figure 131ii) and acts as a hinge, allowing a buckling mode to be activated. Lastly, the stress level within the spot welds along one side of the flange results in “unzipping” of spot welds and failure of the entire flange, as further seen in Figure 131iii.

In general, the ability of the model to predict the buckling response of the 1.2 mm TF crush rails, once the section distortion is account for, is encouraging. Moreover, it is expected that incorporation of the fold initiator geometry within the hot stamping tool would serve to prevent this distortion which should result in improved folding stability. Experimental confirmation of this improvement must await future work, however, the finite element models without distortion certainly suggest that this approach should work.

5.0 Development of Axial Crush Performance Metrics

The previous chapter examined the design of fold initiator patterns to promote progressive folding in axial crush structures with a focus on a UHSS hot stamped 1000 MPa steel, Ductibor® 1000-AS. Those experiments and models have demonstrated that there exists a complex interaction between material strength, fracture resistance, column length, fold initiator pattern and spacing, amongst other factors, that determine crush performance. The complex nature of axial crush performance points to the need for design guidelines pertaining to material selection for axial crush structures. To this end, this chapter examines the development of metrics that can be used to potentially predict crush performance that may serve as design tools for fold initiator design and material selection.

Several metrics are proposed for use in evaluating axial crush performance: (i) Crush Energy Efficiency; (ii) Relative Bending Limit; and (iii) Folding Transition Indicator. These metrics are addressed individually in the balance of this chapter. Of particular interest is the suitability of the developed performance metrics for a wide range of materials; hence, results from a number of axial crush experiments available in the literature were considered in addition to the current work on Ductibor® 1000-AS. The list of these axial crush results and their corresponding geometric configurations are presented in Section 5.1. The balance of this chapter presents the three crush performance metrics developed as part of this research and closes with a “performance map” that combines the bending and folding performance metrics.

5.1. Axial Crush Data Taken from Previous Research

The axial crush results considered for the current study are summarized in Table 20. The range of materials includes two other hot stamped grades, namely Ductibor® 500 and Usibor® 1500-AS, whose respective tensile strengths are in the range of 500-800 MPa and 800-1700 MPa (Samadian *et al.,* 2020; Bardelcik *et al.,* 2012) depending on the die temperature and quench-rate following austenitization. Also considered are hot stamped TWBs of these alloys, which comprise a 290 mm long softer region, tailor-welded to a 210 mm stronger region, as shown in Figure 37b. The list also includes results for three "enhanced DP980" alloys, with tensile strengths in the range of 990-1070 MPa (Zhumagulov *et al.,* 2018) and results for a lower strength 270 MPa steel grade due to Ohkubo *et al.* (1974). The corresponding geometric parameters for each specimen, including cross-sectional features and specimen length, are listed in Table 21. Finally, it is noted that all of the axial crush samples listed in Table 20, except for the top hat samples due to Ohkubo *et al.* (1974), utilized a fold initiator arrangement corresponding to the baseline configuration (BA) described in Chapter 4. The effect of more complex initiator patterns is considered in Section 5.5.

Table 20: List of dynamic axial crush results and test parameters from several previous studies (see citations in table). All specimens correspond to the baseline double hat channels (see Figure 38 for cross-section) except for the single top hat studied by Ohkubo *et al.* (1974). The hot-stamped Usibor® 1500-AS (fully-cooled condition), Ductibor® 500-AS and TWBs of these alloys were austenitized for minimum of 6 minutes and quenched in a water chilled-die with a temperature of approximately at 15 °C. Mean forces were calculated up to the free crush distance. The quasi-static specimens are represented by 'Q' in the impact velocity column.

Crush specimens	Measured UTS [weaker parent metal] (MPa)	Test configuration					Results
		Thickness (mm)	Length [effective column length] (mm)	Free crush distance (mm)	Impact mass (kg)	Impact velocity (m/s)	Mean force (kN)
Monolithic							
Mild ~270 MPa grade (Ohkubo *et al.,* 1974)	311 (Noder *et al.,* 2020)	1.2	300	-	-	**Q**	21.6
Mild ~270 MPa grade (Ohkubo *et al.,* 1974)	311 (Noder *et al.,* 2020)	1.6	300	-	-	**Q**	37.8
Ductibor® 500-AS (Peister *et al.,* 2019)	721 (Samadian *et al.,* 2020b)	1.2	500	165	855	10.6	71.1
Ductibor® 500-AS (Peister *et al.,* 2019)	721 (Samadian *et al.,* 2020b)	1.6	500	165	855	10.6	126
DP980 MAT1 (Butcher *et al.,* 2018)	1067 (Zhumagulov *et al.,* 2018)	1.2	500	115	855	7.1	97.9
DP980 MAT2 (Butcher *et al.,* 2018)	998 (Zhumagulov *et al.,* 2018)	1.6	500	115	855	7	158
DP980 MAT3 (Butcher *et al.,* 2018)	1012 (Zhumagulov *et al.,* 2018)	1.4	500	115	855	7.1	128
Ductibor® 1000-AS (current study)	1121 (Abedini, 2018)	1.2	500	165	855	10.6	87.7

Table 20: Continued.

Crush specimens	Measured UTS [weaker parent metal] (MPa)	Test configuration					Results
		Thickness (mm)	Length [effective column length] (mm)	Free crush distance (mm)	Impact mass (kg)	Impact velocity (m/s)	Mean force (kN)
Ductibor® 1000-AS (current study)	1121 (Abedini, 2018)	1.6	375	-	-	**Q**	166
Usibor® 1500-AS (Omer *et al.,* 2017b)	1447 (Bardelcik *et al.,* 2012)	1.2	500	165	855	10.6	92.3
Usibor® 1500-AS (Omer *et al.,* 2017b)	1447 (Bardelcik *et al.,* 2012)	1.8	500	165	855	10.6	139
TWB							
Ductibor® 500 / Usibor® 1500-AS (Peister, 2019)	[721]	1.2	500 [290]	165	855	10.6	71.7
Ductibor® 500 / Usibor® 1500-AS (Peister, 2019)	[721]	1.6	500 [290]	165	855	10.6	119
Ductibor® 1000 / Usibor® 1500-AS	[1121]	1.2	500 [290]	165	855	10.6	90.9

Table 21: List of cross-section geometric parameters for crush specimens in Table 20, whose definitions are given in Figure 34. All of the results except for the mild steel are from the research work of Waterloo Forming and Crash research group (denoted as "University of Waterloo Materials") and their specimens share the same geometry. Due to the presence of corner radii and obtuse draft angle of the double hat geometry, its dimension 'a' is approximated.

Crush specimen	**Type**	**Geometry**				
		b (mm)	**a (mm)**	**f (mm)**	**Ø (°)**	**R (mm)**
Mild ~270 MPa grade (Ohkubo *et al.,* 1974)	Single hat	60	70	18	90	-
University of Waterloo Crush Rails	Double hat	100	~58	21	95	8

5.2. Energy Absorption Performance Metric

Figure 132 shows the measured mean crush force and predicted values using the analytical Superfolding Element analysis (using Equations A.17 to A.19 and A.2.1 to A.2.7) developed by Wierzbicki and Abramowicz (1983) for the 1.2 mm thick monolithic specimens listed in Table 20. The crush forces are plotted as a function of their measured or hardness-equivalent UTS. The detailed solution procedure for the SE analysis is found in Appendix A.

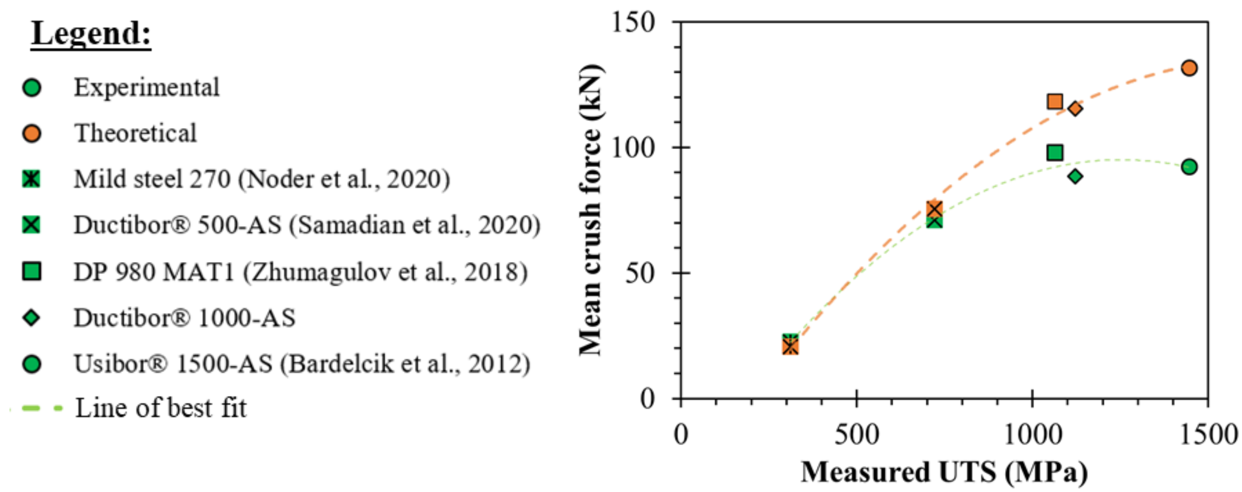

Figure 132: Measured and predicted mean crush force of 1.2 mm monolithic axial crush specimens in Table 20 plotted against their reported UTS level by several authors in parentheses. The dotted lines represent polynomial lines of best fit. The experimental mean force was calculated using the free crush distance. The theoretical mean force was calculated using the SE Analysis (Wierzbicki and Abramowicz, 1983) whose solution procedure can be found in Appendix A.

Several observations can be made regarding the level of agreement between the theoretical and experimental mean force. The lower strength specimens, such as the mild steel (270 MPa) and Ductibor® 500-AS (700 MPa) samples, show a very close agreement between the theoretical and experimental results with an error of only 7.0 % (2.8 kN) and 6.9 % (4.9 kN), respectively. As the strength level increases, however, the magnitude of error increases, rising to 31 % (27.4 kN) for Ductibor® 1000-AS and 52 % (47.7 kN) for Usibor® 1500-AS, reflecting a drop in the measured crush force relative to the analytical predictions. Clearly, the predicted mean crush force of the Superfolding Element exhibits an increasing error for higher strength level alloys. The possible reasons for this trend are explored in the following.

5.2.1. Crush Energy Efficiency

An alternative normalization method to assess crush performance of different alloys is in term of Crush Energy Efficiency (η_{crush}), the ratio of the measured energy absorption (E_{exp}) to the theoretical energy absorption (E_{SE}) using Equations A.17 to A.19 and A.2.1 to A.2.7 (E_{SE}) in the following form:

$$\eta_{crush} = \frac{E_{\exp}}{E_{SE}} = \frac{P_{\exp} d}{P_{SE} d} = \frac{P_{\exp}}{P_{SE}} \tag{50}$$

in which d is the crush distance, and P_{exp} and P_{SE} are the mean crush force obtained from the experiment and the SE analysis, respectively. In essence, Crush Energy Efficiency is taken here as the ratio between the measured energy, which reflects the actual deformation mode and extent of fracture, for example, and the theoretical potential energy absorption if the deformation mode was progressive folding. Thus, a higher value of η_{crush} indicates that the specimen is more "efficient" for a given material strength. One advantage of using the η_{crush} metric is that normalization eliminates the effect of thickness on the mean crush force. To demonstrate this point, Figure 133 shows η_{crush} for all of the monolithic specimens in Table 20 (which have a range of thicknesses) plotted against the UTS level (as opposed to Figure 132, which only shows 1.2 mm thick specimens).

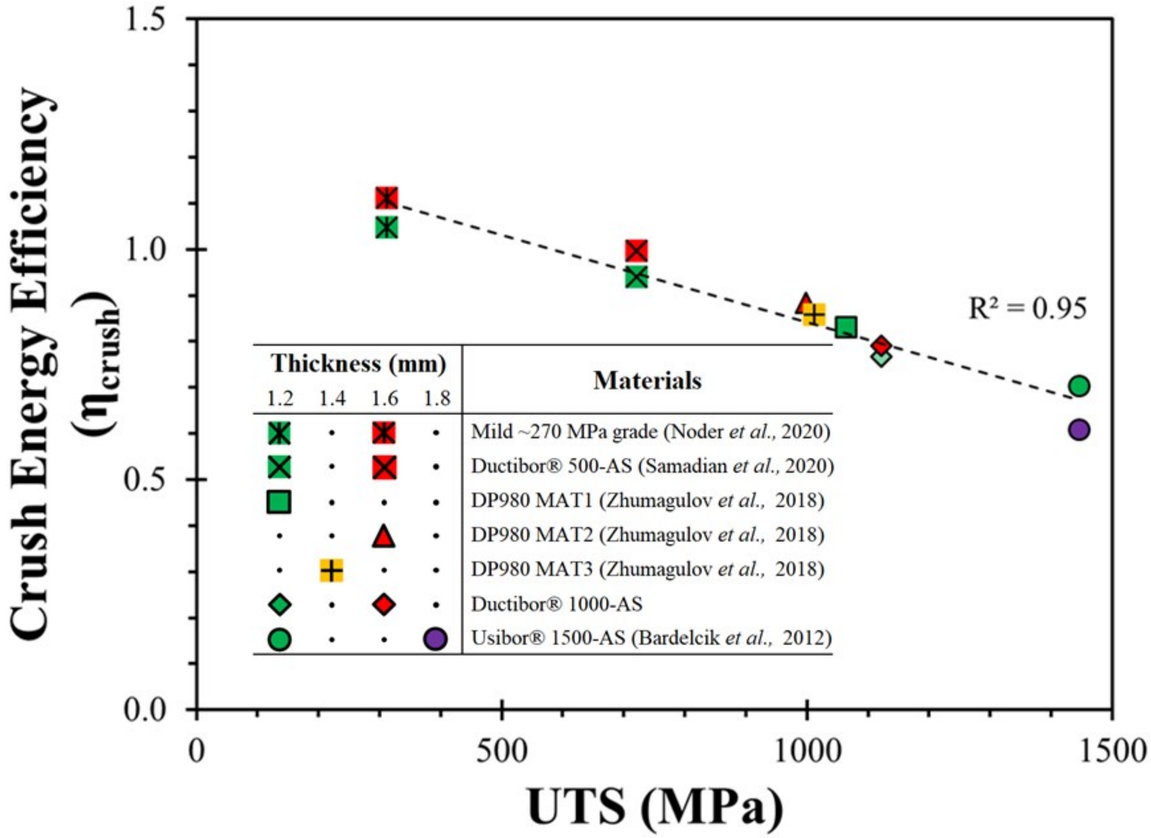

Figure 133: Crush Energy Efficiency (η_{crush}) for all of the steel grades in Table 20 plotted against their reported UTS levels by several authors in parentheses.

Figure 134 shows as-tested samples for the specimens plotted in Figure 133 (note that only one thickness configuration is shown for each material). The extent of fracture for each case is classified as "no fracture", "moderate fracture" or "severe fracture" and each image is highlighted as green, yellow or red, respectively. Comparison of the extent of fracture and Crush Energy Efficiency (η_{crush}) in the figure reveals that η_{crush} is reduced drastically as the extent of fracture increases. The lowest values of η_{crush} were exhibited by the Usibor® 1500-AS, which is accompanied by severe fracture. The mild 270 MPa grade steel and Ductibor® 500-AS, on the other hand, have a value of η_{crush} close to unity and show no evidence of fracture. The DP980 series, whose η_{crush} values fall in the middle of the scale, show a mixed case of irregular folding, buckling and some fracture. The Ductibor® 1000-AS baseline case from the current study, which is slightly stronger than the DP 980 grades, exhibits a similar degree of tearing and global buckling, resulting a slightly lower Crush Energy Efficiency. It also can be seen that decreases in η_{crush} correspond to a transition in deformation mode from stable folding towards buckling.

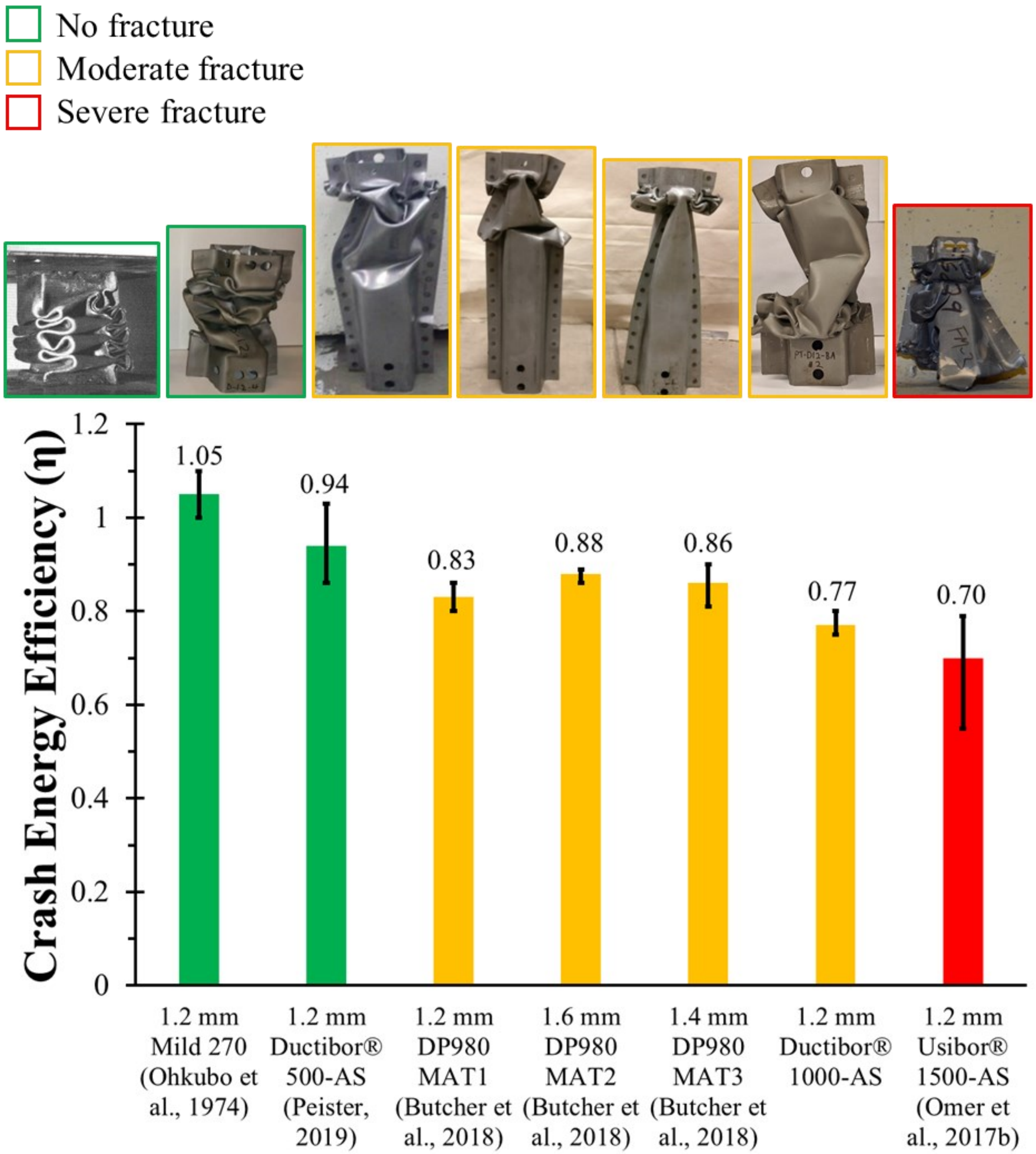

Figure 134: Crush Energy Efficiency (η_{crush}) of the monolithic crush specimens in Table 20 plotted in terms of increasing UTS (left to right). As-tested images of each crush specimen are also shown above the bar chart. For brevity, only one thickness configuration for each steel alloy is shown (*e.g.* Ductibor® 1000-AS 1.2 mm). Note that the DP980 MAT 1 to MAT 3 steels are from different suppliers and are treated as different alloys, herein.

5.3. Fracture Resistance Metric

In vehicle crash events, the ability of a material to crumple and absorb energy, as in the current axial crush experiments, is normally limited by its ability to bend without fracture. Here, fracture is manifest by cracks or tears on the top faces or the sidewalls, as shown in Figure 135a. These top faces or sidewalls of local folds, when compared to the Superfolding Element, correspond to the horizontal bending zone (see Figure 135b) that deforms (bends) under plane strain tension. Thus, the fracture resistance in axial crush will be a strong function of the bending performance of a material.

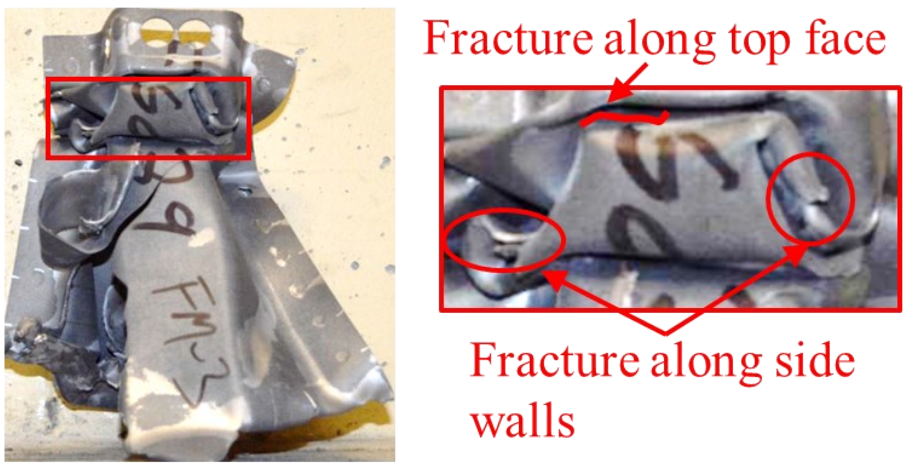

(a) fully-cooled Usibor® 1500-AS crushed specimen (Omer *et al.,* 2017b)

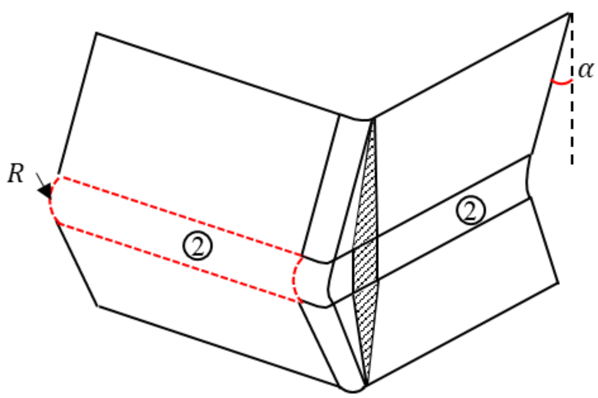

(b) horizontal bending region in SE (Wierzbicki and Abramowicz, 1983)

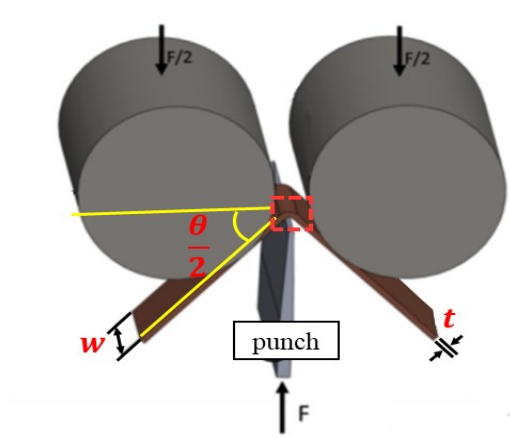

(c) v-bend test (Roth and Mohr, 2016)

Figure 135: Illustration of (a) Usibor® 1500-AS crushed specimen, showing fracture along the sidewall or topwall, which correspond to the (b) SE horizontal bending region and (c) v-bend test. α_{SE} is the SE crush angle in unit of radian and θ is the VDA bend angle (VDA, 2010) in units of degrees (°).

5.3.1. Relative Bending Limit

Whether or not fracture will occur depends on (i) the intrinsic bending performance of a material (*e.g.* the limiting bend angle or plastic work at fracture under plane strain bending), as well as (ii) the extrinsic applied bending strain (or plastic work) imposed during folding in an axial crush event. Fortunately, the material bending limit can be readily evaluated experimentally, using v-bend tests, for example, as shown in Figure 135c. These tests impose a bending deformation that is similar in character to the horizontal bending in the SE (except for contact pressure on the inside radius by the punch). In concert with the material bending limits, the applied bending deformation during axial crush can be predicted using the SE analysis based on the final bending angle (crush angle) in the horizontal bending zone of the SE. In order to predict likelihood of fracture, a new plastic work-based performance metric, termed the *Relative Bending Limit*, is defined as *the ratio of the plastic work to failure in bending to the imposed plastic work due to bending during axial crush*.

Formally, the Relative Bending Limit (χ_{bend}) is based on a normalization approach and uses the following form:

$$\chi_{bend} = \frac{W_{v-bend}}{W_{SE,bend}} \tag{51}$$

in which W_{v-bend} is the plastic work at fracture onset during a V-bend test, calculated using the methodology developed by Noder *et al*. (2020). $W_{SE,bend}$ is the imposed plastic work along the horizontal folding line of the SE (Figure 135b) at full consolidation during axial crush. Both plastic work values are normalized per unit width along the bending axis, expressed in units of kJ/m, and evaluated for the same sheet thickness.

In essence, a lower value of χ_{bend} means the fracture limit of the material is low *relative to the plastic work the material will experience during folding and progressive crush*. In other words, a low value of χ_{bend} is indicative of poor bending performance and severe fracture susceptibility.

The equation for W_{v-bend}, the numerator in Equation (51), is given by Noder *et al.* (2020) in a relationship between bending moment (M_{v-bend}), the VDA bend angle (θ), the fracture bend angle (θ_f) and the width of the specimen (*w*):

$$W_{v-bend} = \frac{1}{w}\int_0^{\theta_f} M_{v-bend}\, d\theta \tag{52}$$

and the bend angle symbols are defined in Figure 135c. The v-bend fracture angle, which can vary significantly depending upon the choice of detection metric, is calculated using a novel approach, developed by Noder *et al.* (2020) and known as the stress metric (Σ), rather than the conventional VDA peak load drop method (VDA, 2017). The stress metric is defined as:

$$\Sigma = \frac{4}{t^2 w} M_{v-bend} \tag{53}$$

in which t is the current cross-section thickness, which accounts for thinning using an empirical thinning equation, as recommended by Noder *et al.* (2020). In their work, the stress metric criterion to detect fracture onset serves to avoid so-called "false positives" that can occur using the conventional VDA load drop method (VDA, 2017)—especially in ductile alloys or thin materials with a low bend severity. For the purpose of the current work, a 5% drop in the stress metric criterion was consistently used, which corresponded well to the onset of visual cracks as reported by Noder *et al.* (2020).

As part of the current research, the plastic work to bending failure, W_{v-bend}, was calculated for a number of the materials listed in Table 20 using Equations (52)-(53) and the v-bend test results (in terms of $M_{v-bend}\ vs.\ \theta$) provided by Noder and Butcher (2020) and Cheong (2019b). Figure 136 shows (d) the measured plastic work at fracture, as well as the intermediate calculations, comprising the evolution (with respect to bending angle) of (a) bending moment (b) stress metric and (c) plastic work.

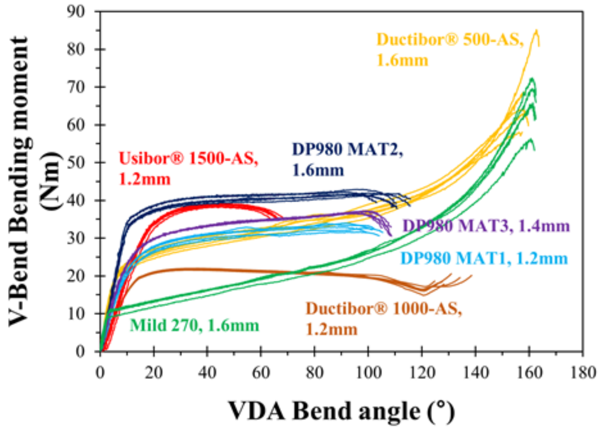

(a) Bending moment evolution

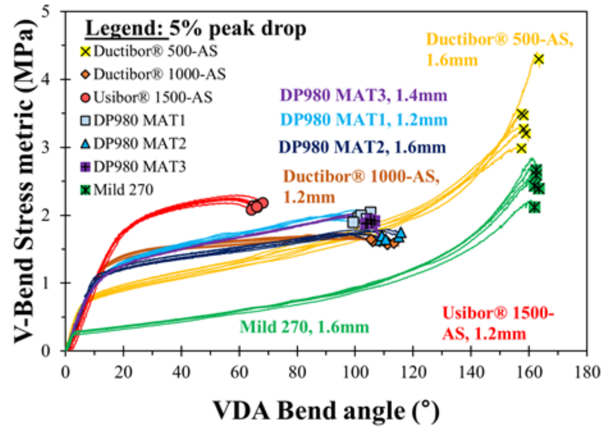

(b) Stress metric evolution

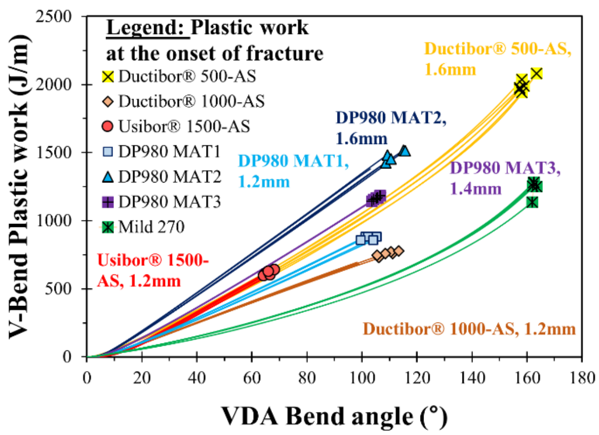

(c) Plastic work evolution

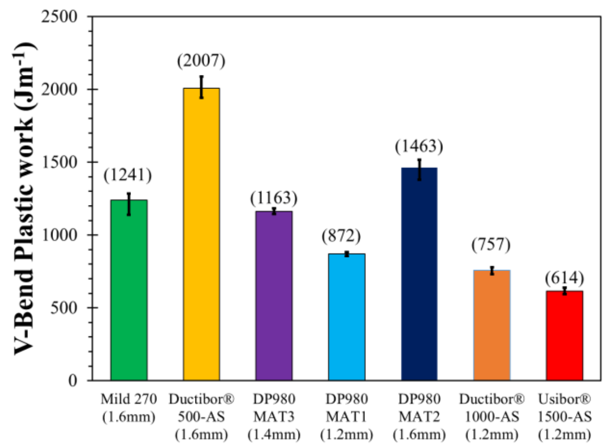

(d) V-bend plastic work at fracture

Figure 136: Measured (a) bending moment evolution from v-bend tests on various materials by Noder and Butcher (2020) and Cheong (2019b). The following properties were calculated using the methodology developed by Noder *et al.* (2020): (b) Stress metric evolution (c) Plastic work evolution and (d) Plastic work at the onset of fracture, using a 5% drop in the stress metric criterion.

Based on examination of Figure 136, higher strength steel grades exhibit earlier fracture onset and lower plastic work to fracture. Interestingly, high strength steels like Usibor® 1500-AS and Ductibor® 1000-AS show a strong linear trend in plastic work evolution with bend angle. The increase in plastic work with bend angle becomes increasingly non-linear as the material strength decreases with the strongest nonlinearity observed in the 270 MPa mild steel grade. Although the non-linear behaviour in the mild steel may be partially attributed to the punch lift-off phenomenon at higher bend angle, its strong hardening behaviour is suggested to play a role since the nonlinearity is observed from the start of the bending process (bend angles of approximately 30° in Figure 136c).

The second building block of Relative Bending Limit, is the plastic bending work in the SE horizontal zone ($W_{SE,bend}$, the denominator in equation (51)), which can be calculated using the relation given by Wierzbicki and Abramowicz (1983):

$$W_{SE,bend} = M_{SE,bend}\alpha_{SE,f} \tag{54}$$

$$M_{SE,bend} = \frac{\sigma_{SE,bend}t^2}{4} \tag{55}$$

in which $\alpha_{SE,f}$ is the SE crush angle (assumed as $\pi/2$), $M_{SE,bend}$ is the energy equivalent plastic bending moment, and $\sigma_{SE,bend}$ is the energy equivalent flow stress in the SE bending region. $\sigma_{SE,bend}$ corresponds to an average flow stress in bending and its expression, given by Wierzbicki and Abramowicz (1987), is in terms of the flow stress ($\bar{\sigma}$) and the SE bending strain ($\varepsilon_{SE,bend}$):

$$\sigma_{SE,bend} = \begin{cases} \dfrac{2}{\varepsilon_{SE,bend}^2}\displaystyle\int_0^{\varepsilon_{SE,bend}} \bar{\sigma}\left(\bar{\varepsilon}_p\right)\bar{\varepsilon}_p d\bar{\varepsilon}_p & \text{hardening assumption} \\ \sigma_y & \text{perfectly plastic assumption} \end{cases} \tag{56}$$

$$\varepsilon_{SE,bend} = \ln\left(1 + 0.926tH\right) \tag{57}$$

in which $\bar{\varepsilon}_p$ is the equivalent plastic strain, t is the sheet thickness, and H is the SE half-wavelength of the folding cell (see Figure A.1). The energy equivalent stress for each material is calculated in Appendix C and shows a considerable difference from the yield strength, pointing to the importance of the hardening assumption. More commentary on the energy equivalent flow stress can be found in Appendix A.

By combining Equations (51), (52), (54), (55), and (56), the Relative Bending Limit (χ_{bend}) can be expressed as follows:

$$\chi_{bend} = \frac{W_{v-bend}}{W_{SE,bend}} = \frac{\dfrac{1}{w}\displaystyle\int_0^{\theta_f} M_{v-bend}d\theta}{\left(\dfrac{2}{\varepsilon_{SE,bend}^2}\displaystyle\int_0^{\varepsilon_{SE,bend}} \bar{\sigma}\left(\bar{\varepsilon}_p\right)\bar{\varepsilon}_p d\bar{\varepsilon}_p\right)\dfrac{t^2}{4}} \tag{58}$$

Note that the hardening models, as well as the calibration constants used to calculate $\bar{\sigma}$ were obtained from multiple publications which are listed in Table 22 in Appendix C. The material data was extracted for consistent material conditions (*e.g.* measured Vickers hardness) with respect to the crush test specimens.

Figure 137 shows the calculated Relative Bending Limit (χ_{bend}) for a subset of materials using Equation (58) with either the hardening or perfectly plastic assumptions. The overall trends for either assumption show that χ_{bend} decreases as the material strength increases, with the highest and lowest values for χ_{bend} corresponding to the 270 MPa mild steel grade and Usibor® 1500-AS, respectively. The calculated values for χ_{bend} using the hardening assumption are all higher than those using the perfectly plastic assumption by a range from 21 to 69 %. Interestingly, the difference in χ_{bend} amongst the DP 980 series was significant (up to 26%) under the perfectly plastic assumption; however, a minimal difference is shown (0.8%) under the hardening assumption. The preceding results point to the importance of using the proper hardening assumption in calculating the energy equivalent flow stress when comparing the bending performance of materials within similar UTS levels.

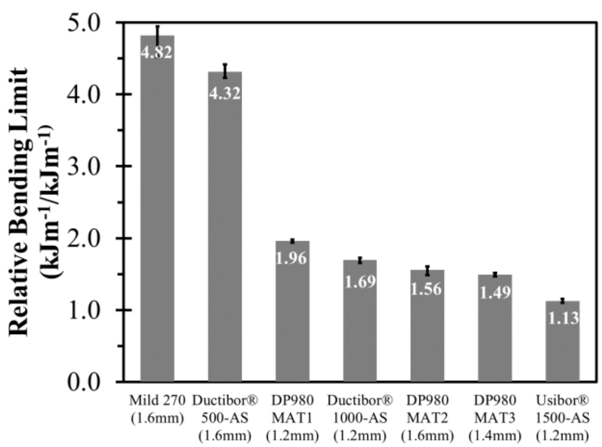

(a) perfectly plastic

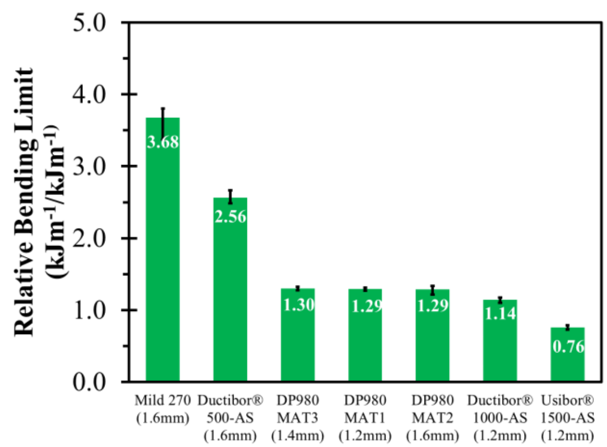

(b) energy equivalent flow stress

Figure 137: Bar chart of χ_{bend} in the descending order, calculated using Equation (58) with two different hardening assumptions: (a) perfectly plastic assumption or (b) hardening assumption in Equation (56). The calibrated hardening models can be found in Appendix C.

Interestingly, the Crush Energy Efficiency values for the materials considered here show a strong correlation with the calculated values of χ_{bend} (R-squared = 0.91), as shown in Figure 138. Also indicated in the figure is the observed extent of fracture from which it can be seen that materials with a lower Relative Bending Limit exhibited a higher extent of fracture and a lower Crush Efficiency. For example, the crush rails fabricated using die-quenched Usibor® 1500-AS, whose χ_{bend} is 0.76, exhibited a very high fracture susceptibility. The die-quenched Ductibor® 500-AS, whose χ_{bend} is 2.56, did not exhibit any indication of fracture. The rest of the materials, with χ_{bend} ranging from 1.1 to 1.3, exhibited a moderate extent of cracking. Thus, the Relative Bending Limit can be used as a reasonable predictor of not only fracture resistance but also the Crush Energy Efficiency of a crush specimen.

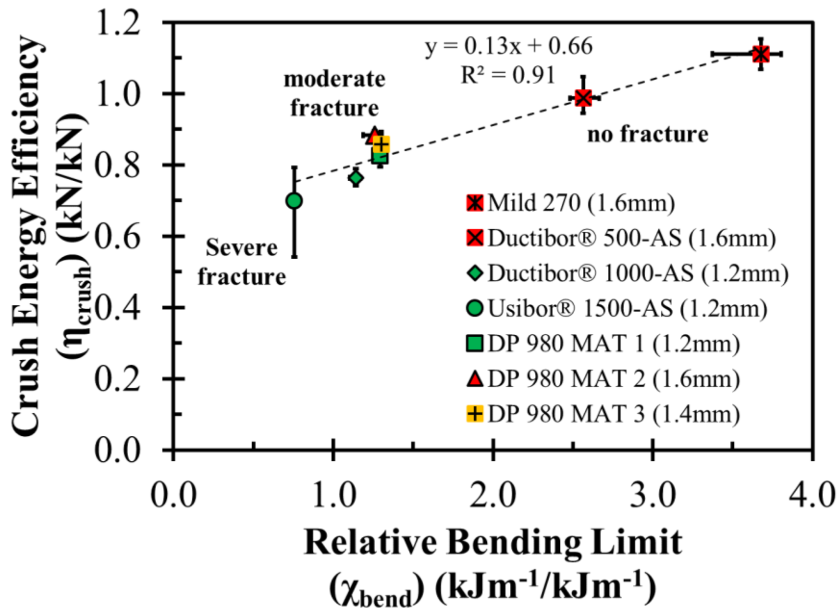

Figure 138: Crush Energy Efficiency *vs.* Relative Bending Limit calculated using Equation (50) and (58).

Calculating the Relative Bending Limit using Equation (58) poses complexity in terms of (i) obtaining V-bend plastic work evolution and (ii) solving for SE energy equivalent flow stress. For this reason, a simplified approximate solution of the Relative Bending Limit has also been derived and is documented in Appendix D. One important aspect which stems from the solution is that the Relative Bending Limit is directly related to the ratio of the v-bend fracture angle (θ_f) to the power-law hardening coefficient (K).

5.4. Folding Stability Metric

5.4.1. Folding Transition Indicator

The previous discussion has centred around the interaction between the material fracture limit and imposed bending deformation during axial crush. Another important aspect of stability during axial crush is the transition between local folding and global buckling which is expected once the slenderness of the axial crush column becomes high. One approach to predict the onset of global buckling is based on the expression for the transition between local folding and global buckling due to Abramowicz and Jones (1997). Their expression is based on the ratio of two critical stresses: (a) the plastic buckling stress of a column, σ_{cr}^{col}, and (b) the mean stress of local folding, σ_{local}:

$$\frac{\sigma_{cr}^{col}}{\sigma_{local}} = 1 \tag{59}$$

in which σ_{local} was taken as the Stowell buckling (folding) stress of a simply supported plate (Iyengar, 1988).

5.4.1.1. Double Hat Channel

Here, a novel approach is introduced in which σ_{local} is taken as the mean crush stress, σ_{SE}, obtained by the SE analysis in Appendix A. The basis of this work assumes that the local collapse of the double hat column can be modeled as eight SEs, as made by White *et al.* (1999) shown in Figure 139.

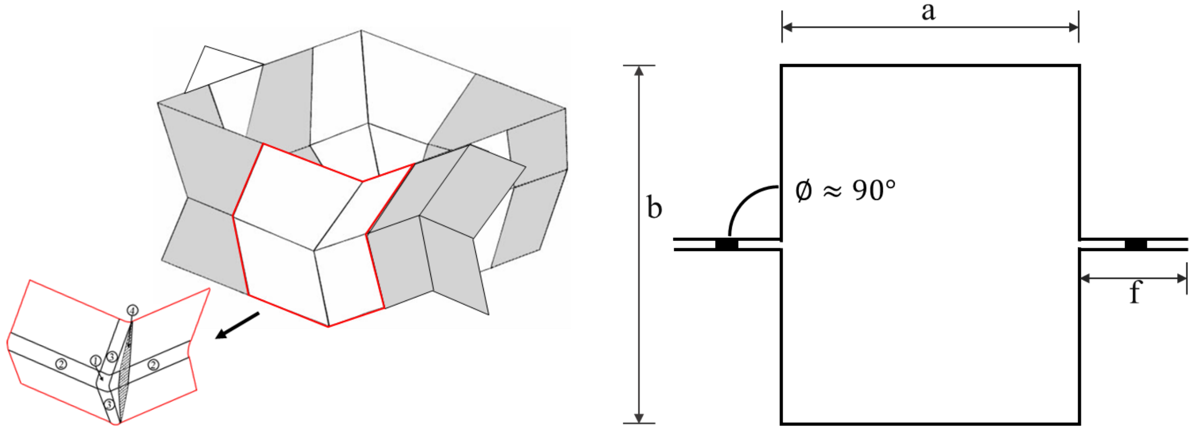

(a) Asymmetric collapse of the double hat column modeled by 8 SEs

(b) double hat cross-section with dimensions

Figure 139: Illustration of (a) asymmetric collapse of double hat column, modeled as 8 joined SE by White *et al.* (1999) and (b) the double hat cross-section with dimensions. The entire perimeter Z can be approximated as $Z \approx 2a + 2b + 4f$. Note that Z was taken as 400 mm for all double hat channels considered in the current thesis.

The equation for σ_{cr}^{col} in Equation (59) is described in terms of tangent modulus (E_t), area moment of inertia (I), cross-sectional area (A) and the specimen length (L):

$$\sigma_{cr}^{col} = \frac{4\pi^2 E_t I}{AL^2} \tag{60}$$

By using a power law hardening approximation, the tangent modulus can be determined using $E_t = nK\varepsilon^{n-1}$. The cross-sectional area and the minimum moment of inertia (mm^4) for a given double hat geometry are approximated by the following empirical relations,

$$I \approx \frac{1}{155} Z^3 t \tag{61}$$

$$A \approx Zt \tag{62}$$

Where Z represents the entire perimeter for the double hat cross-section approximated as $2a + 2b + 4f$ in Figure 139. On the other hand, the mean stress of a double hat channel is readily found using the modified form of the SE equation due to White *et al.* (1999):

$$\sigma_{SE} = 13.05\left(K\varepsilon_{SE}^{n}\right)t^{5/3}Z^{1/3} / A \tag{63}$$

Where ε_{SE} is herein introduced as "energy equivalent strain" and approximated by $0.5[(t/2r)^2(t/2R)]^{1/3}$ (see Appendix A). Inserting Equation (60)-(63) into Equation (59), one obtains

$$\frac{\sigma_{cr}^{col}}{\sigma_{SE}} = \frac{4\pi^2 n Z^{8/3}}{2023\varepsilon_{SE} t^{2/3} L^2} = 1 \tag{64}$$

Furthermore, one can substitute Z with the radius of gyration by $R_g = \sqrt{I/A} \approx \frac{Z}{12.45}$ in Equation (64) which gives

$$\frac{\sigma_{cr}^{col}}{\sigma_{SE}} = \frac{1.646\pi^2 n R_g^{\ 8/3}}{\varepsilon_{SE} t^{2/3} L^2} = 1 \tag{65}$$

The subsequent work follows that of Abramowicz and Jones (1997) who isolated a characteristic aspect ratio in their equation, defined as a ratio of column length (L) to side length (b) of square cross-section. Similarly, a slenderness ratio L/R_g can be isolated by manipulating Equation (65)

$$\left(\frac{L}{R_g}\right)_{cr} = \sqrt{\left(1.646\pi^2\right)\left(n\varepsilon_{SE}^{-1}\right)\left(\frac{R_g}{t}\right)^{2/3}} \tag{66}$$

below which local folding is predicted to occur, whereas for higher slenderness ratios, global buckling is expected. By dividing the right side of Equation (66) by the left side and substituting the actual slenderness ratio (L/R_g), a dimensionless indicator (η_{fold}) is derived, for which a value of unity corresponds to the transition between local folding *versus* global buckling:

$$\eta_{fold} = \frac{\sqrt{\left(1.646\pi^2\right)\left(n\varepsilon_{SE}^{-1}\right)\left(\frac{R_g}{t}\right)^{2/3}}}{\left(L/R_g\right)} \tag{67}$$

Here, η_{fold} is denoted the "folding transition indicator" for which higher values indicate an increased likelihood of local folding over global buckling. Hence, a high value of η_{fold} would indicate superior collapse stability.

5.4.1.2. Single Hat Channel

Similarly, the collapse of top hat channels can be modeled as four SEs and a backing plate (White *et al.,* 1999), as shown in Figure 140.

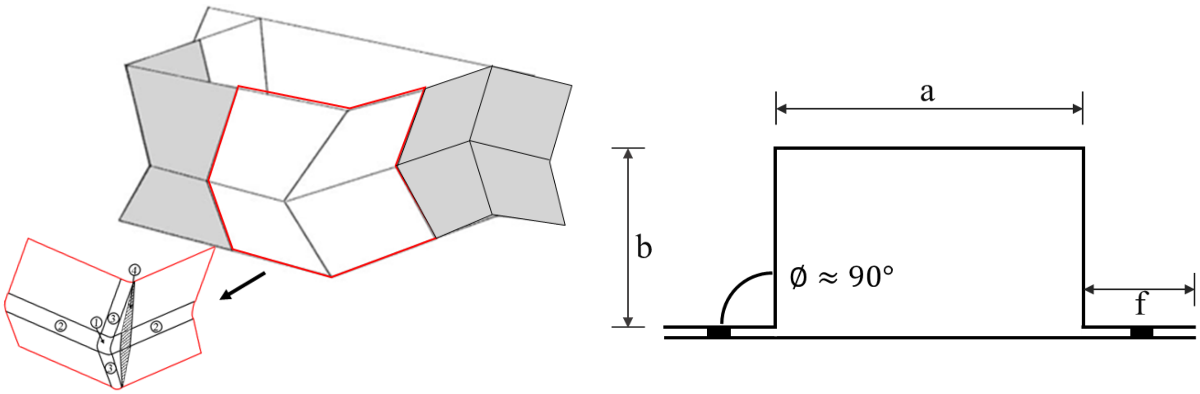

(a) collapse of the top hat column modeled by 4 SEs and a backing plate

(b) top hat cross-section with dimensions

Figure 140: Illustration of (a) asymmetric collapse of single hat column, modeled as 4 joined SE and a backing plate by White et al. (1999) and (b) the single hat cross-section with dimensions shown. The entire perimeter Z can be approximated as $Z \approx 2a + 2b + 4f$. Images adapted from White *et al.* (1999).

The folding transition indicator for the top hat section can be found using the same approach except using the empirical moment of inertia (I) and the mean crush stress of SE (σ_{SE}) for the top hat section as follows

$$I = \frac{1}{266} Z^3 t \tag{68}$$

$$\sigma_{SE} = 8.22\left(K\varepsilon_{SE}^{n}\right)t^{5/3}Z^{1/3} / A \tag{69}$$

Insertion of Equations (60), (68) and (69) into Equation (59) finally gives the expression for the top hat section

$$\eta_{fold} = \frac{\sqrt{\left(3.130\pi^2\right)\left(n\varepsilon_{SE}^{-1}\right)\left(\frac{R_g}{t}\right)^{2/3}}}{\left(L / R_g\right)} \tag{70}$$

Figure 141 shows calculated values of the Folding Transition Indicator (η_{fold}) for each axial crush specimen listed in Table 20. Furthermore, each specimen is classified based on its deformation mode as "severe fracture", "global buckling", "mixed folding and buckling", "irregular folding" or "progressive folding". Comparison of the deformation mode and η_{fold} in the figure reveals that the specimens with η_{fold} above unity underwent stable folding modes, while those with η_{fold} below unity exhibited various unstable modes. The lowest values of η_{fold} corresponded to the 1.2 and 1.6 mm thick Usibor® 1500-AS crush rails that exhibited severe fracture. The DP980 MAT 2 crush rails also had low values of η_{fold} and displayed global buckling. Also exhibiting low η_{fold} values (< 0.5) are the 1.2 mm Ductibor® 1000-AS baseline case and the 1.6 mm baseline case with reduced effective column length, which showed global buckling and mixed folding and buckling, respectively. The mild 270 MPa grade steels and Ductibor® 500-AS / Usibor® 1500-AS TWBs (1.2 and 1.6 mm) have the highest values of η_{fold} and show progressive folding and irregular folding, respectively. The balance of the crush rails in Table 20 include the DP980 MAT1 / MAT3, Ductibor® 1000-AS / Usibor® 1500-AS TWB and Ductibor® 500-AS (1.2 and 1.6 mm) with values of η_{fold} between 0.5 and 1.0. These alloys show varying degrees of mixed folding and buckling. In general, Figure 141 supports the use of the folding transition indicator as a metric to apply in design of axial crush columns to promote folding over global buckling. It should be noted that wider investigation of a broader range of column geometry, beyond the baseline (BA) geometry, is needed prior to general application of this approach.

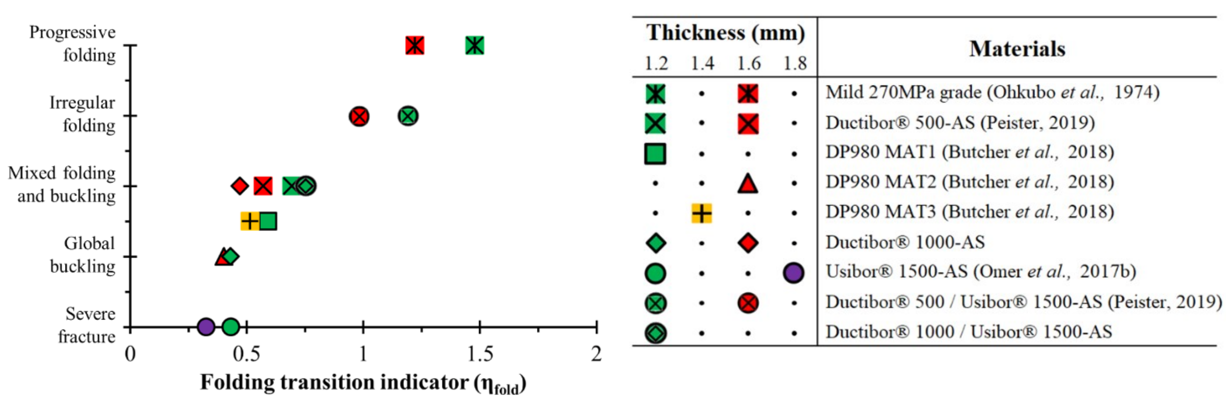

Figure 141: Plot of deformation mode *vs.* Folding Transition Indicator (η_{fold}). The legend is shown in the table. Note that η_{fold} for TWB specimens were calculated by assuming the specimen length (L) in Equations (67) and (70) to be the same as their reduced effective column length.

5.5. Performance Map and Benefit of Enhanced Fold Initiator Design

Figure 142 is a plot of the Relative Bending Limit (χ_{bend}) *versus* the Folding Transition Indicator (η_{fold}) for the set of axial crush columns in Table 1 for which V-bend fracture data was available. Essentially, this figure can be thought of as "Performance Map" in which the horizontal axis indicates the likelihood of folding (as opposed to column buckling), while the vertical axis quantifies the ability of the material to bend without fracture during axial crush. Note that the Relative Bending Limit for the TWB columns was assumed to be the same that of as their monolithic counterparts whereas the length of the softer parent metal section was adopted as their column length. Ideally, a crush column design should exhibit good folding stability and sufficient resistance to fracture during folding (bending), as captured by this Performance Map.

In Figure 142, the expected extent of fracture (from Figure 138) is classified by three regions along the vertical axis, corresponding to "no fracture", "moderate fracture" or "severe fracture." Similarly, three regions of expected collapse stability are indicated along the horizontal axis, as "global buckling", "irregular folding" or "progressive folding". Overall, the various deformation modes / fracture severities observed in the crush specimens fall into the corresponding regions within the performance map. There was one discrepancy, namely the baseline Ductibor®1000-AS / Usibor® 1500-AS TWB column that showed mixed folding and buckling. This column also falls into the moderate fracture category whereas it exhibited extensive fracture in the experiments. Interestingly, this discrepancy is consistent with the predicted eroded energy *vs.* absorbed energy map of various fold initiator patterns in Figure 103 (Section 4.2), which also showed the highest eroded energy for the mixed folding and buckling case. Such behaviour suggests that the complex interaction of multiple deformation modes can lead to more extensive fracture and points to the need for further investigation. In addition, future work should consider incorporating other advanced materials such as 3rd generation steel alloys which are anticipated to shift the relationship between fracture strain and strength.

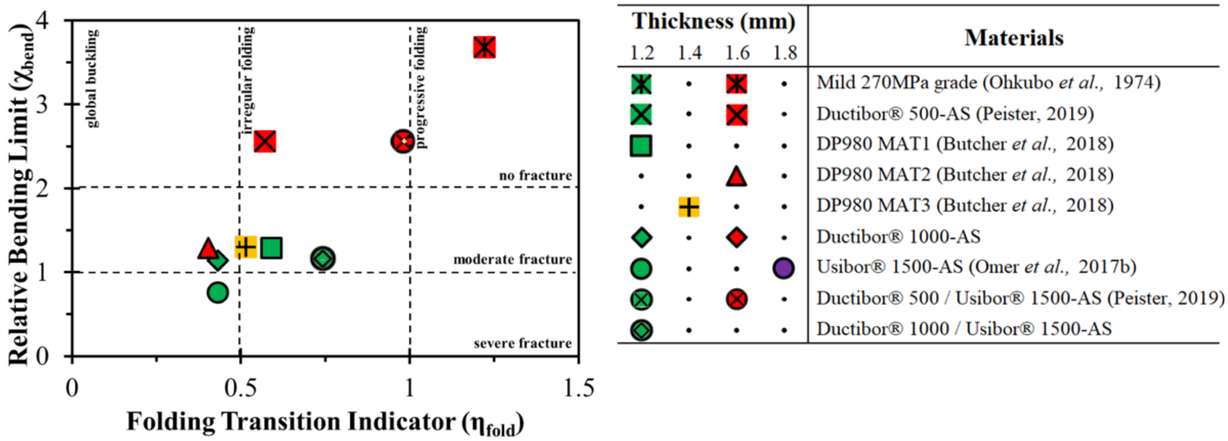

Figure 142: A 2D response map of Relative Bending Limit (χ_{bend}) *vs.* Folding Transition Indicator (η_{fold}) for the monolithic and TWB crush specimens for which material fracture data (v-bend) was available.

Finally, as noted in Section 5.4, the Folding Transition Indicator may be limited to specific column geometries beyond the baseline (BA) cases in the current dataset. This aspect is examined in Figure 143 in which the data in Figure 141 from the previous published studies corresponding to the BA initiator pattern (black symbols) is replotted along with the current Ductibor® 1000-AS results (Chapter 4) using the BA pattern (solid symbols) and the TF initiator pattern (open symbols). The response for the 1.2 mm TF specimens (green symbols) corresponds to the improved initiator spacing of 27.5 mm, while the 1.6 mm TF specimens (red symbols) are for a spacing of 30 mm. The results in Figure 143 clearly demonstrate the benefit of the improved initiator design (TF pattern) in shifting the response from global buckling to irregular or progressive folding for the 1.2 mm thickness and from mixed folding and buckling to progressive folding for the 1.6 mm thickness. In essence, the improved initiators enable stable collapse such that the material is loaded in such as manner as to reach its full bending (folding) potential, reflected in values of Relative Bending Limit of just over unity for the 1.2 mm Ductibor® 1000-AS material.

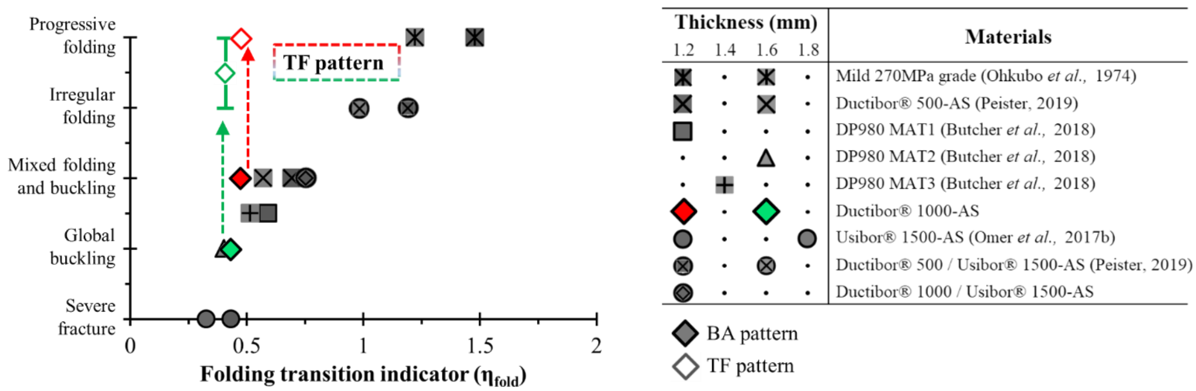

Figure 143: Modified plot of deformation mode *vs.* η_{fold}. The black symbols are from Figure 141. The red and green symbols represent 1.2 mm and 1.6 mm Ductibor® 1000-AS specimens, respectively. The solid and open symbols represent the BA and TF patterns, respectively.

The improved deformation mode in TF patterns can be explained in terms of a reduction in the effective column length. To demonstrate this point, Figure 144 shows the side view images taken immediately following the sled impact for the 1.2 mm BA specimen (repeat #1) that globally buckled, as well as the 1.2 mm TF specimen (repeat #1) that progressively folded. In the TF specimen, the immediate formation of multiple folds is exhibited as the stress wave travels and is evidenced by the pronounced wavy pattern on its sidewall. Essentially, this multiple lobe formation splits the entire column into separate folding zones. It is speculated that this reduces the effective column length from the column length L (500 mm) to the height of each fold, equal to the fold initiator spacing ($2H_{indent}$) (27.5 mm).

(a) baseline
(BA repeat #1)

(b) TF
(TF repeat #1)

Figure 144: Side view images of the baseline and TF specimens from the dynamic experiments, at the crush displacement corresponding to initial peak force in F-D graphs. The corresponding times for the images taken are 0.078 s and 0.070 s for BA and TF, respectively, which are measured relative to the trigger of the data acquisition unit (see Figure 63).

6.0 Conclusions and Recommendations

6.1. Conclusions

The research work presented herein aims to promote the progressive folding mode in axial crush components comprising hot-stamped UHSS. The experimental tasks have served to validate an analysis-driven design method to identify a successful fold initiator pattern, namely Pattern TF. In addition, performance metrics have been developed to predict three aspects of axial crush for a particular material and axial crush geometry, namely (i) Crush Energy Efficiency, (ii) Relative Bending Limit, (iii) Folding Transition Indicator. The conclusions stemming from this research are as follows:

1. The baseline, dynamic axial crush performance of 1.2 mm Ductibor® 1000-AS was characterized in terms of deformation mode, initial peak force, energy absorption, and fracture extent. All three repeat cases of the baseline specimen exhibited a global buckling mode with moderate fracture at the sidewall of the initial fold. The measured peak force was 479 kN, and the absorbed energy was 14.7 kJ and 21.9 kJ at 165 mm and 250 mm crush displacement, respectively.

2. The numerical model of the baseline dynamic axial crush rail accurately predicted the observed global buckling response with an initial peak force of 492 kN and absorbed energy of 23.2 kJ at 250 mm displacement. These predictions were within 2.7 % and 5.9 % of the measured values, respectively.

3. The numerical simulation of the dynamic axial crush response considering six distinct fold initiator patterns revealed four different deformation modes, listed here in order of increasing collapse stability: (i) global buckling, (ii) mixed folding and buckling, (iii) irregular folding and (iv) progressive folding. Of all fold initiator patterns considered, the TCA (Top-Consecutive-Asymmetric), TF (Top-Flange), and TFO (Top-Flange-Offset) patterns predicted the progressive folding mode.

4. The fold initiator spacing also exerted a significant influence on the predicted folding stability, as quantified using the L_2 stability analysis. The use of the TF initiator pattern, at a spacing of 27.5 mm and 30 mm for the 1.2 and 1.6 mm thickness channels, resulted in regular folding and reduced the predicted extent of fracture over that seen using the baseline, single fold initiator

pattern. These spacings correspond to those identified using the SE analysis due to Wierzbicki and Abramowicz (1983).

5. The validation experiments considering the TF fold initiator pattern correlated well with the model predictions for the 1.6 mm thick channels using the simplified “displacement approach” to introduce the fold initiators into the model geometry.

6. The distortion caused by the flange indentation process was shown to have a severe impact in promoting buckling instability, particularly for the 1.2 mm TF specimens. Once the fold initiator indentation process (and distortion) was introduced into the axial crush models, good model-experiment correlation was achieved for the 1.2 mm (and 1.6 mm) TF specimens.

7. Increased folding stability was achieved at the cost of slightly lower energy absorption. For example, the 1.2 mm TF specimens showed a 5.9% reduction in energy absorption compared to the baseline. There was also a 21 % reduction in the peak force, which for some applications may be viewed as beneficial (*e.g.* in reduction of impulse to vehicle occupants).

8. The new performance metrics, namely Relative Bending Limit and Folding Transition Indicator, were successfully demonstrated to be predictors of the fracture extent and deformation mode for baseline configuration hat section axial crush columns encompassing a range of steel grades with UTS values between 270 MPa and 1500 MPa.

6.2. Recommendations

The following recommendations stem from the current research:

1. To reduce the geometric distortion effect, it is strongly recommended to incorporate the fold initiators into the hot stamping dies for future experiments concerning repeating fold initiator patterns. Furthermore, the TF specimens in Parts 2 and 3 should be retested using such improved tooling.
2. The effect of spot weld strength and spot weld placement on the crush performance requires further examination.
3. In the thesis, fold initiator patterns were placed, beginning at 70 mm away from the impact-end. Such a design decision was for consistency with previous axial crush studies (Peister, 2019; Omer *et al.,* 2017b). The effect of the number of initiators and initial offset of the first initiator location relative to the impacted end of the column should be evaluated.
4. To extend the validation of the crush performance metrics developed in Chapter 5, additional data is required for a range of slenderness ratios and materials. In particular, new 3^{rd} generation steels as well as aluminum alloys should be considered in order to encompass a range of strength, fracture resistance and sheet thickness.
5. As for the double hat section, axial crush components comprising UHSS, it is recommended that stable repeating fold initiator patterns be adopted, such as the current TF pattern, to promote stable folding and potentially limit onset of fracture.
6. The effect of cross-section proportions (*e.g.* flange width and section aspect ratio) on the deformation mode and stability requires further investigation.

References

Abedini, A., (2018). Constitutive and Fracture Characterization of an Anisotropic and Asymmetric Alloy Sheet, PhD thesis, University of Waterloo.

Abedini, A., (2018). Private Communication.

Abedini, A., Butcher, C., Worswick, M., (2018). Experimental Fracture Characterisation of an Anisotropic Magnesium Alloy Sheet in Proportional and Non-proportional loading conditions, *International Journal of Solids and Structures*, 144-145, 1-19.

Abedini, A., Butcher, C., (2020). Private Communication.

Abramowicz, W., (1983). The Effective Crushing Distance in Axially Compressed Thin-Walled Metal Columns, *International Journal of Impact Engineering*, 1(3), 309-317.

Abramowicz, W., Jones, N., (1984). Dynamic Axial Crushing of Square Tubes, *International Journal of Impact Engineering*, 2(2), 179-208.

Abramowicz, W., Jones, N., (1986). Dynamic Progressive Buckling of Circular and Square Tubes, *International Journal of Impact Engineering*, 4(4), 243-270.

Abramowicz, W., Wierzbicki, T., (1989). Axial Crushing of Multicorner Sheet Metal Columns, *Journal of Applied Mechanics*, 56(1), 113-120.

Abramowicz, W., Jones, N., (1997). Transition from Initial Global Bending to Progressive Buckling of Tubes Loaded Statically and Dynamically, *International Journal of Impact Engineering*, 19(5-6), 415-437.

Abramowicz, W., (2003). Thin-Walled Structures as Impact Energy Absorbers, *Thin-Walled Structures*, 41(2), 91-107.

Alexander, J.M., (1960). An Approximate Analysis of the Collapse of Thin Cylindrical Shells under Axial Loading, *The Quarterly Journal of Mechanics and Applied Mathematics*, 13(1), 10-15.

American Honda Motor Co., (2016). *2016 Civic: New Model Body Repair Information* [online]. Available at: https://techinfo.honda.com/rjanisis/pubs/web/ABN02539.PDF (Accessed: 16 April 2020).

ArcelorMittal, (2021). Private Communication.

ArcelorMittal, (2016a). *Stress-Strain Curves Hot Forming Steels – Ductibor® 500 Treated* [online]. Available at: https://automotive.arcelormittal.com/files/Ductibor500--bac52373b9ba5e7cb8e80922dba4a6a4.pdf (Accessed: 16 April 2020).

ArcelorMittal, (2016b). *Stress-Strain Curves Hot Forming Steels – Ductibor® 1000 Treated* [online]. Available at: https://automotive.arcelormittal.com/files/Ductibor1000--42232ac6bc73f560a5c18a99582d6c56.pdf (Accessed: 16 April 2020).

ArcelorMittal, (2016c). *Stress-Strain Curves Hot Forming Steels – Usibor® 1500 Treated* [online]. Available at: https://automotive.arcelormittal.com/files/Usibor1500--3a82a9aa69487763bbbba1a960151cc0.pdf (Accessed: 16 April 2020).

ArcelorMittal, (2016d). *Stress-Strain Curves Hot Forming Steels – Usibor® 2000 Treated* [online]. Available at: https://automotive.arcelormittal.com/files/Usibor2000--52a44f48942ccc670a1877266f069a61.pdf (Accessed: 24 Jan 2021)

ArcelorMittal North America, (2019). *Dual Phase Steels Data Sheet* [online]. Available at: https://usa.arcelormittal.com/~/media/Files/A/Arcelormittal-USA-V2/what-we-do/price-list/2019-03-datasheet-dualphase-final.pdf (Accessed: 16 April 2020).

Archer, J.S., (1965). Consistent Matrix Formulations for Structural Analysis using Finite Element Techniques, *Journal of the American Institute of Aeronautics and Astronautics*, 3(10), 1910-1918.

Bai, Y., Wierzbicki, T., (2008). A New Model of Metal Plasticity and Fracture with Pressure and Lode Dependence, *International Journal of Plasticity*, 24(6), 1071-1096.

Bai, Y., Wierzbicki, T., (2010). Application of Extended Mohr-Coulomb Criterion to Ductile Fracture, *International Journal of Fracture*, 161(1), 1-20.

Bardelcik, A., Worswick, M., Winkler, S., Wells, M., (2012). A Strain Rate Sensitive Constitutive Model for Quenched Boron Steel with Tailored Properties, *International Journal of Impact Engineering*, 50, 49-62.

Bardelcik, A., Worswick, M., Wells, M., (2014). The Influence of Martensite, Bainite, and Ferrite on the As-Quenched Constitutive Response of Simultaneously Quenched and Deformed Boron Steel – Experiments and Model, *Materials & Design*, 55, 509-525.

Basaran, M., Wölkerling, S.D., Feucht, M., Neukamm, F., Weichert, D., (2010). An Extension of the GISSMO Damage Model Based on Lode Angle Dependence, In *9th LS-DYNA Anwenderforum*, Bamberg, Germany.

Berglund, G., (2008). The History of Hardening of Boron Steel in Northern Sweden, In *1st International Conference on Hot Sheet Metal Forming of High-Performance Steel*, Kassel, Germany, 175-177.

Bergström, Y., (2015). The Plastic Deformation Process of Metals – 50 Years Development of a Dislocation Based Theory.

Bergström, Y., (1983). The Plastic Deformation of Metals—A Dislocation Model and its Applicability, *Reviews on Powder Metallurgy and Physical Ceramics*, 2(2-3), 79-265.

Billur, E., Cetin, B., Yilmaz, M.M., Oguz., A.G., Atay, A., Ersoy, K., Uguz, R.O., Kaftanoglu, B., (2015). Forming of New Generation AHSS Using Servo Presses, In *5th International Conference on Accuracy in Forming Technology*, Chemnitz, Germany.

Billur, E., (2019). Hot Stamping of Ultra High-Strength Steels, Switzerland: Springer Nature Switzerland AG, 1-18.

Børvik, T., Hopperstad, O.S., Berstad, T., Langseth, M., (2001). A Computational Model of Viscoplasticity and Ductile Damage for Impact and Penetration, *European Journal of Mechanics – A/Solids*, 20(5), 685-712.

Butcher, C., (2019). Private Communication.

Butcher, C., (2020). Private Communication.

Caron, E., Daun, K., Wells, M., (2013). Heat Transfer Coefficient Characterization during Hot Forming Die Quenching of Boron Steel Blanks, In *4th International Conference on Hot Sheet Metal Forming of High-Performance Steel*, Luleå, Sweden.

Chen, W., Deng, X., (2000). Performance of Shell Elements in Modeling Spot-welded Joints, *Finite Elements Analysis and Design*, 35(1), 41-57.

Chen, W., (2001). Crashworthiness Optimization of Ultralight Metal Structures, PhD thesis, Massachusetts Institute of Technology.

Chen, Y., Faruque, O., Xia, C., Akkerman, A., Lam, D., (2014). Meso-Scale FEA Modeling to Simulate Crack Initiation and Propagation in Boron Steel, In *13th International LS-DYNA Users Conference*, Michigan, USA.

Cheong, D-W.K., (2019a). On the Influence of the Through-Thickness Strain Gradients for Characterization of Formability and Fracture of Sheet Metal Alloys, Master's thesis, University of Waterloo.

Cheong, D-W.K., (2019b). Private Communication.

Courant, R., Friedrichs, K., Lewy, H., (1928). Über die partiellen Differenzengleichungen der mathematischen Physik, *Mathematische Annalen*, 100(1), 32-74.

Dreas, K.V., (1998). Spot Weld Modeling for Crash Computations, Requirements and New Functionalities in LS-dyna version 940, In *The Fifth International LS-DYNA Users Conference*, Southfield, USA.

Edmonds, D.V., He, K., Rizzo F.C., De Cooman, B.C., Matlock, D.K., Speer, J.G., (2006). Quenching and Partitioning Martensite—A Novel Steel Heat Treatment, *Materials Science and Engineering: A*, 438-440, 25-34.

Eller, T.K., Greve, L., Andres, M.T., Medricky, M., Hatscher, A., Meinders, V.T., van den Boogaard, A.H., (2014). Plasticity and Fracture Modeling of Quench-Hardenable Boron Steel with Tailored Properties, *Journal of Materials Processing Technology*, 214(6), 1211-1227.

Eren, I., Gür, Y., Aksoy, Z., (2009). Finite Element Analysis of Collapse of Front Side Rails with New Types of Crush Initiators, *International Journal of Automotive Technology*, 10(4), 451-457.

Fenech, H., (1959). Thermal Conductance of Metallic Surfaces in Contact, PhD thesis, Massachusetts Institute of Technology.

Fish, J., Belytschko, T., (2007). A First Course in Finite Elements, Chichester: John Wiley & Sons Ltd., 113-121.

Fyllingen, Ø., Hopperstad, O.S., Hanssen, A.G., Langseth, M., (2010). Modelling of Tubes Subjected to Axial Crushing, *Thin-Walled Structures*, 48(2), 134-142.

George, R., (2011). Hot Forming of Boron Steels with Tailored Mechanical Properties: Experiments and Numerical Simulations, Master's thesis, University of Waterloo.

George, R., Bardelcik, A., Worswick, M., (2012). Hot Forming of Boron Steels Using Heated and Cooled Tooling for Tailored Properties, *Journal of Materials Processing Technology*, 212(11), 2386-2399.

Gray III, G.T., Chen, S.R., Wright, W., Lopez, M.F., (1994). Constitutive Equations for Annealed Metals under Compression at High Strain Rates and High Temperatures, Report LA-12669-MS, Los Alamos National Laboratory.

Grzebieta, R.H., (1990). An Alternative Method for Determining the Behaviour of Round Stocky Tubes Subjected to an Axial Crush Load, *Thin-Walled Structures*, 9(1-4), 61-89.

Gurson, A.L., (1977). Continuum Theory of Ductile Rupture by Void Nucleation and Growth: Part I—Yield Criteria and Flow Rules for Porous Ductile Media, *Journal of Engineering Materials and Technology*, 99(1), 2-15.

Hancock, J.W., Mackenzie, A.C., (1976). On the Mechanisms of Ductile Failure in High-Strength Steels Subjected to Multi-Axial Stress-States, *Journal of the Mechanics and Physics of Solids*, 24(2-3), 147-160.

Hayduk, R., Wierzbicki, T., (1984). Extensional Collapse Modes of Structural Members, *Computers & Structures*, 18(3), 447-458.

Hilfrich, E., Seidner, D., (2008). Crash Safety with High Strength Steels, In *International Automotive Congress*, Shengyang, China.

Hockett, J.E., Sherby, O.D., (1975). Large Strain Deformation of Polycrystalline Metals at Low Homologous Temperatures, *Journal of the Mechanics and Physics of Solids*, 23(2), 87-98.

Hollomon, J.H., (1945). Tensile Deformation, *Transaction of American Institute of Mechanical Engineering*, 162, 268-290.

Hosseinipour, S.J., Daneshi, G.H., (2003). Energy Absorbtion and Mean Crushing Load of Thin-Walled Grooved Tubes under Axial Compression, *Thin-Walled Structures*, 41(1), 31-46.

Hovorun, T.P., Berladir, K.V., Pererva, V.I., Rudenko, S.G., Martynov A.I., (2017). Modern Materials for Automotive Industry, *Journal of Engineering Sciences*, 4(2), F8-F18.

Hu, P., Liang, Y., He, B., (2017). Hot Stamping Advanced Manufacturing Technology of Lightweight Car Body, Singapore: Springer Singapore, 165-178.

Imbert, J., Zhumagulov, A., (2018). Private Communication.

ISO 16630:2017, (2017). Metallic Materials — Sheet and Strip — Hole Expanding Test.

Iyengar, N.G.R., (1988). Structural Stability of Columns and Plates, John Wiley and Sons.

James, M.L., Smith, G.M., Wolford, J.C., (1985). Applied Numerical Methods for Digital Computation, New York: Harper & Row.

Jia, Y., Bai, Y., (2016). Experimental Study on the Mechanical Properties of AZ31B-H24 Magnesium Alloy Sheets under Various Loading Conditions, *International Journal of Fracture*, 197, 25-48.

Johnson, G.R., Cook, W.H., (1983). A Constitutive Model and Data for Metals Subjected to Large Strains, High Strain Rates and High Temperatures, *Proceedings of the 7th International Symposium on Ballistics*, The Hague, The Netherlands, 541-547.

Johnson, G.R., Cook, W.H., (1985). Fracture Characteristics of Three Metals Subjected to Various Strains, Strain Rates, Temperatures and Pressures, *Engineering Fracture Mechanics*, 21(1), 31-48.

Karbasian, H., Tekkaya, A.E., (2010). A Review on Hot Stamping, *Journal of Materials Processing Technology*, 210(15), 2103-2118.

Khan, A., Huang, S., (1995). Continuum Theory of Plasticity, New York: John Wiley & Sons, Inc., 2-13.

Krabbenhoft, K., (2002). Basic Computational Plasticity, Technical University of Denmark, Copenhagen.

Langseth, M., Hopperstad, O.S., Berstad, T., (1999). Crashworthiness of Aluminum Extrusions: Validation of Numerical Simulation, Effect of Mass Ratio and Impact Velocity, *International Journal of Impact Engineering*, 22(9-10), 829-854.

Lee, S., Hahn, C., Rhee, M., Oh, J-E., (1999). Effect of Triggering on the Energy Absorption Capacity of Axially Compressed Aluminum Tubes, *Materials and Design*, 20(1), 31-40.

Lee, S.H., Peister, C., Abedini A., Imbert, J., Butcher, C., Worswick, M., Soldaat, R., Bernert, W., Famchon, E., Penner, P., Yau, C., Malcolm, S., Dykeman, J., (2019). Dynamic Axial Crush Response of Ductibor® 1000-AS - Effect of Fold Initiator Pattern on Performance, In *7th International Conference on Hot Sheet Metal Forming of High-Performance Steel*, Luleå, Sweden.

Lemaitre, J., (1985). A Continuous Damage Mechanics Model for Ductile Fracture, *Journal of Engineering Materials and Technology*, 107(1), 83-89.

Li, L., Wollants, P., He, Y.L., De Cooman, B.C., Wei, X.C., Xu, Z.Y., (2003). Review and Prospect of High Strength Low Alloy TRIP Steel, *ACTA Metallurgica Sinica (English Letters)*, 16(6), 457-465.

Livermore Software Technology Corporation, (2016). LS-DYNA® Keyword User's Manual, Livermore: Livermore Software Technology Corporation.

Logan, D.L., (2012). A First Course in the Finite Element Method, 4th ed., Toronto: Thomson Canada Ltd., 329-342.

Lorenz, D., Haufe, A., (2008). Recent Advances and New Developments in Hot Forming Simulation with LS-DYNA, In *7th LS-DYNA Anwenderforum*, Bamberg, Germany.

Lu, G., Yi, T.X., (2003). Energy Absorption of Structures and Materials, Cambridge: Woodhead Publishing, 55-57.

Ma, J., (2011). Thin-Walled Tubes with Pre-Folded Origami Patterns as Energy Absorption Devices, PhD thesis, University of Oxford.

Maker, B.N., Zhu, X., (2000). Input Parameters for Metal Forming Simulation using LS-DYNA, Livermore Software Technology Corporation.

Malcolm, S., Nutwell, E., (2007). Spotweld Failure Prediction Using Solid Element Assemblies, In *6th European LS-Dyna user's Conference*, Gothenburg, Sweden.

Matzenmiller, A., Schweizerhof, K., Rust, W., (1994). Joint Failure Modeling in Crashworthiness Analysis, In *The Second International LS-DYNA 3D Conference*, San Francisco, USA.

McClintock, F.A., (1968). A Criterion for Ductile Fracture by the Growth of Holes, *Journal of Applied Mechanics*, 35(2), 363-371.

McGregor, I.J., Meadows, D.J., Scott, C.E., Seeds, A.D., (1993). Impact Performance of Aluminium Structures, In Jones, N., Wierzbicki, T., Structural Crashworthiness and Failure, London: Elsevier Science Publishers LTD., 385-418.

Merklein, M., Lechler, J., (2008). Determination of Material and Process Characteristics for Hot Stamping Processes of Quenchenable Ultra High Strength Steels with Respect to a FE-based Process Design, *SAE International Journal of Materials and Manufacturing*, 1(1), 411-426.

Merklein, M., Lechler, J., Stoehr, T., (2009). Investigations on the Thermal Behavior of Ultra High Strength Boron Manganese Steels within Hot Stamping, *International Journal of Material Forming*, 2(1), 259-262.

Merklein, M., Johannes, M., Lechner, M., Kuppert, A., (2014). A Review on Tailored Blanks – Production, Applications and Evaluation, *Journal of Materials Processing Technology*, 214, 151-164.

Mohamadizadeh, A., Biro, E., Worswick, M., (2020). Shear Band Formation at the Fusion Boundary and Failure Behaviour of Resistance Spot Welds in Ultra-high-strength hot-stamped steel, *Science and Technology of Welding and Joining,* 25(7), 556-563.

Mori, K., Bariani, P.F., Behrens, B.-A., Brosius, A., Bruschi, S., Maeno, T., Merklein, M., Yanagimoto, J., (2017). Hot Stamping of Ultra-High Strength Steel Parts, *CIRP Annals – Manufacturing Technology*, 66(2), 755-777.

Múnera, D., Pic, A., Abou-Khalil, D., Shmit, F., Pinard, F., (2008). Innovative Press Hardened Steel Based Laser Welded Blanks Solutions for Weight Savings and Crash Safety Improvements, *SAE International Journal of Materials and Manufacturing*, 1(1), 472-479.

Najafi, A., Rais-Rohani, M., (2008). Influence of Cross-Sectional Geometry on Crush Characteristics of Multi-Cell Prismatic Columns, In *49th AIAA/ASME/ASC/AHS/ASC Structures, Structural Dynamics and Materials Conference*, Schaumburg, IL.

Najafi, A., (2009). Axial Collapse of Thin-Walled, Multi-Corner Single- and Multi-Cell Tubes, Master's thesis, Mississippi State University.

Najafi, A., Rais-Rohani, M., (2011). Mechanics of Axial Plastic Collapse in Multi-Cell, Multi-Corner Crush Tubes, *Thin-Walled Structures*, 49, 1-12.

Nakagawa, Y., Mori, K-I., Maeno, T., (2018). Springback-free Mechanism in Hot Stamping of Ultra-High-Strength Steel Parts and Deformation Behaviour and Quenchability for Thin Sheet, *International Journal of Advanced Manufacturing Technology*, 95, 459-467.

Nakazima, K., Kikuma, T., Hasuka, K., (1968). Study on the Formability of Steel Sheets. *Yamata Technical Report*, 264, 8517-8530.

National Highway Traffic Safety Administration, (2021). 49 C.F.R § 531.5.

Neukamm, F., Feucht, M., Haufe, A., (2009). Considering Damage History in Crashworthiness Simulations, In *7th European LS-DYNA Conference*, At Salzburg, Austria.

Newmark, N.M., (1959). A Method of Computation for Structural Dynamics, *Journal of the Engineering Mechanics Division*, 85(3), 67-94.

Noder, J., Butcher, C., (2019). A Comparative Investigation into the Influence of the Constitutive Model on the Prediction of in-Plane Formability for Nakazima and Marciniak Tests, *International Journal of Mechanical Sciences*, 163, 105138.

Noder, J., Butcher, C., (2020). Private Communication.

Noder, J., Dykeman, J., Butcher, C., (2020). New Methodologies for Fracture Detection of Automotive Steels in Tight Radius Bending: Application to the VDA 238-100 V-bend Test. *Experimental Mechanics*, 61, 367-394.

Ohkubo, Y., Akamatsu, T., Shirasawa, K., (1974). Mean Crushing Strength of Closed-Hat Section Members, SAE Technical Paper 740040.

O'Keeffe, C., (2018). Investigation of Resistance Spot Weld Failure in Tailored Hot Stamped Assemblies. Master's thesis, University of Waterloo.

Oldenburg, M., Lindkvist, G., (2011). Tool Thermal Cycle Design for Manufacturing of Components with Tailored Material Properties, In *3rd International Conference on Hot Sheet Metal Forming of High-Performance Steel*, Kassel, Germany.

Omer, K., (2014). Development and Testing of a Hot Stamped Axial Crush Member with Tailored Properties, Master's thesis, University of Waterloo.

Omer, K., George, R., Bardelcik, A., Worswick, M., Malcolm, S., Detwiler, D., (2017a). Development of a Hot Stamped Channel Section with Axially Tailored Properties – Experiments and Models, *International Journal of Material Forming*, 11, 149-164.

Omer, K., ten Kortenaar, L., Butcher, C., Worswick, M., Malcolm, S., Detwiler, D., (2017b). Testing of a Hot Stamped Axial Crush Member with Tailored Properties – Experiments and Models, *International Journal of Impact Engineering*, 103, 12-28.

Omer, K., Butcher, C., Worswick, M., (2020). Characterization of Heat Transfer Coefficient for Non-isothermal Elevated Temperature Forming of Metal Alloys, *International Journal of Material Forming*, 13, 177-201.

Östlund, R., (2015). Microstructure Based Modelling of Ductile Fracture in Quench-Hardenable Boron Steel, PhD thesis, Luleå University of Technology.

Östlund, R., Golling, S., Oldenburg, M., (2016). Microstructure Based Modeling of Ductile Fracture Initiation in Press-Hardened Sheet Metal Structures, *Computer Methods in Applied Mechanics and Engineering*, 302, 90-108.

Paluszny, A., (1992). State-of-the-Art Review of Automobile Structural Crashworthiness, Report, American Iron and Steel Institute.

Pan, F., Zhu, J., Helminen, A.O., Vatanparast, R., (2006). Three Point Bending Analysis of a Mobile Phone Using LS-DYNA Explicit Integration Method, In *9th International LS-DYNA Users Conference*, Michigan, USA.

Park, S., Ahn, I., Kim, S., (2018). A Study on Modeling Technique for Spot Weld with Sheet Metal Fracture in the Passenger Car 2nd Seat/Belt Anchorage Test, *Transactions of the Korean Society of Automotive Engineers*, 26(5), 605-611.

Peirs, J., Verleysen, P., Degrieck, J., (2012). Novel Technique for Static and Dynamic Shear Testing of Ti6Al4V Sheet. *Experimental Mechanics*, 52, 729-741.

Peister, C., O'Keeffe, C., Imbert, J., Butcher, C., Worswick, M., Malcolm, S., Dykeman, J., Yau, C., Soldaat, R., Bernert, W., (2018). Dynamic and Quasi-Static Testing and Modeling of Hot Stamped Tailor-Welded Axial Crush Rails, In *The 18th International Conference on Experimental Mechanics,* Brussels, Belgium.

Peister, C., (2019). Axial Crush Performance of Hot Stamped Tailor Welded Blanks – Experiments and Numerical Simulations. Master's thesis, University of Waterloo.

Peixinho, N., Soares, D., Vilarinho, C., Pereira, P., Dimas, D., (2012). Experimental Study of Impact Energy Absorption in Aluminum Square Tubes with Thermal Triggers, *Materials Research*, 15(2), 323-332.

POSCO, (2014). *Automotive Steel Data Book* [online]. Available at: http://product.posco.com (Accessed: 7 June 2020).

Rahmaan, T., (2015). Low to High Strain Rate Characterization of DP600, TRIP780, AA5182-O, Master's thesis, University of Waterloo.

Rahmaan, T., Abedini, A., Butcher, C., Pathak, N., Worswick, M.J., (2017). Investigation into the Shear Stress, Localization and Fracture Behaviour of DP600 and AA5182-O Sheet Metal Alloys under Elevated Strain Rates, *International Journal of Impact Engineering*, 108, 303-321.

Reid, S.R., Reddy, T.Y., (1986). Static and Dynamic Crushing of Tapered Sheet Metal Tubes of Rectangular Cross-Section, *International Journal of Mechanical Sciences*, 28(9), 623-637.

Rice, J.R., Tracey, D.M., (1969). On the Ductile Enlargement of Voids in Triaxial Stress Fields, *Journal of the Mechanics and Physics of Solids*, 17(3), 201-217.

Salomonsson, O., Oldenburg, M., (2009). Investigation of Heat Transfer in the Press Hardening Process, In *2nd International Conference on Hot Sheet Metal Forming of High-Performance Steel*, Luleå, Sweden.

Salomonsson, P., Oldenburg, M., Åkerström, P., Bergman, G., (2009). Experimental and Numerical Evaluation of Heat-transfer Coefficient in Press Hardening, *Steel Research International*, 80(11), 841-845.

Samadian, P., (2018). Private Communication.

Samadian, P., Wells, M., Worswick, M., (2018). Constitutive Modelling of the Flow Behavior of the Different Microstructures of Ductibor®500 Steel, In *2nd International Conference on Impact Loading of Structures and Materials*, Xi'an, China.

Samadian, P., Butcher, C., Worswick, M., (2019). The Determination of the Fracture Behavior of the Different Microstructures of Ductibor® 500-AS Steel, In *7th International Conference on Hot Sheet Metal Forming of High-Performance Steel*, Luleå, Sweden.

Samadian, P., Abedini, A., (2020). Private Communication.

Samadian, P., ten Kortenaar, L., Omer, K., Butcher, C., Worswick, M., (2020). Fracture Characterization of Tailored Usibor® 1500-AS and Damage Modelling Based on a Coupled-Micromechanical-Phenomenological Strategy, *Engineering Fracture Mechanics*, 223.

Samadian, P., Butcher, C., Worswick, M., (2020b). Microstructures and Flow Behavior of Ductibor® 500-AS Steel for a Range of As-Quenched Conditions, *Journal of Materials Engineering and Performance*, 29, 7153-7169.

Samek, L., Krizan, D., (2012). Steel - Material of Choice for Automotive Lightweight Applications, In *International Conference on Metallurgy and Materials*, Brno, Czech Republic.

Santosa, S.P., Wierzbicki, T., Hanssen, A.G., Langseth, M., (2000). Experimental and Numerical Studies of Foam-Filled Sections, *International Journal of Impact Engineering*, 24(5), 509-534.

Shapiro, A., (2008). Using LS-DYNA to Model Hot Sheet Metal Stamping, In *1st International Conference of Hot Sheet Metal Forming of High-Performance Steel*, Kassel, Germany.

Speer, J.G., Matlock, D.K., De Cooman, B.C., Schroth, J.G., (2003). Carbon Partitioning into Austenite after Martensite Transformation, *Acta Materialia*, 51(9), 2611-2622.

Suresh, K., Regalla, S.P., (2014). Effect of Time Scaling and Mass Scaling in Numerical Simulation of Incremental Forming, *Applied Mechanics and Materials*, 612, 105-110.

Taylor, K.A., Hansen, S.S., (1990). The Boron Hardenability Effect in Thermomechanically Processed, Direct-Quenched 0.2 Pct C Steels, *Metallurgical Transactions A*, 21, 1697-1708.

Taylor, K.A., (1992). Grain-Boundary Segregation and Precipitation of Boron in 0.2 Percent Carbon Steels, *Metallurgical Transactions A*, 23, 107-119.

Taylor, G.I., (1934). The Mechanism of Plastic Deformation of Crystals. Part I.—Theoretical, *Proceedings of the Royal Society A*, 145(855), 362-387.

Tekkaya, A.E., Karbasian, H., Homberg, W., Kleiner, M., (2007). Thermo-Mechanical Coupled Simulation of Hot Stamping Components for Process Design, *Production Engineering - Research and Development*, 1, 85-89.

ten Kortenaar, L., (2016). Failure Characterization of Hot Formed Boron Steels with Tailored Mechanical Properties, Master's thesis, University of Waterloo.

Toksoy, A.K., Güden, M., (2010). Partial Al Foam Filling of Commercial 1050H14 Al Crash Boxes: The Effect of Box Column Thickness and Foam Relative Density on Energy Absorption, *Thin-Walled Structures*, 48(7), 482-494.

Tolton, C.J., (2020). Characterization of Spot Weld Failure within Weld Groups under Predominantly Shear Loading, Master's thesis, University of Waterloo.

Tummers, M., Omer, K., Abedini, A., Peister, C., Butcher, C., Worswick, M.J., Malcolm, S., Yau, C., Soldaat, R., (2018). Introduction of a 1000 MPa Crush Tip within a Usibor® 1500-AS Axial Crush Rail Using in-Die Heated Hot Stamping, In *37th Conference of International Deep Drawing Research Group*, Waterloo, Canada.

Tummers, M., (2020). Development of a Tailor-Welded Hot Stamped Side Frame Member, Master's thesis, University of Waterloo.

Tvergaard, V., Needleman, A., (1984). Analysis of the Cup-Cone Fracture in a Round Tensile Bar, *Acta Metallurgica*, 32(1), 157-169.

United States Environmental Protection Agency, (2012). EPA and NHTSA Set Standards to Reduce Greenhouse Gases and Improve Fuel Economy for Model Years 2017-2025 Cars and Light Trucks [online]. Available at: https://nepis.epa.gov/Exe/ZyPDF.cgi/P100EZ7C.PDF?Dockey=P100EZ7C.PDF (Accessed: 16 April 2020).

van den Boogaard, A.H., (2002). Thermally Enhanced Forming of Aluminium Sheet Modelling and Experiments, PhD thesis, University of Twente.

VDA 238-100, (2017). Plate Bending Test for Metallic Materials.

Voce, E., (1948). The Relationship between Stress and Strain for Homogeneous Deformation, *Journal of the Institute of Metals*, 74(11), 537-562.

von Mises, R., (1913). Mechanik der festen Körper im plastisch-deformablen Zustand. *Nachrichten von der Gesellschaft der Wissenschaften zu Göttingen*. Mathematisch-Physikalische Klasse. 1, 582-592.

Waldock, W.D., (1997). A Brief History of "Crashworthiness", In *SAFE Association Symposium*, Phoenix, Arizona.

White, M.D., Jones, N., Abramowicz, W., (1999). A Theoretical Analysis for the Quasi-Static Axial Crushing of Top-Hat and Double-Hat Thin-Walled Sections, *International Journal of Mechanical Sciences*, 41(2), 209-233.

White, M.D., Jones, N., (1999). A Theoretical Analysis for the Dynamic Axial Crushing of Top-Hat and Double-Hat Thin-Walled Sections, *Proceedings of the Institution of Mechanical Engineeirng, Part D: Journal of Automobile Engineers*, 213, 307-325.

White, M.D., Jones, N., (1999). Experimental Quasi-Static Axial Crushing of Top-Hat and Double-Hat Thin-Walled Sections, *International Journal of Mechanical Sciences*, 41(2), 179-202

Wierzbicki, T., Abramowicz, W., (1983). On the Crushing Mechanics of Thin-Walled Structures, *Journal of Applied Mechanics*, 50(4a), 727-734.

Wierzbicki, T., Bhat, S.U., Abramowicz, W., Brodkin, D., (1992). Alexander Revisited—A Two Folding Elements Model of Progressive Crushing of Tubes, *International Journal of Solids and Structures*, 29(24), 3269-3288.

Wierzbicki, T., Xue, L., (2005). On the Effect of the Third Invariant of the Stress Deviator on Ductile Fracture, Report 136, Impact and Crashworthiness Laboratory.

Witteman, W.J., (1999). Improved Vehicle Crashworthiness Design by Control of the Energy Absorption for Different Collision Situations, PhD thesis, Technische Universiteit Eindhoven.

Xiang, Y., Wang, Q., Fan, Z., Fang, H., (2006). Optimal Crashworthiness Design of a Spot-welded Thin-walled Hat Section, *Finite Elements in Analysis and Design*, 42(10), 846-855.

Xue, L., (2003). Chain Link Model for Axially Crushed Thin-Walled Tubes, PhD thesis, Massachusetts Institute of Technology.

Ye, L., Lu, G., Yang, J.L., (2011). An Analytical Model for Axial Crushing of a Thin-Walled Cylindrical Shell with a Hollow Foam Core, *Thin-Walled Structures*, 49(11), 1460-1467.

Zerilli, F.J., Armstrong, R.W., (1987). Dislocation-Mechanics-Based Constitutive Relations for Material Dynamics Calculations, *Journal of Applied Physics*, 61(5), 1816-1825.

Zhang, X.W., Su, H., Yu, T.X., (2009). Energy Absorption of an Axially Crushed Square Tube with a buckling Initiator, *International Journal of Impact Engineering*, 36(3), 402-417.

Zhang, X., Huh, H., (2010). Crushing Analysis of Polygonal Columns and Angle Elements, *International Journal of Impact Engineering*, 37(4), 441-451.

Zhumagulov, A., (2017). Crashworthiness and Material Characterization of Multi-cellular AA6063 Extrusions, Master's thesis, University of Waterloo.

Zhumagulov, A., Abedini, A., Rahmaan, T., Imbert, J., Butcher, C., Worswick, M., Malcolm, S., Dykeman, J., Hesham, E., (2018). High Rate Characterization of Three DP980 Steels. In *DYMAT 2018 – 12th International Conference on the Mechanical and Physical Behaviour of Materials under Dynamic Loading*, Arcachon, France.

Appendix A. Solution Procedure for Superfolding Element Analysis

This section serves as a review of the Superfolding Element Analysis (SEA) developed by Wierzbicki and Abramowicz (1983), whose solution procedure solves for the theoretical wavelength ($2H$), plastic work in the horizontal bending zone ($W_{SE,bend}$), and the crush mean force (P_m). The novelty of the work presented here lies in modifying the fundamental SE model to account for the hardening behaviour of a UHSS material, namely, Ductibor® 1000-AS, which is the studied material in the experimental program. Additionally, the SE Analysis was extended to account for other alloys such as 270 MPa mild steel grade, Ductibor® 500-AS, DP 980, and Usibor® 1500-AS. The predicted responses ($2H$, $W_{SE,bend}$, and P_m) for all of these alloys are presented at the end of this section.

The SEA begins with the work balance between plastic internal (E_{int}) and external energy (W_{ext}) in crushing a Superfolding Element as follows:

$$W_{ext} = E_{\text{int}} \tag{A.1}$$

The external energy is simply the mean force (P_m) multiplied by the effective crush distance (δ_e).

$$W_{ext} = P_m \delta_e \tag{A.2}$$

The total plastic internal energy (E_{int}) is calculated by summing the internal energy due to quasi-inextensional deformation (E_1 to E_3) and that due to extensional deformation (E_4 to E_6). These energy values, respectively, are associated with the (1) toroidal surface, (2) horizontal bending surface, (3) inclined rolling surface, (4) conical surface, (5) horizontal bending surface, and (6) inclined cylindrical surface, as shown in Figure A.1.

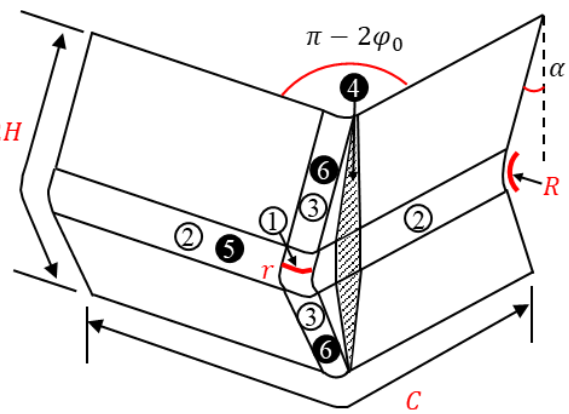

Figure A.1: Illustration of the Superfolding Element and its constitutive surfaces 1 to 6. The surface elements from quasi-inextensional mode (white) and extensional mode (black) are coloured separately for distinguishment.

The significant aspect of the analysis lies in finding the internal dissipated plastic energy, which is defined as

$$E_{\text{int}} = \int_0^{\bar{\alpha}} \dot{E}_{\text{int}} d\alpha + \int_{\bar{\alpha}}^{\alpha_f} \dot{E}_{\text{int}} d\alpha = \sum_{i=1}^{6} E_i \tag{A.3}$$

Where α is the current crush angle, $\bar{\alpha}$ is the transition angle at which the mode switches from the quasi-inextensional mode to the extensional mode and α_f is the final crush angle. The analysis carried out by Abramowicz and Wierzbicki (1989) gives the internal energy associated with each region as

(1) Toroidal extension $$E_1 = 16M_{SE,1}\frac{Hr}{t}I_1(\varphi_o,\bar{\alpha}) \tag{A.4}$$

(2) Horizontal hinge $$E_2 = 2M_{SE,2}C\bar{\alpha} \tag{A.5}$$

(3) Incline hinge $$E_3 = 4M_{SE,3}\frac{H}{r}I_3(\varphi_o,\bar{\alpha}) \tag{A.6}$$

(4) Conical extension $$E_4 = 4M_{SE,4}\frac{H^2}{t}I_4(\varphi_o,\bar{\alpha}) \tag{A.7}$$

(5) Horizontal hinge $$E_5 = 2M_{SE,5}C(\alpha_f - \bar{\alpha}) \tag{A.8}$$

(6) Inclined hinge $$E_6 = M_{SE,6}HI_6(\varphi_o,\bar{\alpha}) \tag{A.9}$$

With geometric constants I_1 to I_6, which appear from rigorous kinematic analysis

$$
\begin{aligned}
I_1 &= \sin\bar{\alpha}\int_0^{\beta(\bar{\alpha})}\frac{d\Phi}{\sqrt{\tan^2\varphi_o+\cos^2\Phi}}-\left[\frac{\pi}{2}-\varphi_o-\tan^{-1}\left(\frac{\cos\beta(\bar{\alpha})}{\tan\varphi_o}\right)\right] \text{ or} \\
&= \int_0^{\frac{\pi}{2}}\frac{d\Phi}{\sqrt{\tan^2\varphi_o+\cos^2\Phi}}-\left(\frac{\pi}{2}-\varphi_o\right) \text{ if } \bar{\alpha}=\frac{\pi}{2}
\end{aligned}
\tag{A.10}
$$

$$
I_3 = \cot\varphi_o\int_0^{\bar{\alpha}}\cos\alpha\sqrt{\tan^2\varphi_o+\sin^2\alpha}\,d\alpha \tag{A.11}
$$

$$
I_4 = \int_{\bar{\alpha}}^{\alpha_f}\left[\frac{\sin\bar{\alpha}\tan\varphi_o\sin 2\alpha}{2\left(\sin^2\bar{\alpha}+\tan^2\varphi_o\sin^2\alpha\right)}+\left(\varphi-\varphi_o\right)\cos\alpha\right]d\alpha \tag{A.12}
$$

$$
I_6 = 2\cot\varphi_o\int_{\bar{\alpha}}^{\alpha_f}\frac{\sin\bar{\alpha}\left(\sin^2\bar{\alpha}+\tan^2\varphi_o\right)}{\sin^2\bar{\alpha}+\tan^2\varphi_o\sin^2\alpha}d\alpha \tag{A.13}
$$

and SE base length (C), half folding wavelength (H), corner angle (φ_o) and crush angle (α) are defined in Figure A.1. Note that the pseudo-bending moment term, $M_{SE,1}$, in Equation (A.4) appears due to a re-arrangement of the term $\frac{1}{4}t^2N_{SE,1}$ for convenience in which $N_{SE,1}$ is the uniaxial stress. There is virtually no bending occurring in the toroidal surface because the larger radius (R) along the meridian direction is assumed fixed. Only uniaxial "stretching" occurs along the circumferential direction (along r) (Wierzbicki and Abramowicz, 1983).

For theoretical prediction of mean crushing force of the double hat channel, the SE analysis can be extended to model the double hat cross-section as eight joined SEs as illustrated in Figure A.2. Hence, in the analysis of the double hat channel, the right side of Equation (A.1) is multiplied by 8, giving

$$
W_{ext} = 8E_{\text{int}} \tag{A.14}
$$

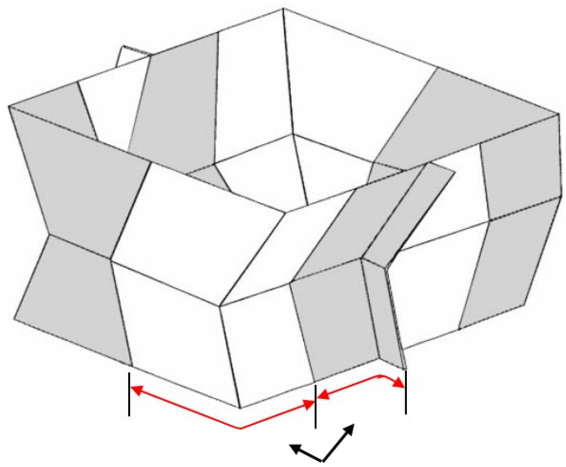

Figure A.2: Illustration of double hat cross-section modelled by eight (8) joined Superfolding Elements (White *et al.*, 1999). Z refers to the entire mid-shell perimeter of the double hat cross-section, which is eight times the base length of the SE ($8 \times C$).

Furthermore, for a SE with $\varphi_o \leq \pi/4$ (acute or right angle), the main governing deformation mode is known to be quasi-inextensional rather than extensional (Abramowicz, 2003). Hence, $\alpha_f = \bar{\alpha}$ can be assumed to be $\pi/2$. With such an assumption, the energy contribution from the extensional modes (E_4 to E_6) vanishes. Subsequent insertion of Equation (A.2) and Equation (A.3)-(A.9) into Equation (A.14) yields the following:

$$\frac{P_m \delta_e}{2H} = \left\{ M_{SE,1} A_1 \frac{r}{t} + M_{SE,2} A_2 \frac{C}{H} + M_{SE,3} A_3 \frac{H}{r} \right\} \tag{A.15}$$

in which C is the entire base length of the SE, and evaluated as one-eighth of Z—the mid-shell cross-section perimeter of the double hat (defined in Figure A.2). The energy equivalent plastic bending moment at the i^{th} region, $M_{SE,i}$, and constants— A_1, A_2, A_3— are defined as

$$M_{SE,i} = \frac{\sigma_{SE,i} t^2}{4} \tag{A.16}$$

$$A_1 = 64 I_1 ; A_2 = 16 \alpha_f ; A_3 = 16 I_3 \tag{A.17}$$

in which $\sigma_{SE,i}$ is the energy equivalent flow stress at the i^{th} region, and $I_1 = 0.567$, and $I_3 = 1.173$ are obtained by using the initial corner angle of the studied geometry ($\varphi_o = 42.5°$ as shown in Figure 38) in Equation (A.10) and (A.11). Fully expanding the plastic bending moment ($M_{SE,i}$) in Equation (A.15) finally gives the mean crushing force

$$\frac{P_m \delta_e}{2H} = \frac{t^2}{4}\left\{\sigma_{SE,1} A_1 \frac{r}{t} + \sigma_{SE,2} A_2 \frac{C}{H} + \sigma_{SE,3} A_3 \frac{H}{r}\right\} \tag{A.18}$$

The collapse mechanism of a SE follows the minimum energy principle; that is to say, the crushing process requires the least possible amount of the crush force (Wierzbicki and Abramowicz, 1983). Thus, Equation (A.18) can be minimized with respect to half wavelength (H) and toroidal radius (r) while treating the flow stresses ($\sigma_{SE,1}$ to $\sigma_{SE,3}$) as some known constants

$$\frac{\partial}{\partial H}\left(\frac{P_m \delta_e}{2H}\right) = 0, \ \frac{\partial}{\partial r}\left(\frac{P_m \delta_e}{2H}\right) = 0 \tag{A.19}$$

Solving Equation (A.19) gives the closed-form solutions of H, r and P_m:

$$H = \left(\frac{\sigma_{SE,2}^2}{\sigma_{SE,3}\sigma_{SE,1}} \frac{A_2^2}{A_3 A_1} C^2 t\right)^{\frac{1}{3}} \tag{A.20}$$

$$r = \left(\frac{\sigma_{SE,3}\sigma_{SE,2}^2}{\sigma_{SE,1}^2} \frac{A_3 A_2}{A_1^2} C t^2\right)^{\frac{1}{3}} \tag{A.21}$$

$$P_m = \frac{3}{4} t^{5/3} \left[\left(\sigma_{SE,1}\sigma_{SE,2}\sigma_{SE,3}\right)\left(A_1 A_2 A_3\right)\left(C\right)\right]^{1/3} \tag{A.22}$$

The observation drawn from Equation (A.22) is two-fold. First, the mean force of the Superfolding Element depends on its geometric properties (*e.g.,* thickness) as well as material properties (*e.g.* plastic flow stresses). Also, the exponent of t, 5/3, in Equation (A.22) arises from the fact that two-thirds of the internal plastic energy dissipation comes from inextensional mode such as bending (Wierzbicki and Abramowicz, 1983)—an important finding that the crush performance correlates with the bending performance of a material.

A.1. Perfectly Plastic Assumption

If one assumes a rigid, perfectly plastic material behaviour and replaces plastic flow stress terms in Equation (A.20) and (A.21) with the yield stress (σ_y), the flow stress-dependent terms reduce to unity. Similarly, the first parenthesis in Equation (A.22) reduces to the first-order yield stress. Further manipulation results in the same solution by White *et al.* (1998):

$$H = \left(\frac{A_2^2}{A_3 A_1} C^2 t \right)^{\frac{1}{3}} \approx 0.247 Z^{2/3} t^{1/3} \tag{A.1.1}$$

$$r = \left(\frac{A_3 A_2}{A_1^2} C t^2 \right)^{\frac{1}{3}} \approx 0.358 Z^{1/3} t^{2/3} \tag{A.1.2}$$

$$P_m = \frac{3}{4} \sigma_y t^{5/3} \left[\left(A_1 A_2 A_3 \right) \left(C \right) \right]^{1/3} \approx 52.20 \sigma_y t^{5/3} Z^{1/3} \tag{A.1.3}$$

in which Z is the mid-shell cross-sectional perimeter of the double hat ($Z = 8C$) illustrated in Figure A.2, and A_1 to A_3 can be found using Equation (A.17).

A.2. Hardening Assumption

As Wierzbicki and Schneider (1999) pointed out, one of the major sources of error in the mean force prediction from the SE analysis, relative to experimental values, is the calculation of the energy equivalent flow stresses. These so-called energy equivalent flow stresses represent the average plastic stress in the uniaxial flow or bending and are derived from the isotropic and perfectly plastic material assumptions. Their expressions are given by Wierzbicki and Abramowicz (1987) as

(Uniaxial in toroidal surface along r) $$\sigma_{SE,1} = \frac{1}{\varepsilon_{SE,1}} \int_0^{\varepsilon_{SE,1}} \bar{\sigma}\left(\bar{\varepsilon}_p, \dot{\varepsilon}\right) d\bar{\varepsilon}_p \tag{A.2.1}$$

(Horizontal bending about R) $$\sigma_{SE,2} = \frac{2}{\left(\varepsilon_{SE,2}\right)^2} \int_0^{\varepsilon_{SE,2}} \bar{\sigma}\left(\bar{\varepsilon}_p, \dot{\varepsilon}\right) \bar{\varepsilon}_p d\bar{\varepsilon}_p \tag{A.2.2}$$

(Inclined bending about r) $$\sigma_{SE,3} = \frac{2}{\left(\varepsilon_{SE,3}\right)^2} \int_0^{\varepsilon_{SE,3}} \bar{\sigma}\left(\bar{\varepsilon}_p, \dot{\varepsilon}\right) \bar{\varepsilon}_p d\bar{\varepsilon}_p \tag{A.2.3}$$

in which $\bar{\varepsilon}_p$ is the current equivalent plastic strain; $\varepsilon_{SE,1}$ to $\varepsilon_{SE,3}$ are the final plastic strains in the outer surfaces of toroidal, horizontal bending, and inclined bending zones, respectively; and $\bar{\sigma}(\bar{\varepsilon}_p, \dot{\varepsilon})$ is the flow stress obtained by a strain rate sensitive hardening model.

The above integrals will be referred to as "plastic work integrals" for convenience. Note that the $\varepsilon_{SE,i}^2$ terms in Equation (A.2.2) and (A.2.3) appear due to the change from expressing the flow stress in terms of bending moments to expressions in terms of stresses. Lastly, the final plastic strains and the average strain rate are expressed (Abramowicz, 1997; Wierzbicki and Abramowicz, 1989) as

$$\varepsilon_{SE,1} = \varepsilon_{SE,3} \approx \ln\left(1 + \frac{t}{2r}\right) \tag{A.2.4}$$

$$\varepsilon_{SE,2} \approx \ln\left(1 + \frac{t}{2R}\right) \tag{A.2.5}$$

$$R \approx 0.54H \tag{A.2.6}$$

$$\dot{\varepsilon}_{avg} \approx \frac{t\left(v_i / 2\right)}{4Hr} \tag{A.2.7}$$

in which R is the larger radius of the toroidal surface defined in Figure A.1, $\dot{\varepsilon}_{avg}$ is the average strain rate in the SE (Abramowicz and Wierzbicki, 1989), and v_i is the initial impact velocity in the axial crush event.

The expressions for H, r, and P_m can now be solved with the flow stresses obtained from (A.2.1) to (A.2.7), but one challenge remains: solving the plastic work integral.

The solution of the integral can be made tractable if one assumes a power-law type hardening model, as done by White *et al.* (2008), but, for high strength steels, such a model can result in a significant error (*i.e.* R^2) in capturing the stress-strain behaviour. As an alternative, the Modified Hockett-Sherby model (Equation (39)), which better describes the hardening response, can be inserted into Equation (A.2.1) to (A.2.3). The plastic integral, then, becomes

$$\int_0^{t/2r} \left[C_1 - \left(C_1 - C_2\right)\exp\left(-C_3\left(\bar{\varepsilon}_p\right)^{C_4}\right) + C_5\sqrt{\bar{\varepsilon}_p} \right] d\bar{\varepsilon}_p \tag{A.2.8}$$

whose closed-form solution does not exist. Hence, utilizing a numerical method such as the trapezoidal rule is inevitable to carry out the calculations for energy equivalent flow stresses.

Once the energy equivalent flow stress at the horizontal bend (surface 2 in Figure A.1) is obtained, its theoretical bend work ($W_{SE,bend}$) can be calculated in terms of the plastic bending moment $M_{SE,bend}$

$$W_{SE,bend} = M_{SE,bend}\alpha_f \tag{A.2.9}$$

with the fully plastic relation

$$M_{SE,bend} = \frac{\sigma_{SE,2}t^2}{4} \tag{A.2.10}$$

A.3. Numerical Solution Procedure

The numerical analysis used in this section is the Newton-Raphson method, in which the roots of residual functions (f_i) are iteratively solved using the function derivatives. The solution procedure is outlined in the flowchart in Figure A.3. The first step in the method is identifying the system of variables, which are the half-wavelength (H) and the toroidal radius (r), in the SE problem. Next, the residual functions of the variables can be set from Equations (A.1.1) and (A.1.2):

$$f_1 = H - \left(\frac{\sigma_{SE,2}^2}{\sigma_{SE,3}\sigma_{SE,1}} \frac{A_2^2}{A_3 A_1} C^2 t \right)^{\frac{1}{3}} \tag{A.3.1}$$

$$f_2 = r - \left(\frac{\sigma_{SE,3}\sigma_{SE,2}^2}{\sigma_{SE,1}^2} \frac{A_3 A_2}{A_1^2} C t^2 \right)^{\frac{1}{3}} \tag{A.3.2}$$

More conveniently, the residual functions and the variables can be expressed in vector forms, and the Jacobian matrix ($\boldsymbol{J}$) is formulated:

$$\mathbf{f} = \begin{bmatrix} f_1 & f_2 \end{bmatrix}^{\mathrm{T}} \tag{A.3.3}$$

$$\mathbf{v} = \begin{bmatrix} H & r \end{bmatrix}^{\mathrm{T}} \tag{A.3.4}$$

$$J_{i,j} = \frac{\partial f_i}{\partial v_j} \tag{A.3.5}$$

in which i and j are indices of the Einstein notation. By combining Equations (A.3.3) to (A.3.5), a system of three equations are established and the subsequent estimates of the roots ($\boldsymbol{v_{i+1}}$) are increased by

$$\mathbf{\Delta v} = \mathbf{J}^{-1}\mathbf{f} \tag{A.3.6}$$

using the following relationship

$$\mathbf{v}_{i+1} = \mathbf{v}_i + \mathbf{\Delta v} \tag{A.3.7}$$

Once the roots are updated, the solution process repeats until the pre-determined convergence condition is met (*i.e.* $|\boldsymbol{v}_{i+1} - \boldsymbol{v}_i| \leq tolerance$). The Newton-Raphson algorithm depicted in Figure A.3 is solved using MATLAB® custom script in Appendix B, which was developed as the part of the current research work.

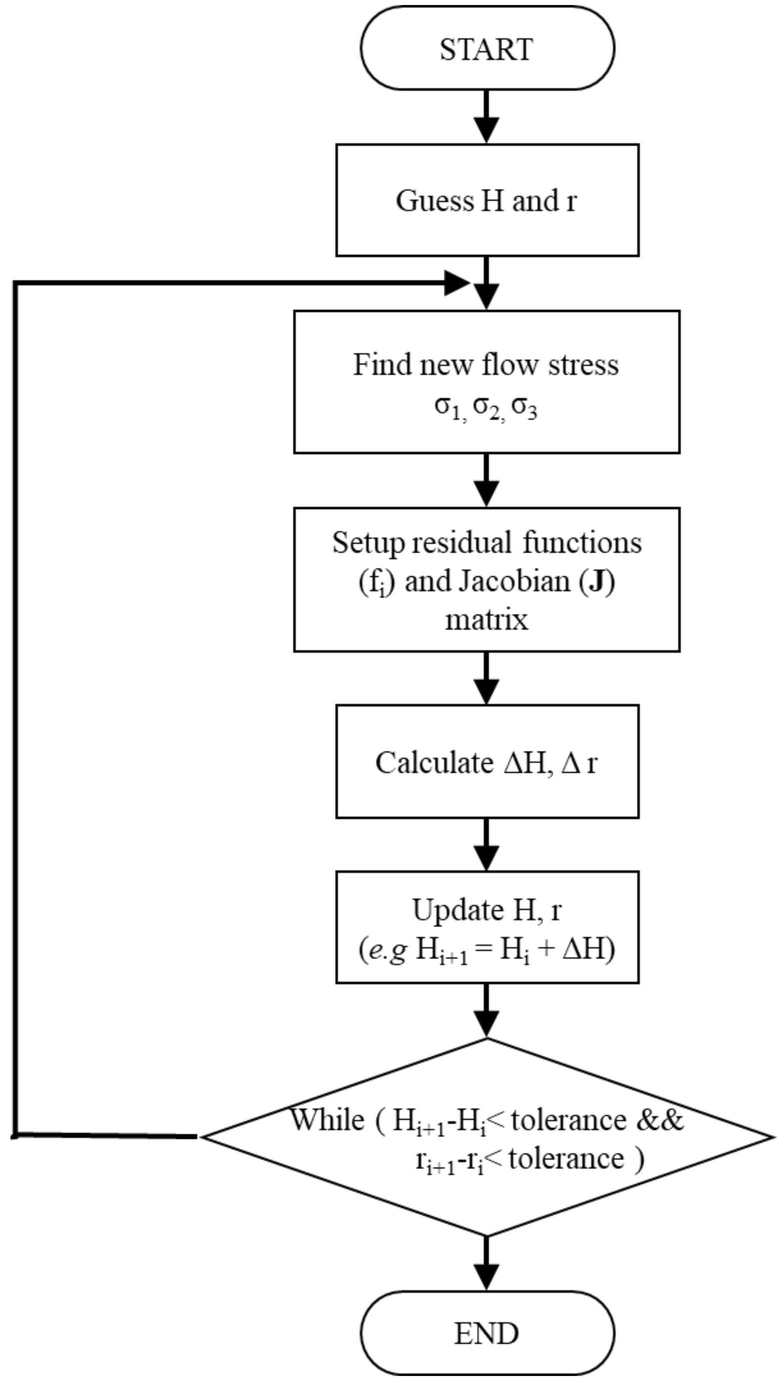

Figure A.3: Flow chart illustration of the Newton-Raphson method used in solving the SE analysis. The initial estimate used for *H* and *r* was 100, while the tolerances for both system variables were set as 0.01.

The solutions to the toroidal radius (r) and folding wavelength (2H) obtained for hot-stamped Ductibor® 1000-AS, as well as five other alloys, are plotted against the sheet thickness range from 1.0 to 1.8 mm in Figure A.4 and Figure A.5.

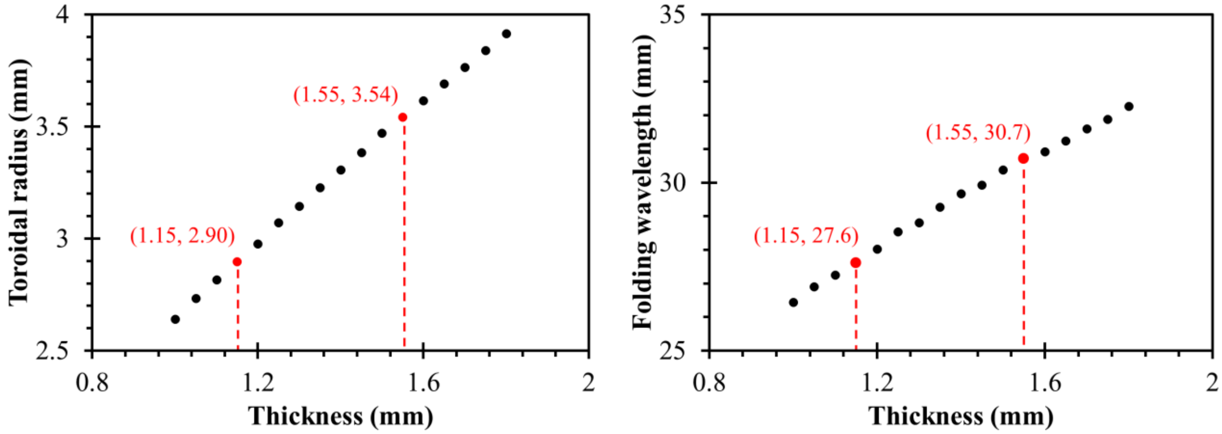

(a) toroidal radius (r) (b) folding wavelength (2H)

Figure A.4: Theoretical prediction of SE system variables: (a) toroidal radius (r) and (b) folding wavelength (2H) plotted against sheet thickness (t) for die-quenched Ductibor® 1000-AS. The predicted toroidal radius are 2.9 mm and 3.54 mm, while the folding wavelengths are 27.6 mm and 30.7 mm for 1.15 mm and 1.55 mm thick sheets, respectively.

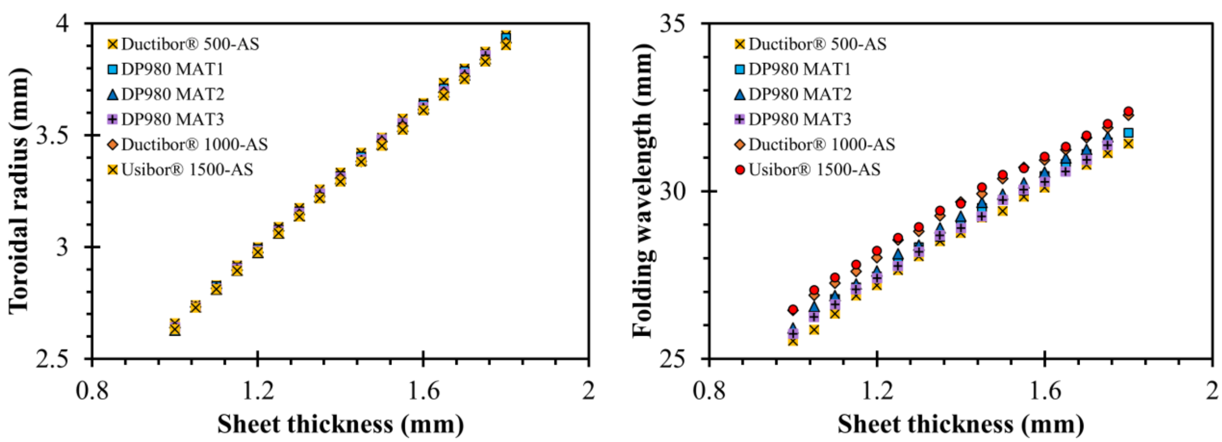

(a) toroidal radius (r) (b) folding wavelength (2H)

Figure A.5: Theoretical prediction of SE system variables: (a) toroidal radius (r) and (b) folding wavelength (2H) plotted against sheet thickness (t) for six different steel alloys. I_1, I_3 were assumed as 0.567 and 1.173 in the solution, given $\varphi_o = 42.5°$ (see Figure A.1)

The general trend in Figure A.5 shows that higher strength alloy possesses a higher predicted folding wavelength at a given sheet thickness. However, the maximum difference amongst the alloys is within 2 mm at a given thickness, indicating that the folding wavelength is weakly dependent on the material property. The mean crushing force (P_m) for each alloy is plotted against the sheet thickness (t) in Figure A.6. Self-evidently, the mean crush force ranking of these alloys follows that of their UTS levels.

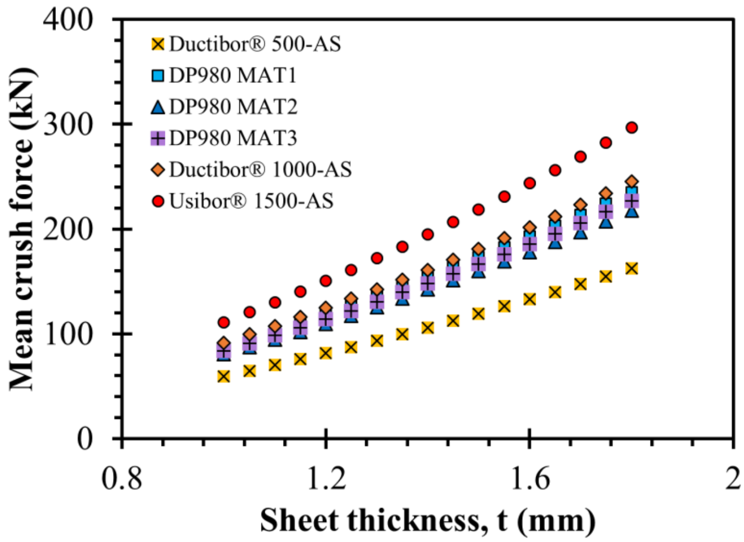

Figure A.6: Theoretical prediction of mean crushing force (P_m) plotted against sheet thickness (t) for six different steel alloys, which is obtained from the SE analysis.

Appendix B. MATLAB® Source Code for SE Analysis

This section presents the MATLAB® custom source code used to carry out the solution procedure of SE analysis in Appendix A. The script consists of three parts—(I) the main program, which executes the Newton-Raphson function and updates the solution results into an array, (II) the Newton-Raphson function, which uses an iterative approach to find the root of H and r, as illustrated in Figure A.3 and (III) a set of other functions, which return SE geometric constants or flow stresses based on different hardening models of given materials. The primary tasks within each part are listed below.

I. Main program

- Call **Geometric constant function** to obtain SE constants: A_1, A_2, A_3, C
- Define dynamic properties: v_i, v_m
- Call **Newton-Raphson function**
- Update SE solutions (r, $2H$, P_m, $\varepsilon_{SE,bend}$, $W_{SE,bend}$) into a list for each material

II. Newton-Raphson function

- Step 0: Declare all system variables ($H, r,$) and constants (A_1, A_2, A_3, C)
- Step 1: Initial guess for H, r
- Step 2: Find new energy equivalent plastic flow stresses ($\sigma_{SE,1}$, …, $\sigma_{SE,3}$)
- Step 3: Setup residual functions (f_1, f_2) and Jacobian matrix (J)
- Step 4: Calculate ΔH and Δr
- Step 5: Update H and r
- Step 6: Compute additional solutions (P_m, $\varepsilon_{SE,bend}$, $W_{SE,bend}$)
- Step 7: Check convergence criterion for H and r; if not met, return to Step 2.

III. Other functions

i. Geometric constant function

- Return A_1, A_2, A_3, C given the final crush angle (α_f), geometric integrals (I_1, I_3) and the mid-shell cross-section perimeter (Z)

ii. Hardening functions: MHS / VOCE / MGV / POWER

- Return flow stress ($\bar{\sigma}$), given the equivalent plastic strain ($\bar{\varepsilon}_p$), and the average strain rate ($\dot{\varepsilon}_{avg}$)

The following sub-appendices (**B.1**) to (**B.3**) serve as documentation for each part of the source code.

B.1. Main Program

```
clc;
clear all;

%***************************************************************************%
%
% AUTHOR: Suh Ho Lee
% DATE: Jan. 20, 2020
% PURPOSE: Calculate following properties using the SE Analysis (SEA):
%
%    1. Toroidal radius           (r)
%    2. Folding Wavelength        (2H)
%    3. Mean crushing force       (Pm)
%    4. Eq. plastic bend strain   (epsilon_bend)
%    5. Horizontal bending Energy (Ebend)
%
% LIST OF HARDENING MODELS CONSIDERED (characterized by)
%
%    1. Mild 270      (Noder et al., 2020)
%    2. Ductibor 500  (Samadian et al., 2020)
%    3. Ductibor 1000 (Abedini et al., 2020)
%    4. Usibor 1500   (Bardelcik et al., 2012)
%    5. DP980 MAT1    (Noder and Buthcer, 2019)
%    6. DP980 MAT2    (Zhumagulov et al., 2018)
%    7. DP980 MAT3    (Zhumagulov et al., 2018)
%
%***************************************************************************%

%******************************START OF THE PROGRAM**********************%

% LIST OF CONSIDERED MATERIALS
    mat = ["270", "D500", "D1000", "U1500", "DP980_MAT1" , "DP980_MAT2",...
          "DP980_MAT3" ];

% DEFINE HARDENING RULE FOR EACH MATERIAL
    hrule = ["MHS", "MHS", "MHS", "VOCE", "MHS", "MGV", "POWER"];

% DEFINE GEOMETRIC CONSTANTS
    geom_const = get_geom(mat); % get A1,A2,A3 and C for Eq. A.17
    t = 1.0;                    % initial sheet thickness

% DEFINE DYNAMIC PROPERTIES
    vi = repmat(7.6*10^3, 1, 7);  % impact velocity for Waterloo UHHS(mm/s)
    vi(1) = 4.13 * 10^3; % impact velocity for mild 270(Ohkubo et al.,1974)
    vm = vi / 2;                  % mean velocity due to Abramowicz (1983)

%% THICKNESS LOOP FROM t = 1mm to 1.85mm
    i=1; %material index
    j=1; %thickness loop index

    while t<=1.85
```

```
    % for each material
    for i=1:length(mat)

        % conduct SE Analysis
        [r,H,Pm,epsilon_bend,Ebend] = SEA(t,mat(i),geom_const(i,:),...,
                                         hrule(i), vm(i));

        % store SEA results into a list
        if i==1      % for Mild 270
            Mild270_list(j,:) = {t, r, 2*H, Pm, epsilon_bend, Ebend};

        elseif i==2 % for Ductibor 500-AS
            Duct500_list(j,:) = {t, r, 2*H, Pm, epsilon_bend, Ebend};

        elseif i==3 % for Ductibor 1000-AS
            Duct1000_list(j,:) = {t, r, 2*H, Pm, epsilon_bend, Ebend};

        elseif i==4 % for Usibor 1500-AS
            Usib1500_list(j,:) = {t, r, 2*H, Pm, epsilon_bend, Ebend};

        elseif i==5 % for DP980 MAT 1
            DP980_MAT1_list(j,:) = {t, r, 2*H, Pm, epsilon_bend, Ebend};

        elseif i==6 % for DP980 MAT 2
            DP980_MAT2_list(j,:) = {t, r, 2*H, Pm, epsilon_bend, Ebend};

        elseif i==7 % for DP980 MAT 3
            DP980_MAT3_list(j,:) = {t, r, 2*H, Pm, epsilon_bend, Ebend};
        end
    end

    t = t + 0.05; % 0.05 mm thickness increment
    j = j+1;      % move onto next material in the list
end
```

B.2. Newton-Raphson Function

```
function [r,H,Pm, epsilon_bend, Ebend] = SEA(t, mat, geom_const, hrule, vm)
%% SOLVE SE Analysis using Newton-Raphson Method

    % STEP 0: Declare variables and constants
    syms H r                % main variables
    syms sig1 sig2 sig3     % energy equivalent flow stresses
    syms int_1 int_2 int_3  % plastic work integrals for zone 1,2,3

    var = [H, r];         % Variable vector for Eq. A.3.4
    J = sym(zeros(2,2)); % Jacobian matrix for Eq. A.3.5

    A1 = geom_const(1); % Constants in Eq. A.17
    A2 = geom_const(2);
    A3 = geom_const(3);
    C = geom_const(4);

    % symbolic variables for residual functions
    f1 = H - ( sig2^2 / (sig3*sig1) * A2^2 / (A3*A1) * C^2 * t)^(1/3);
    f2 = r - (sig3*sig2/sig1^2)^(1/3) * (A3*A2/A1^2)^(1/3) * (C*t^2)^(1/3);

    m = 100;      %num. of iteration pts.
    tol1 = 0.01; % H convergence tolerance
    tol2 = 0.01; % r convergence tolerance

    % STEP 1: Initial guess for H, r
    x(1) = 100; % guess high > 30
    y(1) = 100; % guess high > 30

    % Start of the newton-raphson loop
    for i=1:m

        % new H & r
        H = x(i);
        r = y(i);

        % STEP 2: Find new SIG1, SIG2, SIG3

        % 2a. calculate final strains in zone 1,2,3
        eps1_final = log( 1 + t/(2*double(subs(r))) );     % Equation A.2.4

        eps2_final = log( 1 + (0.926*t/double(subs(H))) );% Equation A.2.5
        eps2_final = 2/3 * sqrt( 3*(eps2_final^2 + eps2_final^2)/2 );

        eps3_final = log( 1 + t/(2*double(subs(r))) );     % Equation A.2.4
        eps3_final = 2/3 * sqrt( 3*(eps3_final^2 + eps3_final^2)/2 );

        % 2b. calculate average strain rate in the SE
        e_dot = t * vm / double(4*subs(H)*subs(r));       % Equation A.2.7

        % 2c. compute "plastic work integrals"
```

```
% initialize the ranges of plastic strain (0,eps_final)
st_inc = 0.0005;
ep1 = 0.0005:st_inc:eps1_final;
ep2 = 0.0005:st_inc:eps2_final;
ep3 = 0.0005:st_inc:eps3_final;

% initialize the ranges of flow stress
if hrule == "MHS"
    flow = MHS(mat, ep1, e_dot);
    flow2= MHS(mat, ep2, e_dot);
    flow3= MHS(mat, ep3, e_dot);
elseif hrule == "VOCE"
    flow  = VOCE(ep1, e_dot);
    flow2 = VOCE(ep2, e_dot);
    flow3 = VOCE(ep3, e_dot);
elseif hrule == "MGV"
    flow  = MGV(ep1, e_dot);
    flow2 = MGV(ep2, e_dot);
    flow3 = MGV(ep3, e_dot);
elseif hrule == "POWER"
    flow  = POWER(ep1, e_dot);
    flow2 = POWER(ep2, e_dot);
    flow3 = POWER(ep3, e_dot);
end

% compute kernels inside the "plastic work integral"
kernel_1 = flow;          % integral kernel in Eq. A.2.1
kernel_2 = flow2 .* ep2; % integral kernel in Eq. A.2.2
kernel_3 = flow3 .* ep3; % integral kernel in Eq. A.2.3

% compute "plastic work integrals" by trapezoidal method
int_1 = trapz(ep1,kernel_1);
int_2 = trapz(ep2,kernel_2);
int_3 = trapz(ep3,kernel_3);

% 2d. compute energy equivalent flow stresses
sig1= 1 / (eps1_final) * int_1;   % per Eq. A.2.1.
sig2= 2 / (eps2_final)^2 * int_2; % per Eq. A.2.2.
sig3= 2 / (eps3_final)^2 * int_3; % per Eq. A.2.3.

% STEP 3: Setup Residual functions (f1, f2) and Jacobian Matrix (J)
f = [f1, f2]; % residual functions

for k=1:2 % loop to setup Jacobian matrix
    for l=1:2
        J(k,l) = diff ( f(k),var(l) );
    end
end

% STEP 4: Calculate new H and new r
Jnum = double(subs(J));
f = double(subs(f.'));
ans = [x(i); y(i)] - inv(Jnum) * f;

% STEP 5: Update H and r
```

```
        x(i+1) = ans(1); %new H
        y(i+1) = ans(2); %new r

        % STEP 6: Compute Pm, epsilon_bend, Ebend
        % 6a. mean force
        Pm = t^2/4 * (sig1 * A1 * r/t + sig2 * A2 ...
             * C / H + sig3 * A3 * H / r);

        % 6b. plastic bend strain
        epsilon_bend = eps2_final;

        % 6c. theoretical SE bend work
        Ebend = sig2 * t^2 / 4 * pi/2;

        %error message for non-convergence
        if m==99
           frptinf('not converged \n')
        end

        % STEP 7: Check for convergence criteria for H, r
        if abs(x(i+1)-x(i)) < tol1 && abs(y(i+1)-y(i)) < tol2
             % if converged,
             break; %get out of the loop
        end
    end % convergence reached
end
```

B.3. Other Functions

B.3.1. Geometric Constant Function

```
function [geom_const] = get_geom(mat)
%% Calculate SEA Constants A1, A2, A3, and C

    num_mat = length(mat);
    geom_const = zeros(num_mat, 4);

    % Define geometric constants
    alpha_f = pi/2;      % Assume final crush angle as 90 deg
    I(1) = 0.566538605; % for 95 deg corner angle (see Fig A.1)
    I(3) = 1.172829246;

    for i=1:num_mat
        if mat(i) == "270" % single hat specimen (Ohkubo et al., 1974)
            % constants for single hat
            A1 = 32*I(1);
            A2 = 2*alpha_f;
            A3 = 8*I(3);
            C = 332; % cross-section perimeter of single hat due to
                     % Ohkubo et al. (1974)

        else % all other UWaterloo specimens are double hat
            % constants for double hat
            A1 = 64*I(1);
            A2 = 16*alpha_f;
            A3 = 16*I(3);
            Z = 402.082; % mid-shell cross section perimeter of double hat
            C = Z/8;     % SE base length
        end

        geom_const(i,:) = [A1, A2, A3, C]; %return constants
    end
end
```

B.3.2. Hardening Model Function

The materials considered in the SE analysis, in addition to the die-quenched Ductibor® 1000-AS, constitute a long list of steel alloys, as shown in Table 22. The hardening models adopted for flow stress calculation of these alloys are (i) Modified Hockett-Sherby (Noder and Butcher, 2019), (ii) Voce (1948), (iii) Modified Generalized Voce (Zhumagulov, 2017), and (iv) power-law (Hollomon, 1945). The complete list of steel alloys, hardening models, as well as corresponding hardening coefficients used in the SE analysis is found in Table 22. These hardening models were incorporated in the source code as separate functions to calculate the flow stresses at a given plastic strain and documented below.

```
function [sig] = MHS(mat, ep, e_dot)
%% Compute flow stress for MHS hardening model
% Coefficients C1-C6 are defined in Table 22 in Appendix C

% Material indices:
% 1. Mild 270
% 2. Ductibor(r) 500-AS
% 3. Ductibor(r) 1000-AS
% 4. DP980

    C1 = [621.92, 742.17, 1183.57, 1092.54 ];
    C2 = [215.00, 397.63, 731.55, 615.99 ];
    C3 = [2.03, 10.00, 29.37, 11.54 ];
    C4 = [0.79, 0.57, 0.67, 0.5 ];
    C5 = [0, 256.39, 57.84, 333.25 ];
    C6 = [0.076, 0.011, 0.011, 0.00558];

    i=0; %initialize material index
    %set material index based on material
    if mat == "270"
        i = 1;
    elseif mat == "D500"
        i = 2;
        e_dot_ref = 0.01; %reference strain rate
    elseif mat == "D1000"
        i = 3;
        e_dot_ref = 0.01;
    elseif mat == "DP980_MAT1"
        i = 4;
        e_dot_ref = 0.001;
    end

    % find strain rate sensitivity multiplier
    if mat == "270" % cowper-symonds
        rate_multiple = 1 + 0.076*log(e_dot);
    else % johnson-cook
        rate_multiple = (1 + C6(i) * log(e_dot/e_dot_ref));
    end

    sig = ( C1(i) - (C1(i)-C2(i))*exp(-C3(i)*(ep).^C4(i))+C5(i) ...
```

```
            *sqrt(ep) ) * rate_multiple  ;
end

function [sig] = VOCE(ep, e_dot)
%% Compute flow stress for VOCE hardening model
% Coefficients C1-C7 are defined in Table 22 in Appendix C
% for Usibor(r) 1500-AS

    C1 = 1480.5;
    C2 = 1113.6;
    C3 = 0.0079;
    C7 = 0.0180;

    %C1 = 1388.6;
    %C2 = 1019.7;
    %C3 = 0.0069;
    %C7 = 0.0180;
    sig = ( C1 + (C2-C1)*exp(-ep/C3) ) * (1 + e_dot)^C7 ;
end

function [sig] = MGV(ep, e_dot)
%% Compute flow stress for Modified Generalized Voce (MGV) hardening model
% Coefficients C1-C7 are defined in Table 22 in Appendix C
% for DP980 MAT 2

    C1 = 887.7;
    C2 = 113.9;
    C3 = 282;
    C4 = 62.57;
    C6= 0.000732903;
    C7= 1.871237;
    e_dot_ref =0.001;

    sig = ( C1+(C2+C3*sqrt(ep)) .* (1-exp(-C4 .* ep)) ) * ...
          (1 + C6*log(e_dot/e_dot_ref)^C7) ;
end

function [sig] = POWER(ep, e_dot)
%% Compute flow stress for Power Law model
% Coefficients C1-C7 are defined in Table 22 in Appendix C
% for DP980 MAT 3

    C1 = 1318;
    C3 = 0.07403;
    C6 = 0.00052924414;
    C7 = 2.1791225848;
    e_dot_ref =0.001;

    sig = ( C1 * ep .^C3 ) * (1 + C6*log(e_dot/e_dot_ref)^C7) ;
end
```

Appendix C. List of Alloys and Hardening Models for SE Analysis

This appendix serves as documentation to list all the materials and their corresponding hardening models considered in the Superfolding Element Analysis. A total number of seven different steel alloys were considered. Their names and the hardening models (as well as characterized coefficients) are listed in Table 22.

Table 22: Quasi-static hardening models and strain rate sensitivity functions for flow stress calculation of different materials. Note that all hot-stamping materials listed here were die-quenched at 13°C after heating in the oven above 930 for 6 minutes, minimum.

Material	Quasi-static hardening model (QS)	C_1 (MPa)	C_2 (MPa)	C_3	C_4	C_5 (MPa)	R-sq	Strain rate function (RATE)	C_6	C_7	$\dot{\varepsilon}_{ref}$ (s^{-1})
270 MPa grade Mild steel	MHS (Noder *et al.*, 2020)	622	215	2.03	0.79	0	0.984	Johnson-Cook (Vedantam *et al.,* 2005)	0.076	-	1
Ductibor® 500-AS	MHS (Samadian *et al.*, 2020)	742	398	10	0.57	256	0.9997	Johnson-Cook	0.011	-	0.001
Ductibor® 1000-AS	MHS (Abedini, 2018)	1184	732	29.37	0.67	58	0.999	Johnson-Cook	0.011	-	0.01
Usibor® 1500-AS	Voce (Bardelcik *et al.*, 2012)	1481	1114	0.0079	-	-	0.95	Borvik	-	0.018	1
DP980 MAT1	MHS (Noder and Butcher, 2019)	1093	616	11.54	0.50	333	0.993	Modified Johnson-Cook			0.001
DP980 MAT2	Power law (Zhumagulov *et al.*, 2018)	1233	-	0.0533	-	-	-	Modified Johnson-Cook	0.00073	1.8712	0.001
DP980 MAT3	Power law (Zhumagulov *et al.*, 2018)	1318	-	0.073	-	-	-	Modified Johnson-Cook	0.00053	2.1791	0.001

The flow stress was calculated by assuming a multiplicative form of a quasi-static hardening law (QS) and a strain-rate sensitivity function ($RATE$) as follows

$$\bar{\sigma} = QS\left(\bar{\varepsilon}_p\right) * RATE\left(\dot{\varepsilon}, \dot{\varepsilon}_o\right) \tag{C.1}$$

in which $\bar{\varepsilon}_p$ is equivalent plastic strain, $\dot{\varepsilon}$ is current strain rate, $\dot{\varepsilon}_o$ is the reference strain rate, and the quasi-static hardening model (QS) is defined in following forms

$$QS = \begin{cases} C_1 - \left(C_1 - C_2\right)\exp\left(-C_3\left(\bar{\varepsilon}_p\right)^{C_4}\right) + C_5\sqrt{\bar{\varepsilon}_p} & \{\text{MHS}\} \\ C_1 + \left(\left(C_2 - C_1\right)\exp\left(\dfrac{\bar{\varepsilon}_p}{C_3}\right)\right) & \{\text{Voce}\} \\ C_1\left(\bar{\varepsilon}_p\right)^{C_3} & \{\text{Power Law}\} \end{cases} \tag{C.2}$$

in which C_1 to C_7 are material constants listed in Table 22. The strain rate sensitivity function, $RATE$, is defined below.

$$RATE = \begin{cases} 1 + C_6 \ln\left(\dfrac{\dot{\varepsilon}}{\dot{\varepsilon}_o}\right) & \{\text{Johnson-Cook}\} \\ \left(1 + \dfrac{\dot{\varepsilon}}{\dot{\varepsilon}_o}\right)^{C_7} & \{\text{Borvik}\} \\ 1 + C_6 \ln\left(\dfrac{\dot{\varepsilon}}{\dot{\varepsilon}_o}\right)^{C_7} & \{\text{Modified Johnson-Cook}\} \end{cases} \tag{C.3}$$

Next, Table 23 lists the energy equivalent flow stress used for calculating the theoretical plastic work ($W_{SE,bend}$) by the SE horizontal bending region in Chapter 5. The energy equivalent flow stress ($\sigma_{SE,bend}$) was calculated using Equation (A.2.2) for each material. Once $\sigma_{SE,bend}$ was calculated, $W_{SE,bend}$ was found by Equation (A.2.9) and (A.2.10). For the current analysis, α_f was assumed as $\pi/2$.

Table 23 List of energy equivalent flow stress in horizontal bending region of the SE (numbered 2 and 5 in Figure A.1), calculated using Equation (A.2.2) for the considered materials.

Material	Thickness (mm)	Energy Equivalent Flow Stress, $\boldsymbol{\sigma_{SE,bend}}$ (MPa)
270 MPa grade Mild steel (Noder *et al.*, 2020)	1.6	336
Ductibor® 500-AS (Samadian *et al.*, 2020)	1.6	830
Ductibor® 1000-AS (Abedini, 2018)	1.2	1273
Usibor® 1500-AS (Bardelcik *et al.*, 2012	1.2	1558
DP980 MAT1 (Noder and Butcher, 2019)	1.2	1189
DP980 MAT2 (Zhumagulov *et al.*, 2018)	1.6	1121
DP980 MAT3 (Zhumagulov *et al.*, 2018)	1.4	1156

Appendix D. Simplified Approximation of Relative Bending Limit

Appendix D serves to document the derivation procedure for a simplified solution for the Relative Bending Limit (χ_{bend}) introduced in Chapter 5. The current analysis derived here considered a limited range of steel alloys. Thus, the application of the derived equations beyond this range of materials needs to be validated and remains for future work.

For reference, the full solution for χ_{bend} introduced in Chapter 5 is given as follows

$$\chi_{bend} = \frac{W_{v-bend}}{W_{SE,bend}} = \frac{\frac{1}{w}\int_0^{\theta_f} M_{v-bend} d\theta}{\left(\frac{2}{\varepsilon_{SE,bend}^2}\int_0^{\varepsilon_{SE,bend}} \bar{\sigma}\left(\bar{\varepsilon}_p\right)\bar{\varepsilon}_p d\bar{\varepsilon}_p\right)\frac{t^2}{4}} \tag{D.1}$$

Calculating the Relative Bending Limit using Equation (D.1) poses complexity in terms of (i) obtaining V-bend plastic work evolution and (ii) solving for SE energy equivalent flow stress. To this end, a need arises for simple solution. To approximate a closed-form solution of the Relative Bending Limit, approximations for the SE bending plastic work ($W_{SE,bend}$) and v-bend plastic work (W_{v-bend}) first need to be derived.

D.1. Approximate Solution for W_{SE}

The approximation procedure of $W_{SE,bend}$ is relatively short and begins with simplifying the energy equivalent flow stress

$$\sigma_{SE,bend} = \frac{2}{\varepsilon_{SE,bend}^2}\int_0^{\varepsilon_{SE,bend}} \bar{\sigma}\left(\bar{\varepsilon}_p\right)\bar{\varepsilon}_p d\bar{\varepsilon}_p \tag{D.2}$$

in which one could assume its hardening function as a power law, $\bar{\sigma} = K\left(\bar{\varepsilon}_p\right)^n$. Rewriting Equation (D.2) gives

$$\sigma_{SE,bend} = \frac{2}{\varepsilon_{SE,bend}^2}\int_0^{\varepsilon_{SE,bend}} K\left(\bar{\varepsilon}_p\right)^n \bar{\varepsilon}_p d\bar{\varepsilon}_p \tag{D.3}$$

whose closed form solution exists when the hardening exponent (n) is not -2, which would be non-physical. As such, solving the integral and rearranging the terms in Equation (D.3) yields

$$\sigma_{SE,bend} = \frac{2K\left(\varepsilon_{SE,bend}\right)^n}{n+2} \tag{D.4}$$

Finally, the derivation for $W_{SE,bend}$ is obtained by the following relations

$$W_{SE,bend} = M_{SE,bend}\alpha_{SE,f} \tag{D.5}$$

$$M_{SE,bend} = \frac{\sigma_{SE,bend}t^2}{4} \tag{D.6}$$

Combining Equations (D.4) and (D.6) with Equation (D.5) gives

$$W_{SE,bend} = \frac{K\left(\varepsilon_{SE,bend}\right)^n t^2}{2\left(n+2\right)}\alpha_{SE,f} \tag{D.7}$$

D.2. Approximate Solution for W$_{\text{v-bend}}$

D.2.1. Weak Work Hardening Assumption

As for the closed-form approximation of W_{v-bend}, one could adopt a phenomenological modelling approach. For weak work hardening materials ($n \ll 0.2$), the v-bend plastic work evolves linearly with θ, as shown in Figure 136c. Furthermore, the bending moment of a sheet metal is assumed to be a function of t^2 which gives the approximate form of

$$W_{v-bend} = \int_0^{\theta_f} Md\theta \approx \theta_f a_1 t^2 \tag{D.8}$$

in which a_1 is a calibration constant. Figure D.1 shows a plot of $\frac{W_{v-bend}}{t^2}$ plotted against θ_f for all materials whose hardening exponent is below 0.2. Note that mild 270 MPa grade steel has a hardening exponent of 0.271. As a result, it is not considered here but in the subsequent analysis that considers strong work hardening assumption.

The calibration constant, a_1, corresponds to the slope of a linear fit (dashed line in Figure D.1) which is 5.56 kJ/(m$^3\cdot°$).

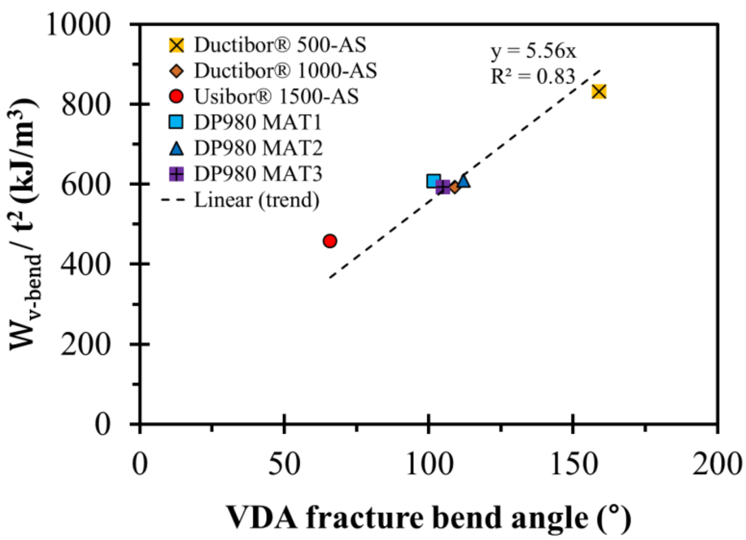

Figure D.1: θ_f vs. W_{v-bend}/t^2 for all materials whose hardening exponent is below 0.2. Mild 270 steel grade, whose uniform elongation is 0.271 (Noder *et al.*, 2020), is excluded here. The dashed line represents a line of best fit.

Combining Equation (D.8) and Equation (D.7) with Equation (D.1) yields the final closed form of the Relative Bending Limit (χ_{bend}) for materials with weak work-hardening:

$$\chi_{bend} = \frac{W_{v-bend}}{W_{SE,bend}} = \left[\frac{a_1\theta_f}{2K/(n+2)}\right]\left[\frac{8}{\alpha_{SE,f}}\right] \tag{D.9}$$

in which the first term in parentheses is related to the material properties from the v-bend and tensile test, while the second term reflects the final bend angle during the crush of the SE and is largely controlled by the geometry of the SE. Since the considered materials exhibit a low work hardening exponent ($n \approx 0 \ll 0.2$), the first term can be further simplified to a dimensionless parameter:

$$\chi_{bend} \propto \frac{a_1\theta_f}{K} \tag{D.10}$$

which is a scaled form of Relative Bending Limit, as shown in Figure D.2. Therefore, if the characterized tensile properties (*e.g.* the power-law strength coefficient, K) and the v-bend test results (*e.g.* fracture angle, θ_f) are known for a given material, it becomes possible to quantify the bending performance, gauge the fracture severity in the axial crush, and ultimately predict the Crush Energy Efficiency based on the linear correlation shown in Figure 138.

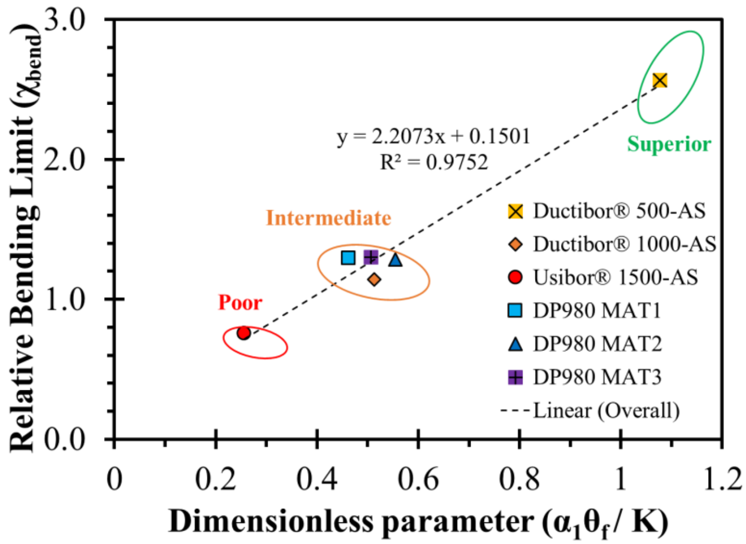

Figure D.2: Relative Bending Limit (χ_{bend}) *vs.* $a_1\theta_f/K$ in Equation (D.9). The different levels of fracture severity are commented. The dotted line represents the linear line of best fit.

D.2.2. Strong Work Hardening Assumption

As for a closed-form solution of W_{v-bend} that accounts for strongly work-hardening materials, one can adopt an analytical approach in which the plastic bending moment (M_p) is given from a mathematical plane-strain bending model (Wang *et al.* 1993) in terms of

$$M_p = \int_0^{\varepsilon_{max}} KF^{n+1}(\varepsilon_1)^n R_n (e^{\varepsilon_1} - 1) R_n e^{\varepsilon_1} d\varepsilon_1 \tag{D.11}$$

in which ε_{max} is the maximum outer tensile strain, F is an calibration parameter for anisotropic material which takes a value of $2/\sqrt{3}$ for isotropic material, R_n is the neutral radius, defined as $R_n = \sqrt{R_i R_o} \approx \sqrt{R_i(R_i + t)}$, and ε_1 is the tensile strain (major) across the sheet thickness. Note that K and n are strength and strain hardening parameters of the power-law consistently used throughout the section. By casting a Taylor series expansion, $e^{\varepsilon_1} = \sum_{j=0}^{\infty} \frac{\varepsilon_1^j}{j!}$, the theoretical plastic bending moment at the punch tip is obtained as follows (Wang *et al.,* 1993):

$$M_p = 2F^{n+1} K R_n^2 \sum_{j=0}^{\infty} \left\{ \frac{(2^j - 1)(\varepsilon_{max})^{j+n+1}}{(j+n+1)\, j!} \right\} \tag{D.12}$$

Furthermore, the plastic bending moment can be roughly estimated by the first two terms of the Taylor series and assuming $\varepsilon_{max} = \ln{(R_o/R_n)} \approx t/2R_n$, which gives

$$M_p \approx \frac{2KF^{n+1}}{(n+2)}\left(\frac{1}{R_n}\right)^n\left(\frac{t}{2}\right)^{n+2} \tag{D.13}$$

We proceed with the fully plastic bending approximation to formulate the measured v-bend plastic work (W_{v-bend}) in terms of the plastic moment (M_p) obtained from Equation (D.13):

$$W_{v-bend} = \int_0^{\theta_f} M d\theta \approx A_1 M_p \theta_f \tag{D.14}$$

in which A_1 is a calibration parameter, expressed as a ratio between the measured plastic work (W_{v-bend}) to the theoretical plastic work ($M_p\theta_f$), as shown in Figure D.3. Interestingly, the new proposed model in Equation (D.14) shows a close approximation of the measured v-bend plastic work (*i.e.* $R^2 = 0.931$), which justifies the fully plastic approximation and the assumed form in Equation (D.14).

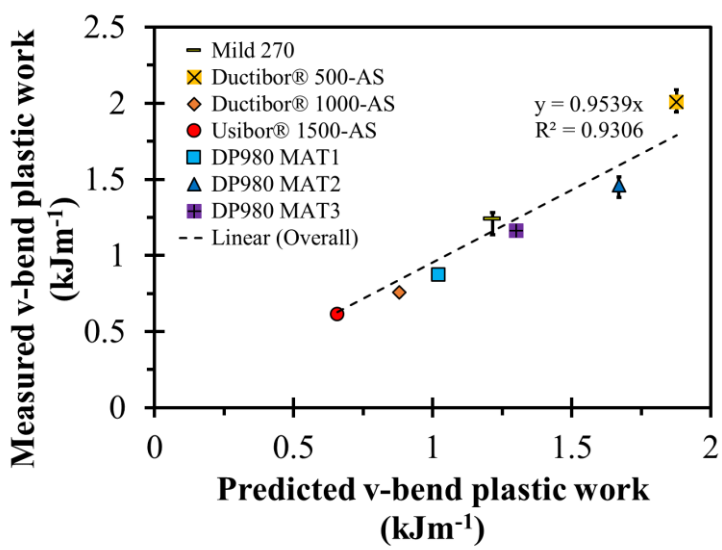

Figure D.3: Response plot of the predicted *vs.* measured v-bend plastic work, showing a good, linear correlation. The predicted v-bend plastic works for all materials are calculated using Equation (D.13) and (D.14) .

Combining the new proposed expression of v-bend plastic work in Equation (D.14) with that of the SE horizontal bend work in Equation (D.7) into Equation (D.1) yields a final closed-form solution of Relative Bending Limit for all work hardenable materials:

$$\chi_{bend} = \frac{W_{v-bend}}{W_{SE,bend}} = \left[\frac{4}{\varepsilon_{SE,bend}^{n}\alpha_{SE,f}}\right]\left[F\frac{t}{2R_n}\right]^{n}\left[A_1 F\theta_f\right] \tag{D.15}$$

Unlike the previous solution for weak work-hardening materials, the new solution shows a very strong dependence on the hardening exponent (n), as shown in Figure D.4.

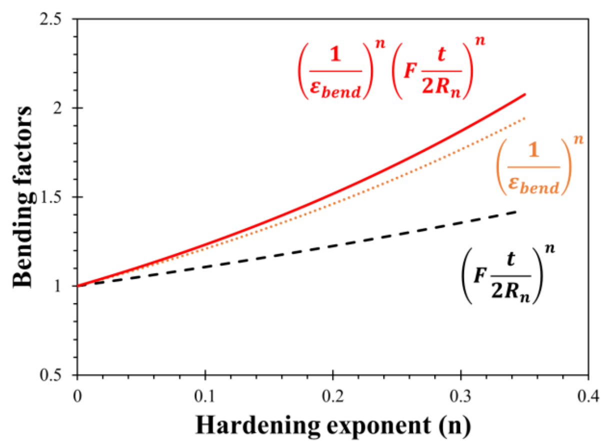

Figure D.4: Different terms in Equation (D.15) plotted against the hardening exponent (n).

Appendix E. High Strain Rate Tensile Test

Appendix E serves as documentation for the measured tensile stress *vs.* strain responses and strain rates from the High Strain Rate Tensile (HISR) tests and the Hopkinson bar test of die-quenched Ductibor® 1000-As. These tests were conducted by Imbert and Zhumagulov (2019) as part of the broader material characterization project. Figure E.1 shows the stress-strain curves obtained from these tests, which cover the nominal equivalent strain rate of 1, 10, 100, and 1000 s^{-1}.

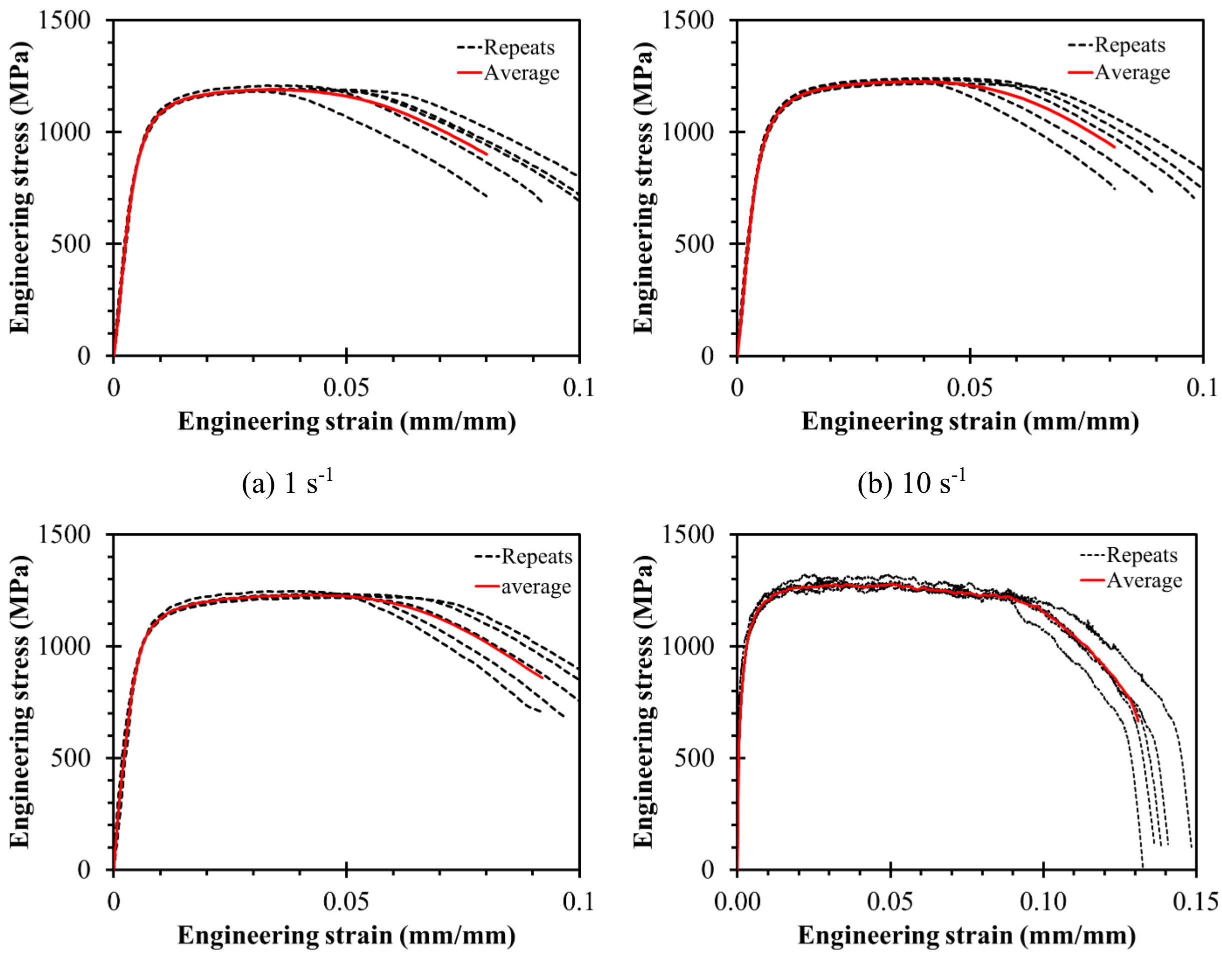

(a) 1 s^{-1} (b) 10 s^{-1} (c) 100 s^{-1} (d) 1000 s^{-1}

Figure E.1: Measured tensile stress *vs.* strain responses at nominal strain rate of (a) 1 s^{-1} (b) 10 s^{-1} (c) 100 s^{-1} high strain rate tensile tests and (d) Hopkinson bar test with 1000 s^{-1}. Five repeats were conducted for each test (Imbert and Zhumagulov, 2019).

In the interest of measuring the actual strain rates during these tests, the strain rates in major strain direction ($\dot{\varepsilon}_i$) were estimated from using the following relation

$$\dot{\varepsilon}_i = \frac{\varepsilon_{1,i} - \varepsilon_{1,i-1}}{t_i - t_{i-1}} \tag{E.1}$$

In which $\varepsilon_{1,i}$ is the measured major true strain and t_i is the time at the i^{th} index. By using Equation (E.1), strain rate was estimated for each repeat case, and the overall interpolated strain rate was obtained by taking the average. Figure E.2 shows the measured strain rate *vs.* equivalent plastic strain responses for each test condition.

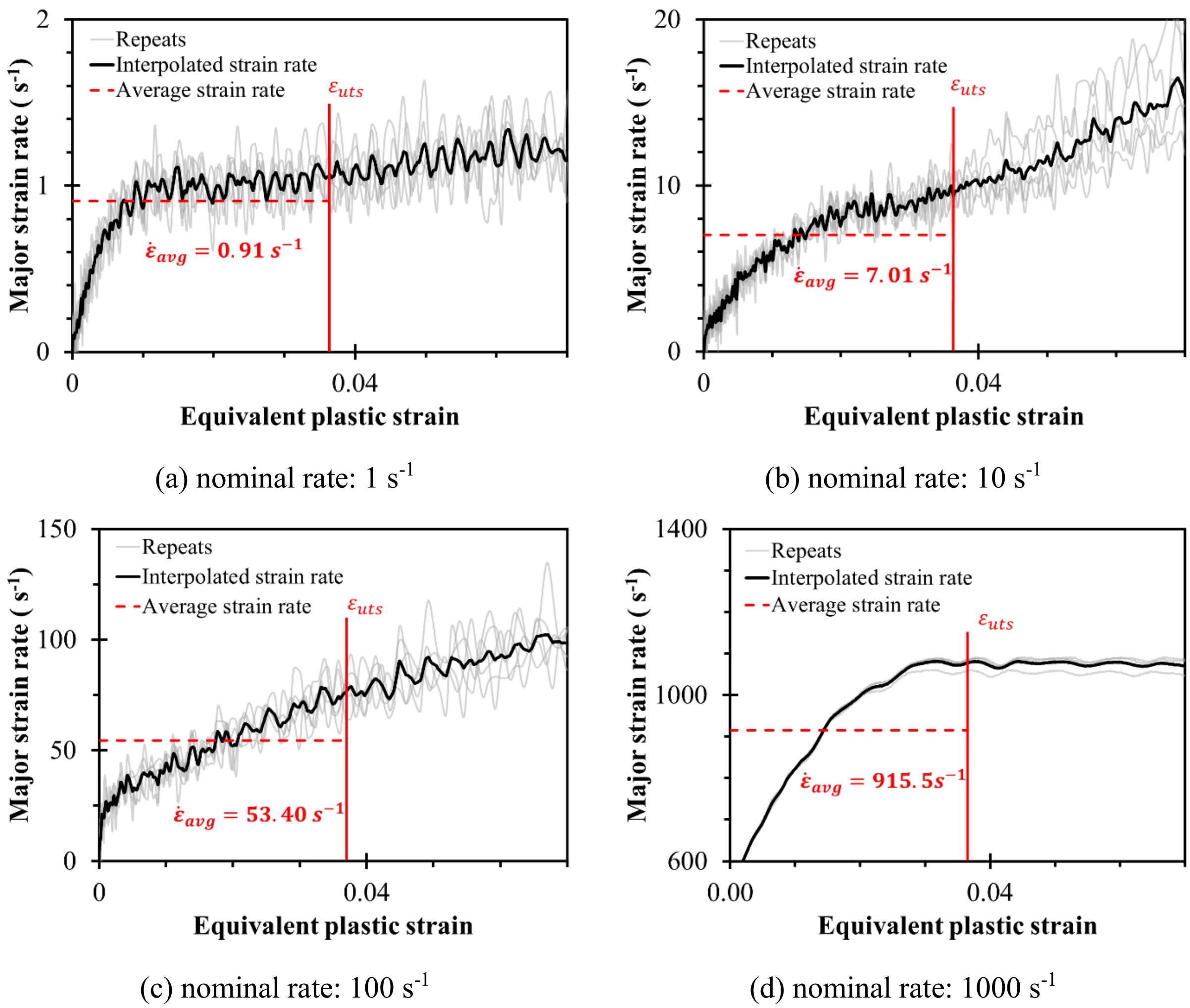

Figure E.2: Measured strain rates for tensile tests at nominal strain rate of (a) 1 s^{-1} (b) 10 s^{-1} (c) 100 s^{-1} and (d) Hopkinson bar test with 1000 s^{-1}. Five repeats were conducted for each test.

The average of each interpolated strain rate was taken up to the plastic strain of 0.036 (equivalent to 0.04 engineering strain, approximately). The measured average strain rates calculated for each test conducted at nominal rate of 1, 10, 100, 1000 s^{-1} were 0.91, 7.01, 53.40, 915.5 s^{-1}.

Appendix F. FE Model Description and Results of Nakazima 50 mm Biaxial Dome Test

Appendix F documents the finite element (FE) model setup of the 50 mm Nakazima dome test. The model was developed as part of the FE mesh regularization process in which the so-called regularization factor for experimental fracture *locus* is determined by matching the predicted and measured limiting dome height (LDH) responses. A detailed description of the regularization process is found in Chapter 3.

The original numerical model of the dome test was developed by Omer and Rahmaan (2019) and modified as part of the thesis work. The significance of the new model is on incorporating the lock bead geometry of the forming die and binder, as well as the shims used during the Nakazima dome test by Samadian (2018). The punch load *vs.* dome height responses with and without the lock bead and shim are presented at the end of the appendix.

F.1. Boundary Condition

The finite element model setup of the 50 mm Nakazima dome test consists of blank, upper die, lower binder, punch and shim, as shown in Figure F.1. Quarter symmetry was imposed about the x-y plane and y-z plane.

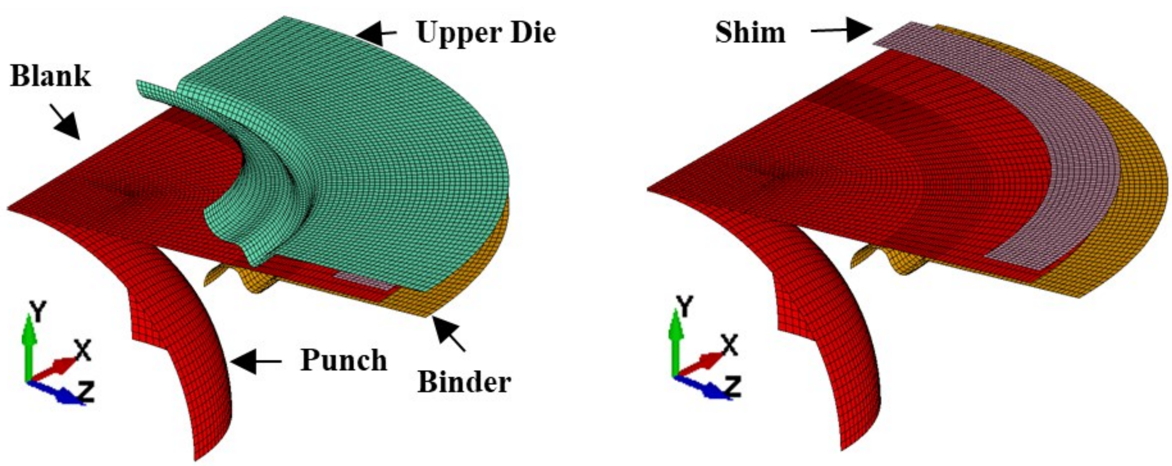

(a) Overall model setup (b) model setup, highlighting shim

Figure F.1: Numerical model for the Nakazima 50 mm dome simulations: (a) overall setup and (b) setup, highlighting shim. Quarter symmetry were imposed about x-y plane and y-z plane.

The binder load of 175 kN was given in y-direction, while the upper die was fully constrained in all degrees of freedom. Upon closure of the die with the blank, the punch was given a constant motion in y-direction at 250 mm/s. Note the magnitude of punch speed is 1000 times the scaled value of 0.25 mm/s, the actual punch speed in the experiment, for time scaling. To account for the increased punch speed, strain rates of the hardening curves were also scaled by 1000, accordingly. An additional approach in decreasing the solving time was applying selective mass scaling by dt2ms keyword in LS-Dyna. The keyword was assigned a value of -1.0e-6 s, which artificially increases the density of elements whose critical time step is below 1.0e-6 (Livermore Software Technology Corporation).

F.2. Material model and Mesh

The material model used for each part is listed in Table 24.

Table 24 List of LS-Dyna material models used in the Nakazima dome model

	Part	Material Model
1	Blank	PIECEWISE_LINEAR_ PLASTICITY
2	Binder	RIGID
3	Upper Die	RIGID
4	Punch	RIGID
5	Shim	ELASTIC

All parts are meshed using type 16, 4 node quadrilateral elements with seven through-thickness integration points. The element sizes of binder, upper die, punch, and shim were selected as an order of magnitude smaller than the blank. The element thickness for tools was given 1.15 mm, while that of the shim was given a thickness of 2.0 mm to represent the total thickness of shims used in the Nakazima test (Samadian, 2018). For the blank, four element sizes were considered, which range from 5.0 mm to 0.6 mm, as shown in Figure F.2. Note that the region between 60 mm and 75 mm radii was meshed with smaller element size to ensure the proper contact with the lock bead surface of the forming die and binder.

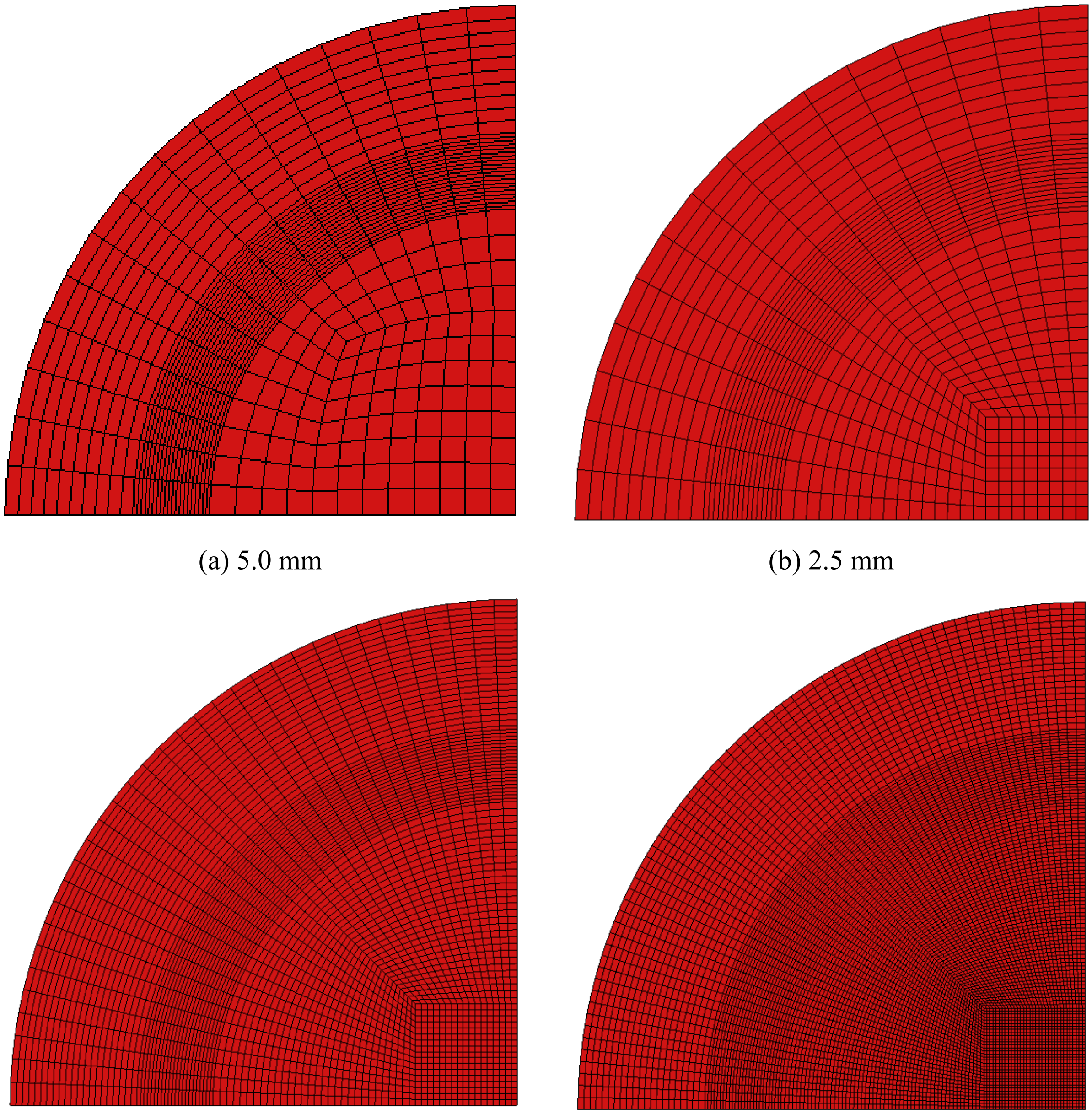

(a) 5.0 mm

(b) 2.5 mm

(c) 1.2 mm

(d) 0.6 mm

Figure F.2: Four different blank mesh sizes considered in the dome simulations: (a) 5.0 mm, (b) 2.5 mm, (c) 1.2 mm, and (d) 0.6 mm. The region between 60 mm and 75 mm radii was meshed finely.

F.3. Contact Algorithm

All contact algorithms used in the numerical model are penalty-based and are listed in Table 25. Additionally, the soft=2 option in LS-Dyna was applied to all contact definitions, except between blank and punch, to invoke a segment-based penalty formulation. This option provides special treatment for cases of edge-to-surface interface or edge-to-edge interface, which otherwise can be un-detected in the standard penalty-based (*i.e.,* node-based) contact algorithm, and thus, result in unrealistic penetrations. Such treatment was applied to all contact incidents that involve the sharp radius of lock bead profile, as illustrated in Figure F.1a. A more detailed explanation of the soft=2 option can be found in the LS-Dyna manual (Livermore Software Technology Corporation, 2016). Lastly, a friction coefficient (μ) of 0.25 was assigned to all contact definitions.

Table 25: A list of LS-Dyna contact keywords used for 50 mm Nakazima dome models. The Soft=2 algorithm (LSTC, 2016) was assigned to all contact incidents that involve the lock bead profile in the forming die and binder.

	Slave	Master	Contact
1	Shim	Die	AUTOMATIC_SURFACE_TO_SURFACE
2	Blank	Shim	AUTOMATIC_SURFACE_TO_SURFACE
3	Blank	Punch	FORMING_ONE_WAY_SURFACE_TO_SURFACE
4	Blank	Die	AUTOMATIC_SURFACE_TO_SURFACE
5	Blank	Binder	FORMING_ONE_WAY_SURFACE_TO_SURFACE

F.4. Results

F.4.1. Damage Contour Plot

The predicted damage (D) contour plot for the 50 mm blank is taken at the measured limiting dome height (24.0 mm) for each element size and shown in Figure F.3. All numerical models reveal a similar trend in that the damage (D) is maximum at the dome apex and decreases moving radially away from the apex. The radius of dome apex region at which $D = 1$ also decreases with the blank element size.

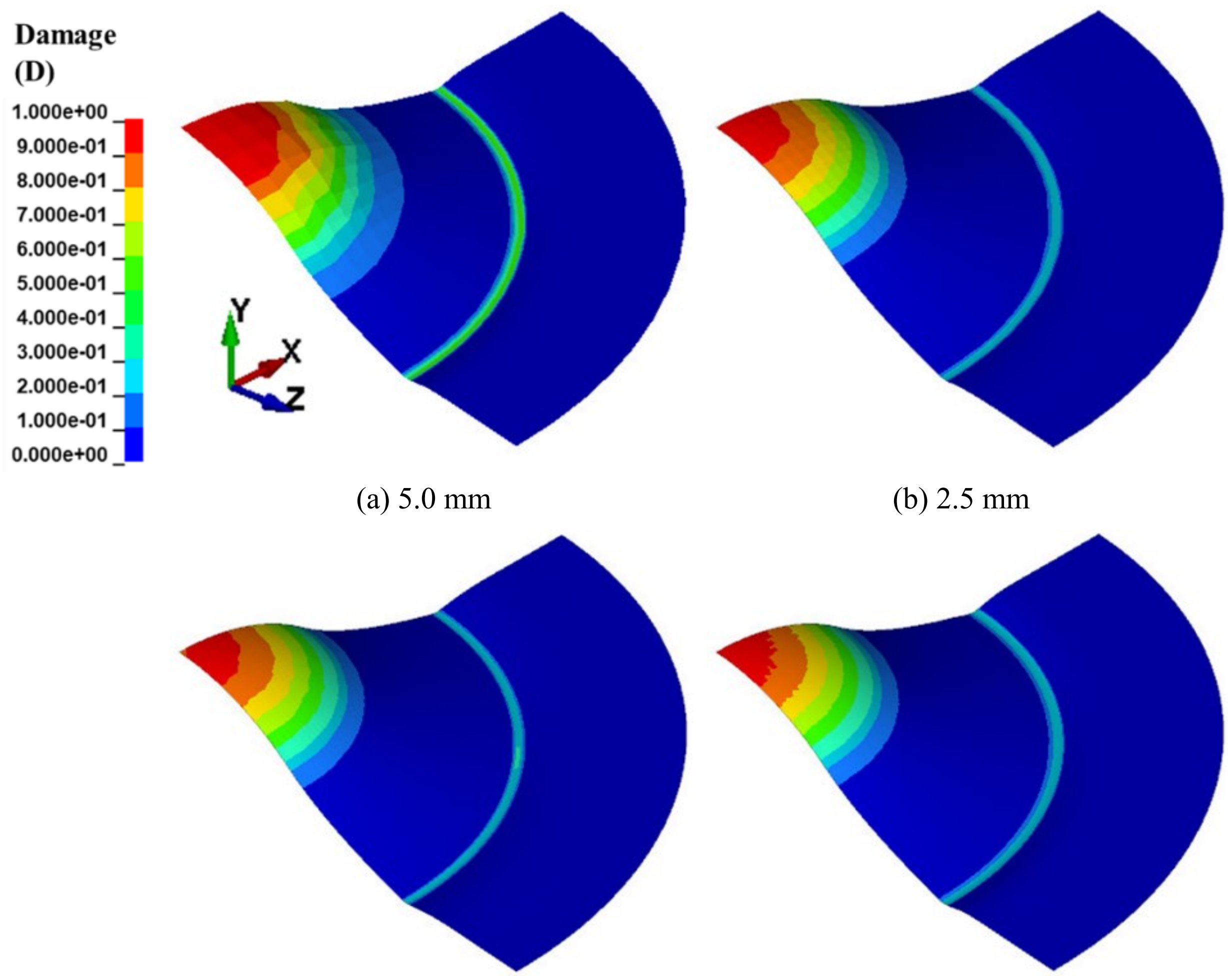

(a) 5.0 mm (b) 2.5 mm

(c) 1.2 mm (d) 0.6 mm

Figure F.3: Damage (D) contour plot of the 50 mm blanks, whose element sizes range from (a) 5.0 mm to (d) 0.6 mm. The images are taken at the measured (average) limiting dome height, which is 24.0 mm, approximately, reported by Samadian (2018).

F.4.2. Punch Force *vs.* Punch Height

The predicted punch force *vs.* punch height responses for simulations of all element sizes are shown in Figure F.4, along with the measured response by Samadian (2018). Next to the predicted responses of the models with the lock bead geometry and shim are those without the lock bead geometry and shim for comparison. As evidenced in the figure, incorporating the lock bead and shim has a significant effect on the predicted force trend. The predicted forces at limiting dome height are minimum 128 kN and 140 kN in the former and latter numerical models, respectively, giving a difference of 12 kN.

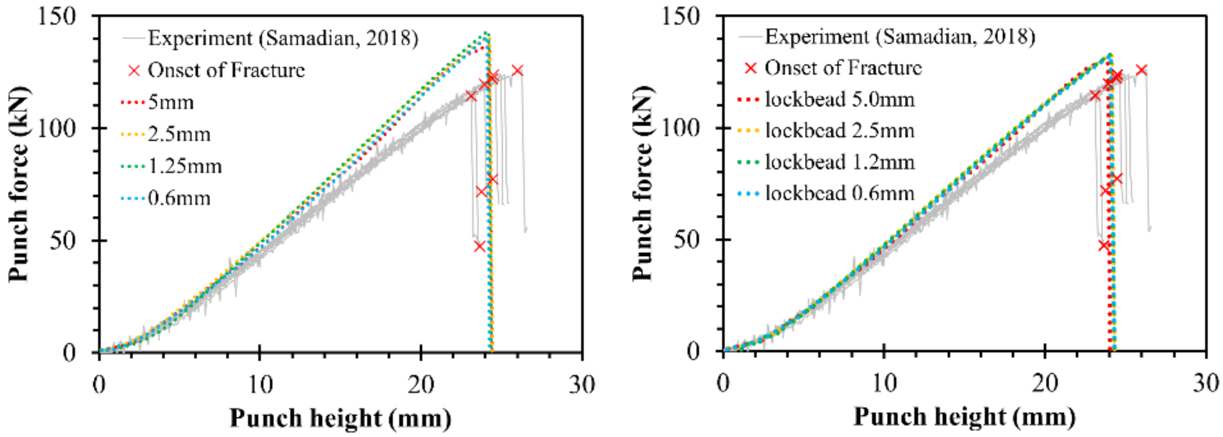

(a) Without lockbead and shim (b) With lockbead and shim

Figure F.4: Predicted punch force *vs.* punch height responses for Nakazima dome (50 mm) models of die-quenched Ductibor® 1000-AS: (a) numerical model without the lockbead and shim (b) model with lockbead and shim. The measured test results by Samadian (2018) are overlaid for comparison.